Universität Rostock

Traditio et Innovatio

Spherically symmetric continuum approach to the simulation of molecular ionization processes

Kumulative Dissertation

zur Erlangung des akademischen Grades

doctor rerum naturalium (Dr. rer. nat.)

der Mathematisch-Naturwissenschaftlichen Fakultät
der Universität Rostock

vorgelegt am 10. Dezember 2019 in Rostock

von

GILBERT GRELL,

geboren am 25. Februar 1990 in Schwerin

@ɔq • KɐƉà[à̧¦* ƀƑ€ɖ̀Ì ̀ì í H Ɖ[• å[\´ ã€€€Ɔî Í H

DISSERTATION

MATHEMATISCH-NATURWISSENSCHAFTLICHE FAKULTÄT

Die vorliegende kumulative Dissertation wurde am 07.02.2020 im Rahmen eines öffentlichen wissenschaftlichen Kolloquiums am Institut für Physik der Universität Rostock erfolgreich verteidigt.

Abstract

Photoionization and autoionization lead to the emission of electrons whose kinetic energy encodes the electronic structure of the parent system. The widespread photoelectron and autoionization spectroscopic techniques employ this effect to decipher the electronic structure of molecules in the full range of excitation states and in particular during ultrafast dynamical processes. The usually complicated and feature rich experimental spectra, however, can often not be unambiguously assigned and interpreted without support from theoretical modeling.

This thesis is dedicated to the development of a numerically efficient protocol to evaluate molecular photoionization cross sections and autoionization rates. Such simulations require an accurate quantum mechanical description of the continuum orbital of the outgoing electron and the wave function of the remaining bound system. In particular, many molecules of current scientific interest, such as transition metal compounds, require a multiconfigurational treatment and possibly the inclusion of spin-orbit coupling effects, if core excitations play a role, to obtain the bound electronic structure, which is carried out herein with the restricted active space family of quantum chemistry methods. For such molecules, however, the continuum orbital can usually only be treated at the most approximate levels. These comprise the so called sudden approximation, completely neglecting it, and either disregarding the molecular potential completely or modeling it as an effective point charge, leading to analytic expressions for the continuum orbital. These models have been tested for the evaluation of X-ray core photoelectron spectra from aqueous Fe^{2+} and I_3^- ions, where an occupation number analysis that facilitates the assignment of such spectra despite the strong multi-configurational and spin-orbit coupling effects has been demonstrated as well. Further, the ultrafast spin crossover mechanism in the iron tris-bipyridine complex has been unraveled with their aid.

Although these approaches are usually well applicable to model core ionization spectra, they might be insufficient to treat ionization from valence orbitals and autoionization in general, as underlined in this thesis. To bridge the gap between these simple continuum orbital models and the accurate but numerically unfeasible multi-centered ones, this work suggests to numerically construct spherically symmetric continuum orbitals that take into account the spherically averaged molecular potential of the leftover ion. This approach has been applied herein to the simulation of photoelectron and autinization spectra of atoms and small second row molecules as a first benchmark, yielding promising results. Overall, the spherically symmetric continuum orbital approach is versatile method for deciphering molecular photoionization and autoionization processes in a numerical tractable way, opening up a broad scope of possible applications.

Zusammenfassung

Photo- und Autoionisationsprozesse führen zur Emission von Elektronen, deren kinetische Energie ein Abbild der Elektronenstruktur des ursprünglichen Systems enthält. Die verbreiteten Techniken der Photoelektronen- und Autoionisationsspektroskopie nutzen dies um die Elektronenstruktur von Molekülen in allen Anregungszuständen und insbesondere während ultraschneller dynamischer Prozesse zu entschlüsseln. Die häufig komplizierten experimentellen Spektren können allerdings oft nicht ohne simulationsseitige Unterstützung zweifelsfrei charakterisiert und interpretiert werden.

Diese Dissertation widmet sich der Entwicklung einer numerisch günstigen Methode zur Berechnung molekularer Photoionisationsquerschnitte und Autoionisationsraten. Solche Simulationen verlangen die quantenmechanisch korrekte Beschreibung sowohl des Kontinuumsorbitals des ausgehenden Elektrons, als auch der Wellenfunktion des verbleibenden gebundenen Systems. Insbesondere viele Moleküle von wissenschaftlichem Interesse, wie Übergangsmetallkomplexe, verlangen jedoch das Einbeziehen von Multikonfigurations- und Spin-Bahn Kopplungseffekten (sofern Rumpfanregungen eine Rolle spielen) um ihre Elektronenstruktur zu berechnen, was in der vorliegenden Arbeit mit Quantenchemiemethoden aus der „restricted active space" Familie vollführt wurde. Für solche Moleküle kann jedoch das Kontinuumsorbital in der Regel nur im Rahmen gröbster Näherungen modelliert werden. Dabei handelt es sich um die „sudden approximation", worin das Kontinuumsorbital vernachlssigt wird, sowie die Möglichkeit das molekulare Potential entweder vollständig zu vernachlässigen oder es durch eine Punktladung anzunähern, was zu analytischen Darstellungen des Kontinuumsorbitals führt. Diese Modelle sind für die Simulation von Röntgen-Rumpf-Photoelektronenspektren von in Wasser gelösten Fe^{2+} und I_3^- Ionen angewand worden, wobei eine spezielle Besetzungszahlanalyse, welche die Charakterisierung solcher Spektren trotz der starken Multikonfigurations- und Spin-Bahn Kopplungseffekte ermöglicht, demonstriert wurde. Des weiteren konnte mit ihrer Hilfe der ultraschnelle Spin-Flip Mechanismus im Eisentrisbipyridinkomplex entschlüsselt werden.

Obwohl sich diese Methoden sehr gut eignen um Rumpf-Ionisationsspektren zu modellieren, eignen sie sich häufig nicht um Ionisation aus Valenzorbitalen, sowie Autoionisation im Allgemeinen zu beschreiben. Um die Lücke zwischen den einfachsten Näherungen an das Kontinuumsorbital, sowie den genauen, aber numerisch nicht leistbaren Multizentrenmethoden zu schließen, schlägt diese Arbeit vor kugelsymmetrische Kontinuumsorbitale zu konstruieren, welche das sphärisch gemittelte Potential des Ions beachten. Dieser Ansatz wurde hier im Rahmen einer ersten Anwendung anhand der Simulation von Photoelektronen- und Autoionisationsspektren atomarer sowie kleiner molekularer Systeme aus der zweiten Periode mit vielversprechenden Resultaten getestet. Im Allgemeinen ist der sphärische Kontinuumsansatz ein vielfältiges Werkzeug um molekulare Photo- und Autoionisationsprozesse in einer numerisch handhabbaren Weise zu entschlüsseln, was ein weites Feld an möglichen Anwendungen eröffnet.

Table of abbreviations

1CA one-center approximation

2CA two-center approximation

2RTD two-electron reduced transition density

AES Auger electron spectrum

AIS autoionization spectrum

CI configuration interaction

DFT density functional theory

DO Dyson orbital

ETMD electron transfer mediated decay

FANO-ADC Fano-Stieltjes algebraic diagrammatic construction

FWHM full width at half maximum

GS Gram-Schmidt

GTO Gaussian-type orbital

HHG high harmonic generation

ICD interatomic Coulombic decay

IP ionization potential

MLCT metal-to-ligand charge-transfer

NO nonorthogonality

PES photoelectron spectrum

PT2 second-order perturbation theory

QC quantum chemistry

RAES resonant Auger electron spectrum

RAS restricted active space

RASPT2 restricted active space second-order perturbation theory

RASSCF restricted active space self-consistent field

RASSI restricted active space state interaction

SA sudden approximation

SCF self-consistent field

SCI spherical continuum for ionization

SD Slater determinant

SE Schrödinger equation

SO strong orthogonality

SOC spin-orbit coupling

TDA Tamm-Dancoff aproximation

TDDFT time-dependent density functional theory (DFT)

TME transition matrix element

UV/vis ultraviolet/visible

XFEL X-ray free-electron laser

XUV extreme ultraviolet

Contents

1 Introduction

Ionization in the most general sense encompasses all processes in which neutral atoms or molecules acquire a charge. Negatively charged species (anions) are created by capturing slow electrons [1], while positively charged cations are the result of imparting energy larger than the so called ionization potential (IP) into the system, propelling one or multiple electrons out of the compound [2]. For instance, extreme temperatures and electromagnetic fields can strip the electrons from the nuclei forming a plasma, which is the most abundant state of stellar matter, occuring naturally in e.g. lightning bolts and polar lights, and has numerous technical applications [3]. On the molecular scale, ionization is caused by the absorption of photons as well as the impact of electrons and collisions with other particles. In particular photon induced ionization [4], which is the subject of this thesis occurs along two general pathways [2].
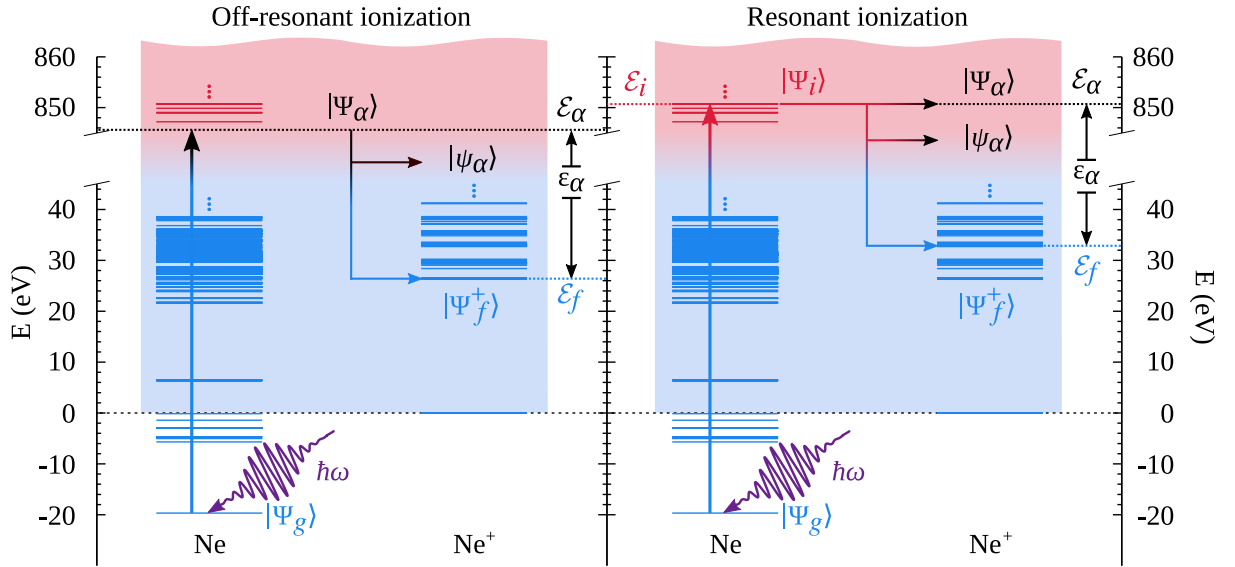

Figure 1: Schemes for the resonant and off-resonant ionization mechanisms exemplified for the neon atom. Off-resonant absorption (left) of a photon with frequency ω, directly maps the ground state $|\Psi_g\rangle$ with energy $\mathcal{E}_g$ to a continuum state $|\Psi_\alpha\rangle$ (black) composed of the ionic bound state $|\Psi_f^+\rangle$ with energy $\mathcal{E}_f$ (blue) and the ionized particle in the continuum orbital $|\psi_\alpha\rangle$. The energy of the ionized electron is $\varepsilon_\alpha = \hbar\omega - (\mathcal{E}_f - \mathcal{E}_g)$ [5]. Resonant absorption (right) of such a photon creates a core-excited state $|\Psi_i\rangle$ with energy $\mathcal{E}_i$ (red) embedded in the ionization continuum (color gradient). This resonance decays isoenergetically ($\mathcal{E}_\alpha = \mathcal{E}_i$) into the continuum state $|\Psi_\alpha\rangle$, where the outgoing electron bears the excess energy $\varepsilon_\alpha = \mathcal{E}_i - \mathcal{E}_f$ [6, 7].

Let us consider a molecular or atomic system, e.g. the neon atom in its ground state $|\Psi_g\rangle$ being irradiated by photons with frequency ω, Fig. 1. In off-resonant or direct photoionization the photon energy is directly transferred to the outgoing particle, promoting the system into the continuum state $|\Psi_\alpha\rangle$ that contains the discrete state $|\Psi_f^+\rangle$ of the ion and the emitted electron, $|\psi_\alpha\rangle$. The kinetic energy of the photoelectron is described by Einstein's photoelectric equation $\varepsilon_\alpha = \hbar\omega - (\mathcal{E}_f - \mathcal{E}_g)$ [5]. Resonant ionization denotes the case when the incoming photon energy matches a discrete transition. Here, in addition to being directly ionized, the system may first be resonantly excited to a metastable core vacancy state $|\Psi_i\rangle$ that subsequently decays via autoionization. Both contributions might interfere with each other [8]. The resonant pathway

can be approximately understood as a two-step process, in which the decay is decoupled from the excitation and the outgoing electron bears the excess energy $\varepsilon_\alpha = \mathcal{E}_i - \mathcal{E}_f$ [6, 7]. Thus photoionization and (resonant) autoionization encode different complementary parts of the system's electronic structure into the kinetic energy of the respective ejected electrons. In molecular autoionization, which is the dominant decay pathway for core vacancies [9], the local Auger decay [6] as well as nonlocal interatomic Coulombic decay (ICD) [10] and electron transfer mediated decay (ETMD) [11] can be distinguished. In ICD and ETMD the core vacancy, the electron filling the core hole, and the emitted electron may be localized at up to three atomic sites, whereas Auger decay refers to the completely local process.

Both photoionization and autoionization are interesting phenomena in their own right, since they not only probe but initiate and couple to intricate electronic and nuclear dynamics [12–18]. In particular, ultrafast charge migration after ionization, taking place on timescales of few tens of attoseconds up to to a few tens of femtoseconds [19–23] can induce structural alterations [24], and fragmentation [25–29] of the molecule. These processes are among the most frequently studied effects with widespread relevance. For instance biological radiation damage is an entangled process where an initial ionization causes a cascade of autoionization events. These in turn emit a series of highly reactive slow electrons and induce the fragmentation of the cation. All effects combined lead to the formation of toxic radical species [15, 30–33]. Further, ultrafast charge migration processes are fundamental to photosynthesis [34], photovoltaics [35, 36], molecular electronics [37]; and generally to all charge-transfer reactions [34]. Unraveling the details of these processes is a central goal within the newly emerging field of attosecond chemistry that provides the means to monitor and control the dynamics of an electronic wave packet which has been created by an initial ionization [22].

Spectroscopy Since the energy spectrum of the ionized electrons encodes the electronic structure, Fig. 1, measuring the photoelectron spectra (PES) and autoionization spectra (AIS) provides a formidable tool not only to track the aforementioned processes but also to decipher a system's properties at a fundamental level. This motivated Siegbahn et al. to develop the first spectrometers that allowed to record highly resolved PES and AIS, at once providing the machinery for electronic structure investigations of atoms, molecules, solids, and liquids in the X-ray regime [38–40]. This resulted in an avalanche of new insights into the chemical properties of a wide range of systems and has driven an unprecedented and still ongoing development of experimental [41, 42] and theoretical methods [2, 43].

A particular advantage of these electron-out spectroscopies is that they map bound to continuum states, which makes them less susceptible to selection rule suppression and more flexible than spectroscopies that target transitions between bound states [41, 42, 44]. For instance, photoionization in the ultraviolet/visible (UV/vis) regime probes delocalized valence molecular orbitals [44]. In the X-ray regime, however, ionization from all orbitals, up to the energetically lowest lying and spatially localized core orbitals is accessible, which allows to characterize the

complete electronic structure. Further, the binding energies of core electrons are significantly different for various elements, which is why X-ray core PES provides an element specific local probe of the molecular electronic structure in the vicinity of an atom [9, 41, 42]. In addition, the combination of X-ray valence PES and resonant AIS has been found to unravel specific solute-solvent interactions of transition metal complexes in solutions [45–50] which are essential for understanding processes in catalysis, biochemistry, and material sciences [51–53]. Starting with conventional X-ray tubes [54], the range of capabilities of X-ray spectroscopies was considerably enhanced with the advent of extraordinary intense and tunable light sources such as synchrotrons [55] and X-ray free-electron lasers (XFELs) [56]. Here XFELs yield femtosecond pulses [57] and have been reported only recently to have reached the attosecond scale [58]. Unprecedented time resolution is provided by the high harmonic generation (HHG) method, regularly reaching the attosecond regime at extreme ultraviolet (XUV) and soft X-ray energies using table top setups [22, 44, 59]. In sum, these experimental techniques provide a plethora of tools to study the molecular electronic structure at rest and during ultrafast processes [60].

The different spectroscopic methods, irrespective of the incoming photon energy and the actual subject at hand, share the common feature that the resulting spectra are feature-rich and difficult to interpret and assign based on the experimental data alone [22, 53]. For instance, transition metal complexes often have a complicated multi-configurational electronic structure and in particular the core-excited states show strong spin-orbit coupling (SOC) [9]. Hence, the development of theoretical methods for the simulation of PES and (resonant) AIS always has accompanied the experimental advancement during the last decades.

Theoretical approaches   Notably, modelling ionization processes remains challenging until today, although the fundamental theory has been known for decades [8, 61–63]. The problem can roughly be divided into the treatment of the initial bound and ionized continuum states, which have different requirements to be satisfied by the numerical methods. The discrete bound states are spatially confined square-integrable wave functions that can be expressed to a high accuracy in terms of multi-centered Gaussian-type orbital (GTO) basis functions. A key feature to the success of modern quantum chemistry (QC) has been that this basis permits the otherwise costly evaluation of the two-electron integrals during the numerical solution of the Schrödinger equation to be carried out analytically. On this foundation a plethora of different methods has emerged in the field of theoretical QC that meanwhile allow the prediction of bound state wave functions, energy levels, transition dipole moments, and other observables with unprecedented accuracy, even including their time evolution on a regular basis [64–66].

These bound state methods, however, can in general not be used directly to treat ionized continuum states due to the inability of the GTO basis to represent their non square-integrable character and continuum normalization, which is secured by asymptotic boundary conditions [67]. To still employ the power of the bound QC methods, continuum states are usually constructed by coupling square-integrable wave functions of the cationic bound states with a continuum orbital

that describes the outgoing electron. Here the most general framework, multi-channel scattering theory derived from Fano's configuration interaction (CI) in the continuum [62], allows to treat continuum and bound states on the same level, even including correlation effects between the two manifolds [2, 67]. In the molecular case, the resulting coupled equations for the continuum orbitals must be projected onto a suitable basis set to allow an efficient solution with algebraic techniques. This, however, has proven to be a very delicate problem, since the multi-centered local as well as the oscillatory asymptotic character must be described by such a basis. Further it should lead to analytic expressions for the multi-centered coupling integrals, limiting the choice. At this level of accuracy, solving the bound and continuum problems in a B-spline basis has proven to be a very versatile approach for atoms and diatomic molecules [68, 69]. Further, specialized Gaussian basis sets and a resolution of the molecular potential have been used to evaluate molecular autoionization [70–72]. However, only the recently presented XCHEM approach [73] employs a hybrid GTO and B-spline basis [74] to account for the short-range multi-centered molecular field and the long-range oscillatory character of the continuum orbitals, respectively. It is to be stressed that XCHEM is the only currently available code that allows to construct correlated continua on top of bound states obtained with conventional QC codes and in particular irrespective of the molecular geometry. Still, these very accurate methods have until now only been applied to the simulation of photoionization cross sections and autoionization widths of small molecules such as diatomics and first-row hydrides [68, 71, 75, 76].

More approximate approaches are usually obtained in the single-channel scattering picture, disregarding or approximating the correlation between the bound and continuum parts [67]. Here, the multi-centered B-spline static-exchange density functional theory (DFT) method [77] has been applied with remarkable success to the simulation of photoionization observables of molecules reaching the size of small organometallic complexes [20, 78–81]. In particular, it has been extended to include autoionization [80] and applied to the simulation of vibrationally resolved PES [82, 83].

Further down the ladder are methods that project the molecular problem on a one-center expansion of basis functions, allowing to evaluate PES and AIS of small molecular systems with remarkable accuracy [84–86]. A particular efficient scheme is obtained, if the molecular continuum orbital problem is approximated by an atomic one. These methods have been succesfully applied for the evaluation of molecular AIS [87–89] and can be applied on top of high-level electronic structure methods [90]. The XMOLECULE package [91, 92] employs it in conjunction with a very cost efficient electronic structure method to facilitate the evaluation of ionization cascades, although its applicability for strongly correlated systems might be limited. Here, the simplest approaches model the outgoing electron as a free particle or distorted wave corresponding to the Coulomb potential of an effective point charge [93, 94], which has been in particular applied to PES studies of rather large molecules [95–98].

An entirely different set of methods relies on an implicit continuum representation with Stieltjes imaging [99–103] or a Green's operator [104] formalism. Here, the Fano-Stieltjes

algebraic diagrammatic construction (FANO-ADC) [101, 102] method has been applied to the simulation of Auger decay, ICD and ETMD rates of systems up to the size of the $[Mg(H_2O)_6]^{2+}$ cluster [15]. Therein the continuum is approximately represented with spatially confined basis functions making these methods more suited for low kinetic energies of the outgoing particle. Energies of several hundreds of eV, targeted in X-ray PES and AIS necessitate large basis sets leading to demanding computations. At these high energies, relative photoionization intensities can be approximately obtained in the so called sudden approximation (SA) [105, 106] neglecting the detailed character and kinetic energy dependence of the photoelectron. The intensities are naturally obtained as pole strengths within Green's function approaches [107–109], and as the squared norms of the Dyson orbital [110] in orbital based methods [111–113].

While each of the discussed methods has its justification, there still exists a certain tradeoff between the accuracy that can be afforded for modelling the bound states and the continuum part, respectively. In particular the most accurate multi-channel treatments that allow the fully correlated treatment of both, photoionization and autoionization have yet only been applied to the smallest molecular systems. Treating larger molecules, such as transition metal complexes, usually requires a restriction to the single-channel scattering approach as well as an approximate representation of the continuum orbital, although the static-exchange B-spline DFT method has recently been extended towards interchannel coupling [80]. Reportedly, PES and AIS of such systems have been obtained within the FANO-ADC [101, 102], XMOLECULE [91, 92], and B-spline DFT approaches [77, 80]. These methods, however, have a single reference character and are not suited to treat systems possessing multi-configurational wave functions. This puts studies of some chemically interesting systems having near-degeneracies, for example, transition metal compounds, or of photodynamics in the excited electronic states, e.g., near conical intersections, out of reach. Further, these methods generally do not cover SOC effects that are regularly required for the study of core PES and AIS of molecules including transition metals or other heavier atoms. Here one usually must resort to the SA to describe the PES intensities [112] or even to analyzing only the ionization energies [114, 115], while the AIS of such compounds regularly remain out of reach.

Open questions This overview of methods has shown that the theoretical description of PES and especially AIS of larger molecules that have multi-configurational and SOC character is still far from becoming a common practice. In particular for complex systems such as solvated transition metal compounds, however, recent experimental advancements have shown that X-ray PES and (resonant) AIS can unravel intricate solute-solvent interactions [47–50, 53, 114], allowing to investigate crucial processes in biochemistry [51, 52], catalysis [116] and organic photovolatics [36] in their natural environment. Due to the inherent complexity of the electronic structure of the target systems in these studies, there is a high demand for theoretical support to assign, analyze, and interpret the experimentally measured spectra. As such, a newly developed protocol shall (i) provide photoionization cross sections and autoionization rates for

the construction of PES and AIS allowing the unambiguous assignment of experimental data; (ii) be numerically tractable for systems as large as transition metal complexes; (iii) take into account multi-configurational and SOC effects; (iv) be transferable, i.e., not restricted to a particular type of QC method.

Developments presented in this thesis   Approaching these goals has been the constant driving force behind the scientific work presented in this thesis. The QC method for the bound part was identified as the multi-configurational restricted active space self-consistent field (RASSCF) [117] family. Therein it is possible to account for dynamic correlation effects via the restricted active space second-order perturbation theory (RASPT2) [118] formalism and to include SOC with the restricted active space state interaction (RASSI) [119] approach in an LS coupling fashion. Further, these methods have been shown to yield good results in the framework of X-ray spectroscopies [112, 114, 120–125], suggesting their application to simulate X-ray PES and AIS as well. To cover cases in which a RASSCF treatment is numerically too demanding already at the bound state level, an interface that allows to evaluate PES and in principle AIS based on DFT [126] and linear response time-dependent DFT (TDDFT) [127] bound states has been established as well.

Finding a compromise with respect to the accuracy of the continuum orbital treatment, however, was a very delicate task. The two existing poles are the multi-channel approaches [70, 73] on the one hand, providing an unprecedented accuracy, and the simplistic free-particle and effective Coulomb potential models on the other hand [93–98], see Fig. 2. While the former is numerically unfeasible for systems as large as transition metal complexes, the latter disregard the local molecular field completely. Still, they yield analytic expressions for the continuum orbitals, simplifying the computational protocol considerably. In a first step, the free-particle and effective Coulomb potential models have been applied for the evaluation of X-ray core PES including SOC in [GG1], [GG3] and [50] with remarkable accuracy, while the valence PES of various molecules could be represented only to lesser extent in Ref. 98. Further, transient valence PES of iron complexes have been computed to support the analysis of ultrafast dynamics observed in pump-probe experiment in [GG2] and [128, 129]. Therein, the experimental data could be assigned, however, the calculated spectra agreed only qualitatively to the experimental ones, indicating that the free-particle and point-charge approaches are too simplistic.

To finally facilitate the evaluation of AIS and improve the accuracy of the PES, the spherical continuum for ionization (SCI) approach has been developed [GG4], [GG5]. Therein, the continuum states are constructed in the single-channel scattering picture [67] and the continuum orbitals are modeled as spherically symmetric functions. The novelty of this approach lies in the fact that it allows to incorporate the molecular field into the continuum orbital construction in a simple way that is numerically tractable even for large molecules. This is achieved by averaging out the angular dependence of the molecular potential, which transforms the three-dimensional continuum orbital problem to the radial dimension. The corresponding radial Schrödinger
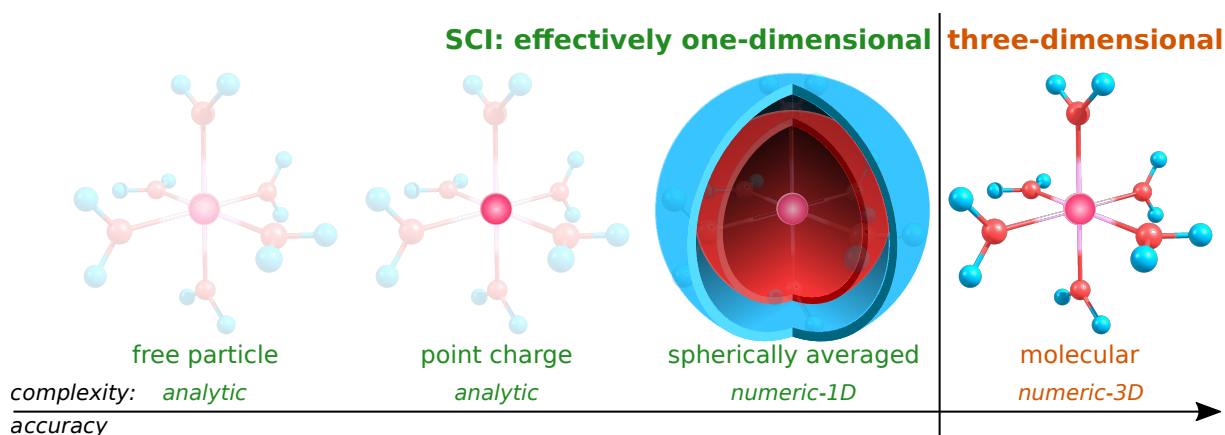
Figure 2: Pictorial representation of different approximate levels to obtain the continuum orbital for an ionized electron. The SCI approach takes into account the molecular potential at a spherically averaged level, reducing the continuum orbital problem to the radial dimension. The concentric hollow spheres correspond to the different layers of oxygen (red) and hydrogen (blue) atoms being smeared out by the spherical averaging procedure. In this picture, the free-particle and point-charge models correspond to further approximations of the SCI approach. The most accurate treatments account for the true molecular symmetry but at least require a solution of the one-particle Schrödinger equation in three dimensions.

equations can be solved with cheap numerical methods to construct spherically symmetric continuum orbitals. Note that the averaging procedure smears out the atomic point charges into charged hollow spheres and transforms the molecular electron density into a spherically symmetric one, defining an effective system, see Fig. 2. Further, the free-particle and effective Coulomb potential approaches can be understood as additional approximations within the SCI framework that allow for analytic solutions of the radial continuum orbital problem. Despite the still considerable approximation inherent to the SCI approach, Fig. 2, it provides the necessary numerical efficiency to be applicable to the simulation of PES and AIS of transition metal compounds in an attempt to bridge the gap between the most accurate and simplistic continuum orbital approaches, respectively.

Structure of the thesis To begin with, the theoretical framework of the SCI approach that has been demonstrated in [GG1]-[GG5] is discussed in Sec. 2 in light of the RASSCF/RASSI and DFT/TDDFT bound state QC methods. The different implementations that have been carried out are presented in Sec. 2.6. Subsequently, the applicability of the SA and free-particle approaches to the simulation of X-ray core PES in a liquid environment, [GG1] and [GG3], as well as to the simulation of transient valence PES for the assignment of ultrafast dynamical processes [GG2] is reviewed in Sec. 3. Further, the capability of the SCI approach to accurately predict AIS and total decay rates is investigated on the example of the neon $1s^{-1}3p$ resonant Auger electron spectrum (RAES) [GG4] in Sec. 4.1. Here, particular focus is put onto the influence of different approximations to the potential used to obtain the continuum orbitals. Finally, in Sec. 4.2 the numerical SCI approach is applied to the simulation of the PES and RAES of methane, molecular oxygen and pyrimidine [GG5], serving as showcases. A summary of the presented work is given in Sec. 5

2 Theoretical framework

In this chapter, the general formal framework of the SCI approach is presented in a concise manner. The details can be found in [GG1], [GG3], [GG4], and [GG5]. Note that molecular autoionization encompasses the local Auger decay [6] as well as the nonlocal ICD [10] and ETMD [11] that are differentiated by the localization of the residual holes. Herein, no such distinction is made and the term Auger decay is used as a synonym for local and non-local decay pathways. Further, atomic units (a.u.) are employed, if not stated otherwise. Although ionization is a highly correlated phenomenon that often induces or couples to ultrafast electronic and nuclear dynamics [22], this work restricts itself to the time-independent picture, neglecting all dynamical effects. In addition, the usual limits of first order perturbation theory and dipole approximation are assumed for photoionization. Moreover, the average over random molecular orientations with respect to the polarization vector of the incoming light is taken, which results in the photoionization cross section [61]

$$\sigma_{i\alpha} = \frac{4\pi^2}{3c}\omega k \left| \langle \Psi_\alpha | \boldsymbol{\mu} | \Psi_g \rangle \right|^2 . \tag{1}$$

To describe the resonantly driven Auger decay process the so called two-step model [7] is employed throughout this work. Therein the influence of the excitation, which couples decay pathways corresponding to neighboring resonances and allows for interference with direct photoionization terms, is neglected and the partial decay rate is obtained as [8]

$$\Gamma_{i\alpha} = 2\pi \left| \langle \Psi_\alpha | \mathcal{H} - \mathcal{E}_i | \Psi_i \rangle \right|^2 . \tag{2}$$

In Eqs. (1) and (2), $|\Psi_g\rangle$, $|\Psi_i\rangle$, and $|\Psi_\alpha\rangle$ denote the respective ground or valence-excited, core-excited, and ionized continuum states (open channels) of the system. The N-electron dipole operator is denoted by $\boldsymbol{\mu} = -\sum_{u=1}^{N} \boldsymbol{r}_u$, $\mathcal{H}$ is the molecular Hamiltonian, and $\mathcal{E}_i$, ω, and $k = \sqrt{2\varepsilon_\alpha}$ are the energies of $|\Psi_i\rangle$ and the ionizaing radiation, as well as the wavenumber of the ionized electron, respectively, cf. Fig. 1. The composite channel index α contains all quantum numbers to uniquely identify the bound and continuum parts of $|\Psi_\alpha\rangle$.

2.1 Construction of continuum states

A prerequisite for a reliable calculation of ionization spectra is an accurately evaluated underlying bound state electronic structure. For the sake of flexibility of the approach, the only *a priori* requirement that is applied in this work shall be that all bound wave functions $|\Psi_g\rangle$, $|\Psi_i\rangle$, and $|\Psi_f^+\rangle$ are CI like expansions of Slater determinants (SDs)

$$|\Psi\rangle = \sum_j C_j \boldsymbol{a}_{j_1,\sigma_1}^\dagger \cdots \boldsymbol{a}_{j_N,\sigma_N}^\dagger |0\rangle , \tag{3}$$

with the respective orbitals $|\varphi_{i,\sigma}\rangle = a^\dagger_{i,\sigma}|0\rangle$ being defined in terms of atomic GTO basis functions. N indicates the number of electrons in the unionized molecule. Wave functions of this type are obtained by a large subset of the conventional QC approaches.

The treatment of (resonant) Auger decay necessitates an equal-footed description of the ground and core-excited states of the neutral system as well as of the complete valence-excited manifold of the ionized species. The latter are the foundation upon which the N-electron ionized continuum states are constructed. Photoionization is less complicated, usually requiring the description of only the ground or lowest valence-excited states of the neutral species, and the valence-excited manifold of the cation. Depending on the photon energy, a subset of the cationic valence-excited manifold will often cover the most important effects.

RASSCF bound states Herein, the multi-configurational RASSCF [117] method has been employed to treat both, autoionization and photoionization. It allows a fine grained control over the included physical effects and the amount of correlation by choosing the three active orbital subspaces RAS1-3. RAS1 and RAS3 contain fully occupied and virtual orbitals, respectively, allowing for fixed numbers of holes and electrons within each space. In contrast, the occupation of the orbitals in RAS2 is not restricted, corresponding to full CI within this subspace. Further, the lack of correlation energy resulting from the truncation of the active space can be compensated with the RASPT2 method [118], often leading to good agreement with the experimental binding energies [GG1]-[GG5].

The RASSCF/RASPT2 approach yields true eigenstates to the squared total spin $\boldsymbol{S}^2$ that are referred to as 'spin-free' in the following. Hence, the total spins of the bound neutral and cationic states S, S^+ and their quantization axis projections M, M^+, respectively, are good quantum numbers. They will be indicated only when required and dropped generally. S and M need to be conserved during the ionization, which can be achieved by constructing the continuum states as

$$|\Psi_\alpha\rangle = \sum_{M^+=-S^+}^{S^+} \sum_{\sigma=-\frac{1}{2},\frac{1}{2}} \left\langle S, M \middle| S^+, M^+; \frac{1}{2}, \sigma \right\rangle \underbrace{a^\dagger_{\alpha,\sigma}\middle|\Psi^+_{f,M^+}\right\rangle}_{\left|\Upsilon^{\sigma M^+}_\alpha\right\rangle}. \tag{4}$$

The Clebsch-Gordan coefficients $\langle S, M|S^+, M^+; \frac{1}{2}, \sigma\rangle$ couple different pairings of the continuum orbital and cationic state spin projections σ and M^+ such as to conserve S and M. The channel functions $|\Upsilon^{\sigma M^+}_\alpha\rangle$ are constructed by inserting an additional electron with the continuum orbital $|\psi_{\alpha,\sigma}\rangle$ into the cationic states $|\Psi^+_{f,M^+}\rangle$, while retaining the antisymmetry. They are only eigenfunctions of $\boldsymbol{S}_z$ and will be used in the upcoming chapters to express the transition matrix elements (TMEs) independent on the underlying QC method. Note that in practical calculations of spin-free states, the maximum projections $M = S$ and $M^+ = S^+$ are usually obtained, albeit the others are also possible. This reduces the number of terms in Eq. (4) to two.

Spin-orbit coupled RASSCF/RASSI bound states The matter becomes more complicated, if SOC is concerned. The RASSI approach [119] implements the atomic mean-field integral approximation [130] of the SOC operator to couple RASSCF wave functions of different spins to obtain a set of SOC states. Assuming that the ground state spin of the neutral molecule is S_0, three spin-free manifolds, $S = S_0$, $S_0 \pm 1$, need to be coupled in the general case as dictated by the selection rule $\Delta S = \pm 1$ [119]. The corresponding cationic SOC states include four manifolds, $S^+ = S_0 \pm 1/2$, $S_0 \pm 3/2$, to account for the fact that the total spin may change by $\pm 1/2$, upon electron removal

$$|\Psi_G\rangle = \sum_{S=S_0-1}^{S_0+1} \sum_{g=1}^{N_S} \sum_{M=-S}^{S} \xi_{Gg}^{SM} |\Psi_{g,SM}\rangle, \tag{5a}$$

$$|\Psi_F^+\rangle = \sum_{S^+=S_0-3/2}^{S_0+3/2} \sum_{f=1}^{N_{S^+}} \sum_{M^+=-S^+}^{S^+} \xi_{Ff}^{S^+M^+} |\Psi_{f,S^+M^+}^+\rangle. \tag{5b}$$

Here, ξ denotes the SOC coefficients obtained from the RASSI procedure. The capital indices (G, F) refer to SOC states, while small letters (g, f) indicate the spin-free ones. N_S and N_{S^+} are the numbers of spin-free states corresponding to the respective manifolds. These SOC states, however, are no eigenstates of total angular momentum operators $\mathbf{J}^2$ and $\mathbf{J}_z$, because the non-spherical molecular symmetry prohibits the construction of total orbital angular momentum $\mathbf{L}^2$ eigenstates. Therefore, no J or M_J conserving continuum states similar to Eq. (4) can be constructed. An approximate solution is to define the SOC continua equivalent to channel functions, wherein the spin function of the continuum electron is left undetermined, denoted by ς

$$|\Psi_\alpha\rangle = \underbrace{\boldsymbol{a}_{\alpha,\varsigma}^\dagger |\Psi_F^+\rangle}_{|\Upsilon_\alpha^\varsigma\rangle}. \tag{6}$$

It is assigned at the stage of the matrix element evaluation, see Sec. 2.3.2.

DFT and TDDFT bound states DFT [126] and linear response TDDFT [127] provide a computationally efficient means to evaluate the ground and valence-excited states of rather large molecules containing several tens of atoms. In particular within the Tamm-Dancoff aproximation (TDA) [131], linear response TDDFT effectively yields CI expansions of singly excited SDs in terms of Kohn-Sham orbitals for the excited states. This allows for PES studies of systems that are hardly tractable with the RASSCF methods [98, 128, 129]. However, the obtained bound states are only eigenfunctions of $\boldsymbol{S}_z$. Thus, only M is conserved during the ionization, which is achieved by choosing the spin projection of the continuum orbital as $\sigma = M - M^+$ [1]. Again, the

---

[1] In practice $\sigma = S - S^+$, since again $M = S$ and $M^+ = S^+$ are obtained in DFT/TDDFT calculations.

continuum states are equal to the TDDFT channel functions.

$$\left|\Psi_\alpha\right\rangle = \underbrace{a^\dagger_{\alpha,\sigma}\left|\Psi^+_{f,M^+}\right\rangle\bigg|_{\sigma=M-M^+}}_{\left|\Upsilon^{\sigma M^+}_\alpha\right\rangle} \tag{7}$$

2.2 Spherical continuum approach to ionization

2.2.1 Continuum orbitals

The stage is now set to advance to the construction of the continuum orbitals. The assumption of spherical symmetry, central to the SCI approach, allows to reduce the continuum orbital problem to the radial dimension at the expense of averaging over the angular domain. The inherent loss of accuracy is justified by the computational simplicity of the approach, which resembles an atomic problem. Here only the most important landmarks of the procedure are given, while the details can be found in [GG4] and [GG5].

The continuum orbitals are treated as spherical waves, subject to the spherically symmetric potential $V_f(r)$ of the cationic residual $|\Psi^+_f\rangle$. They take the form

$$\psi_{\alpha,\sigma}(r,\Omega) = \frac{1}{r}w^{fk}_l(r)Y^m_l(\Omega)\zeta(\sigma), \tag{8}$$

with $\frac{1}{r}w^{fk}_l(r)$, spherical harmonics $Y^m_l(\Omega)$, and $\zeta(\sigma)$ being the radial, angular, and spin parts, respectively. Ω denotes the solid angle. The spin function will be generally omitted in the following, if not explicitly needed. The composite channel index $\alpha = (f,l,m,k)$ contains the index of the ionized state f, the orbital and magnetic quantum numbers l, m, and the wave number $k = \sqrt{2\varepsilon_\alpha}$ of the continuum orbital. It uniquely identifies the total energy $\mathcal{E}_\alpha = \mathcal{E}_f + \varepsilon_\alpha$, the spatial part of the continuum orbital, and the bound cationic state for each channel $|\Psi_\alpha\rangle$. The functions $w^{fk}_l(r)$ are determined by solving the radial Schrödinger equation (SE)

$$\left(\frac{d^2}{dr^2} + 2\left(\frac{k^2}{2} - V_f(r)\right) - \frac{l(l+1)}{r^2}\right)w^{fk}_l(r) = 0, \tag{9}$$

which has to be carried out numerically in the general case. The appropriate normalization and asymptotic behavior is ensured by implementing the boundary conditions [67]

$$w^{fk}_l(r \to 0) = nr^{l+1}, \tag{10a}$$

$$w^{fk}_l(r \to \infty) = \sqrt{\frac{2}{\pi k}}\left(\cos\delta^f_l(k)F_l(\eta,kr) + \sin\delta^f_l(k)G_l(\eta,kr)\right). \tag{10b}$$

Therein $\delta^f_l(k)$ are the scattering phases and $F_l(\eta,kr)$ and $G_l(\eta,kr)$ are the regular and irregular Coulomb functions [132] corresponding to the long-range Coulomb potential of the cation's

net charge ($\eta = -Z_{\text{net}}/2k$). The matching is carried out in the asymptotic region where $V_f(r)$ is well approximated by $-Z_{\text{net}}/r$. Note that in the photodetachment case leading to a neutral leftover, $Z_{\text{net}} = 0$, the Coulomb functions reduce to spherical Bessel and Neuman functions $F_l(\eta, kr); G_l(\eta, kr) \longrightarrow kr\, j_l(kr); kr\, n_l(kr)$ [132], respectively.

Another consequence of the spherical approximation within the SCI approach is the need to define an origin of the continuum orbital $\boldsymbol{r}_c$. Its location is often ambiguous and there exists no general procedure to define it. Setting the origin to the spatial expectation value obtained from the respective Dyson orbitals, Sec. 2.3, as suggested in Ref. 94 is possible for photoionization only. Further, this mechanism introduces a different origin for each transition, which breaks the central numerical advantage of the present implementation, see Sec. 2.6. Therefore it is disregarded and a fixed origin $\boldsymbol{r}_c$ is used for the calculation of each spectrum. Thus $\boldsymbol{r}_s(r, \Omega) = \boldsymbol{r} - \boldsymbol{r}_c$ defines the reference frame for all continuum orbitals, potentials, and the radial SE. The practical definition of $\boldsymbol{r}_c$ depends on the molecular structure as well as on the properties under study. For instance, the accuracy of the Auger decay rates might benefit from placing $\boldsymbol{r}_c$ at the core-hole site, whereas valence ionization cross sections could be better reproduced if the center of molecular mass is chosen to treat the whole molecule in a balanced manner [GG5].

2.2.2 Models for the radial potential

The radial potentials $V_f(r)$ generate the continuum orbitals through Eq. (9). Hence, their quality is central to the accuracy of the calculated observables. A reasonable approximation to the radial potential can be obtained by averaging over the angular dependence of the molecular electrostatic potential $V_f(r) = \frac{1}{4\pi} \int V_f(\boldsymbol{r}(r, \Omega)) \mathrm{d}\Omega$, where $\boldsymbol{r}(r, \Omega) = \boldsymbol{r}_c + \boldsymbol{r}_s(r, \Omega)$. Hitherto, the potential is split into nuclear and electronic components $V_f(r) = V_f^{\text{nuc}}(r) + V_f^{\text{el}}(r)$, which are treated individually. The nuclear part resembles the classical potential of a set of concentric hollow spheres with the radii $R_{cA} = |\boldsymbol{r}_c - \boldsymbol{R}_A|$ centered at $\boldsymbol{r}_c$ and carrying the charge Z_A [GG5]

$$V^{\text{nuc}}(r) = \sum_A \begin{cases} -\frac{Z_A}{R_{cA}}, & r < R_{cA} \\ -\frac{Z_A}{r}, & r \geq R_{cA} \end{cases}. \tag{11}$$

The electronic part is the classical electrostatic potential $J_f(r)$ of the spherically averaged electron density $\rho_f(r)$ from the cationic state $|\Psi_f^+\rangle$. In addition, a radial Slater exchange term $X_f^{\text{S}}(r)$ [133] may be included, leading to the approaches [GG4], [GG5]

$$V_f^{\text{J}}(r) = V^{\text{nuc}}(r) + J_f(r), \tag{12a}$$

$$V_f^{\text{JX}}(r) = V^{\text{nuc}}(r) + J_f(r) + X_f^{\text{S}}(r). \tag{12b}$$

These potentials in a sense correspond to the Hartree and Slater-X_α levels of accuracy, respectively. They provide the most complete treatment within the present implementation of the SCI approach and yield a pictorial interpretation. Namely, the spherical averaging smears out the

atomic point charges Z_A into concentric shells centered at $\boldsymbol{r}_c$. The radius of which, R_{cA}, is the distance of the respective atom from the continuum orbital origin. Consequently, the spherical continuum orbitals correspond to an effective system consisting of charged concentric hollow spheres and a spherically symmetric charge distribution $\rho_f(r)$.

Finally, more approximate treatments are possible within the present implementation [GG4]. For atoms a screened charge model $V_f^{\text{scr}}(r) = Z_f(r)/r$ might be used. Further, $V_f(r)$ might be neglected completely, or modeled as the Coulomb potential of an effective point charge Z_{eff}, e.g. the net charge of the cation. The latter two approaches have the advantage that they lead to analytic solutions of Eq. (9) in terms of spherical Bessel, j_l, and regular Coulomb functions, F_l, respectively. In this way, the numerical evaluation of the spherically averaged electron densities, potentials and radial functions can be circumvented, which simplifies the approach considerably. These models are also implemented elsewhere, for instance in the EZDYSON code [134] that has been originally established by Oana and Krylova [93, 94]. EZDYSON allows to evaluate angular resolved photoionization cross sections, but does not feature autoionization.

Note that the continuum orbitals obtained by any of the methods described herein are not orthogonal to the bound orbitals of the neutral and cationic species. This is in contrast to the behavior that an exact continuum orbital would possess and leads to additional terms in the TMEs, see Secs. 2.3 and 2.4.

2.2.3 Ionization spectra

Having defined the spherical continuum orbitals, the stage is now set to give the working expressions for the spectra. Within the SCI approach, the PES and RAES are constructed by integrating over the cross sections $\sigma_{g\alpha}$ and decay rates $\Gamma_{i\alpha}$ for all open channels α, respectively, Eqs. (1) and (2). Since the energy conservation has therein already been taken into account, the remainder of the continuum channel integration is just a summation over the target ionized states f and the l and m quantum numbers of the continuum orbitals. Using $\mathcal{X}_{n\alpha}$ to abbreviate $\sigma_{g\alpha}$ and $\Gamma_{i\alpha}$ and further assigning a phenomenological lineshape $\Lambda_{n\alpha}$ ($n = i, g$) to each transition leads to the expression

$$I_n(\varepsilon) \propto \sum_f \sum_{l=1}^{l_{\text{max}}} \sum_{m=-l}^{l} \mathcal{X}_{n\alpha} \Lambda_{n\alpha}(\varepsilon - \varepsilon_\alpha), \tag{13}$$

for the spectral shape of the calculated PES and RAES, respectively, where l and m entered the α index. Note that the convergence with respect to the maximum orbital angular momentum l_{max} is a critical issue in the practical evaluation of PES and RAES [GG5].

2.3 Photoionization transition matrix elements

To begin with, the continuum-bound dipole TMEs in Eq. (1) are introduced for the cases where the bound states have been obtained with the conventional RASSCF/RASPT2 and TDDFT approaches. The inclusion of SOC via the RASSI method is discussed thereafter.

2.3.1 Spin-free bound states

The TMEs are given herein in terms of the channel functions $|\Upsilon_\alpha^{\sigma M^+}\rangle$, Eqs. (4), (6), and (7). Importantly, the neutral and cationic bound states are obtained in separate SCF calculations to include orbital relaxation effects due to the electron removal. Consequently, they have different sets of N_{orb} spin-orbitals $\{\varphi_i\}$ and $\{\varphi_i^+\}$ that are not mutually orthogonal, which needs to be accounted for in all evaluations. The respective creation and annilation operators are $a_i^\dagger$, a_i and $(a_i^+)^\dagger$, a_i^+. Using Löwdins SD calculus [135], the ionization dipole TME, Eq. (1), can be rearranged as

$$\sum_u \left\langle \Upsilon_\alpha^{\sigma M^+} \middle| r_u \middle| \Psi_g \right\rangle = \underbrace{\left\langle \psi_{\alpha,\sigma} \middle| r \middle| \Phi_{gf}^{M^+} \right\rangle}_{\text{SO}} + \left\langle \psi_{\alpha,\sigma} \middle| \tilde{\Phi}_{gf}^{r,M^+} \right\rangle, \tag{14}$$

in terms of 1-particle dipole and overlap integrals. The former corresponds to ionization from the Dyson orbital (DO) $|\Phi_{gf}^{M^+}\rangle$, whereas the latter denotes a monopole transition from the one-electron conjugated dipole DO $|\tilde{\Phi}_{gf}^{r,M^+}\rangle$ into the continuum [22]. The DO is defined as the N-1 particle integral over the transition density of the bound neutral and cationic states [110]. In second quantization it can be written as an expansion in terms of the neutral species' spin orbitals

$$\left| \Phi_{gf}^{M^+} \right\rangle = \sum_{s=1}^{N_{\text{orb}}} \left\langle \Psi_{f,M^+}^+ \middle| a_s \middle| \Psi_g \right\rangle |\varphi_s\rangle . \tag{15}$$

The monopole contribution, however, is a consequence of the aforementioned continuum-bound nonorthogonality (NO). Its magnitude is determined by the continuum-bound overlap integrals, bound dipole contributions, and residual overlap terms [GG4]. It is often negligible, unless the energy of the outgoing electron is small, e.g. in threshold ionization [22]. Hence, the present implementaion of the SCI approach for photoionization assumes the strong orthogonality (SO) approximation. Therein all overlap integrals between the continuum and the neutral species' orbitals are set to zero, $\langle \psi_{\alpha,\sigma} | \varphi_i \rangle = 0$, disregarding the monopole term as denoted in Eq. (14).

2.3.2 Spin-orbit coupled bound states

Spin-coupled DOs can be obtained by contracting the spin-free ones with the SOC coefficients of the neutral and cationic states in Eqs. (5a) and (5b). For practical reasons, the fact that the spin-free states take on the highest spin projections $M = S$ and $M^+ = S^+$, respectively, is used and the construction of the other spin projections is disregarded. Assuming that the spin-free DO for a pair of neutral and cationic states g, f with spins S and S^+ is independent on the particular spin projections, allows to write the SOC DO as

$$\left| \Phi_{GF} \right\rangle = \sum_{S^+=S_0-3/2}^{S_0+3/2} \sum_{f=1}^{N_{S^+}} \sum_{S=S_0-1}^{S_0+1} \sum_{g=1}^{N_S} \left| \Phi_{gf}^{SS^+} \right\rangle \cdot \left[\sum_{M^+=-S^+}^{S^+} \sum_{M=-S}^{S} \left(\xi_{Ff}^{S^+ M^+} \right)^* \xi_{Gg}^{SM} \right] . \tag{16}$$

Where, $|\Phi_{gf}^{SS^+}\rangle$ are the respective spin-free DOs as defined in Eq. (15). The spin-coupled DOs $|\Phi_{GF}\rangle$ are complex and have a nontrivial spin mixture. The dipole TMEs in SO approximation are evaluated analogously to the spin-free ones in Eq. (14). Thereby, the still undetermined spin function $\eta(\varsigma)$ of the continuum orbital in Eq. (6) is set equal to the one of the spin-coupled DO.

2.4 Autoionization transition matrix elements

The autoionization TME, bearing two-electron character, however, is more complicated. Partitioning the Hamiltonian into its one- and two-electron parts $\mathcal{H} = \sum_u \boldsymbol{h}_u + \sum_{u<v} 1/r_{uv}$, where $\boldsymbol{h}_u$ contains the kinetic energy and nuclear attraction operators and $1/r_{uv}$ is the electron repulsion, yields

$$\left\langle \Upsilon_\alpha^{\sigma M^+} \middle| \mathcal{H} - \mathcal{E}_i \middle| \Psi_i \right\rangle = \tag{17}$$

$$\left\langle \psi_{\alpha,\sigma} \middle| h \middle| \Phi_{if}^{M^+} \right\rangle + \overbrace{\sum_{q=1}^{N_{\mathrm{orb}}} \left\langle \psi_{\alpha,\sigma} \varphi_q^+ \middle| \frac{1}{r_{12}} \middle| \Xi_{i\alpha}^{M^+,q} \right\rangle}^{r^{-1}\ \mathrm{coupling}} + \left\langle \psi_{\alpha,\sigma} \middle| \tilde\Phi_{i\alpha}^{1,M^+} \right\rangle + \overbrace{\left\langle \psi_{\alpha,\sigma} \middle| \tilde\Phi_{i\alpha}^{2,M^+} \right\rangle}^{r^{-1}\ \mathrm{coupling}} - \mathcal{E}_i \left\langle \psi_{\alpha,\sigma} \middle| \Phi_{if}^{M^+} \right\rangle .$$

$$\underbrace{\phantom{\left\langle \psi_{\alpha,\sigma} \middle| h \middle| \Phi_{if}^{M^+} \right\rangle + \sum_{q=1}^{N_{\mathrm{orb}}}}}_{\mathrm{SO}}$$

$$\underbrace{\phantom{\mathrm{NO\ long\ brace\ span}}}_{\mathrm{NO}}$$

Here, the two-electron reduced transition densities (2RTDs),

$$\left| \Xi_{i\alpha}^{M^+,q} \right\rangle = \sum_{s_1 \neq s_2}^{N_{\mathrm{orb}}} \left\langle \Psi_{f,M^+}^+ \middle| (a_q^+)^\dagger a_{s_1} a_{s_2} \middle| \Psi_i \right\rangle \middle| \varphi_{s_1} \varphi_{s_2} \right\rangle , \tag{18}$$

determine the continuum-bound Coulomb coupling which is the major contribution to the decay rate [7, 136]. In addition, the DOs dictate the leading one-electron and overlap contributions to the matrix element. Moreover, the overlap terms with the conjugated Dyson orbitals, $|\tilde\Phi_{i\alpha}^{n,M^+}\rangle$, again correspond to monopole transitions to the continuum. Their amplitude is dictated by the continuum-bound overlaps, the bound one- and two-electron TMEs for $n = 1$ and 2, respectively, and further residual overlap terms, see [GG4]. In this case, the SO approximation implies not only that the overlap integrals involving the conjugated DOs vanish, but also demands that the overlap term proportional to $\mathcal{E}_i$ is neglected, as indicated in Eq. (17). Another ad-hoc way to mitigate the nonorthogonality problem is to use the Gram-Schmidt (GS) orthogonalization to project the orbitals of the ionized system out of the continuum functions and enforce $\langle \psi_{\alpha,\sigma}^{\mathrm{GS}} | \varphi_{i,\sigma_i}^+ \rangle = 0$. The labels SO, NO and GS will be used in the following to indicate the following nonorthogonality approaches. The overlap terms in Eq (17) can be neglected (SO), incorporated (NO), and GS-orthogonalized continuum functions can be employed to evaluate the partial rates accounting for the NO terms. Another popular approximation is to account only for the leading two-electron terms instead of using the "full" Hamiltonian coupling. These approaches are denoted as the

r^{-1} and $\mathcal{H}$ couplings, respectively, as indicated in Eq. (17).

Further, the computational effort can be greatly reduced by truncating the number of different atomic centers allowed to contribute to the two-electron integral. In addition to the origin of the ionized electron, contributions from up to three different atomic centers may be permitted. The popular one-center approximation (1CA) [87] is motivated by the locality of the Auger decay. It is obtained by setting the continuum orbital origin to the vacancy bearing atom and disregarding all contributions from other atoms. This approximation has been investigated in [GG5].

Since different RAES may be obtained for each set of approximations, the shorthand notation *coupling · potential · nonorthogonality*, or subsets of it, will be used where applicable. For instance, $\mathcal{H} \cdot V_f^{\mathrm{JX}}(r) \cdot \mathrm{NO}$ denotes partial decay rates obtained using the $\mathcal{H}$ coupling, radial waves corresponding to the $V_f^{\mathrm{JX}}(r)$ potential, and incorporating the NO terms.

2.5 Dyson orbital approach to photoionization

2.5.1 Sudden approximation

Disregarding the description of the ionized particle, the Dyson orbitals alone provide already a simple means to obtain photoionization intensities within the so called sudden approximation (SA) [105, 106]. Therein, the squared norm of the DO serves as a measure for the ionization cross section

$$\sigma_{i\alpha} \propto \left\| \Phi_{gf} \right\|^2 \underbrace{\left| \left\langle \psi_{\alpha,\sigma} \middle| \boldsymbol{r} \middle| \frac{\Phi_{gf}}{\left\| \Phi_{gf} \right\|} \right\rangle \right|^2}_{\approx \mathrm{const.}} . \tag{19}$$

It is an approximation based on the assumption that the dipole integral over the continuum electron and the normalized DO can be regarded as constant over the whole spectrum. This is generally only the case for high kinetic energies of the outgoing particle, e.g. in X-ray ionization, and if the character of the DOs does not change throughout the spectrum. Both conditions are often fulfilled in X-ray core or inner valence ionization, where good agreement with experimental reference data can be obtained, see [GG1] and [GG3]. Its application to valence PES, however, might be less successfull, because ionization from molecular orbitals having different character in terms of localization, radial, and angular structure usually contributes to these spectra [98, 111].

2.5.2 Occupation number analysis

The DO may be interpreted as the wave function of the photoelectron before the ionization. This is a rough approximation, which holds strictly only in a single-configurational treatment that additionally assumes frozen orbitals. However, within this picture an analysis of the occupation number changes during the ionization is possible and allows to unravel the character of each transition in a comparatively simple orbital picture. The procedure is detailed in [GG3]. In brief, neglecting the influence of SOC and dropping the M and M^+ indices, vectors in terms of

the spin orbital occupation numbers n_g and n_f^+ may be defined for the bound neutral and cationic states $|\Psi_g\rangle$ and $|\Psi_f^+\rangle$, respectively,

$$\boldsymbol{n}_g = \left(n_g(\varphi_1),\ n_g(\varphi_2),\ \ldots,\ n_g(\varphi_{N_{\text{orb}}}) \right), \tag{20a}$$

$$\boldsymbol{n}_f^+ = \left(n_f^+(\varphi_1^+),\ n_f^+(\varphi_2^+),\ \ldots,\ n_f^+(\varphi_{N_{\text{orb}}}^+) \right). \tag{20b}$$

The components of these vectors sum to the respective total numbers of electrons, N and N-1. For the DO, $|\Phi_{gf}\rangle$, one can define an occupation-like vector by projecting onto the neutral species' orbitals,

$$\boldsymbol{n}_{gf} = \left(|\langle \Phi_{gf}|\varphi_1\rangle|,\ |\langle \Phi_{gf}|\varphi_2\rangle|,\ \ldots,\ |\langle \Phi_{gf}|\varphi_{N_{\text{orb}}}\rangle| \right), \tag{21}$$

where it is assumed that $|\Phi_{gf}\rangle$ has been normalized for the purpose of this analysis. Transferred to multi-configurational QC approaches accounting for correlation and orbital relaxation, the normalized DO corresponds to a quasiparticle with its wave function being a superposition of the neutral species' spin orbitals. Hence, $\boldsymbol{n}_{gf}$ unravels the contributions of different spin orbitals to the hole created by the ionization and its components sum to one. In addition, ionization may be accompanied by electronic excitations, leading to satellite features in the PES. These excitations can be assigned within the residual occupation vector

$$\boldsymbol{n}_{gf}^{\text{res}} = \boldsymbol{n}_f^+ + \boldsymbol{n}_{gf} - \boldsymbol{n}_g, \tag{22}$$

the components of which approximately sum to zero. Here, negative and positive entries denote the 'hole' and 'particle' parts of the accompanying excitation. Note that this analysis requires that the orbital bases of the neutral and cationic species are approximately equal $\{\varphi_i\} \approx \{\varphi_i^+\}$. Strong orbital relaxation complicates the situation and may prevent the residual occupation analysis from being applicable in some cases, as discussed in [GG3].

2.6 Implemented numerical protocols

At the heart of any numerical implementation of the SCI approach lie three tasks that have to be completed in a computationally feasible way. First, the evaluation of the (conjugated) DOs and 2RTDs, has to be carried out. Second, the spherical continuum orbitals have to be constructed. Third and most problematic, the continuum-bound TMEs have to be estimated numerically for each transition. To this end, they are usually transformed into the respective atomic GTO basis representation of the (conjugated) DOs and 2RTDs, wherein the numerical integration is carried out. Subsequently, these results are transformed back to yield the actual TMEs. Herein two different protocols have been developed. Both are interfaced to a locally modified version of MOLCAS 8.0 [137], and to the GAUSSIAN09 program [138], which provide the RASSCF/RASPT2/RASSI and DFT/TDDFT bound states, respectively.

The first one, termed Dyson/ezDyson, allows the evaluation of ionization cross sections between spin-free and SOC states and has been used in [GG1]-[GG3] and [50, 98, 128, 129]. It interfaces the Dyson code wherein the evaluation of spin-free and spin-coupled DOs as well as the occupation number analysis have been implemented to the ezDyson program [94, 134], which contributes the numerical integration of the dipole TMEs. ezDyson provides spherical Bessel and Coulomb wave functions to describe the radial part of the continuum orbitals, corresponding to the free-particle and effective Coulomb potential models, respectively (Sec. 2.2.2).

To permit the evaluation of molecular Auger decay rates, another program with the working title Auger has been written. Its first applications are presented in [GG4] and [GG5]. This code implements the complete spin-free SCI approach as discussed in Secs. 2.2-2.4. In particular, it includes the more accurate numerical continuum orbitals generated by the spherically averaged molecular potentials in addition to the analytic ones. The evaluation of the Auger decay TMEs in Eq. (17), corresponding to the SO, NO, and GS approaches as well as of the photoionization dipole TMEs, Eq. (14), in the SO approximation are the core of this program. Modeling Auger decay requires $O(N_b^3)$ (N_b = number of basis functions) continuum-bound Coulomb integrals and 2RTD coefficients, respectively, to be evaluated and stored for each transition $i \rightarrow \alpha$, whereas only $O(N_b)$ are required for photoionization. Therefore, efficient algorithms, detailed in [GG4], for adaptive numerical integration and interpolation, as well as specialized GTO integral libraries needed to be incorporated in this code.

To reduce the numerical effort considerably, the fact that the kinetic energy of the outgoing electron is encoded only in the radial function $w_l^{fk}(r)$ is exploited. To this end all atomic basis continuum-bound TMEs are evaluated in the continuum-orbital-centered spherical coordinates $\boldsymbol{r}_s(r, \Omega)$, allowing to separate each integral into its radial and angular parts

$$\langle \psi_\alpha | f_n | \chi_b \rangle = \int_0^\infty r w_l^{fk}(r) \underbrace{\left[\int_\Omega Y_l^m(\Omega) f_n(\boldsymbol{r}(r, \Omega)) \chi_b(\boldsymbol{r}(r, \Omega)) d\Omega \right]}_{F_{nb}^{lm}(r)} dr \,. \tag{23}$$

Here, $\chi_b(\boldsymbol{r})$ are the atomic basis functions and $\boldsymbol{r}(r, \Omega) = \boldsymbol{r}_s(r, \Omega) + \boldsymbol{r}_c$ is the coordinate in the molecular frame. Further, $f_n(\boldsymbol{r})$ generically denotes one-electron operators and $f_n(\boldsymbol{r}) = \int \chi_a^*(\boldsymbol{r}')|\boldsymbol{r} - \boldsymbol{r}'|^{-1}\chi_c(\boldsymbol{r}')d\boldsymbol{r}'^3$ in the two-electron case. This allows to first evaluate and store the angular integrals as radial functions $F_{nb}^{lm}(r)$ and subsequently to reuse them for the energy dependent radial integrations for all transitions. Therefore, TMEs for several tens of thousands of transitions can be computed efficiently. Note that even for the evaluation of PES this numerical protocol is much faster than the ezDyson approach, in which three-dimensional integrations are carried out for each transition. Depending on the number of transitions, Auger can save up to several orders of magnitude in computational time in comparison to the well-established ezDyson protocol, thereby allowing a considerably more accurate treatment of the continuum orbitals. In addition, the code uses a hybrid MPI/openMP parallelization scheme, allowing to scale calculations over multiple nodes with multiple CPUs.

3 Molecular photoionization with simple models

Herein, the application of the Dyson orbital approach implemented in the DYSON/EZDYSON protocol, Sec. 2.6, to the simulation and assignment of molecular PES is presented in light of various scientific questions. It starts with a scrutinization of the sudden approximation, Eq. (19) and the free-particle continuum model (Sec. 2.2.2) for the simulation of the valence PES of gaseous water and the X-ray L-edge core PES of aqueous iron(II) ions, respectively [GG1]. Next, still in the framework of X-ray photoionization, the $4d$ PES of I_3^- in ethanol solution is investigated as a probe for solvent-induced nuclear asymmetry effects [GG3]. Therein, the occupation number analysis, Sec. 2.5.2, has been carried out to unambiguously characterize the spectra. Finally, PES obtained for representative configurations at the free-particle continuum level are used to disentangle the pathways of experimentally observed ultrafast electronic dynamics, exemplified for the photoinduced spin crossover in the iron tris-bipyridine complex $[Fe(bpy)_3]^{2+}$ [GG2].

The respective bound wave functions were computed by different combinations of the RASSCF, RASPT2, and RASSI methods using a locally modified version of MOLCAS 8.0 [137]. The phenomenological broadenings, Eq. (13), and absolute energetic shifts that have been applied to achieve visual correspondence to the experimental spectra are detailed in the respective manuscripts

3.1 X-ray photoionization

The experimental data have been obtained with synchrotron radiation at the U41 PGM undulator beamline of BESSY II, Berlin, using the liquid microject technique [45, 139], for details see [GG1] and [GG3].

3.1.1 Benchmark of the sudden approximation and the free-particle continuum model

The boundaries of the SA, which neglects the integration with the continuum orbital for the sake of computational efficiency, Eq. (19), encompass a high kinetic energy of the outgoing particles and a similar character of the ionization throughout the spectrum. The free-particle continuum model, neglecting the molecular potential, can be expected to hold under similar constraints, although it provides direct access to the kinetic energy of the outgoing particle.

Water The valence PES of water at 180 eV fulfills the requirement of a comparatively high photoelectron energy but comprises distinct peaks for each of its molecular orbitals, violating the second SA requirement. Therefore, the well understood H_2O PES [111, 140–142] allows to test the applicability of the SA and free-particle approaches at the respective limits of the approximations. Panel (a) of Fig. 3, taken from [GG1] and the respective erratum, contains the experimental and theoretical PES of gas phase water at 180 eV photon energy. Both, the SA and free-particle (denoted as full calculation) spectra are depicted. For the free-particle approach,
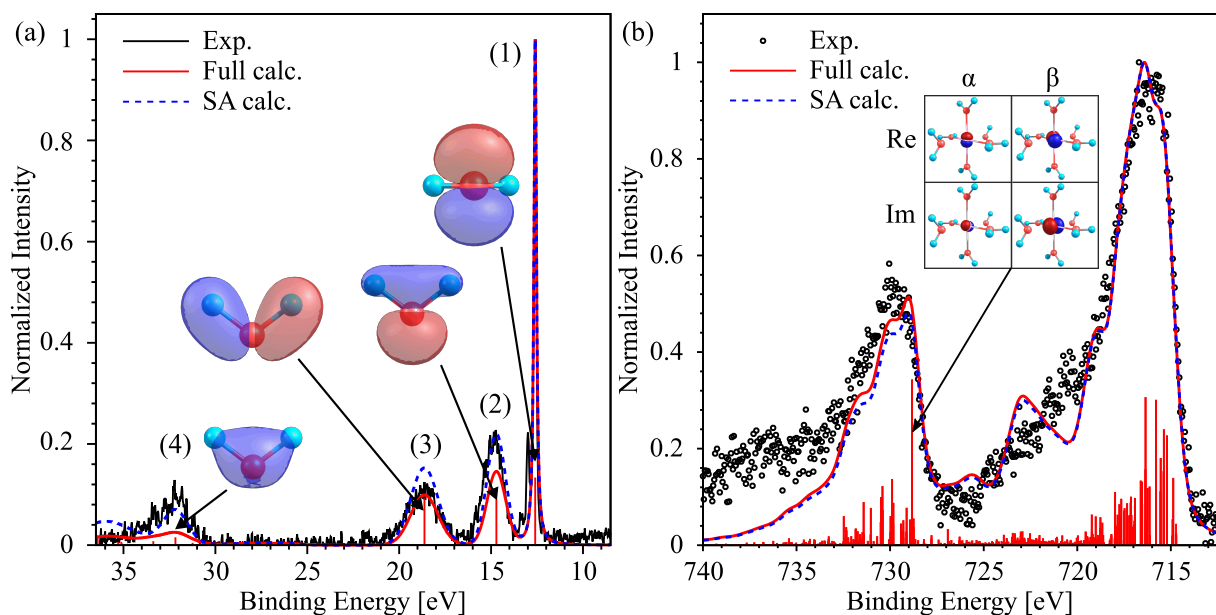
Figure 3: Modified with permission from [GG1] and the respective erratum. (a) Calculated and experimental PES of gas phase water for 180 eV incoming photon energy. Full calculation corresponds to the free-particle continuum model, SA means sudden approximation [105, 106]. The DOs corresponding to the respective features are shown. (b) Experimental (2M $FeCl_2$ aqueous solution) and calculated ($[Fe(H_2O)_6]^{2+}$) L-edge core PES of aqueous iron(II) ions for a photon energy of 925 eV. The real and imaginary parts of the α and β spin contributions to the spin-coupled DOs are exemplified for one transition.

the cross sections corresponding to each transition are plotted as sticks in addition. The bound neutral and cationic states have been obtained at the RASSCF/RASPT2 level, predicting the relative energetic positions of the peaks with very high accuracy [GG1]. Therein, a complete active space considering the lowest 7 molecular orbitals of water has been used. Concerning the intensities, both calculated spectra demonstrate a good agreement with the experimental result. The individual peaks can be assigned in terms of their respective DOs, indicated in Fig. 3 (a). Thus peaks (1)-(4) correspond to ionization from the $1b_1$, $3a_1$, $1b_2$, and $2a_1$ orbitals of water, respectively, which is in agreement with established assignments [111, 140–142]. Note that the single orbital ionization picture holds to high accuracy for peaks (1)-(3) and approximately for peak (4). However, relative to peak (1) the SA results in larger intensities for peaks (2)-(4), respectively, thereby representing peaks (2) and (4) better than the free-particle model. Most striking, the free-particle intensities underestimate peak (4) by a factor of 2.5 with respect to the SA ones.

In summary, the PES of gaseous water at 180 eV can be predicted qualitatively correct and unambiguously assigned within the SA, providing slightly better agreement with the experiment than the free-particle model. The deviations between the SA and free-particle results can be naively understood as a measure for the sensitivity of the spectrum to the differences in energy and character of each transition. This indicates that this case is indeed at the limits of the SA, but can still be approximately described by it. To improve the spectrum, one should employ a better continuum orbital model that considers the system as an effective point charge or takes into account the spherically averaged molecular potential.

Iron(II) ions in aqueous solution   In contrast to the valence ionization of water, the L-edge core PES of solvated iron(II) ions at 925 eV, lies well within the realm of the SA, since only ionization from the iron $2p$ orbitals is contributing. Here, the complications lie in the bound electronic structure, necessitating the inclusion of the first solvation shell that forms the $[Fe(H_2O)_6]^{2+}$ complex. Further the system has a quintet ground state but strongly spin-mixed core-excited and core-ionized states. This requires a SOC calculation at the RASSCF/RASSI level that includes the quintet and triplet, as well as sextet, quartet, and doublet manifolds for the Fe^{2+} and Fe^{3+} systems, respectively. The active space comprises the 3 $Fe(2p)$ and 5 predominant $Fe(3d)$ orbitals in the respective RAS1 and RAS2 subspaces [GG1].

Panel (b) of Fig. 3, contains the experimental (2M $FeCl_2$ aqueous solution [GG1]) and theoretical ($[Fe(H_2O)_6]^{2+}$) L-edge core PES results at 925 eV photon energy. Notably, the splitting, relative intensities, and asymmetric shapes of the L_3 and L_2 bands around 716 eV and 730 eV, respectively, are very well reproduced by the theory. These bands correspond to the total angular momenta of 3/2 and 1/2 of the created atomic $2p$ core hole, respectively. In particular, the SA and free-particle models yield almost coinciding results, underlining that the SA, i.e., disregarding the costly numerical integration of the dipole TMEs, is indeed perfectly applicable in this case. Notably, almost all of the 1260 transitions bear a nonzero intensity and contribute to the spectrum. This is a remedy of the strong multi-configurational and spin-mixed character of the core-ionized states, see [GG1] and its supplement. The spin-coupled DOs, Eq. (16), exemplified for one transition in Fig. 3 (b), bearing nonzero real and imaginary parts of α and β spin, reflect this mixing as well. The remaining discrepancies between theory and experiment could be ascribed to the lack of dynamic correlation (no RASPT2 correction) and to the presence of chlorinated species in the solution, which have been excluded in the calculations [GG1]. Further, employing a broadening scheme with higher flexibility might improve the agreement [GG1].

In summary, this shows that accurate X-ray core PES can be obtained based on multi-configurational SOC DOs derived from RASSCF/RASSI wave functions. Further, the computationally cheap SA, neglecting any actual treatment of the continuum orbitals, provides a means to evaluate such spectra very efficiently in an approach similar to the one in Ref. 112. Note that the SA based protocol is now publicly available within the recent version of OPENMOLCAS [143].

3.1.2 Unraveling solvent-induced molecular asymmetry effects

The $4d$ X-ray PES of the linear I_3^- molecule has been investigated theoretically in [GG3]. Thereby a symmetric $[I\text{-}I\text{-}I]^-$ and an asymmetric geometry corresponding more to $I_2 \cdots I^-$ have been treated with the aim to explore the effects of solvent-induced nuclear asymmetry on the observed PES [114, 144]. Herein, the focus is put onto the modeling aspect for the symmetric geometry.

The $4d$ X-ray PES of symmetric I_3^- can be considered an intermediate case between the valence spectrum of water and the core ionization of solvated iron ions. For instance, the

inclusion of SOC, over the singlet and triplet spin-free states of I_3^-, as well as the doublet, quartet and sextet manifolds of I_3 is mandatory to reproduce the spin-orbit splitting of the $4d_{3/2}$ and $4d_{5/2}$ levels. To this end, the RASSCF/RASPT2/RASSI approach accounting for dynamic correlation energy effects as well as SOC has been employed with 15 $4d$ and 3 $\sigma(5p_z)$ orbitals in the RAS1 and RAS2 subspaces, respectively [GG3]. However, the $4d$ DOs can be localized at the central iodine atom or delocalized over the whole molecule as well as only the terminal atoms, introducing more variety in terms of the DOs as in the solvated iron(II) case. Further, being measured at 600 eV, the kinetic energies of the outgoing electrons are the highest of all considered cases, suggesting that the SA might be well justified.

Investigating the influence of an explicit continuum treatment, Fig. 4 depicts the simulated $4d$ PES of symmetric I_3^- obtained in SA, as well as with the free-particle model for an incoming photon energy of 600 eV. These results are compared against the experimental I_3^- $4d$ PES of a 0.5M I_3^- ethanol solution, which stabilizes the symmetric geometry [114]. Evidently, the relative intensities of the main and shake up bands at 52.5-57.5 eV and 58-62 eV and are matched to a high accuracy with both theoretical approaches. The minute differences between the theoretical spectra demonstrate the applicability of the com-
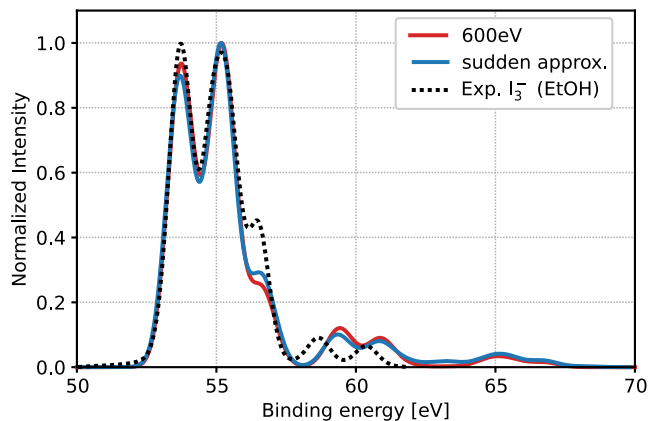

Figure 4: Modified witch permission from [GG3] and the respective supplement. Comparison between experimental and theoretical X-ray PES of I_3^- at at 600 eV photon energy. The experimental spectrum represents the isolated 4d signal of I_3^- in ethanol (EtOH) solution [114]. The theoretical spectra have been obtained for an isolated I_3^- molecule using the free-particle model as well as the sudden approximation.

putationally much cheaper SA. The remaining differences are an underestimation of the shoulder at 57 eV and a general 0.7 eV shift of the shake up part towards higher binding energies. Notably, the inclusion of the RASPT2 correlation energy correction is necessary to reproduce both the relative position and intensity of the shake up feature [GG3].

Occupation number analysis The detailed assignment of the $4d$ I_3^- X-ray PES can not be made on the basis of the DOs alone, which do not allow to unveil the character of the excitations that accompany the $4d$ ionization in the shake up peak. Here, the occupation number analysis introduced in Sec. 2.5.2, provides the means to characterize the DO (ionization) and the accompanying excitation for each pair of I_3^- and I_3 states, (g, f), in terms of the bound orbitals of the initial I_3^- species. The resulting DO ($\boldsymbol{n}_{gf}$) and residual occupation vectors ($\boldsymbol{n}_{gf}^{\text{res}}$), Eqs. (21) and (22), are shown in panels (a) and (b) of Fig. 5, respectively. In each panel, the entries of the respective occupation vector for a particular transition (binding energy, x-axis) are organized vertically, representing a slice of the 2D plot. The different vertical segments of these slices
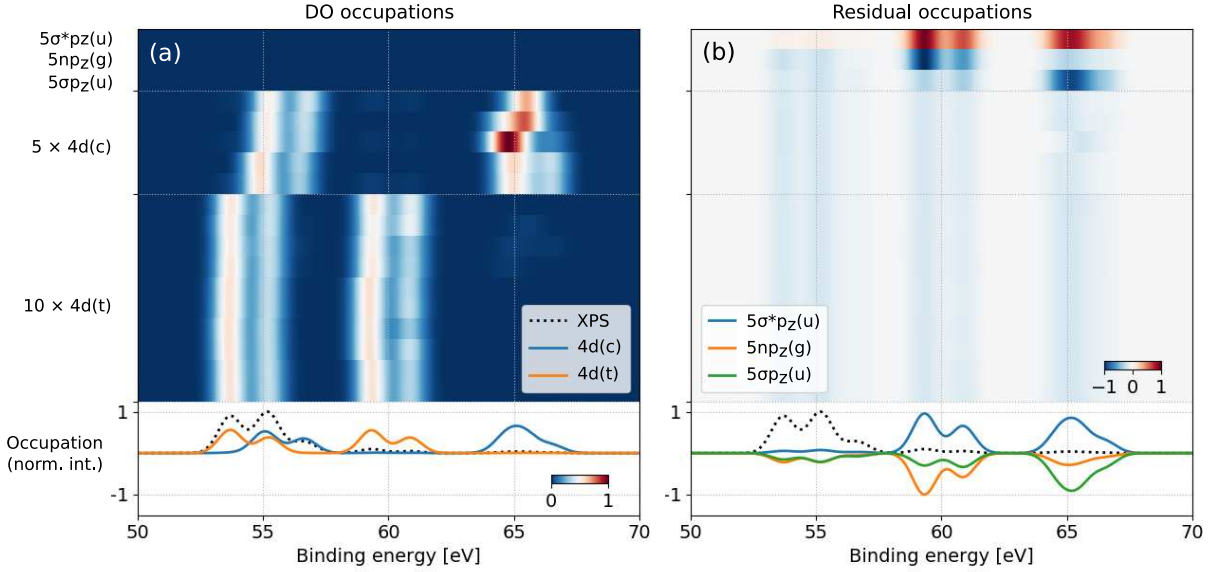
Figure 5: Reproduced with permission from [GG3]. Occupation number analysis of the main and shake-up transitions in the symmetric I_3^- $4d$ PES. DO ($\boldsymbol{n}_{gf}$) and residual ($\boldsymbol{n}_{gf}^{\mathrm{res}}$) occupation numbers, see Eq. (22), are given in panels (a) and (b), respectively. The occupation vectors for a particular transition (binding energy) represent a vertical slice. Each y-axis segment of these slices corresponds to one of the active orbitals depicted on the left. The occupation numbers have been broadened along the binding energy axis in the same way as the intensities in Fig. 4. In addition, they have been renormalized to a range of -1 to 1. The lower part of each panel shows a comparison of the SA spectrum (dashed) and the occupation numbers averaged over the different orbital types (y-axis) to indicate the different contributions. Note that for the sake of clarity only relevant transitions that contribute at least 5% of the maximum intensity have been taken into account.

correspond to the indicated molecular orbitals. According to their localization the $4d$ orbitals can be identified as, 10 central, $4d$(c), and 5 terminal ones, $4d$(t), respectively. Further, the $5p$ orbitals correspond to bonding, $5\sigma p_z(u)$, non-bonding, $5np_z(g)$, and anti-bonding $5\sigma^* p_z(u)$ character, respectively, where u and g are the usual inversion symmetry labels. The molecular orbitals are pictured in [GG3].

In accordance with previous results [114, 144], the main features can be assigned to ionization from the terminal, $4d$(t), or central, $4d$(c), sites. Here, each type gives rise to the $4d_{3/2}$ and $4d_{5/2}$ features that are spin-orbit split by 1.6 eV, respectively, occuring as parallel vertical lines in the DO occupations, Fig. 5 (a). The sum of transitions around 55 eV gives rise to the double peak and the shoulder of the main feature. The two peaks in the shake-up feature around 60 eV, however, corresond to the spin-orbit split $4d$(t) contribution. Their distance from the main feature is the result of the accompanying $5np_z(g) \rightarrow 5\sigma^* p_z(u)$ excitation that can be clearly identified in the associated residual occupations, Fig. 5 (b). Since the combination of shake-up excitations from g to u orbitals with ionization from central site g orbitals is symmetry forbidden [145], ionization from the $4d$(c) orbitals does not contribute at this energy. Ionization from the terminal sites can occur, however, because the terminal hole breaks the symmetry. Central site shake-up features associated with the parity conserving $5\sigma p_z(u) \rightarrow 5\sigma^* p_z(u)$ excitation, are only seen at much lower intensity near 65 eV.
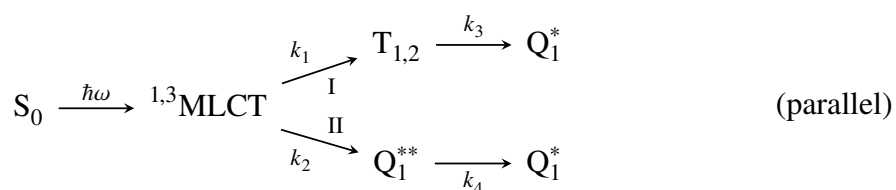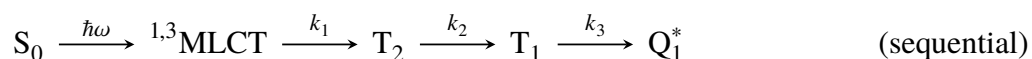
Note that for the asymmetric $I_2 \cdots I^-$ case ionization from all three sites contributes to the

shake up feature which consequently has an increased absolute intensity, as discussed in [GG3]. The degree of nuclear asymmetry is directly reflected in the relative intensity of main and shake-up features, suggesting that this single scalar observable can evidence solvent-induced nuclear asymmetry in the I_3^- ion, which simplifies the analysis. Moreover, the SA is indeed a good approximation not only for the simulation of the more or less atomic iron(II) L-edge core PES of $[Fe(H_2O)_6]^{2+}$, but also for the molecular inner valence $4d$ PES of I_3^- at soft X-ray energies.

3.2 Deciphering ultrafast dynamics: spin crossover

The analysis of time-resolved pump-probe experiments, unraveling electron and nuclear dynamics on ultrafast timescales is a common task in modern molecular science [43]. In the framework of UV/vis pump XUV photoionization probe experiments the DYSON/ezDYSON approach has been used to provide theoretical snapshot PES of transient states to aid the assignment of femtosecond dynamics that are initiated by the excitation created with the pump pulse in various iron complexes. In particular, electronic relaxation dynamics of $[Fe(CN)_6]^{3-}$ [128], linkage isomerism of the NO group in $[Fe(CN_5)NO]^{2-}$ [129] and ultrafast spin crossover in the iron tris-bipyridine complex, $[Fe(bpy)_3]^{2+}$ [GG2], have been studied.

Herein, the latter case is presented to exemplify the procedure. The sample has been prepared as a 50mM aqueous solution of $[Fe(bpy)_3]Cl_2$ and was investigated using a liquid microjet technique [45, 139]. The pump-probe measurement has been carried out using a table-top Ti:sapphire laser system that provides the optical 2.34 eV pump and the 32.55 eV XUV probe pulses via a HHG setup [146] with a resolution of $\approx$ 60 fs, see [GG2] and the supplement therein. The pump has been tuned to resonantly excite a short lived singlet metal-to-ligand charge-transfer (MLCT) state, ^{1}MLCT, that is known to decay within 100 fs into a metastable quintet state, Q_1, providing a change of the total spin by $\Delta S = 2$ [147–153]. In Refs. 148 and 152 the spin crossover pathway has been argued to be sequential, involving intermediate triplet states T_n (^{1,3}MLCT $\rightarrow$ T_n $\rightarrow$ Q_1, model I). Further, a direct mechanism (^{1,3}MLCT $\rightarrow$ Q_1, model II) that is in principle unlikely to occur since it necessitates the spin flip of two electrons has been suggested to become available due to coupling to non-totally-symmetric vibrational modes [147]. In [GG2], two extended kinetic models, sequential and parallel, have been found to yield good agreement with the experimental transient signal within a global fit analysis.

$$S_0 \xrightarrow{\hbar\omega} {}^{1,3}MLCT \xrightarrow{k_1} T_2 \xrightarrow{k_2} T_1 \xrightarrow{k_3} Q_1^* \qquad \text{(sequential)}$$

$$S_0 \xrightarrow{\hbar\omega} {}^{1,3}MLCT \begin{array}{c} \xrightarrow[\text{I}]{k_1} T_{1,2} \xrightarrow{k_3} Q_1^* \\ \xrightarrow[\text{II}]{k_2} Q_1^{**} \xrightarrow{k_4} Q_1^* \end{array} \qquad \text{(parallel)}$$

The sequential model corresponds to the triplet cascade (model I) [148, 152], whereas the parallel

one includes both, the direct (model II) [147] and cascade pathways. The lowest triplet states, T_1 and T_2, the vertically populated vibrationally hot Q_1^{**} and the partially equilibrated Q_1^* quintet states are included in the models. Note that the $Q_1^{**} \rightarrow Q_1^*$ transition occurs via vibrational cooling. Due to ultrafast intersystem crossing [153] and internal conversion [152], the singlet to triplet MLCT and $T_2 \rightarrow T_1$ transitions, respectively, can not be resolved experimentally. This permits to regard them as single states ^{1,3}MLCT and $T_{1,2}$, respectively. In the sequential model, however, the T_2 and T_1 states enter separately. The k_n are the respective time constants given in [GG2].

For both extended models, the global fit produced rather similar results for the 2D transient signal and the decay time constants of the short-lived states (Table S1 and Fig. S6 in the supplement to [GG2]). Hence, the global fit and statistical analysis needed to be complemented by a theoretical study to deduce whether the parallel or sequential model is the proper one. To this end theoretical PES of the S_0 ground and the transient T_1, T_2 and Q_1^{**} states, populated in the Franck-Condon region, have been obtained. The theoretical $T_{1,2}$ PES has been obtained by evenly averaging the T_1 and T_2 spectra. The outgoing electrons have been modeled as free particles. The bound states have been obtained at the RASSCF level using an active space involving 3 σ(bpy), 5 Fe($3d$), and 3 σ^*(bpy) orbitals in the RAS1, RAS2, and RAS3 subspaces, respectively [GG2]. The doublet, quartet, and sextet valence manifolds of $[Fe(bpy)_3]^{3+}$ have
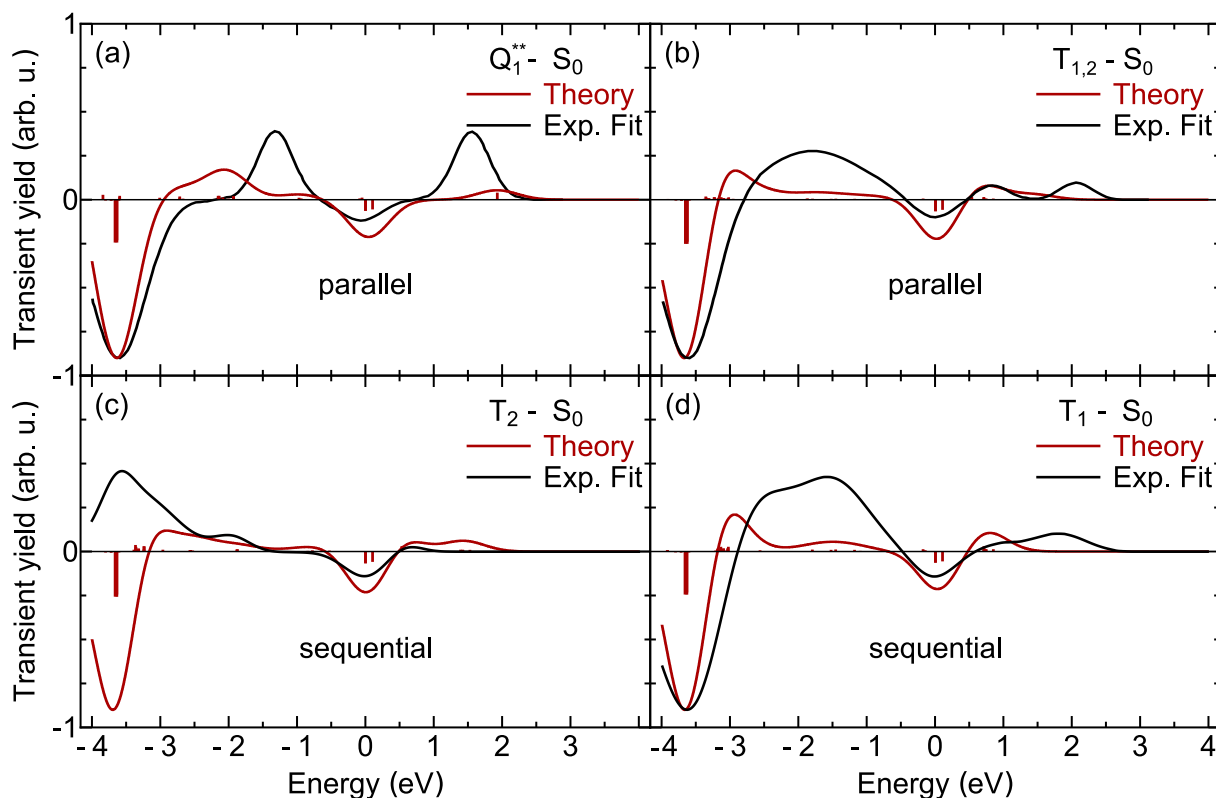

Figure 6: Revised version of the results shown in [GG2] and the respective supplement.[2] (a), (b) Comparison of the PES of the Q_1^{**} and $T_{1,2}$ states obtained from the global fit for the parallel model with the spectra predicted by theory. (c), (d) Comparison of theory and global fit results for the sequential model. Emission spectra of the triplet T_2 and T_1 states are shown. For consistency with the experimental transient signal [GG2], the ground state S_0 PES has been subtracted everywhere.

been considered as the target states for the ionization process.

The comparison of the respective theoretically predicted PES with the global fit results for the short lived $T_{1,2}$ and Q_1^{**} species is shown in Fig. 6, where the S_0 spectra have been subtracted for consistency with the transient signal plot in [GG2]. Panels (a) and (b) correspond to the parallel, (c) and (d) to the sequential models, respectively.[2] For convenience, the origin of the energy scale has therein been shifted to the ionization from the iron $3d(t_{2g})$ orbitals, visible as negative signal around 0 eV. One can see that the theory qualitatively reproduces the emission band structure of the $T_{1,2}$ and Q_1^{**} states populated in the parallel relaxation process. However, only the T_1 PES can be reproduced for the sequential model. For the T_2 state, the fit results do not contain the negative signal between -4.2 eV and -3.2 eV, which is a trace of the ground state depletion that decays in the experimental signal within < 100 fs due to the population of the Q_1^* state, which contributes in the same spectral region. Therefore, the T_2 spectrum should contain such a contribution as well and the fact that it does not has lead to the rejection of the purely sequential model in [GG2]. However, the sequential channel I of the parallel model was found to be the dominant one with a branching ratio of $4.5^{+4.8}_{-1.5}$.

These results demonstrate, how intricate electron dynamical processes in transition metal complexes can be assigned by complementing the experimental spectra with theoretical PES that have been obtained with a simple free-particle continuum model. However, the agreement between the global fit and theoretical results is only qualitative. While the energetic positions of the features may be improved by including the RASPT2 correction, better intensities require a more involved model for the ionized electron, for instance the numerical SCI approach suggested in Sec. 2.2.1 that will be discussed in the following.

---

[2]   The results correspond to updated versions of Figs. 2 and S7 of [GG2] and its supplement, respectively, taking into account the spin conservation, Eq. (4), which was treated only approximately in the original paper. The conclusions drawn within [GG2], however, remain unchanged. Note that the labels T_1 and T_2 are exchanged in the supplement therein.

4 Numerical continua for photo- and autoionization

In this section the application of the numerical continuum orbitals derived from the spherically averaged direct and direct-exchange potentials $V_f^{\text{J}}(r)$ and $V_f^{\text{JX}}(r)$ to the simulation of atomic and molecular RAES and PES is presented. To this end, results obtained with the AUGER implementation, Sec. 2.6, that have been presented in [GG4] and [GG5] are reviewed.

4.1 Auger decay of the neon $1s^{-1}3p$ resonance

To begin with, the respective impact of the r^{-1} and $\mathcal{H}$ couplings, radial potential approaches, and treatments of the continuum-bound nonorthogonality (Secs. 2.2 & 2.4) on the Auger decay rates is investigated on the paradigmic example of the neon $1s^{-1}3p$ resonance, ruling out molecular effects [GG4]. Six different models, V^{free}, $-1/r$, and $-6/r$, corresponding to the free-particle and effective Coulomb potentials, respectively; as well as $V_f^{\text{scr}}(r)$, $V_f^{\text{J}}(r)$, and $V_f^{\text{JX}}(r)$, i.e., the spherically averaged screened charge, direct, and direct-exchange potentials have been introduced in Sec. 2.2.2. Combining each of these with either the complete $\mathcal{H}$ or approximate r^{-1} coupling and one of the NO, SO, or GS nonorthogonality approaches results in 36 different variants how to evaluate partial Auger decay rates using Eq. (17), that have been analysed in [GG4].

4.1.1 Benchmark of theoretical models

All of these approaches are analyzed in Fig. 7, taken from [GG4]. Therein, the atomic and cationic bound states have been obtained at the RASSCF/RASPT2 level using an active space containing the $1s$, $2s2p$, and $3s3p4s4p$ orbitals in the RAS1, RAS2, and RAS3 subspaces, respectively. In addition, a specifically designed Rydberg basis set has been employed [156]. This scheme, labeled QC I, is detailed in [GG4], and the respective supplement. Panel (a) depicts the neon $1s^{-1}3p$ RAES obtained using the $\mathcal{H} \cdot V_f^{\text{JX}}(r) \cdot$ NO and $r^{-1} \cdot V_f^{\text{JX}}(r) \cdot$ NO approaches to unravel the impact of the r^{-1} coupling approximation on the spectrum. A reference at the MCDF level, employing r^{-1} coupling and four-component continuum orbitals corresponding to the potentials of the respective cationic states, published by Stock et al. [154], serves as a theoretical benchmark. For consistency, the spectra have been aligned to the 811.5 eV peak in the experimental data taken from Kivimäki et al. [157], Fig. 8, and broadened using the same 0.1 eV Gaussian full width at half maximum (FWHM) as in Ref. 154. The dominant continuum orbital angular momentum contribution to the intensity that has been indicated for each peak shows that the regions 743-765 eV, 765-800 eV, and 800-825 eV predominantly correspond to the emission of s, p, and d waves, respectively. This regions will thus be referred to as s, p, and d in what follows.

Fig. 7 (a) shows that the $\mathcal{H}$ and r^{-1} coupling RAES are almost indistinguishable in the s and d regions, whereas the p region demonstrates some variation. Overall, neglecting the contributions beyond the r^{-1} coupling in the partial rate evaluation seems to be justified in this
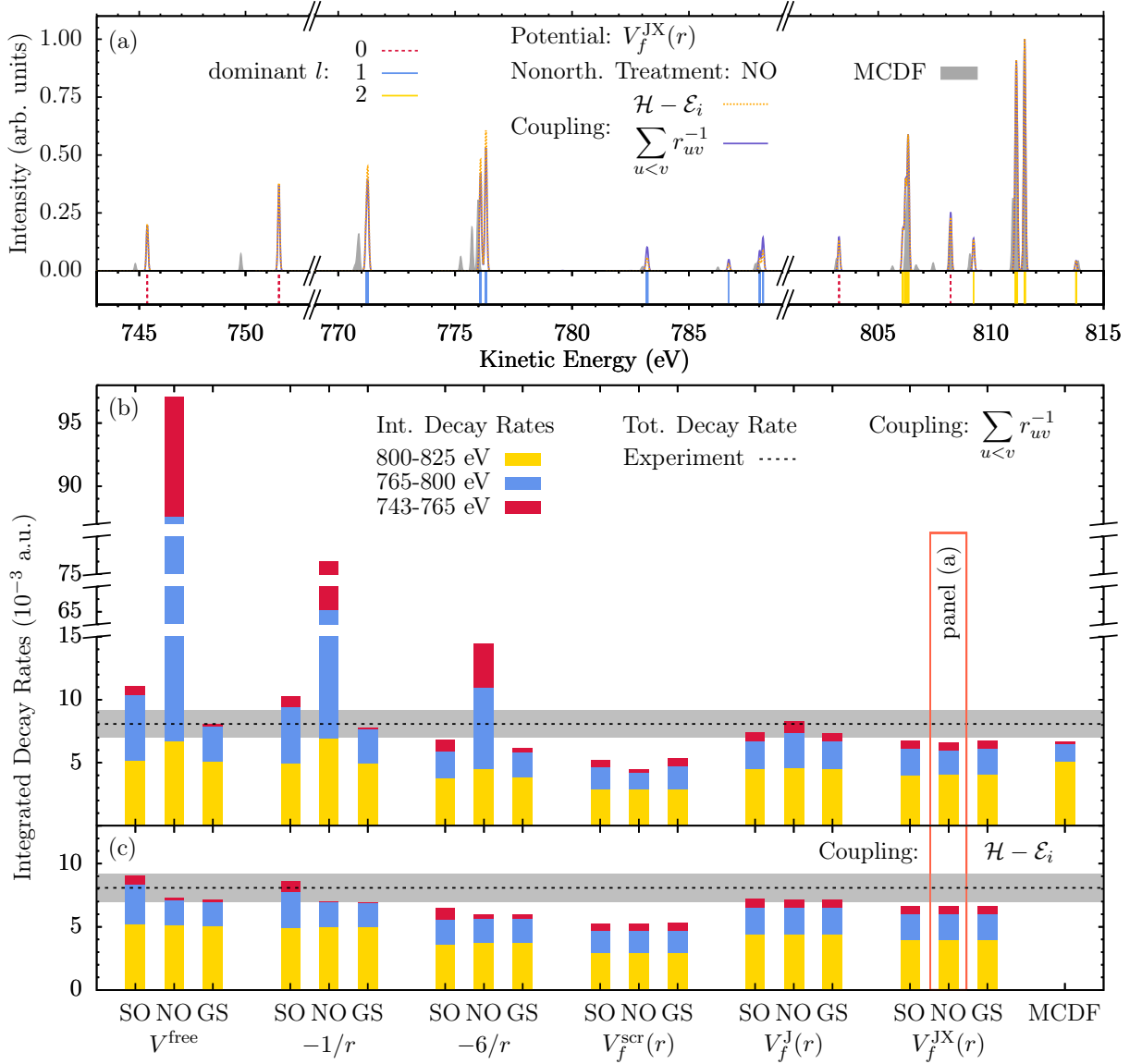
Figure 7: Reproduced from [GG4] with permission. (a) Neon $1s^{-1}3p$ RAES obtained with the r^{-1} and $\mathcal{H}$ couplings and the NO approach using continuum orbitals generated by the $V_f^{JX}(r)$ potential are shown in comparison to the MCDF results reported by Stock et al. [154]. The spectra from (a) correspond to the NO histograms of the $V_f^{JX}(r)$ potential in panels (b) and (c). The vertical lines at the bottom of panel (a) indicate the predominant continuum orbital angular momentum, l, contribution to each peak. (b) & (c) r^{-1} and $\mathcal{H}$ coupling Auger decay rates, respectively, integrated over the given energy ranges corresponding to distinct l contributions. The SO, NO, and GS nonorthogonality approaches have been employed. The depicted potentials have been used to generate the continuum orbitals. The MCDF data have been scaled such that the total decay rate matches the one obtained for the $r^{-1} \cdot V_f^{JX}(r) \cdot$ NO approach. The experimentally determined total rate of $8.08 \pm 1.1 \times 10^{-3}$ a.u. (0.22 ± 0.03 eV) [155] is depicted as a horizontal dashed line surrounded by a gray region indicating the uncertainty.

case. The MCDF data is well reproduced by the SCI approach only in the d region, whereas the p and s regions bear blue shifts and an overestimation of the intensities that increases towards the low energy flank of the spectrum. The higher number of small satellite features present in the MCDF spectrum can be attributed to the larger configuration space employed in Ref. 154.

Panels (b) and (c) of Fig. 7 contain the integral partial decay rates for the s, p, and d regions, respectively, facilitating the comparison of all 36 different approaches to compute the decay

rates. The data shows that the integral decay rates converge for both couplings as the quality of the potential is increased from the free-particle approximation V^{free} to the spherically averaged direct-exchange potential $V_f^{\text{JX}}(r)$. The $s : p : d$ - ratio obtained from the MCDF spectrum, however, is not matched. Generally, the complete $\mathcal{H}$ coupling, panel (c), yields mostly smaller total decay rates and less pronounced differences between the SO, NO and GS results. In particular, it mitigates the immense overestimation due to the combination of r^{-1} coupling and NO terms for the V^{free}, $-1/r$, and $-6/r$ potentials completely. This can be ascribed to cancellation effects between the different one- and two-electron NO terms in Eq. (17), that are broken by the r^{-1} coupling approximation. Ultimately, the impact of the SO, NO and GS treatments is determined by the magnitude of the continuum-bound overlap integrals, which is small for the physically sound potentials $V_f^{\text{scr}}(r)$, $V_f^{\text{J}}(r)$, and $V_f^{\text{JX}}(r)$ [GG4]. This explains the stability of the decay rates obtained with these potentials with regard to the different nonorthogonality approaches. Note that the total decay rates obtained with the $V_f^{\text{J}}(r)$, and $V_f^{\text{JX}}(r)$ potentials reproduce the experimentally observed one [155]. The slight underestimation obtained with $V_f^{\text{JX}}(r)$ can be attributed to the inclusion of the attractive exchange term, Eq. (12b). The $V_f^{\text{scr}}(r)$ potential, even more attractive [GG4], leads to the smallest total rates.

It seems that only the potentials $V_f^{\text{J}}(r)$ and $V_f^{\text{JX}}(r)$ yield both, satisfactory total decay rates and RAES independent on the chosen coupling model and nonorthogonality treatment. Consequently, employing the r^{-1} and SO approximations seems to be well justified for this potentials, providing a computationally cheap protocol. Interestingly, the $-6/r$ potential yields results that are in approximate agreement with the more accurate ones for all but the $r^{-1} \cdot$ NO cases, providing a compromise between computational effort and accuracy [GG4]. Since it remains unclear whether the cancellation effects observed when using $\mathcal{H}$ coupling with the NO terms are a general feature or a peculiarity of the neon RAES, the NO terms should only be employed with caution. Generally, they should only be used, if the description of the potential and radial waves are sufficiently accurate. Otherwise, it seems to be safer to employ the GS or SO approaches, out of which the SO one is to be preferrred due to its computational simplicity.

4.1.2 Comparison with the experiment

To further examine the previous finding that reliable RAES can be obtained with the $r^{-1} \cdot V_f^{\text{JX}}(r) \cdot$ SO approach, the simulated spectra are compared against experimental data from Yoshida et al. [158] and Kivimäki et al. [157] in Fig. 8, taken from [GG4]. Therein, panels (a) and (b) contain the s and p as well as the d region spectra, respectively. Note that both experimental spectra have been recorded at the (pseudo) magic angle, ruling out anisotropy effects. In addition to QC scheme I, however, the QC models II, containing an uncontracted s basis and an account for scalar relativistic effects, as well as III, employing a larger active space than in QC I, have been tested [GG4]. The simulated RAES in both panels have been collectively aligned to the main peak at 811.5 eV in the experimental d region spectrum [157]. Broadening and normalization, however have been applied individually in each panel [GG4].
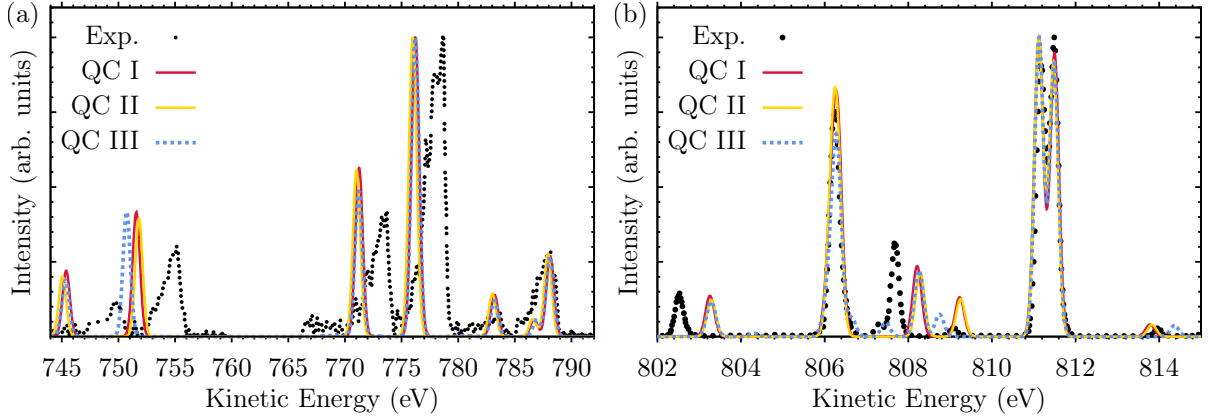
Figure 8: Reproduced from [GG4] with permission. Experimental and theoretical neon $1s^{-1}3p$ RAES obtained with the $r^{-1} \cdot V_f^{\mathrm{JX}}(r) \cdot \mathrm{SO}$ method combined with the QC schemes I - III, see text. The experimental spectra have been digitized from Refs. 157 (a) and 158 (b), respectively. The theoretical results have been collectively aligned to the peak at 811.5 eV in the experimental spectrum in panel (b). Broadening and normalization, however have been applied individually for each panel, see [GG4].

In the d region, the overall agreement between the simulated and experimental spectra is fairly good for all QC schemes regarding both, the relative intensities and energetic positions of the peaks. The main features are predicted more accurately than the small satellites. In the s and p regions, however, the experimental features are reproduced less exact. In particular, the kinetic energies are progressively underestimated towards the low energy end of the spectrum. This is a typical result of lacking excited state correlation in the QC, resulting in too high energies of the highest ionic valence-excited states. The different QC schemes I and II practically yield the same RAES, whereas the larger active space in QC III leads to a better reproduction of the small satellite features. It is to note, that the theoretical $r^{-1} \cdot V_f^{\mathrm{JX}}(r) \cdot \mathrm{SO}$ spectra obtained in [GG4] agree better with the experimental references [157, 158] than with the MCDF spectrum [154].

Importantly, the present investigation has shown that the SCI approach, employing the spherically averaged direct or direct-exchange potentials $V_f^{\mathrm{J}}(r)$ and $V_f^{\mathrm{JX}}(r)$ yields overall good agreement with experimental [157, 158] and theoretical [154] references for the neon $1s^{-1}3p$ RAES. For these approaches the computationally cheap $r^{-1} \cdot \mathrm{SO}$ treatment produces results close to the full $\mathcal{H} \cdot \mathrm{NO}$ one. Further, the experimentally obtained total decay rate [155] can be reproduced [GG4]. This opens the door to molecular systems, which are subsequently discussed.

4.2 Molecular photoionization and autoionization

The stage is now set to apply the SCI approach to simulate molecular PES and RAES using numerically obtained continuum orbitals that take into account the spherically averaged molecular potential (Sec. 2.2.2). The manuscript [GG5] contains its first application to molecular systems, demonstrating that molecular PES and RAES allowing an unambiguous assignment of the experimental data can be obtained with this method. Therein, the results from the previous section [GG4], have been followed in that the SO approximation, Eqs. (14) and (17), is employed always. Further, the direct potential $V_f^{\mathrm{J}}(r)$, Eq. (12a), has been used, since the influence of the

radial exchange term in $V_f^{\mathrm{JX}}(r)$, Eq. (12b), in the molecular case is not yet well understood within the SCI framework. Particular emphasis has been put into the applicability of the 1CA, see Sec. 2.4, to the decay rate evaluation, Eq. (17), and the influence of the continuum orbital origin, $\boldsymbol{r}_c$, which needs to be defined manually, see Sec. 2.2. The results that have been obtained for methane, CH_4, molecular oxygen, O_2, and pyrimidine, $C_4H_4N_2$ are summarized in the following. For all presented cases the bound wave functions have been obtained using the RASSCF/RASPT2 method with a locally modified version of MOLCAS 8.0. Further, the spin conserving continuum states, Eq. (4) have been employed. To introduce a common reference for the ionization spectra, they are presented on the binding energy scale. Therefore, the theoretical results and digitized experimental reference spectra have been aligned to accepted values for the respective vertical IPs, as detailed in [GG5]. Further, the broadening of the spectra has been tuned to achieve good visual correspondence with the experimental references. The obtained parameter sets are given in [GG5] and the respective supplement. Note that the current maximum angular momentum implemented in AUGER, $l_{\max} = 15$, is enough to ensure convergence of all spectra discussed herein, Eq. (13), apart from the case of the pyrimidine PES, which is only partially converged. Finally, all experimental PES and RAES correspond to (pseudo) magic angle measurements, which rules out anisotropy effects [GG5].

4.2.1 Methane

CH_4 is a well-suited test case because it is isoelectronic to the neon atom [GG4]; thorough studies regarding its XAS, PES and RAES have been carried out experimentally [159–161] and theoretically [162, 163]; and its tetrahedral geometry resembles a spherical system, indicating that the SCI approach could provide a good model. Fig. 9 contains the SCI results for the methane PES and RAES from various resonances, as well as the XAS for guidance. The respective experimental reference data have been digitized from Ref. 159. The bound states have been calculated with the $1a_1$, i.e., C($1s$) and the $2a_1$ and $1t_2$ orbitals forming the RAS1 and RAS2 subspaces, respectively. RAS3, however, contains the $ns(a_1)$, with $n = 3 - 5$, and $np(t_2)$, $nd(t_2)$, and $nd(e)$ Rydberg orbitals, with $n = 3, 4$. Note that the a_1, t_2, and e symmetries correspond to one, three, and two degenerate orbitals, respectively. In addition, a specialized Rydberg basis set, see Supplement of [GG5], has been used.

XAS   Fig. 9 (a) contains the experimental [159] and calculated XAS. The experimental spectrum is strongly influenced by vibrational broadening and vibronic coupling [160, 161], thus only the main features can be reproduced within the vertical excitation scheme used in [GG5]. The B($3s$) peak for instance, corresponds to the dipole forbidden core excitation to the $3s(a_1)$ Rydberg orbital that gains intensity due to a coupling to t_2 vibrational modes [161]. Generally, the theoretically obtained dominant Rydberg character is denoted in parenthesis for each resonance in the following. The labeling and assignment of the remaining resonances [159–161] is detailed in [GG5]. Overall, the energetic positions and XAS intensities of the Rydberg resonances are well described within the static RASSCF/RASPT2 method. Further improvements mandate the
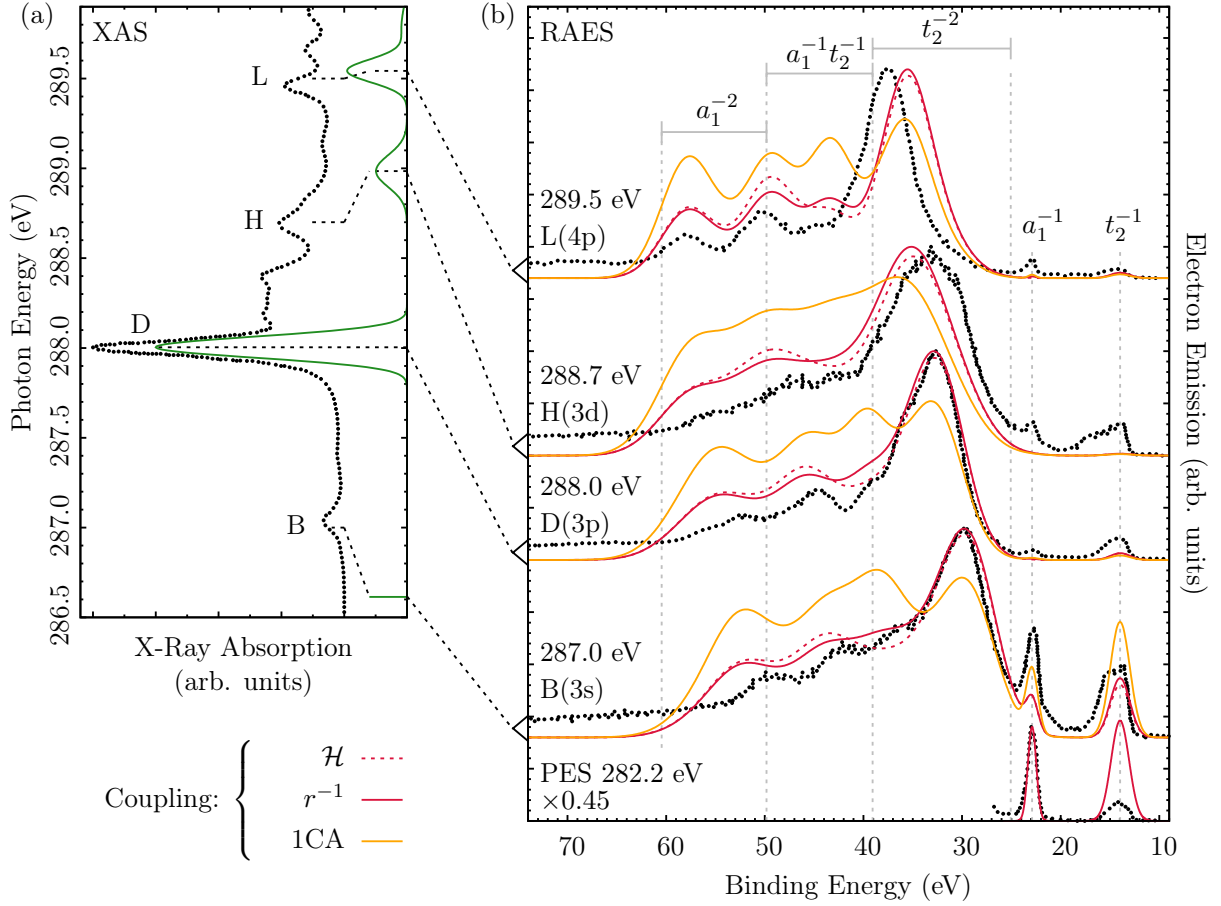
Figure 9: Reproduced from [GG5]. All experimental data (dotted) have been digitized from Kivimaeki et al [159]. (a) Calculated (green) and experimental XAS of methane at the carbon K-edge. The dipole-forbidden $3s(a_1)$ excitation is indicated by a single stick. The assignment of the experimental spectrum [160, 161] is connected to the corresponding calculated core-excited states of CH_4. (b) For each resonance depicted in (a) the RAES calculated using the $V_f^J(r)$ potential and the indicated couplings, as well as the spectra measured at the indicated excitation energies are shown. The $\mathcal{H}$, r^{-1}, and 1CA spectra for one resonance have been normalized with the same constant. The respective calculated carbon Rydberg contributions are given in paranthesis for each resonance. Further, spectral regions have been assigned to different valence hole states of CH_4^+ (gray). The experimental and theoretical valence PES obtained at a photon energy of 282.2 eV are shown as well. Shifts and broadening parameters: [GG5].

inclusion of nuclear dynamics and vibronic coupling.

PES and RAES   Panel (b) of Fig. 9 compares the theoretical and experimental [159] results for the RAES of the indicated resonances, as well as the valence PES below the carbon K-edge at 282.20 eV. The theoretical RAES have been obtained for the $\mathcal{H}$ and r^{-1} couplings, as well as the 1CA applied to the r^{-1} coupling in Eq. (17). The origin of the continuum orbitals has been naturally placed onto the central carbon atom. Notably, the relative PES intensities of the a_1^{-1} and the t_2^{-1} peaks, corresponding to emission from the $2a_1$ and $1t_2$ valence orbitals are not reproduced correctly. The t_2^{-1} feature is in fact overestimated by a factor of 4. A detailed analysis [GG5] indicates that the $a_1^{-1} : t_2^{-1}$ PES intensity ratio at this energy is a difficult case, which might require a continuum model that accounts for the true molecular symmetry.

The RAES can be divided into the participator and spectator decay regions, below and above 25 eV binding energy. Participator decay, leading to the same a_1^{-1} and t_2^{-1} single-

hole states as direct ionization, involves the excited electron in the decay process. In contrast, spectator decay resulting in the t_2^{-2}, $a_1^{-1}t_2^{-1}$, and a_1^{-2} double-hole states, leaves the excited electron unperturbed. The respective spectral regions that have been identified with an occupation number analysis [GG5], are depicted in Fig. 9 (b). Spectator decay is the predominant contribution to all RAES and considerable participator decay is only found in the theoretical B($3s$) decay spectrum.

Notably, the $\mathcal{H}$ and r^{-1} coupling spectra reproduce the experimental RAES with good accuracy, whereas the 1CA coupling leads to qualitatively different results due to an intensity redistribution from the main peak to the high energy tail. Consequently, the 1CA is not a suitable approximation when evaluating RAES of methane with the present approach, and the non-local contributions from the hydrogen atoms should not be disregarded. The remaining deviations between the $\mathcal{H}$ and r^{-1} coupling results and the experimental data can be rationalized as follows (see [GG5] for details). The blue and red shifts with respect to the experimental H($3d$) and L($4p$) RAES are most probably due to the lack of vibronic coupling and excited state correlation in the underlying QC. Further, the underestimation of the participator region for all but the B($3s$) resonances can be attributed to the two-step model employed throughout this work, which prohibits direct ionization contributions in the spectra.

Given the limitation to the two-step model, as well as the neglect of nuclear dynamics, the RAES of all investigated resonances have been reproduced quite well with the $V_f^J(r)$ potential and either of the $\mathcal{H}$ or r^{-1} couplings. These promising results indicate that the SCI approach can indeed predict correct molecular RAES and motivates the application to larger systems containing more than one "heavy" atom, which is presented hereafter.

4.2.2 Molecular oxygen

Molecular oxygen is a radical open shell system with a triplet ground state multiplicity that has drawn scientific attention since the realization of its relevance to all known higher lifeforms. Incidentally, the core-hole decay of O_2 is a textbook example of strong lifetime-vibrational interference effects [166–169], leading to a wealth of experimental XAS [164, 170–172], RAES [165, 166, 169, 172, 173], and PES [165, 166] studies which allows for a detailed test of the SCI approach. Its homonuclear linear geometry, however, leads to delocalized core holes in the calculation [GG5] and introduces ambiguity regarding the coordinate origin of the continuum wave functions. In [GG5], the variants $\boldsymbol{R}_O$ and $\overline{\boldsymbol{R}}_{O_2}$, i.e., putting the origin on one atom and at the interatomic center, respectively, have been employed. The bound states have been obtained at the equilibruum bond length of 1.208 Å [174]. Therein, O($1s$) core orbitals occupy the RAS1 subspace and all valence orbitals until the $1\pi_g$ and $3\sigma_u$ ones form RAS2, whereas the RAS3 subspace is empty. Note that the $1\pi_g$ orbital is doubly degenerate. In the ground state, the terminal $1\pi_g^2$ and $3\sigma_u^0$ orbitals are half filled and empty, respectively, leading to the triplet multiplicity according to Hund's rule [175].

XAS   The comparison of the theoretical K-edge XAS of O_2 against experimental data from Ma et al. [164] is presented in Fig. 10 (a). The main feature at 531 eV is the core excitation to
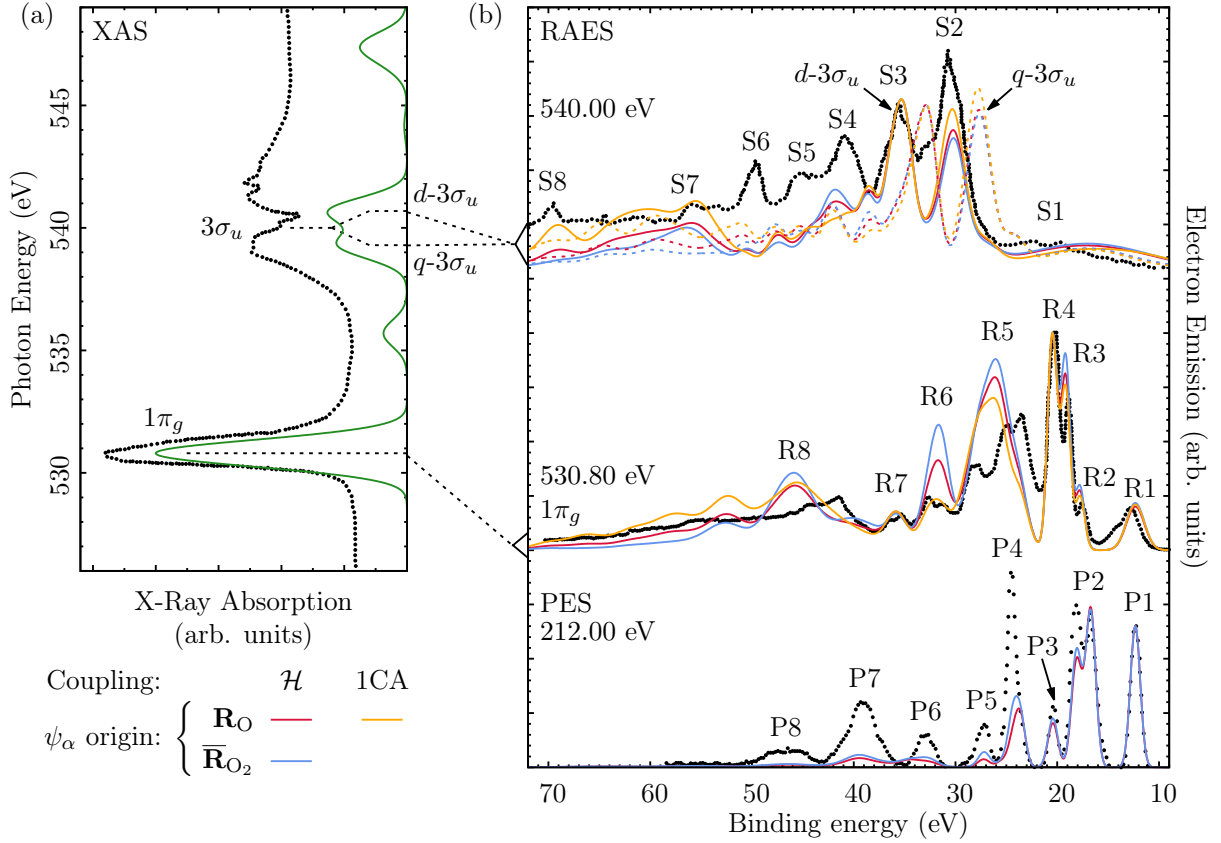
Figure 10: Reproduced from [GG5]. (a) Calculated (green) and experimental [164] (dotted) K-edge XAS of O_2. The theoretically obtained $1\pi_g$, $q\text{-}3\sigma_u$, and $d\text{-}3\sigma_u$ resonance positions are connected to the experimental excitation energies that have been used to obtain the respective RAES in (b). Therein, the simulated PES and RAES are compared to the measurements by Caldwell et al. [165]. Note that due to the high bandwidth of ~ 2.7 eV, the whole exchange-split $3\sigma_u$ double peak is excited by the incoming radiation at 540 eV. Hence the theoretical RAES for the $q\text{-}3\sigma_u$ (dashed) and $d\text{-}3\sigma_u$ (solid) resonances are depicted. The theoretical results employ the $V_f^J(r)$ potential originating either at one atom, $\boldsymbol{R}_O$, or at the molecular center, $\overline{\boldsymbol{R}}_{O_2}$. The RAES have been obtained with the indicated coupling approaches. The applied shifts and broadenings are detailed in [GG5].

the $1\pi_g$ orbital. The structured double peak at 539-545 eV, however, is due to the exchange-split $q\text{-}3\sigma_u$ and $d\text{-}3\sigma_u$ resonances corresponding to quartet and doublet spin coupling in the valence shell, respectively [164], [GG5]. Further, Rydberg excitations not included in this active space contribute there as well [164]. The assignment of the smaller features is detailed in [GG5]. The photon energies of 530.8 eV and 540.0 eV, at which the RAES have been recorded by Caldwell et al. [165], have been assigned to the theoretically found $1\pi_g$ and both of the exchange split $q\text{-}3\sigma_u$ and $d\text{-}3\sigma_u$ resonances, respectively, due to the bandwidth of ~ 2.7 eV.

PES and RAES Fig. 10 (b) compares the computed valence PES and the $1\pi_g$, $q\text{-}3\sigma_u$, and $d\text{-}3\sigma_u$ RAES of O_2 to the respective experimental results obtained at the depicted photon energies [165]. The $\mathcal{H}$ and 1CA couplings (only for $\boldsymbol{R}_O$), have been employed to evaluate the partial decay rates. Regarding the PES, it is remarkable that the energetic positions of the experimental features are reproduced almost exactly by the SCI approach. Moreover, the theoretical and experimental intensities coincide almost perfectly for P1-3. The features P4-8, however, involving multiple excitations [GG5], are progressively underestimated for higher binding en-

ergies, indicating that a larger active space might be required to achieve a better agreement. Interestingly, the continuum origin barely influences the PES, although it affects the absolute cross sections [GG5]. Note that the assignment in terms of the occupation numbers that is detailed in [GG5] agrees with a previous one. [176].

Concerning the RAES. Overall, the 1CA and $\mathcal{H}$ coupling results agree much better than for CH_4, see Fig. 9. In particular the simulated $1\pi_g$ RAES resemble the experimental data especially well for the low binding energy peaks R1-4. For higher binding energies, R5-8, however, the rendition of the experiment becomes less optimal, although an assignment is still possible [GG5]. Further, the deviations between the spectra obtained with different origins and couplings increase in this region as well. Here, the overestimations with the $\overline{R}_{O_2}$ origin can be assigned to an enhancement of the quartet decay branch [GG5]. The experimental $3\sigma_u$ RAES, however, is represented to a lesser extent by the theory. The q-$3\sigma_u$ and d-$3\sigma_u$ RAES appear to be shifted with respect to each other due to the exchange splitting and preferential decay to the respective spin manifolds of O_2^+. Comparing to the experiment, the q-$3\sigma_u$ spectrum remains shifted to lower binding energies by ~ 2.5 eV and the intensity of the S4-6 features is considerably underestimated. Here, previous studies [164, 172, 173, 177] have indicated that this can be attributed to two reasons. First, the photon beam with a bandwidth of ~ 2.7 eV simultaneously excites the q-$3\sigma_u$, d-$3\sigma_u$, and underlying Rydberg resonances, suggesting that the measured spectrum [165] contains contributions from all these resonances. Second, the $3\sigma_u$ resonances are dissociative, inducing a fast bond elongation on the time-scale of the Auger decay [165, 172, 173]. Hence it seems that the one-step model for resonant Auger decay [8] has to be employed together with nuclear dynamics and a larger active space, allowing for Rydberg excitations, to reproduce this experimental spectrum. Independent of the continuum origin, the $\mathcal{H}$ coupling results recover approximately 84% of the experimental total decay rate [171], whereas the 1CA provides only about 45%, which can be attributed to the $O(1s)$ core-hole delocalization, see [GG5].

Overall, the total Auger decay rates, valence PES, and $1\pi_g$ RAES of O_2 agree with the experimental reference. A better reproduction of the experimental results in the high binding energy regions and in particular for the $3\sigma_u$ spectrum requires the inclusion of Rydberg excitations into the active space, as well as the extension of the SCI approach to the one-step model for resonant Auger decay [8]. Further, the inclusion of nuclear effects needs to be considered as well. In contrast to the methane case, the 1CA predicts spectra of the same quality as the $\mathcal{H}$ coupling approach. Finally, the choice of the continuum origin has no strong effect on the obtained spectra and total decay rates.

4.2.3 Pyrimidine

Finally the SCI approach has been applied in a preliminary study to the pyrimidine molecule ($C_4H_4N_2$), which is computationally considerably more involved than CH_4 or O_2. Further, it is a precursor of several nucleic acids, which induced a large number of experimental and
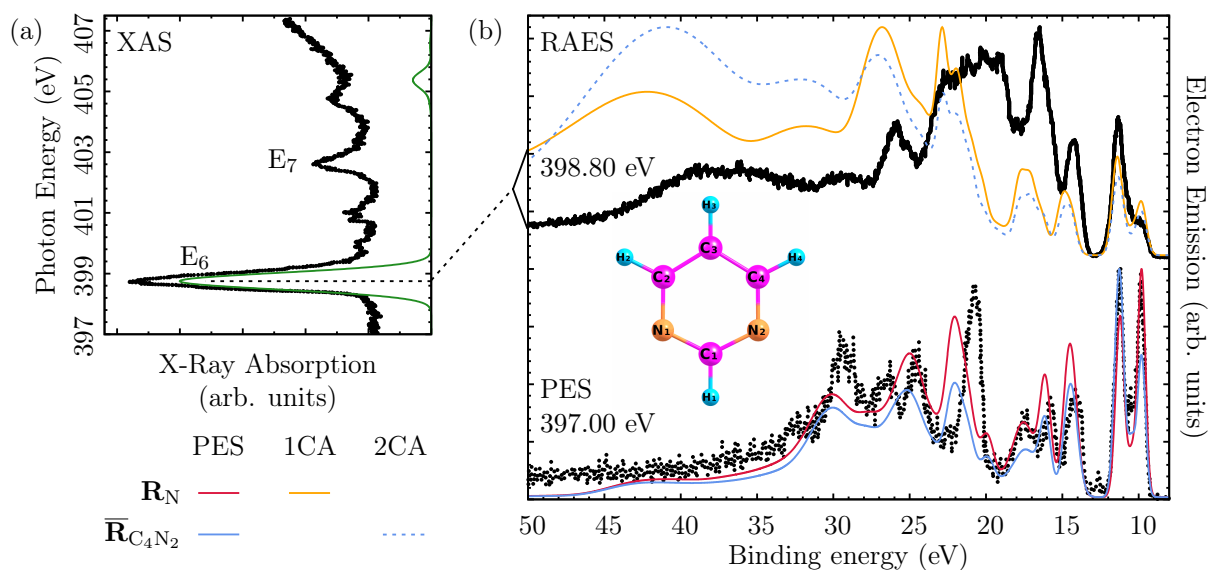
Figure 11: Taken from [GG5]. (a) Theoretical nitrogen K-edge XAS of pyrimidine (green) and the respective experimental measurement digitized from Bolognesi et al. [178] (dotted). (b) Theoretical and experimental [178] RAES of the E6 resonance and the pre-edge PES obtained at the indicated energies. The continuum orbitals have been centered at one nitrogen atom, $\boldsymbol{R}_{\mathrm{N}}$, or at the geometric center of the ring, $\overline{\boldsymbol{R}}_{\mathrm{C_4N_2}}$. For the sake of computational efficiency, the RAES were obtained at the 1CA and 2CA levels of accuracy, see text. Applied shifts and broadenings are detailed in [GG5].

theoretical investigations regarding its XAS [178–180], PES [178, 181–184], and Auger emission [178, 185]. In particular, Bolognesi et al. [178] recently reported complete sets of XAS, PES, and RAES measurements of pyrimidine. In [GG5], only the nitrogen K-edge spectra have been investigated. Therefore, the N(1s) core orbitals have been put into RAS1, whereas the C(1s) ones were kept frozen. RAS2 is formed by 10 σ and 3 π orbitals as well as both nitrogen lone pairs, and RAS3 comprises of 3 π^*, 3 π, and 2 σ Rydberg virtual orbitals, respectively. The continuum orbital origin, however, is ambiguous again. Two variants, $\boldsymbol{R}_{\mathrm{N}}$ and $\overline{\boldsymbol{R}}_{\mathrm{C_4N_2}}$, indicating the origin at one of the nitrogen atoms and in the geometric center of the ring, respectively, have been used in [GG5].

XAS   Panel (a) of Fig. 11, taken from [GG5], presents the theoretical (green) and experimental [178] (dotted) nitrogen K-edge XAS of pyrimidine. For this case, the QC calculation yields a less satisfactory agreement with the experimental XAS, than for the other molecules. In particular two peaks, which can be assigned to the E6 and E7 resonances, labeled according to Ref. 178, are present but their relative intensities and energetic positions deviate from the reference. As discussed in [GG5], this can be attributed to a lack of core-excited state correlation and Rydberg character in the active space.

PES and RAES   Fig. 11 (b) compares the SCI results for the valence PES at 397 eV and the E6 RAES together with the respective experimental spectra digitized from [178]. The PES have been evaluated with both, the $\boldsymbol{R}_{\mathrm{N}}$ and $\overline{\boldsymbol{R}}_{\mathrm{C_4N_2}}$ origins, whereas the RAES, due to the computational costs, have only been obtained within the 1CA ($\boldsymbol{R}_{\mathrm{N}}$) and two-center approximation (2CA) levels of accuracy. For the latter spectrum, contributions from up to two different atoms of the

C_4N_2 ring have been accounted for in a two-center approximate fashion in the evaluation of the Auger TMEs, Eq. 17, with continuum orbitals centered at $\overline{R}_{C_4N_2}$. Concerning the convergence of the spectra with respect to the continuum orbital angular momentum, l, it is to note that the $l = 15$ contribution can reach up to 15%, 18% and 25% for the 2CA RAES, the $\overline{R}_{C_4N_2}$ PES, and the R_N PES, respectively. Based on the cationic state character, the binding energy range can be divided into three spectral regions, see [178] and [GG5] for details. Region (1), up to 13 eV, contains clearly distinguishable single-hole states, whereas (2), up to 20 eV, marks the transition from single to double-hole states. Finally, region (3), > 20 eV, contains a high density of ionized double-hole states, indicating that the features therein are due to a manifold of transitions.

The overall reproduction of the experimental PES is quite good, in particular in regions (1) and (2). In region (3), however, only three out of the four distinct experimental features are clearly restored in the simulation that also bears blue shifts of up to 1.3 eV [GG5]. Further the difference between the PES obtained with both continuum origins is larger than for O_2, see Fig. 10, which might be due to the incomplete convergence of this spectra with respect to l. Overall, the origin has still a rather weak influence on the spectral shape.

In contrast to the PES results, both the 1CA and 2CA RAES match the experimental data to a lesser extent [GG5]. Region (1), comprising participator decay into the same cationic states that contribute to the PES, yields the best agreement with the reference. The double peak in region (2) is recovered in the theory, but appears slightly blue shifted and considerably underestimated. Finally, the high energy tail > 25.0 eV in region (3) carries too much intensity in the simulation. While an assignment of the most distinct experimental features is still possible, the extent of the disagreement between theory and experiment is surprising. This is especially true in light of the convincing PES results which indicate that the cationic valence electronic structure is well described within the present active space and that the continuum orbitals corresponding to the $V_f^J(r)$ potential cover the most important effects. Notably, the 2CA leads to an increase in the total decay rate from 32.5 meV (1CA) to 114.7 meV but does not improve the spectral shape, which indicates that relevant contributions are still not covered. A tentative analysis in [GG5] found that the exclusion of contributions of the hydrogen atoms within the 1CA and 2CA might explain this behavior. Further, the current active space might exclude configurations that contribute to the RAES, but not to PES.

In conclusion, the experimental PES has been reproduced quite well with the SCI approach, independent from the continuum orbital origin. However, the theoretical RAES show notable deviations from the experimental reference [178], which is tentatively ascribed to the exclusion of the hydrogen contributions within the 1CA and 2CA, as well as a too small active space [GG5]. Further calculations with a converged l expansion, a larger active space, and taking into account contributions from all atoms to the RAES are required in this case. Stepping back, the results presented in this chapter and [GG4] as well as [GG5] show that the AUGER implementation of the SCI approach indeed facilitates the simulation of molecular PES and RAES that allow the unambiguous assignment of experimental spectra for a wide range of molecular systems.

5 Conclusions and outlook

This thesis is dedicated to the development of a continuum orbital model that allows an efficient evaluation of the photoelectron spectra (PES) and autoionization spectra (AIS) of intricate molecular systems such as transition metal compounds, which are regularly investigated with X-ray spectroscopic techniques. For such systems, evaluating the bound electronic structure, involving multi-configurational and spin-orbit coupling (SOC) effects, is already a challenging task, which has been solved herein by employing different members of the restricted active space family of quantum chemistry (QC) methods leading to mostly accurate results. The continuum orbital of the outgoing electron, however, can usually only be modeled at the most basic levels by neglecting the molecular potential completely or treating it as a point charge.

To begin with, the sudden approximation (SA), neglecting the continuum treatment entirely, and the free-particle model have been scrutinized for the evaluation of the L-edge core PES of $[Fe(H_2O)_6]^{2+}$, the inner valence PES of I_3^-, and the valence PES of H_2O in the X-ray regime. In all cases a very good reproduction of the experimental data has been obtained. In particular for $[Fe(H_2O)_6]^{2+}$ and I_3^-, the SA and free-particle approaches are in almost perfect agreement, whereas some deviations are obtained for H_2O. This has been attributed to the fact that the SA is well applicable in the two former cases, while the H_2O valence PES probes its limits. Importantly, this does not justify the free-particle model but in fact demonstrates that the continuum orbital does not add to the accuracy if the SA is applicable. Further, a special occupation number analysis in the Dyson orbital picture that allows to disentangle the ionization and excitation contributions for each transition has been proposed and exemplified for I_3^-.

As a next step, the free-particle model has been applied to simulate extreme ultraviolet valence PES from transient excited states of the iron tris-bipyridine complex, to support the analysis of the experimentally obtained pump-probe spectra. Here, the SA is not applicable since ionization from orbitals that are localized at the metal center or delocalized over the ligands contributes to the spectrum. The central question regarding the ultrafast spin crossover pathway could be answered based on the free-particle PES, demonstrating the usefulness of such simulations. However, the agreement between the simulated and experimentally deduced spectra is considerably worse than in the aforementioned cases, indicating that the free-particle model has only limited applicability when the SA is violated. This conclusion has been supported by further studies targeting the valence PES of different molecules [98, 128, 129].

To finally improve the resemblance of the experimental PES and facilitate the evaluation of molecular AIS, the spherical continuum for ionization (SCI) approach has been developed and implemented with interfaces to the restricted active space and density functional theory bound state QC methods. Therein, the three dimensional continuum orbital problem is reduced to the radial dimension by averaging out the angular structure of the molecular potential. The resulting spherically symmetric continuum orbitals account for the molecular field in an averaged manner and can be obtained with small numerical effort, representing a considerable advancement over

the free-particle and point-charge models which are contained as limiting cases.

This protocol has been scrutinized for the showcase of the autoionization of the neon $1s^{-1}3p$ resonance. Here, 36 different combinations of approximations to the radial potential and the transition matrix elements have been compared with respect to their ability to reproduce high-level theoretical and experimental reference data. This proof of concept showed that both, the experimental total decay rates and spectra can be reproduced with the numerically obtained continuum orbitals that correspond to the spherically averaged direct potential of the cation. Motivated by this result, the test of the SCI protocol has been extended to the simulation of the X-ray valence PES and resonant Auger electron spectra (RAES) of the methane, oxygen, and pyrimidine molecules. Here it has been demonstrated that continuum orbitals corresponding to the spherically averaged molecular potential indeed lead to PES and resonant RAES that are in most cases in good agreement with the experimental references. In particular, the measurements could be thoroughly analyzed and assigned with the aid of the simulated spectra and the information from the electronic structure calculations. Further, the experimentally obtained total decay rate of the core vacancy in the O_2 molecule could be reproduced. An interesting discovery is that the one-center approximation to the simulation of partial decay rates seems to have only a limited applicability, though it is commonly used in other approaches [25, 90, 91]. Overall, a considerable portion of the remaining deviations between the theoretical and experimental data can be ascribed to deficiencies in the bound QC, the lack of vibrational effects, and the two-step model, which disregards interference effects between autoionization and photoionization terms.

Although the addition of SOC to the current SCI implementation in the AUGER code and a proof of concept study regarding an actual transition metal complex still need to be carried out to fully accomplish all of the initially set goals, a considerable step forward has been made. Despite the deficiencies in the pyrimidine case that require further investigation, already the ability to evaluate the RAES of molecules of this size can be regarded as an advancement, since the literature regarding such simulations is very scarce.

To conclude, the free-particle and SA approaches have been successfully applied to simulate the PES of small molecules and large complexes of current scientific interest. Further, the SCI approach has been developed and implemented as a promising tool to improve the calculated PES and facilitate the simulation of AIS of larger molecules. A benchmark application to the neon atom and small to medium sized molecular systems has shown its potential in this respect. Further, the inclusion of SOC, vibrational effects, and interference between autoionization and photoionization contributions are natural starting points for improvements of the present protocol that should be sought after in future works. In fact, the SCI approach complements the present set of tools for theoretical X-ray spectroscopy of larger molecules, opening up the possibilities for studies with a considerably higher accuracy than it was available during the creation of [GG1]-[GG3].

6 Bibliography

[1] R. W. Giese, Electron–capture mass spectrometry: Recent advances, *Journal of Chromatography A*, **892** (1-2), 329 (2000), doi:10.1016/S0021-9673(00)00364-2.

[2] T. Åberg, G. Howat, L. Karlsson, J. A. R. Samson, H. Siegbahn, and A. F. Starace, *Corpuscles and Radiation in Matter I*, volume 31 of *Encyclopedia of Physics*, Springer, Berlin (1982).

[3] U. Stroth, *Plasmaphysik: Phänomene, Grundlagen und Anwendungen*, Springer Spektrum, Berlin, 2 edition (2018).

[4] H. Hertz, Ueber einen Einfluss des ultravioletten Lichtes auf die electrische Entladung, *Ann. Phys. Chem.*, **267** (8), 983 (1887), doi:10.1002/andp.18872670827.

[5] A. Einstein, Über einen die Erzeugung und Verwandlung des Lichtes betreffenden heuristischen Gesichtspunkt, *Ann. Phys.*, **322** (6), 132 (1905), doi:10.1002/andp.19053220607.

[6] L. Meitner, Über die β-Strahl-Spektra und ihren Zusammenhang mit der γ-Strahlung, *Z. Physik*, **11** (1), 35 (1922), doi:10.1007/BF01328399.

[7] V. G. Wentzel, Über strahlungslose Quantensprünge., *Z. Physik*, **43** (8), 524 (1927), doi:10.1007/BF01397631.

[8] T. Åberg and G. Howat, Theory of the Auger Effect, in *Corpuscles and Radiation in Matter I*, edited by W. Mehlhorn, volume 31 of *Encyclopedia of Physics*, pages 469–619, Springer, Berlin (1982).

[9] F. de Groot and A. Kotani, *Core Level Spectroscopy of Solids*, CRC Press, Boca Raton (2008).

[10] L. S. Cederbaum, J. Zobeley, and F. Tarantelli, Giant Intermolecular Decay and Fragmentation of Clusters, *Phys. Rev. Lett.*, **79** (24), 4778 (1997), doi:10.1103/PhysRevLett.79.4778.

[11] J. Zobeley, R. Santra, and L. S. Cederbaum, Electronic decay in weakly bound heteroclusters: Energy transfer versus electron transfer, *J. Chem. Phys.*, **115** (11), 5076 (2001), doi:10.1063/1.1395555.

[12] H. Wang, T. Möhle, O. Kühn, and S. I. Bokarev, Ultrafast dissipative spin-state dynamics triggered by x-ray pulse trains, *Phys. Rev. A*, **98** (1), 013408 (2018), doi:10.1103/PhysRevA.98.013408.

[13] A. RUDENKO, L. INHESTER, K. HANASAKI, X. LI, S. J. ROBATJAZI, B. ERK, R. BOLL, K. TOYOTA, Y. HAO, O. VENDRELL, C. BOMME, E. SAVELYEV, B. RUDEK, L. FOUCAR, S. H. SOUTHWORTH, C. S. LEHMANN, B. KRAESSIG, T. MARCHENKO, M. SIMON, K. UEDA, K. R. FERGUSON, M. BUCHER, T. GORKHOVER, S. CARRON, R. ALONSO-MORI, J. E. KOGLIN, J. CORREA, G. J. WILLIAMS, S. BOUTET, L. YOUNG, C. BOSTEDT, S.-K. SON, R. SANTRA, and D. ROLLES, Femtosecond response of polyatomic molecules to ultra-intense hard X-rays, *Nature*, **546** (7656), 129 (2017), doi:10.1038/nature22373.

[14] I. UNGER, R. SEIDEL, S. THÜRMER, M. N. POHL, E. F. AZIZ, L. S. CEDERBAUM, E. MUCHOVÁ, P. SLAVÍČEK, B. WINTER, and N. V. KRYZHEVOI, Observation of electron-transfer-mediated decay in aqueous solution, *Nat. Chem.*, **9** (7), 708 (2017), doi:10.1038/nchem.2727.

[15] V. STUMPF, K. GOKHBERG, and L. S. CEDERBAUM, The role of metal ions in X-ray-induced photochemistry, *Nat. Chem.*, **8** (3), 237 (2016), doi:10.1038/nchem.2429.

[16] P. SLAVÍČEK, N. V. KRYZHEVOI, E. F. AZIZ, and B. WINTER, Relaxation Processes in Aqueous Systems upon X-ray Ionization: Entanglement of Electronic and Nuclear Dynamics, *J. Phys. Chem. Lett.*, **7** (2), 234 (2016), doi:10.1021/acs.jpclett.5b02665.

[17] P. SLAVÍČEK, B. WINTER, L. S. CEDERBAUM, and N. V. KRYZHEVOI, Proton-Transfer Mediated Enhancement of Nonlocal Electronic Relaxation Processes in X-ray Irradiated Liquid Water, *J. Am. Chem. Soc.*, **136** (52), 18170 (2014), doi:10.1021/ja5117588.

[18] M. A. BROWN, M. FAUBEL, and B. WINTER, X-Ray photo- and resonant Auger-electron spectroscopy studies of liquid water and aqueous solutions, *Annu. Rep. Sect. C Phys. Chem.*, **105**, 174 (2009), doi:10.1039/b803023p.

[19] B. MIGNOLET, R. D. LEVINE, and F. REMACLE, Charge migration in the bifunctional PENNA cation induced and probed by ultrafast ionization: A dynamical study, *J. Phys. B At. Mol. Opt. Phys.*, **47** (12), 124011 (2014), doi:10.1088/0953-4075/47/12/124011.

[20] F. CALEGARI, D. AYUSO, A. TRABATTONI, L. BELSHAW, S. D. CAMILLIS, S. ANUMULA, F. FRASSETTO, L. POLETTO, A. PALACIOS, P. DECLEVA, J. B. GREENWOOD, F. MARTÍN, and M. NISOLI, Ultrafast electron dynamics in phenylalanine initiated by attosecond pulses, *Science*, **346** (6207), 336 (2014), doi:10.1126/science.1254061.

[21] P. M. KRAUS, B. MIGNOLET, D. BAYKUSHEVA, A. RUPENYAN, L. HORNY, E. F. PENKA, G. GRASSI, O. I. TOLSTIKHIN, J. SCHNEIDER, F. JENSEN, L. B. MADSEN, A. D. BANDRAUK, F. REMACLE, and H. J. WORNER, Measurement and laser control of attosecond charge migration in ionized iodoacetylene, *Science*, **350** (6262), 790 (2015), doi:10.1126/science.aab2160.

[22] M. Nisoli, P. Decleva, F. Calegari, A. Palacios, and F. Martín, Attosecond Electron Dynamics in Molecules, *Chem. Rev.*, **117** (16), 10760 (2017), doi:10.1021/acs.chemrev.6b00453.

[23] A. Trabattoni, M. Galli, M. Lara-Astiaso, A. Palacios, J. Greenwood, I. Tavernelli, P. Decleva, M. Nisoli, F. Martín, and F. Calegari, Charge migration in photoionized aromatic amino acids, *Philos. Trans. R. Soc. Math. Phys. Eng. Sci.*, **377** (2145), 20170472 (2019), doi:10.1098/rsta.2017.0472.

[24] K. Khalili, L. Inhester, C. Arnold, R. Welsch, J. W. Andreasen, and R. Santra, Hole dynamics in a photovoltaic donor-acceptor couple revealed by simulated time-resolved X-ray absorption spectroscopy, *Struct. Dyn.*, **6** (4), 044102 (2019), doi:10.1063/1.5097653.

[25] L. Inhester, B. Oostenrijk, M. Patanen, E. Kokkonen, S. H. Southworth, C. Bostedt, O. Travnikova, T. Marchenko, S.-K. Son, R. Santra, M. Simon, L. Young, and S. L. Sorensen, Chemical Understanding of the Limited Site-Specificity in Molecular Inner-Shell Photofragmentation, *J. Phys. Chem. Lett.*, **9** (5), 1156 (2018), doi:10.1021/acs.jpclett.7b03235.

[26] A. Picón, C. S. Lehmann, C. Bostedt, A. Rudenko, A. Marinelli, T. Osipov, D. Rolles, N. Berrah, C. Bomme, M. Bucher, G. Doumy, B. Erk, K. R. Ferguson, T. Gorkhover, P. J. Ho, E. P. Kanter, B. Krässig, J. Krzywinski, A. A. Lutman, A. M. March, D. Moonshiram, D. Ray, L. Young, S. T. Pratt, and S. H. Southworth, Hetero-site-specific X-ray pump-probe spectroscopy for femtosecond intramolecular dynamics, *Nat. Commun.*, **7**, 11652 (2016), doi:10.1038/ncomms11652.

[27] A. Reinköster, S. Korica, G. Prümper, J. Viefhaus, K. Godehusen, O. Schwarzkopf, M. Mast, and U. Becker, The photoionization and fragmentation of C_{60} in the energy range 26–130 eV, *J. Phys. B At. Mol. Opt. Phys.*, **37** (10), 2135 (2004), doi:10.1088/0953-4075/37/10/010.

[28] I. Hjelte, M. Piancastelli, C. Jansson, K. Wiesner, O. Björneholm, M. Bässler, S. Sorensen, and S. Svensson, Evidence of ultra-fast dissociation in ammonia observed by resonant Auger electron spectroscopy, *Chem. Phys. Lett.*, **370** (5-6), 781 (2003), doi:10.1016/S0009-2614(03)00161-1.

[29] R. Weinkauf, P. Schanen, D. Yang, S. Soukara, and E. W. Schlag, Elementary Processes in Peptides: Electron Mobility and Dissociation in Peptide Cations in the Gas Phase, *J. Phys. Chem.*, **99** (28), 11255 (1995), doi:10.1021/j100028a029.

[30] R. W. Howell, Auger processes in the 21st century, *Int. J. Radiat. Biol.*, **84** (12), 959 (2008), doi:10.1080/09553000802395527.

[31] E. ALIZADEH, T. M. ORLANDO, and L. SANCHE, Biomolecular Damage Induced by Ionizing Radiation: The Direct and Indirect Effects of Low-Energy Electrons on DNA, *Annu. Rev. Phys. Chem.*, **66** (1), 379 (2015), doi:10.1146/annurev-physchem-040513-103605.

[32] R. F. MARTIN and L. E. FEINENDEGEN, The quest to exploit the Auger effect in cancer radiotherapy – a reflective review, *Int. J. Radiat. Biol.*, **92** (11), 617 (2016), doi:10.3109/09553002.2015.1136854.

[33] A. YOKOYA and T. ITO, Photon-induced Auger effect in biological systems: A review, *Int. J. Radiat. Biol.*, **93** (8), 743 (2017), doi:10.1080/09553002.2017.1312670.

[34] V. MAY and O. KÜHN, *Charge and Energy Transfer Dynamics in Molecular Systems*, Wiley-VCH, Weinheim (2011).

[35] S. K. KURINEC (ed.), *Emerging Photovoltaic Materials*, Scrivenger Publishing LLC, Beverly, MA (2019).

[36] C. BRABEC, U. SCHERF, and V. DYAKONOV (eds.), *Organic Photovoltaics*, Wiley-VCH, Weinheim, 2 edition (2014).

[37] J.-P. LAUNAY and M. VERDAGUER, *Electrons in Molecules: From Basic Principles to Molecular Electronics*, Oxford University Press, Oxford, United Kingdom, first edition edition (2014).

[38] A. FAHLMANN, C. NORDLING, and K. SIEGBAHN, *ESCA: Atomic, Molecular and Solid State Structure Studied by Means of Electron Spectroscopy*, Almqvist & Wiksells, Uppsala (1967).

[39] K. SIEGBAHN, *ESCA Applied to Free Molecules*, North-Holland Pub. Co., Amsterdam (1969).

[40] H. SIEGBAHN and K. SIEGBAHN, ESCA applied to liquids, *J. Electron Spectrosc. Relat. Phenom.*, **2** (3), 319 (1973), doi:10.1016/0368-2048(73)80023-4.

[41] S. HOFMANN, *Auger- and X-Ray Photoelectron Spectroscopy in Materials Science: A User-Oriented Guide*, number 49 in Springer Series in Surface Sciences, Springer, Heidelberg , New York (2013).

[42] S. HÜFNER, *Photoelectron Spectroscopy: Principles and Applications*, Springer, Berlin, Heidelberg (2003).

[43] K. TAKATSUKA, T. YONEHARA, K. HANASAKI, and Y. ARASAKI, *Chemical Theory beyond the Born-Oppenheimer Paradigm – Nonadiabatic Electronic and Nuclear Dynamics in Chemical Reactions*, World Scientific Publishing, Singapore (2015).

[44] A. STOLOW, A. E. BRAGG, and D. M. NEUMARK, Femtosecond Time-Resolved Photoelectron Spectroscopy, *Chem. Rev.*, **104** (4), 1719 (2004), doi:10.1021/cr020683w.

[45] B. WINTER, Liquid microjet for photoelectron spectroscopy, *Nucl. Instrum. Methods Phys. Res. Sect. Accel. Spectrometers Detect. Assoc. Equip.*, **601** (1-2), 139 (2009), doi:10.1016/j.nima.2008.12.108.

[46] D. YEPES, R. SEIDEL, B. WINTER, J. BLUMBERGER, and P. JAQUE, Photoemission Spectra and Density Functional Theory Calculations of 3d Transition Metal–Aqua Complexes (Ti–Cu) in Aqueous Solution, *J. Phys. Chem. B*, **118** (24), 6850 (2014), doi:10.1021/jp5012389.

[47] R. SEIDEL, S. THÜRMER, and B. WINTER, Photoelectron Spectroscopy Meets Aqueous Solution: Studies from a Vacuum Liquid Microjet, *J. Phys. Chem. Lett.*, **2** (6), 633 (2011), doi:10.1021/jz101636y.

[48] J. MOENS, R. SEIDEL, P. GEERLINGS, M. FAUBEL, B. WINTER, and J. BLUMBERGER, Energy Levels and Redox Properties of Aqueous Mn $^{2+/3+}$ from Photoemission Spectroscopy and Density Functional Molecular Dynamics Simulation, *J. Phys. Chem. B*, **114** (28), 9173 (2010), doi:10.1021/jp101527v.

[49] S. THÜRMER, R. SEIDEL, W. EBERHARDT, S. E. BRADFORTH, and B. WINTER, Ultrafast Hybridization Screening in Fe $^{3+}$ Aqueous Solution, *J. Am. Chem. Soc.*, **133** (32), 12528 (2011), doi:10.1021/ja200268b.

[50] R. GOLNAK, S. I. BOKAREV, R. SEIDEL, J. XIAO, G. GRELL, K. ATAK, I. UNGER, S. THÜRMER, S. G. AZIZ, O. KÜHN, B. WINTER, and E. F. AZIZ, Joint Analysis of Radiative and Non-Radiative Electronic Relaxation Upon X-ray Irradiation of Transition Metal Aqueous Solutions, *Sci. Rep.*, **6**, 24659 (2016), doi:10.1038/srep24659.

[51] J. F. DA SILVA and R. WILLIAMS, *The Biological Chemistry of the Elements: The Inorganic Chemsitry of Life*, Oxford University Press, New York (1991).

[52] P. BALL, Water as an Active Constituent in Cell Biology, *Chem. Rev.*, **108** (1), 74 (2008), doi:10.1021/cr068037a.

[53] S. I. BOKAREV and O. KÜHN, Theoretical X-ray spectroscopy of transition metal compounds, *Wiley Interdisc. Rev. Comput. Mol. Sci.*, page e1433 (2019), doi:10.1002/wcms.1433.

[54] W. D. COOLIDGE, A Powerful Röntgen Ray Tube with a Pure Electron Discharge, *Phys. Rev.*, **2** (6), 409 (1913), doi:10.1103/PhysRev.2.409.

[55] M. L. PERLMAN, R. E. WATSON, and E. M. ROWE, Synchrotron radiation—light fantastic, *Physics Today*, **27** (7), 30 (1974), doi:10.1063/1.3128691.

[56] B. W. J. McNeil and N. R. Thompson, X-ray free-electron lasers, *Nature Photon*, **4** (12), 814 (2010), doi:10.1038/nphoton.2010.239.

[57] L. Young, K. Ueda, M. Gühr, P. H. Bucksbaum, M. Simon, S. Mukamel, N. Rohringer, K. C. Prince, C. Masciovecchio, M. Meyer, A. Rudenko, D. Rolles, C. Bostedt, M. Fuchs, D. A. Reis, R. Santra, H. Kapteyn, M. Murnane, H. Ibrahim, F. Légaré, M. Vrakking, M. Isinger, D. Kroon, M. Gisselbrecht, A. L'Huillier, H. J. Wörner, and S. R. Leone, Roadmap of ultrafast x-ray atomic and molecular physics, *J. Phys. B*, **51** (3), 032003 (2018), doi:10.1088/1361-6455/aa9735.

[58] R. N. Coffee, J. P. Cryan, J. Duris, W. Helml, S. Li, and A. Marinelli, Development of ultrafast capabilities for X-ray free-electron lasers at the linac coherent light source, *Phil. Trans. R. Soc. A*, **377** (2145), 20180386 (2019), doi:10.1098/rsta.2018.0386.

[59] F. Krausz and M. Ivanov, Attosecond physics, *Rev. Mod. Phys.*, **81** (1), 163 (2009), doi:10.1103/RevModPhys.81.163.

[60] M. Chergui and E. Collet, Photoinduced Structural Dynamics of Molecular Systems Mapped by Time-Resolved X-ray Methods, *Chem. Rev.* (2017), doi:10.1021/acs.chemrev.6b00831.

[61] A. F. Starace, Theory of Atomic Photoionization, in *Corpuscles and Radiation in Matter I*, edited by W. Mehlhorn, volume 31 of *Encyclopedia of Physics*, pages 1–121, Springer, Berlin (1982).

[62] U. Fano, Effects of Configuration Interaction on Intensities and Phase Shifts, *Phys. Rev.*, **124** (6), 1866 (1961), doi:10.1103/PhysRev.124.1866.

[63] G. Breit and H. A. Bethe, Ingoing Waves in Final State of Scattering Problems, *Phys. Rev.*, **93** (4), 888 (1954), doi:10.1103/PhysRev.93.888.

[64] J. Leszczynski, A. Kaczmarek-Kędziera, T. Puzyn, M. G. Papadopulos, H. Reis, and M. Shukla (eds.), *Handbook of Computational Chemistry*, Springer, Cham, second edition edition (2017).

[65] B. O. Roos, R. Lindh, P. Å. Malmqvist, V. Veryazov, and P.-O. Widmark, *Multiconfigurational Quantum Chemistry*, Wiley, Hoboken, New Jersey (2016).

[66] A. Aspuru-Guzik, R. Lindh, and M. Reiher, The Matter Simulation (R)evolution, *ACS Cent. Sci.*, **4** (2), 144 (2018), doi:10.1021/acscentsci.7b00550.

[67] P. G. Burke, *R-Matrix Theory of Atomic Collisions: Application to Atomic, Molecular and Optical Processes*, number 61 in Springer Series on Atomic, Optical, and Plasma Physics, Springer, Heidelberg (2011).

[68] F. Martín, Ionization and dissociation using B-splines: Photoionization of the hydrogen molecule, *J. Phys. B At. Mol. Opt. Phys.*, **32** (16), R197 (1999), doi:10.1088/0953-4075/32/16/201.

[69] H. Bachau, E. Cormier, P. Decleva, J. E. Hansen, and F. Martín, Applications of *B*-splines in atomic and molecular physics, *Rep. Prog. Phys.*, **64** (12), 1815 (2001), doi:10.1088/0034-4885/64/12/205.

[70] R. Colle and S. Simonucci, Method for calculating Auger decay rates in molecules, *Phys. Rev. A*, **39** (12), 6247 (1989), doi:10.1103/PhysRevA.39.6247.

[71] R. Colle and S. Simonucci, Multichannel resonance processes: Theory and application to the Auger spectra of the CO molecule, *Phys. Rev. A*, **48** (1), 392 (1993), doi:10.1103/PhysRevA.48.392.

[72] R. Colle and S. Simonucci, On the use of a Hamiltonian with projected potential for the calculation of scattering wave functions: Method and general properties, *Il Nuovo Cimento D*, **18** (1), 11 (1996), doi:10.1007/BF02532283.

[73] C. Marante, M. Klinker, I. Corral, J. González-Vázquez, L. Argenti, and F. Martín, Hybrid-Basis Close-Coupling Interface to Quantum Chemistry Packages for the Treatment of Ionization Problems, *J. Chem. Theor. Comput.*, **13** (2), 499 (2017), doi:10.1021/acs.jctc.6b00907.

[74] C. Marante, L. Argenti, and F. Martín, Hybrid Gaussian– B -spline basis for the electronic continuum: Photoionization of atomic hydrogen, *Phys. Rev. A*, **90** (1) (2014), doi:10.1103/PhysRevA.90.012506.

[75] R. Colle, D. Embriaco, M. Massini, S. Simonucci, and S. Taioli, Ab initio calculation of the normal Auger spectrum of C_2H_2, *J. Phys. B At. Mol. Opt. Phys.*, **37** (6), 1237 (2004), doi:10.1088/0953-4075/37/6/008.

[76] M. Klinker, C. Marante, L. Argenti, J. González-Vázquez, and F. Martín, Partial cross sections and interfering resonances in photoionization of molecular nitrogen, *Phys. Rev. A*, **98** (3), 033413 (2018), doi:10.1103/PhysRevA.98.033413.

[77] D. Toffoli, M. Stener, G. Fronzoni, and P. Decleva, Convergence of the multicenter B-spline DFT approach for the continuum, *Chemical Physics*, **276** (1), 25 (2002), doi:10.1016/S0301-0104(01)00549-3.

[78] M. Stener, G. Fronzoni, D. D. Tommaso, and P. Decleva, Density functional study on the circular dichroism of photoelectron angular distribution from chiral derivatives of oxirane, *The Journal of Chemical Physics*, **120** (7), 3284 (2004), doi:10.1063/1.1640617.

[79] M. STENER, D. TOFFOLI, G. FRONZONI, and P. DECLEVA, Recent advances in molecular photoionization by density functional theory based approaches, *Theor Chem Account*, **117** (5-6), 943 (2007), doi:10.1007/s00214-006-0212-3.

[80] D. CATONE, M. STENER, P. DECLEVA, G. CONTINI, N. ZEMA, T. PROSPERI, V. FEYER, K. C. PRINCE, and S. TURCHINI, Resonant Circular Dichroism of Chiral Metal-Organic Complex, *Phys. Rev. Lett.*, **108** (8), 083001 (2012), doi:10.1103/PhysRevLett.108.083001.

[81] E. PLÉSIAT, S. E. CANTON, J. D. BOZEK, P. DECLEVA, and F. MARTÍN, Resonant Photoelectron Confinement in the SF_6 Molecule, *J. Phys. Chem. A*, **123**, 1062 (2019), doi:10.1021/acs.jpca.8b12237.

[82] E. PLÉSIAT, P. DECLEVA, and F. MARTÍN, Vibrational branching ratios in the photoelectron spectra of N_2 and CO: Interference and diffraction effects, *Phys. Chem. Chem. Phys.*, **14** (31), 10853 (2012), doi:10.1039/c2cp40693d.

[83] S. ENGIN, J. GONZÁLEZ-VÁZQUEZ, G. G. MALIYAR, A. R. MILOSAVLJEVIĆ, T. ONO, S. NANDI, D. IABLONSKYI, K. KOOSER, J. D. BOZEK, P. DECLEVA, E. KUKK, K. UEDA, and F. MARTÍN, Full-dimensional theoretical description of vibrationally resolved valence-shell photoionization of H_2O, *Structural Dynamics*, **6** (5), 054101 (2019), doi:10.1063/1.5106431.

[84] P. V. DEMEKHIN, D. V. OMEL'YANENKO, B. M. LAGUTIN, V. L. SUKHORUKOV, L. WERNER, A. EHRESMANN, K.-H. SCHARTNER, and H. SCHMORANZER, Investigation of photoionization and photodissociation of an oxygen molecule by the method of coupled differential equations, *Opt. Spectrosc.*, **102** (3), 318 (2007), doi:10.1134/S0030400X07030022.

[85] P. V. DEMEKHIN, I. D. PETROV, V. L. SUKHORUKOV, W. KIELICH, P. REISS, R. HENTGES, I. HAAR, H. SCHMORANZER, and A. EHRESMANN, Interference effects during the Auger decay of the C^*O $1s^{-1}\pi^*$ resonance studied by angular distribution of the $CO^+(A)$ photoelectrons and polarization analysis of the $CO^+(A-X)$ fluorescence, *Phys. Rev. A*, **80** (6), 063425 (2009), doi:10.1103/PhysRevA.80.063425.

[86] H. I. B. BANKS, D. A. LITTLE, J. TENNYSON, and A. EMMANOUILIDOU, Interaction of molecular nitrogen with free-electron-laser radiation, *Phys. Chem. Chem. Phys.*, **19** (30), 19794 (2017), doi:10.1039/C7CP02345F.

[87] H. SIEGBAHN, L. ASPLUND, and P. KELFVE, The Auger electron spectrum of water vapour, *Chem. Phys. Lett.*, **35** (3), 330 (1975), doi:10.1016/0009-2614(75)85615-6.

[88] F. P. LARKINS, L. C. TULEA, and E. Z. CHELKOWSKA, Auger electron spectra of molecules: The first row hydrides, *Aust. J. Phys.*, **43** (5), 625 (1990), doi:10.1071/PH900625.

[89] R. FINK, Theoretical autoionization spectra of excited N_2 and N_2O, *J. Electron Spectrosc. Relat. Phenom.*, **76**, 295 (1995), doi:10.1016/0368-2048(95)02469-7.

[90] O. TRAVNIKOVA, R. F. FINK, A. KIVIMÄKI, D. CÉOLIN, Z. BAO, and M. N. PIANCASTELLI, Assignment of the $L_{2,3}VV$ normal Auger decay spectrum of Cl_2 by ab initio calculations, *Chem. Phys. Lett.*, **474** (1-3), 67 (2009), doi:10.1016/j.cplett.2009.04.058.

[91] L. INHESTER, K. HANASAKI, Y. HAO, S.-K. SON, and R. SANTRA, X-ray multiphoton ionization dynamics of a water molecule irradiated by an x-ray free-electron laser pulse, *Phys. Rev. A*, **94** (2), 023422 (2016), doi:10.1103/PhysRevA.94.023422.

[92] Y. HAO, L. INHESTER, K. HANSAKI, and R. SANTRA, Efficient electronic structure calculation for molecular ionization dynamics at high X-ray intensity, *Struct. Dyn.*, **2** (4), 041707 (2015), doi:10.1063/1.4919794.

[93] C. M. OANA and A. I. KRYLOV, Cross sections and photoelectron angular distributions in photodetachment from negative ions using equation-of-motion coupled-cluster Dyson orbitals, *J. Chem. Phys.*, **131** (12), 124114 (2009), doi:10.1063/1.3231143.

[94] C. M. OANA and A. I. KRYLOV, Dyson orbitals for ionization from the ground and electronically excited states within equation-of-motion coupled-cluster formalism: Theory, implementation, and examples, *J. Chem. Phys.*, **127** (23), 234106 (2007), doi:10.1063/1.2805393.

[95] B. MIGNOLET, J. O. JOHANSSON, E. E. B. CAMPBELL, and F. REMACLE, Probing Rapidly-Ionizing Super-Atom Molecular Orbitals in C_{60} : A Computational and Femtosecond Photoelectron Spectroscopy Study, *ChemPhysChem*, **14** (14), 3332 (2013), doi:10.1002/cphc.201300585.

[96] A. O. GUNINA and A. I. KRYLOV, Probing Electronic Wave Functions of Sodium-Doped Clusters: Dyson Orbitals, Anisotropy Parameters, and Ionization Cross-Sections, *J. Phys. Chem. A*, **120** (49), 9841 (2016), doi:10.1021/acs.jpca.6b10098.

[97] A. HUMENIUK, M. WOHLGEMUTH, T. SUZUKI, and R. MITRIĆ, Time-resolved photoelectron imaging spectra from non-adiabatic molecular dynamics simulations, *J. Chem. Phys.*, **139** (13), 134104 (2013), doi:10.1063/1.4820238.

[98] T. MÖHLE, O. S. BOKAREVA, G. GRELL, O. KÜHN, and S. I. BOKAREV, Tuned Range-Separated Density Functional Theory and Dyson Orbital Formalism for Photoelectron Spectra, *J. Chem. Theor. Comput.*, **14** (11), 5870 (2018), doi:10.1021/acs.jctc.8b00707.

[99] V. CARRAVETTA, H. ÅGREN, O. VAHTRAS, and H. J. A. JENSEN, Ab initio calculations of molecular resonant photoemission spectra, *J. Chem. Phys.*, **113** (18), 7790 (2000), doi:10.1063/1.1316046.

[100] K. Gokhberg, V. Vysotskiy, L. S. Cederbaum, L. Storchi, F. Tarantelli, and V. Averbukh, Molecular photoionization cross sections by Stieltjes–Chebyshev moment theory applied to Lanczos pseudospectra, *J. Chem. Phys.*, **130** (6), 064104 (2009), doi:10.1063/1.3073821.

[101] V. Averbukh and L. S. Cederbaum, Ab initio calculation of interatomic decay rates by a combination of the Fano ansatz, Green's-function methods, and the Stieltjes imaging technique, *J. Chem. Phys.*, **123** (20), 204107 (2005), doi:10.1063/1.2126976.

[102] P. Kolorenč, V. Averbukh, K. Gokhberg, and L. S. Cederbaum, *Ab Initio* calculation of interatomic decay rates of excited doubly ionized states in clusters, *J. Chem. Phys.*, **129** (24), 244102 (2008), doi:10.1063/1.3043437.

[103] M. Stener, P. Decleva, and A. Lisini, Molecular photoionization cross sections by the local density LCAO Stieltjes imaging approach, *J. Electron. Spectrosc. Relat. Phenom.*, **74** (1), 29 (1995), doi:10.1016/0368-2048(95)02357-7.

[104] B. Schimmelpfennig, B. Nestmann, and S. Peyerimhoff, Ab initio calculation of transition rates for autoionization: The Auger spectra of HF and F^-, *J. Electron. Spectrosc. Relat. Phenom.*, **74** (3), 173 (1995), doi:10.1016/0368-2048(95)02373-9.

[105] T. Åberg, Theory of X-Ray Satellites, *Phys. Rev.*, **156** (1), 35 (1967), doi:10.1103/PhysRev.156.35.

[106] R. Manne and T. Åberg, Koopmanns' Theorem for Inner-Shell Ionization, *Chem. Phys. Lett.*, **7** (2), 282 (1970), doi:10.1016/0009-2614(70)80309-8.

[107] L. S. Cederbaum and W. Domcke, Theoretical Aspects of Ionization Potentials and Photoelectron Spectroscopy: A Green's Function approach, in *Adv. Chem. Phys.*, edited by I. Prigogine and S. A. Rice, pages 205–344, John Wiley, New York; London (1977).

[108] N. V. Kryzhevoi and L. S. Cederbaum, Core ionization of Na^+ microsolvated in water and ammonia, *J. Chem. Phys.*, **130** (8), 084302 (2009), doi:10.1063/1.3077919.

[109] R. Santra, N. V. Kryzhevoi, and L. S. Cederbaum, X-ray Two-Photon Photoelectron Spectroscopy: A Theoretical Study of Inner-Shell Spectra of the Organic Para-Aminophenol Molecule, *Phys. Rev. Lett.*, **103** (1) (2009), doi:10.1103/PhysRevLett.103.013002.

[110] B. T. Pickup, On the theory of fast photoionization processes, *Chem. Phys.*, **19** (2), 193 (1977), doi:10.1016/0301-0104(77)85131-8.

[111] R. Arneberg, J. Müller, and R. Manne, Configuration interaction calculations of satellite structure in photoelectron spectra of H_2O, *Chem. Phys.*, **64** (2), 249 (1982), doi:10.1016/0301-0104(82)87091-2.

[112] R. KLOOSTER, R. BROER, and M. FILATOV, Calculation of X-ray photoelectron spectra with the use of the normalized elimination of the small component method, *Chem. Phys.*, **395**, 122 (2012), doi:10.1016/j.chemphys.2011.05.009.

[113] H. HAFIED, A. ESCHENBRENNER, C. CHAMPION, M. RUIZ-LÓPEZ, C. D. CAPPELLO, I. CHARPENTIER, and P.-A. HERVIEUX, Electron momentum spectroscopy of the valence orbitals of the water molecule in gas and liquid phase: A comparative study, *Chem. Phys. Lett.*, **439** (1-3), 55 (2007), doi:10.1016/j.cplett.2007.03.067.

[114] I. JOSEFSSON, S. K. ERIKSSON, N. OTTOSSON, G. ÖHRWALL, H. SIEGBAHN, A. HAGFELDT, H. RENSMO, O. BJÖRNEHOLM, and M. ODELIUS, Collective hydrogen-bond dynamics dictates the electronic structure of aqueous I_3^-, *Phys. Chem. Chem. Phys.*, **15** (46), 20189 (2013), doi:10.1039/c3cp52866a.

[115] M. BARYSZ and Ł. SYROCKI, Relativistic calculations of X-ray photoelectron spectra and the accuracy of the IOTC method, *Mol. Phys.*, **112** (5-6), 583 (2014), doi:10.1080/00268976.2013.843033.

[116] M. NEWTON, Time Resolved Operando X-ray Techniques in Catalysis, a Case Study: CO Oxidation by O_2 over Pt Surfaces and Alumina Supported Pt Catalysts, *Catalysts*, **7** (12), 58 (2017), doi:10.3390/catal7020058.

[117] P.-Å. MALMQVIST, A. RENDELL, and B. O. ROOS, The restricted active space self-consistent-field method, implemented with a split graph unitary group approach, *J. Phys. Chem.*, **94** (14), 5477 (1990), doi:10.1021/j100377a011.

[118] P. Å. MALMQVIST, K. PIERLOOT, A. R. M. SHAHI, C. J. CRAMER, and L. GAGLIARDI, The restricted active space followed by second-order perturbation theory method: Theory and application to the study of CuO_2 and Cu_2O_2 systems, *J. Chem. Phys.*, **128** (20), 204109 (2008), doi:10.1063/1.2920188.

[119] P. Å. MALMQVIST, B. O. ROOS, and B. SCHIMMELPFENNIG, The restricted active space (RAS) state interaction approach with spin–orbit coupling, *Chem. Phys. Lett.*, **357** (3-4), 230 (2002), doi:10.1016/S0009-2614(02)00498-0.

[120] S. I. BOKAREV, M. DANTZ, E. SULJOTI, O. KÜHN, and E. F. AZIZ, State-Dependent Electron Delocalization Dynamics at the Solute-Solvent Interface: Soft-X-Ray Absorption Spectroscopy and Ab Initio Calculations, *Phys. Rev. Lett.*, **111** (8), 083002 (2013), doi:10.1103/PhysRevLett.111.083002.

[121] S. I. BOKAREV, M. KHAN, M. K. ABDEL-LATIF, J. XIAO, R. HILAL, S. G. AZIZ, E. F. AZIZ, and O. KÜHN, Unraveling the Electronic Structure of Photocatalytic Manganese Complexes by L-Edge X-ray Spectroscopy, *J. Phys. Chem. C*, **119** (33), 19192 (2015), doi:10.1021/acs.jpcc.5b05169.

[122] K. Atak, S. I. Bokarev, M. Gotz, R. Golnak, K. M. Lange, N. Engel, M. Dantz, E. Suljoti, O. Kühn, and E. F. Aziz, Nature of the Chemical Bond of Aqueous Fe^{2+} Probed by Soft X-ray Spectroscopies and ab Initio Calculations, *J. Phys. Chem. B*, **117** (41), 12613 (2013), doi:10.1021/jp408212u.

[123] N. Engel, S. I. Bokarev, E. Suljoti, R. Garcia-Diez, K. M. Lange, K. Atak, R. Golnak, A. Kothe, M. Dantz, O. Kühn, and E. F. Aziz, Chemical Bonding in Aqueous Ferrocyanide: Experimental and Theoretical X-ray Spectroscopic Study, *J. Phys. Chem. B*, **118** (6), 1555 (2014), doi:10.1021/jp411782y.

[124] E. Suljoti, R. Garcia-Diez, S. I. Bokarev, K. M. Lange, R. Schoch, B. Dierker, M. Dantz, K. Yamamoto, N. Engel, K. Atak, O. Kühn, M. Bauer, J.-E. Rubensson, and E. F. Aziz, Direct Observation of Molecular Orbital Mixing in a Solvated Organometallic Complex, *Angew. Chem. Int. Ed.*, **52** (37), 9841 (2013), doi:10.1002/anie.201303310.

[125] M. Preusse, S. I. Bokarev, S. G. Aziz, and O. Kühn, Towards an ab initio theory for metal L-edge soft X-ray spectroscopy of molecular aggregates, *Struct. Dyn.*, **3** (6), 062601 (2016), doi:10.1063/1.4961953.

[126] W. Kohn and L. J. Sham, Self-Consistent Equations Including Exchange and Correlation Effects, *Phys. Rev.*, **140** (4A), A1133 (1965), doi:10.1103/PhysRev.140.A1133.

[127] M. E. Casida, Time-Dependent Density Functional Response Theory for Molecules, in *Recent Advances in Computational Chemistry*, volume 1, pages 155–192, World Scientific (1995), doi:10.1142/9789812830586_0005.

[128] N. Engel, S. I. Bokarev, A. Moguilevski, A. A. Raheem, R. Al-Obaidi, T. Möhle, G. Grell, K. R. Siefermann, B. Abel, S. G. Aziz, O. Kühn, M. Borgwardt, I. Y. Kiyan, and E. F. Aziz, Light-induced relaxation dynamics of the ferricyanide ion revisited by ultrafast XUV photoelectron spectroscopy, *Phys. Chem. Chem. Phys.*, **19** (22), 14248 (2017), doi:10.1039/C7CP01288H.

[129] A. A. Raheem, M. Wilke, M. Borgwardt, N. Engel, S. I. Bokarev, G. Grell, S. G. Aziz, O. Kühn, I. Y. Kiyan, C. Merschjann, and E. F. Aziz, Ultrafast Kinetics of Linkage Isomerism in Na$_2$[Fe(CN)$_5$NO] aqueous solution revealed by time-resolved photoelectron spectroscopy, *Struct. Dyn.*, **4** (4), 044031 (2017), doi:10.1063/1.4990567.

[130] B. A. Hess, C. M. Marian, U. Wahlgren, and O. Gropen, A mean-field spin-orbit method applicable to correlated wavefunctions, *Chem. Phys. Lett.*, **251**, 365 (1996), doi:10.1016/0009-2614(96)00119-4.

[131] S. Hirata and M. Head-Gordon, Time-dependent density functional theory within the Tamm–Dancoff approximation, *Chem. Phys. Lett.*, **314** (3), 291 (1999), doi:10.1016/S0009-2614(99)01149-5.

[132] F. W. J. Olver, D. W. Lozier, R. F. Boisvert, and C. W. Clark (eds.), *NIST Handbook of Mathematical Functions*, Cambridge University Press, 1 edition (2010).

[133] J. C. Slater, A Simplification of the Hartree-Fock Method, *Phys. Rev.*, **81** (3), 385 (1951), doi:10.1103/PhysRev.81.385.

[134] S. Gozem and A. I. Krylov, ezDyson (2017).

[135] P.-O. Löwdin, Quantum theory of many-particle systems. I. Physical interpretations by means of density matrices, natural spin-orbitals, and convergence problems in the method of configurational interaction, *Phys. Rev.*, **97** (6), 1474 (1955), doi:10.1103/PhysRev.97.1474.

[136] T. A. Carlson, *Photoelectron and Auger Spectroscopy*, Springer US, Boston, MA (1975).

[137] F. Aquilante, J. Autschbach, R. K. Carlson, L. F. Chibotaru, M. G. Delcey, L. De Vico, I. F. Galván, N. Ferré, L. M. Frutos, L. Gagliardi, M. Garavelli, A. Giussani, C. E. Hoyer, G. Li Manni, H. Lischka, D. Ma, P. Å. Malmqvist, T. Müller, A. Nenov, M. Olivucci, T. B. Pedersen, D. Peng, F. Plasser, B. Pritchard, M. Reiher, I. Rivalta, I. Schapiro, J. Segarra-Martí, M. Stenrup, D. G. Truhlar, L. Ungur, A. Valentini, S. Vancoillie, V. Veryazov, V. P. Vysotskiy, O. Weingart, F. Zapata, and R. Lindh, New capabilities for multiconfigurational quantum chemical calculations across the periodic table: Molcas 8, *J. Comput. Chem.*, **37** (5), 506 (2016), doi:10.1002/jcc.24221.

[138] M. J. Frisch, G. W. Trucks, H. B. Schlegel, G. E. Scuseria, M. A. Robb, J. R. Cheeseman, G. Scalmani, V. Barone, B. Mennucci, G. A. Petersson, H. Nakatsuji, M. Caricato, X. Li, H. P. Hratchian, A. F. Izmaylov, J. Bloino, G. Zheng, J. L. Sonnenberg, M. Hada, M. Ehara, K. Toyota, R. Fukuda, J. Hasegawa, M. Ishida, T. Nakajima, Y. Honda, O. Kitao, H. Nakai, T. Vreven, J. J. A. Montgomery, J. E. Peralta, F. Ogliaro, M. Bearpark, J. J. Heyd, E. Brothers, K. N. Kudin, V. N. Staroverov, R. Kobayashi, J. Normand, K. Raghavachari, A. Rendell, J. C. Burant, S. S. Iyengar, J. Tomasi, M. Cossi, N. Rega, J. M. Millam, M. Klene, J. E. Knox, J. B. Cross, V. Bakken, C. Adamo, J. Jaramillo, R. Gomperts, R. E. Stratmann, O. Yazyev, A. J. Austin, R. Cammi, C. Pomelli, J. W. Ochterski, R. L. Martin, K. Morokuma, V. G. Zakrzewski, G. A. Voth, P. Salvador, J. J. Dannenberg, S. Dapprich, A. D. Daniels, O. Farkas, J. B. Foresman, J. V. Ortiz, J. Cioslowski, and D. J. Fox, Gaussian 09, Revision D.01, Technical report, Gaussian Inc., Wallingford, CT (2009).

[139] B. WINTER and M. FAUBEL, Photoemission from Liquid Aqueous Solutions, *Chem. Rev.*, **106** (4), 1176 (2006), doi:10.1021/cr040381p.

[140] B. WINTER, R. WEBER, W. WIDDRA, M. DITTMAR, M. FAUBEL, and I. V. HERTEL, Full Valence Band Photoemission from Liquid Water Using EUV Synchrotron Radiation, *J. Phys. Chem. A*, **108** (14), 2625 (2004), doi:10.1021/jp030263q.

[141] M. S. BANNA, B. H. MCQUAIDE, R. MALUTZKI, and V. SCHMIDT, The photoelectron spectrum of water in the 30 to 140 eV photon energy range, *The Journal of Chemical Physics*, **84** (9), 4739 (1986), doi:10.1063/1.450008.

[142] A. PALMA, E. GONZÁLEZ, and O. GOSCINSKI, ESCA peak intensities for small molecules in the sudden approximation:, *Int. J. Quantum Chem.*, **18** (1), 237 (1980), doi:10.1002/qua.560180133.

[143] I. FERNÁNDEZ GALVÁN, M. VACHER, A. ALAVI, C. ANGELI, F. AQUILANTE, J. AUTSCHBACH, J. J. BAO, S. I. BOKAREV, N. A. BOGDANOV, R. K. CARLSON, L. F. CHIBOTARU, J. CREUTZBERG, N. DATTANI, M. G. DELCEY, S. S. DONG, A. DREUW, L. FREITAG, L. M. FRUTOS, L. GAGLIARDI, F. GENDRON, A. GIUSSANI, L. GONZÁLEZ, G. GRELL, M. GUO, C. E. HOYER, M. JOHANSSON, S. KELLER, S. KNECHT, G. KOVAČEVIĆ, E. KÄLL-MAN, G. LI MANNI, M. LUNDBERG, Y. MA, S. MAI, J. P. MALHADO, P. Å. MALMQVIST, P. MARQUETAND, S. A. MEWES, J. NORELL, M. OLIVUCCI, M. OPPEL, Q. M. PHUNG, K. PIERLOOT, F. PLASSER, M. REIHER, A. M. SAND, I. SCHAPIRO, P. SHARMA, C. J. STEIN, L. K. SØRENSEN, D. G. TRUHLAR, M. UGANDI, L. UNGUR, A. VALENTINI, S. VANCOILLIE, V. VERYAZOV, O. WESER, T. A. WESOŁOWSKI, P.-O. WIDMARK, S. WOUTERS, A. ZECH, J. P. ZOBEL, and R. LINDH, OpenMolcas: From Source Code to Insight, *J. Chem. Theory Comput.*, **15** (11), 5925 (2019), doi:10.1021/acs.jctc.9b00532.

[144] N. K. JENA, I. JOSEFSSON, S. K. ERIKSSON, A. HAGFELDT, H. SIEGBAHN, O. BJÖRNEHOLM, H. RENSMO, and M. ODELIUS, Solvent-Dependent Structure of the I_3^- Ion Derived from Photoelectron Spectroscopy and Ab Initio Molecular Dynamics Simulations, *Chem. - Eur. J.*, **21** (10), 4049 (2015), doi:10.1002/chem.201405549.

[145] M. ARBMAN, S. HOLMBERG, M. LUNDHOLM, and H. SIEGBAHN, Liquid ESCA Measurements and ECP calculations on the 3d Spectrum of I_3^-, *Chem. Phys.*, **81**, 113 (1983), doi:10.1016/0301-0104(83)85306-3.

[146] J. METJE, M. BORGWARDT, A. MOGUILEVSKI, A. KOTHE, N. ENGEL, M. WILKE, R. AL-OBAIDI, D. TOLKSDORF, A. FIRSOV, M. BRZHEZINSKAYA, A. ERKO, I. Y. KIYAN, and E. F. AZIZ, Monochromatization of femtosecond XUV light pulses with the use of reflection zone plates, *Opt. Express*, **22** (9), 10747 (2014), doi:10.1364/OE.22.010747.

[147] G. Auböck and M. Chergui, Sub-50-fs photoinduced spin crossover in [Fe(bpy)$_3$]$^{2+}$, *Nat. Chem.*, **7**, 629 (2015), doi:10.1038/nchem.2305.

[148] W. Zhang, R. Alonso-Mori, U. Bergmann, C. Bressler, M. Chollet, A. Galler, W. Gawelda, R. G. Hadt, R. W. Hartsock, T. Kroll, K. S. Kjær, K. Kubiček, H. T. Lemke, H. W. Liang, D. A. Meyer, M. M. Nielsen, C. Purser, J. S. Robinson, E. I. Solomon, Z. Sun, D. Sokaras, T. B. van Driel, G. Vankó, T.-C. Weng, D. Zhu, and K. J. Gaffney, Tracking excited-state charge and spin dynamics in iron coordination complexes, *Nature*, **509** (7500), 345 (2014), doi:10.1038/nature13252.

[149] C. Bressler, C. Milne, V.-T. Pham, A. ElNahhas, R. M. van der Veen, W. Gawelda, S. Johnson, P. Beaud, D. Grolimund, M. Kaiser, C. N. Borca, G. Ingold, R. Abela, and M. Chergui, Femtosecond XANES Study of the Light-Induced Spin Crossover Dynamics in an Iron(II) Complex, *Science*, **323**, 489 (2009), doi:10.1126/science.1165733.

[150] A. Cannizzo, C. Milne, C. Consani, W. Gawelda, C. Bressler, F. van Mourik, and M. Chergui, Light-induced spin crossover in Fe(II)-based complexes: The full photocycle unraveled by ultrafast optical and X-ray spectroscopies, *Coord. Chem. Rev.*, **254** (21-22), 2677 (2010), doi:10.1016/j.ccr.2009.12.007.

[151] H. T. Lemke, C. Bressler, L. X. Chen, D. M. Fritz, K. J. Gaffney, A. Galler, W. Gawelda, K. Haldrup, R. W. Hartsock, H. Ihee, J. Kim, K. H. Kim, J. H. Lee, M. M. Nielsen, A. B. Stickrath, W. Zhang, D. Zhu, and M. Cammarata, Femtosecond X-ray Absorption Spectroscopy at a Hard X-ray Free Electron Laser: Application to Spin Crossover Dynamics, *J. Phys. Chem. A*, **117** (4), 735 (2013), doi:10.1021/jp312559h.

[152] C. Sousa, C. de Graaf, A. Rudavskyi, R. Broer, J. Tatchen, M. Etinski, and C. M. Marian, Ultrafast Deactivation Mechanism of the Excited Singlet in the Light-Induced Spin Crossover of [Fe(2,2'-bipyridine)$_3$]$^{2+}$, *Chem. Eur. J.*, **19**, 17541 (2013), doi:10.1002/chem.201302992.

[153] W. Gawelda, Andrea Cannizzo, V.-T. Pham, Frank van Mourik, C. Bressler, and Majed Chergui, Ultrafast Nonadiabatic Dynamics of [Fe^{II}(bpy)$_3$]$^{2+}$ in Solution, *J. Am. Chem. Soc.*, **129**, 8199 (2007), doi:10.1021/ja070454x.

[154] S. Stock, R. Beerwerth, and S. Fritzsche, Auger cascades in resonantly excited neon, *Phys. Rev. A*, **95** (5), 053407 (2017), doi:10.1103/PhysRevA.95.053407.

[155] L. Avaldi, G. Dawber, R. Camilloni, G. C. King, M. Roper, M. R. F. Siggel, G. Stefani, M. Zitnik, A. Lisini, and P. Decleva, Measurement of Ne1s and 1snl satellite photoelectron spectra near threshold, *Phys. Rev. A*, **51** (6), 5025 (1995), doi:10.1103/PhysRevA.51.5025.

[156] K. KAUFMANN, W. BAUMEISTER, and M. JUNGEN, Universal Gaussian basis sets for an optimum representation of Rydberg and continuum wavefunctions, *J. Phys. B At. Mol. Opt. Phys.*, **22** (14), 2223 (1989), doi:10.1088/0953-4075/22/14/007.

[157] A. KIVIMÄKI, S. HEINÄSMÄKI, M. JURVANSUU, S. ALITALO, E. NÕMMISTE, H. AKSELA, and S. AKSELA, Auger decay at the $1s^{-1}np$ (n= 3–5) resonances of Ne, *J. Electron Spectrosc. Relat. Phenom.*, **114-116**, 49 (2001), doi:10.1016/S0368-2048(00)00259-0.

[158] H. YOSHIDA, K. UEDA, N. M. KABACHNIK, Y. SHIMIZU, Y. SENBA, Y. TAMENORI, H. OHASHI, I. KOYANO, I. H. SUZUKI, R. HENTGES, J. VIEFHAUS, and U. BECKER, Angle-resolved study of the Auger electron cascades following the $1s \rightarrow 3p$ photoexcitation of Ne, *J. Phys. B At. Mol. Opt. Phys.*, **33** (20), 4343 (2000), doi:10.1088/0953-4075/33/20/311.

[159] A. KIVIMÄKI, M. NEEB, B. KEMPGENS, H. M. KÖPPE, and A. M. BRADSHAW, The C 1s Auger decay spectrum of the CH_4 molecule: The effects of vibrational fine structure, double excitations and shake-up transitions, *J. Phys. B At. Mol. Opt. Phys.*, **29** (13), 2701 (1996), doi:10.1088/0953-4075/29/13/009.

[160] K. UEDA, M. OKUNISHI, H. CHIBA, Y. SHIMIZU, K. OHMORI, K. SATO, E. SHIGEMASA, and N. KOSUGI, Rydberg-valence mixing in the C 1s excited states of CH_4 probed by electron spectroscopy, *Chem. Phys. Let.*, **236**, 311 (1995), doi:10.1016/0009-2614(95)00227-U.

[161] J. SCHIRMER, A. B. TROFIMOV, K. J. RANDALL, J. FELDHAUS, A. M. BRADSHAW, Y. MA, C. T. CHEN, and F. SETTE, K -shell excitation of the water, ammonia, and methane molecules using high-resolution photoabsorption spectroscopy, *Phys. Rev. A*, **47** (2), 1136 (1993), doi:10.1103/PhysRevA.47.1136.

[162] M. HIGASHI, E. HIROIKE, and T. NAKAJIMA, Calculations of the Auger transition rates in molecules. I. Effect of the nonspherical potential: Application to CH_4, *Chem. Phys.*, **68** (3), 377 (1982), doi:10.1016/0301-0104(82)87045-6.

[163] O. M. KVALHEIM, Final state correlation effects on the auger transition rates of methane, *Chem. Phys. Lett.*, **86** (2), 159 (1982), doi:10.1016/0009-2614(82)83261-2.

[164] Y. MA, C. T. CHEN, G. MEIGS, K. RANDALL, and F. SETTE, High-resolution K-shell photoabsorption measurements of simple molecules, *Phys. Rev. A*, **44** (3), 1848 (1991), doi:10.1103/PhysRevA.44.1848.

[165] C. D. CALDWELL, S. J. SCHAPHORST, M. O. KRAUSE, and J. JIMÉNEZ-MIER, Photoexcited K Auger spectra of atomic and molecular oxygen, *J. Electron Spectrosc. Relat. Phenom.*, **67** (2), 243 (1994), doi:10.1016/0368-2048(93)02055-Q.

[166] S. L. SORENSEN, R. FINK, R. FEIFEL, M. N. PIANCASTELLI, M. BÄSSLER, C. MIRON, H. WANG, I. HJELTE, O. BJÖRNEHOLM, and S. SVENSSON, High-resolution excitation-energy-dependent study of the Auger decay of the O 1s-1π_g core-excited state in oxygen, *Phys. Rev. A*, **64** (1), 012719 (2001), doi:10.1103/PhysRevA.64.012719.

[167] M. NEEB, J.-E. RUBENSSON, M. BIERMANN, W. EBERHARDT, K. RANDALL, J. FELDHAUS, A. KILCOYNE, A. BRADSHAW, Z. XU, P. JOHNSON, and Y. MA, Effects of time evolution of coherently excited vibrations in molecular core—hole decay spectra of O2, *Chemical Physics Letters*, **212** (1-2), 205 (1993), doi:10.1016/0009-2614(93)87131-L.

[168] T. X. CARROLL and T. D. THOMAS, Lifetime-vibrational interference in the autoionization of core-excited O_2, *J. Chem. Phys.*, **89** (10), 5983 (1988), doi:10.1063/1.455467.

[169] T. X. CARROLL, N. BERRAH, J. BOZEK, J. HAHNE, E. KUKK, L. J. SÆTHRE, and T. D. THOMAS, Carbon 1s photoelectron spectrum of methane: Vibrational excitation and core-hole lifetime, *Phys. Rev. A*, **59** (5), 3386 (1999), doi:10.1103/PhysRevA.59.3386.

[170] W. WURTH, J. STÖHR, P. FEULNER, X. PAN, K. R. BAUCHSPIESS, Y. BABA, E. HUDEL, G. ROCKER, and D. MENZEL, Bonding, structure, and magnetism of physisorbed and chemisorbed O_2 on Pt(111), *Phys. Rev. Lett.*, **65** (19), 2426 (1990), doi:10.1103/PhysRevLett.65.2426.

[171] M. CORENO, M. DE SIMONE, K. C. PRINCE, R. RICHTER, M. VONDRÁČEK, L. AVALDI, and R. CAMILLONI, Vibrationally resolved oxygen K-P spectra of O_2 and CO, *Chem. Phys. Lett.*, **306**, 269 (1999), doi:10.1016/S0009-2614(99)00468-6.

[172] P. KUIPER and B. I. DUNLAP, The σ^* absorption peak at the oxygen 1s edge of O_2 : Exchange splitting, ultrafast dissociation, and atomiclike Auger spectra, *The Journal of Chemical Physics*, **100** (6), 4087 (1994), doi:10.1063/1.466346.

[173] S. SCHAPHORST, C. CALDWELL, M. KRAUSE, and J. JIMÉNEZ-MIER, Evidence for atomic features in the decay of resonantly excited molecular oxygen, *Chemical Physics Letters*, **213** (3-4), 315 (1993), doi:10.1016/0009-2614(93)85138-E.

[174] K. P. HUBER and G. HERZBERG, Constants of diatomic molecules, in *Molecular Spectra and Molecular Structure*, pages 8–689, Springer, Boston, MA (1979).

[175] F. HUND, Zur Deutung der Molekelspektren. I, *Z. Physik*, **40** (10), 742 (1927), doi:10.1007/BF01400234.

[176] O. EDQVIST, E. LINDHOLM, L. E. SELIN, and L. ÅSBRINK, On the Photoelectron Spectrum of O^2, *Phys. Scr.*, **1** (1), 25 (1970), doi:10.1088/0031-8949/1/1/004.

[177] D. Lapiano-Smith, K. Lee, C.-I. Ma, K. T. Wu, and D. M. Hanson, Electronic decay of core hole excited states in molecular oxygen, *The Journal of Chemical Physics*, **93** (4), 2169 (1990), doi:10.1063/1.459048.

[178] P. Bolognesi, P. O'Keeffe, Y. Ovcharenko, L. Avaldi, and V. Carravetta, Resonant Auger spectroscopy at the carbon and nitrogen K-edges of pyrimidine, *J. Chem. Phys.*, **136** (15), 154308 (2012), doi:10.1063/1.4704893.

[179] G. Vall-llosera, B. Gao, A. Kivimäki, M. Coreno, J. Álvarez Ruiz, M. de Simone, H. Ågren, and E. Rachlew, The C 1s and N 1s near edge X-ray absorption fine structure spectra of five azabenzenes in the gas phase, *The Journal of Chemical Physics*, **128** (4), 044316 (2008), doi:10.1063/1.2822985.

[180] P. Bolognesi, P. O'Keeffe, Y. Ovcharenko, M. Coreno, L. Avaldi, V. Feyer, O. Plekan, K. C. Prince, W. Zhang, and V. Carravetta, Pyrimidine and halogenated pyrimidines near edge x-ray absorption fine structure spectra at C and N K-edges: Experiment and theory, *The Journal of Chemical Physics*, **133** (3), 034302 (2010), doi:10.1063/1.3442489.

[181] D. Holland, A. Potts, L. Karlsson, M. Stener, and P. Decleva, A study of the valence shell photoionisation dynamics of pyrimidine and pyrazine, *Chemical Physics*, **390** (1), 25 (2011), doi:10.1016/j.chemphys.2011.09.025.

[182] P. O'Keeffe, P. Bolognesi, A. R. Casavola, D. Catone, N. Zema, S. Turchini, and L. Avaldi, An experimental and computational study of the valence photoelectron spectra of halogenated pyrimidines, *Molecular Physics*, **107** (19), 2025 (2009), doi:10.1080/00268970903120328.

[183] A. W. Potts, D. M. P. Holland, A. B. Trofimov, J. Schirmer, L. Karlsson, and K. Siegbahn, An experimental and theoretical study of the valence shell photoelectron spectra of purine and pyrimidine molecules, *J. Phys. B: At. Mol. Opt. Phys.*, **36** (14), 3129 (2003), doi:10.1088/0953-4075/36/14/314.

[184] U. Lottermoser, P. Rademacher, M. Mazik, and K. Kowski, Photoelectron Spectra and Electronic Structures of Substituted Pyrimidines, *Eur. J. Org. Chem.*, **2005** (3), 522 (2005), doi:10.1002/ejoc.200400534.

[185] L. Storchi, F. Tarantelli, S. Veronesi, P. Bolognesi, E. Fainelli, and L. Avaldi, The Auger spectroscopy of pyrimidine and halogen-substituted pyrimidines, *The Journal of Chemical Physics*, **129** (15), 154309 (2008), doi:10.1063/1.2993317.

7 Own contributions to the manuscripts

Peer reviewed publications

[GG1]: <u>Gilbert Grell</u>, Sergey I. Bokarev, Bernd Winter, Robert Seidel, Emad F. Aziz, Saadullah G. Aziz, and Oliver Kühn
Multi-reference approach to the calculation of photoelectron spectra including spin-orbit coupling,
The Journal of Chemical Physics **143**, 074104 (2015)

My contribution: The working expressions for the numerical evaluation of Dyson orbitals for spin-free RASSCF and spin-orbit-coupled RASSI wave functions have been developed by me and **SIB**. The numerical protocol for the Dyson orbital evaluation and the interface to the ezDyson 3.0 code have been implemented by me. I have performed all simulations and produced the presented figures. The results have been interpreted together with the coauthors. The text apart from the experimental details section, which has been supplied by **BW**, has been drafted by me and **SIB**. Subsequently, the manuscript has been converged to its final form mainly by **SIB**, with support from me and the coauthors.

[GG2]: Alexandre Moguilevski, Martin Wilke, <u>Gilbert Grell</u>, Sergey I. Bokarev, Saadullah G. Aziz, Nicholas Engel, Azhr A. Raheem, Oliver Kühn, Igor Yu. Kiyan, and Emad F. Aziz,
Ultrafast Spin Crossover in $[Fe^{II}(bpy)_3]^{2+}$: Revealing Two Competing Mechanisms by Extreme Ultraviolet Photoemission Spectroscopy,
ChemPhysChem **18**, 465 (2017)

My contribution: Using the numerical protocol devised in [GG1], I conducted all simulations and produced the panels c and d of Fig. 2, as well as Fig. S7 in the Supplement. A collaborative analysis of the theoretical and experimental results by me and the coauthors has lead to the 'Extended Model' devised in the contribution. The theoretical parts of the manuscript (mainly in Supplement) have been drafted by me. I contributed to the revision process until the manuscript reached its final form, but here the main part was done by the coauthors.

[GG3]: Jesper Norell, <u>Gilbert Grell</u>, Oliver Kühn, Michael Odelius, and Sergey I. Bokarev,
Photoelectron shake-ups as a probe of molecular symmetry: 4d XPS analysis of I_3^- in solution,
Physical Chemistry Chemical Physics **20**, 19916 (2018)

My contribution: I have developed the formalism for the occupation number analysis

and extended the protocol from [GG1] by a respective numerical implementation. Within this collaboration, I have transferred this implementation to **JN**, who has carried out all simulations. The results have been analyzed by me and the coauthors. The occupation number formalism contributed by me has been condensed in section 2.4 and lead to the analysis presented in Fig.3. The drafted manuscript has been iterated to its final form by me and the coauthors.

[GG4]: Gilbert Grell, Oliver Kühn, and Sergey I. Bokarev,
Multireference quantum chemistry protocol for simulating autoionization spectra: Test of ionization continuum models for the neon atom,
Physical Review A **100**, 042512 (2019)

My contribution: I have derived the complete formalism which lead to a protocol that has been implemented in a Fortran program by me. I have conducted all simulations and compiled all figures. The results have been analyzed by me and the coauthors. I have drafted the manuscript which was iterated to its final stage together with the coauthors.

Additional manuscripts

[GG5]: Gilbert Grell, and Sergey I. Bokarev,

Multi-reference protocol for (auto)ionization spectra: application to molecules,

*arXiv:*1912.04139 [physics.chem-ph] (2019)

My contribution: I have extended the numerical implementation presented in [GG4] to allow larger scale calculations for molecular systems. All simulations have been carried out by me and I produced all figures. The results have been analyzed mainly by me. I have drafted the manuscript apart from the introduction and conclusions sections, which have been drafted mainly by **SIB**. The manuscript has been converged to its final form by me and **SIB**.

8 Peer reviewed publications

[GG1] Multi-reference approach to the calculation of photoelectron spectra including spin-orbit coupling

GILBERT GRELL, SERGEY I. BOKAREV, BERND WINTER, ROBERT SEIDEL, EMAD F. AZIZ, SAADULLAH G. AZIZ, and OLIVER KÜHN

Multi-reference approach to the calculation of photoelectron spectra including spin-orbit coupling

Gilbert Grell,[1] Sergey I. Bokarev,[1,a)] Bernd Winter,[2] Robert Seidel,[2] Emad F. Aziz,[2,3] Saadullah G. Aziz,[4] and Oliver Kühn[1]

[1]*Institut für Physik, Universität Rostock, D-18051 Rostock, Germany*
[2]*Helmholtz-Zentrum Berlin für Materialien und Energie, Methods for Material Development, Albert-Einstein-Strasse 15, D-12489 Berlin, Germany*
[3]*Department of Physics, Freie Universität Berlin, Arnimalle 14, D-14159 Berlin, Germany*
[4]*Chemistry Department, Faculty of Science, King Abdulaziz University, 21589 Jeddah, Saudi Arabia*

X-ray photoelectron spectra provide a wealth of information on the electronic structure. The extraction of molecular details requires adequate theoretical methods, which in case of transition metal complexes has to account for effects due to the multi-configurational and spin-mixed nature of the many-electron wave function. Here, the restricted active space self-consistent field method including spin-orbit coupling is used to cope with this challenge and to calculate valence- and core-level photoelectron spectra. The intensities are estimated within the frameworks of the Dyson orbital formalism and the sudden approximation. Thereby, we utilize an efficient computational algorithm that is based on a biorthonormal basis transformation. The approach is applied to the valence photoionization of the gas phase water molecule and to the core ionization spectrum of the $[Fe(H_2O)_6]^{2+}$ complex. The results show good agreement with the experimental data obtained in this work, whereas the sudden approximation demonstrates distinct deviations from experiments. © *2015 AIP Publishing LLC.* [http://dx.doi.org/10.1063/1.4928511]

I. INTRODUCTION

Spectroscopy, tracing the changes of the energetic levels upon various physical interactions and in course of dynamical processes, is one of the most powerful analytical tools finding applications in almost every field of natural sciences, medicine, and engineering. Among the various spectroscopic methods, experiments in the X-ray regime are suitable to explore the structure of materials in all aggregation states.[1] The most popular variants of X-ray spectroscopies comprise first order absorption and photoelectron spectroscopy as well as second order fluorescence and Auger spectroscopy.[1,2]

Upon X-ray irradiation, a core hole is created either resonantly or non-resonantly, i.e., an electron is excited to a bound or continuum state. Since the binding energies of core electrons are significantly different for various elements and core orbitals have a very localized probability density, X-ray spectroscopy can be used as an element specific local probe of the electronic structure of an atom in its environment. This in particular distinguishes spectroscopy in the X-ray and UV/VIS regime, since the latter gives insight into transitions between delocalized molecular orbitals (MO).[3]

Remarkably, photoelectron spectroscopy was found to be sensitive to specific solute–solvent interactions of transition metal (TM) complexes in solutions[4–8] which are essential for understanding processes in catalysis, biochemistry, and material sciences.[9–15] However, due to the complex electronic structure and notable (especially for core ionization) spin-orbit coupling (SOC) of TM compounds, photoelectron spectra (PES) are rich in features, and an unambiguous assignment is difficult without the aid from theoretical calculations.[1]

On the theory side, a number of methods have been proposed for the assignment of PES. The simplest ones are Hartree-Fock or Kohn-Sham density functional theory.[16,17] Here, MO energies are attributed to the PES transition energies via Koopmans' theorem[18] and intensities are not analyzed. In some cases, this may provide already a good interpretation of the observed spectrum.[5,6] However, such a simple picture is not able to describe more complex effects such as combination transitions. For that purpose, methods based on a Green's function approach have been introduced, see, e.g., Ref. 19. For instance, the algebraic diagrammatic construction formulation[20] enjoys particular popularity.[21–23] These methods directly deliver the spectroscopic observables, i.e., transition energies and intensities, as poles and residues of the Green's function,[19] respectively, avoiding the calculation of the stationary wave functions. The relativistic treatment necessary for TM compounds has been implemented within a four-component formalism[24] which is computationally quite demanding. In addition, Green's function methods are single-configurational, whereas TM complexes in some cases require multi-configurational treatment.

In principle, any quantum chemical method capable of describing excited electronic states can be used to obtain the PES peak positions of main and combination transitions as energy differences between the N-electron initial and $N-1$-electron final states. Methods which have been

a)Electronic mail: sergey.bokarev@uni-rostock.de

143, 074104-1

previously used in PES calculations include Configuration Interaction (CI),[25–29] Time-Dependent Density Functional Theory (TDDFT),[30,31] Equation-of-motion Coupled Cluster (EOM-CCSD),[32,33] and multiconfigurational methods based on Complete or Restricted Active Space Self-Consistent Field (CASSCF/RASSCF) wave function.[34–37] The latter group is of particular importance for TM compounds, since they are known to sometimes have wave functions which, even in the ground state, cannot be represented by a single configuration.[38] Alternatively, the semi-empirical valence bond Ligand-Field Multiplet (LFM) technique[1,39] is widely used for X-ray photoelectron spectroscopy of TM compounds. In all these methods, the SOC is either not included or treated within the multi-configurational Dirac-Fock method in jj-coupling limit[40] or within semi-empirically parametrized (LFM[1,39]) and *ab initio* (RASSCF[35–37]) LS-coupling limit.

The intensities in LFM and most of CI studies are estimated in the sudden approximation (SA)[41,42] neglecting the kinetic energy dependence of the transition strength and approximating it in a form of a wave function overlap, see Sec. II. In principle, the SA should be valid for high kinetic energies of the outgoing electron. However, for certain applications the SA has been shown to be unable to make reliable prediction of intensities.[28,34]

For TDDFT,[30,31] EOM-CCSD,[32,33] CI,[27] and CASSCF[34] based methods, the Dyson Orbital (DO) formalism[43] has been applied. Although computationally more demanding, it gives a rather accurate description of intensities. Further, it provides a compact representation of the PES matrix elements by virtue of reducing the N-particle to a one-particle integration, see Sec. II. Finally, DOs can be rigorously employed for the determination of angular-resolved PES.[44]

The present work sets the focus onto formulating and testing a simulation protocol for the incorporation of SOC and multi-reference effects into the DO formalism for accurate description of PES intensities of TM complexes. Thereby, we employ the RASSCF multi-reference approach[45–47] and include SOC within state interaction (RASSI) method[48] in the atomic mean field integral approximation.[49] The paper is organized as follows. In Sec. II, we give a general overview of the theoretical background and of the developed methodology. Computational details are provided in Sec. III and experimental details in Sec. IV. Section V discusses application of the described protocol to two model systems, i.e., gas phase water (valence PES) and the $[Fe(H_2O)_6]^{2+}$ complex (core PES), which corresponds to solvated iron(II) ions in water. In Sec. VI, we conclude that the proposed approach allows the description of PES on the same footing as processes involving photons, i.e., X-ray absorption and resonant inelastic scattering, reported recently.[50–57]

II. THEORY

We consider neutral or charged molecules with N electrons, which are initially in their ground state $|\Psi_I^N\rangle$. In the sudden ionization limit,[41,43] the final state can be written as an antisymmetrized product $|\Psi_F^{N-1}\psi^{el}(\mathbf{k})\rangle$ of the continuum state of the photoelectron $\psi^{el}(\mathbf{k})$ and the wave function of the $N-1$-electron remainder Ψ_F^{N-1}.

Assuming that all photoelectrons with a certain kinetic energy ($\mathcal{E}_k = \hbar^2 k^2/(2m_e)$) are detected regardless of their outgoing direction and spin, their number per unit time is proportional to the transition rate, including all possible initial and final states with energies $\mathcal{E}_I$ and $\mathcal{E}_F$ and integrated over all directions, $d\Omega_k$, of the outgoing electron. In the long wavelength approximation, it reads

$$\sigma(\mathcal{E}_k) \propto \frac{2\pi}{\hbar} \sum_I f^B(\mathcal{E}_I) \sum_F \Lambda(\mathcal{E}_F + \mathcal{E}_k - \mathcal{E}_I - \hbar\omega)$$
$$\times \int d\Omega_k \left| \left\langle \Psi_F^{N-1}\psi^{el}(\mathbf{k}) \left| \vec{\varepsilon}\cdot\hat{\mathbf{d}} \right| \Psi_I^N \right\rangle \right|^2, \qquad (1)$$

where $\hat{\mathbf{d}}$ is the dipole operator, $\vec{\varepsilon}$ is the polarization of the incoming photon, the lineshape function $\Lambda(\mathcal{E})$ accounts for the finite width of the excitation pulse, inhomogeneous, and other broadening effects. The thermal population of the initial states enters Eq. (1) via the Boltzmann factor $f^B(\mathcal{E}_I)$.

In the following, we will specify the many-body states Ψ_I^N and Ψ_F^{N-1} in terms of Slater determinants (SD), Θ_i, composed of single particle MOs, φ_i^k. Let us consider the PES matrix elements in Eq. (1) for two SDs giving a contribution to the initial state Ψ_I^N, i.e., Θ_j^N, and the final state Ψ_F^{N-1}, i.e., Θ_i^{N-1}. Omitting for convenience the polarization and $\mathbf{k}$ dependence and applying the strong orthogonality condition between the free electron function and initial molecular orbitals ($\langle\psi^{el}|\varphi_j^k\rangle = 0$, see, e.g., Ref. 58), one can write

$$D_{ij}^{SD} = \left\langle \Theta_i^{N-1}\psi^{el} \left| \hat{\mathbf{d}} \right| \Theta_j^N \right\rangle = \left\langle \psi^{el} \left| \hat{\mathbf{d}} \right| \Phi_{ij}^{SD} \right\rangle, \qquad (2)$$

where we introduced the DO

$$\Phi_{ij}^{SD} = \sum_{\mathcal{P}\in S_N} (-1)^p \left\langle \varphi_i^1 \middle| \varphi_j^{\mathcal{P}(1)} \right\rangle \cdots \left\langle \varphi_i^{N-1} \middle| \varphi_j^{\mathcal{P}(N-1)} \right\rangle \times \varphi_j^{\mathcal{P}(N)}. \qquad (3)$$

Here, $\mathcal{P} \in S_N$ denotes all possible permutations of N orbital indices with parity p coming from the structure of the SDs. Thus, the expression for the PES matrix element simplifies to a one-particle integration because the $N-1$-dimensional integration over electron coordinates $\mathbf{x}_k$ is comprised into the DO with the normalization factor $\sqrt{N}$,

$$\Phi_{ij}^{SD}(\mathbf{x}_N) = \sqrt{N} \int \left(\Theta_i^{N-1}(\mathbf{x}_1,\ldots,\mathbf{x}_{N-1})\right)^*$$
$$\times \Theta_j^N(\mathbf{x}_1,\ldots,\mathbf{x}_N)d\mathbf{x}_1\cdots d\mathbf{x}_{N-1}. \qquad (4)$$

Note that in general the one-electron orbitals of the initial N-electron and final $N-1$-electron bound states are not ortho-normal due to electronic relaxation upon electron removal. The DO can be considered as an analogue of the reduced one-electron transition density. Its direct correspondence is the wave function of the photoelectron before the ionization. Further, the DO is not normalized and the PES intensity is proportional to its norm. The convenience of the DO formulation of the PES matrix elements stems from the fact that the DO contains all system- and method-specific information. Therefore, one can vary the approximations for ψ_{el}, without changing the DO.

In practice, the $N!$-fold summation in Eq. (3) can be circumvented by calculating N determinants of $N-1 \times N-1$ dimensional overlap matrices, similar to Ref. 42.

Thus, the computational effort reduces to $O(N^4)$. A more efficient scheme can be obtained upon transformation of the nonorthonormal MO basis sets and CI coefficients of the initial and final states Ψ_I^N and Ψ_F^{N-1} to biorthonormal sets.[48,59] This strongly simplifies the DO expression in Eq. (3), which reduces to a single term. To show this, we consider the case where the removed electron was in orbital φ_j^τ in the initial state Θ_j^N. If this orbital is not contained in the final state Θ_i^{N-1}, then only one permutation in Eq. (3) leads to nonzero results. That is, the permutation $\mathcal{P}$, which shifts the electron in φ_j^τ into the Nth half space of the initial state which does not take part in the integration. The parity of the permutation $\mathcal{P}$ is $p = N - \tau$. Thus, we arrive at a simple expression for the DO in the biorthonormal basis

$$\Phi_{ij}^{SD} = (-1)^{N-\tau} \varphi_j^\tau. \qquad (5)$$

The most important feature of the representation in the biorthonormal basis is that the DO for a pair of determinants corresponds to a spin-orbital of the initial SD taken with the appropriate sign. Thus, the computational effort does not depend on the number of electrons, which makes this approach very efficient.

In the single SD picture, the DO depends on the coordinates of only one electron. Thus, no combination transitions, where one electron is ejected and others are simultaneously excited, are taken into account. However, in a multi-reference description of the DO, these effects are included. To obtain wave functions, which account for the multi-reference character of transition metal complexes, as well as SOC effects, we follow a two-step strategy. First, the spin-free RASSCF wave functions having ground state spin S as well as $S \pm 1$ are calculated. They have the form of a linear combination of different SDs Θ_i, weighted with CI coefficients C_{Ki} (omitting the superscript for the number of electrons in the following),

$$\Psi_{K=F,I}^{CI} = \sum_{i=1}^{N_{CI}} C_{Ki} \Theta_i. \qquad (6)$$

Assuming that the initial state can be described by a single SD (Θ_0), the DO within the CI approach, omitting for convenience I and F indices, can be written in the form

$$\Phi_{FI}^{CI} = \sum_i \underbrace{C_i^* C_0 \langle \Theta_i | \Theta_0 \rangle}_{1h} + \sum_{ija} \underbrace{\left(C_{ij}^a\right)^* C_j^a \langle \Theta_{ij}^a | \Theta_j^a \rangle}_{2h1p}$$
$$+ \sum_{ijkab} \underbrace{\left(C_{ijk}^{ab}\right)^* C_{jk}^{ab} \langle \Theta_{ijk}^{ab} | \Theta_{jk}^{ab} \rangle}_{3h2p} + \cdots. \qquad (7)$$

Here, the brackets denote the $N - 1$-dimensional integration, $i, j, k, \ldots$ are indices of the occupied orbitals from which the electrons are removed, $a, b, \ldots$ correspond to the unoccupied orbitals into which the electrons are excited. The first three sums represent the main 1h (single hole), combination 2h1p (two holes, single particle), and 3h2p (three holes, two particles) transitions, respectively.

The concept of active space within RASSCF as applied to Eq. (7) allows to flexibly vary the highest order of correlation terms, in principle up to full CI within the given orbital subspace. However, this subspace needs to be large enough

to include all relevant ionization channels. Interestingly, when employing the biorthonormal basis set transformation, orbital relaxation effects, which can cause satellites due to non-orthogonality of initial and final orbitals,[26] are shifted completely to correlation effects, i.e., the CI expansion.

At the second step, these wave functions are coupled with the SOC operator in atomic mean-field integral approximation[49] to generate spin-orbit wave functions within the RASSI approach.[48,59] These spin-orbit wave functions are expanded in terms of the spin-free states $\Psi_{Kn,M_\sigma,\sigma}^{CI}$, where $K = F, I$, (Eq. (6)) with spin σ (N_σ states in total), magnetic quantum numbers M_σ and SOC coefficients $\xi_{Kn,M_\sigma,\sigma}$,

$$\Psi_{K=F,I}^{SO} = \sum_{\sigma=S-1}^{S+1} \sum_{n=1}^{N_\sigma} \sum_{M_\sigma=-\sigma}^{\sigma} \xi_{Kn,M_\sigma,\sigma} \Psi_{Kn,M_\sigma,\sigma}^{CI}. \qquad (8)$$

The particular choice of spin manifolds is dictated by the SOC selection rules $\Delta S = 0, \pm 1$.

Thus, the multi-configurational DO including SOC for the transition from initial state I to final state F can be expanded in terms of single determinant DO Φ_{ij}^{SD} (Eq. (3)),

$$\Phi_{FI}^{SO} = \sum_{k=1}^{N_F^{SO}} \sum_{l=1}^{N_I^{SO}} \xi_{Fk}^* \xi_{Il} \sum_{i=1}^{N_F^{SD}} \sum_{j=1}^{N_I^{SD}} C_{ki}^* C_{lj} \Phi_{ij}^{SD}. \qquad (9)$$

Here, the nested sums over spin, magnetic quantum number, and spin-free states are replaced by one sum over all different spin-orbit states with the total number of final and initial SOC states N_F^{SO} and N_I^{SO}, respectively. The above Eq. (9) can be used to calculate the PES matrix elements $D_{FI}^{SO} = \langle \psi^{el} | \hat{\mathbf{d}} | \Phi_{FI}^{SO} \rangle$, which is the main working expression used in this work.

Since an electron with either α or β spin is removed from the initial spin-free states with spins S and $S \pm 1$, the final states with $\Delta S = \pm 1/2$ need to be considered. That is why in general, seven spin manifolds of the unionized molecule with N electrons and its $N - 1$-electron ion need to be taken into account as depicted in Fig. 1.

Frequently, the SA is used for the calculation of the transition dipole matrix element in Eq. (1).[41,42] Here, the matrix element is approximated as an overlap integral neglecting the **k**-dependence of the transition strength,

$$D_{FI}^{SA} = \left| \left\langle \Psi_F^{N-1} \psi^{el}(\mathbf{k}) \left| \hat{\mathbf{d}} \right| \Psi_I^N \right\rangle \right|^2 \approx \left| \left\langle \Psi_F^{N-1} \left| \hat{a} \Psi_I^N \right\rangle \right|^2, \qquad (10)$$
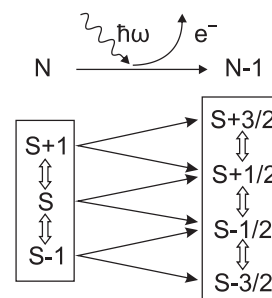

FIG. 1. Schematic of the directly spin-coupled manifolds of states (the double-sided arrows, $\Delta S = 0, \pm 1$) of the N and $N - 1$ electron systems. Depending on the spin of the outgoing electron, the spin of final $N - 1$ electron states changes by $\Delta S = \pm 1/2$ (single-sided arrows).

where the operator $\hat{a}$ annihilates the electron from the occupied MO. Expressed in terms of DOs in the SA approach, the one-electron integration for $\langle \psi^{el}|\hat{\mathbf{d}}|\Phi_{FI}\rangle$ is omitted and the intensity is approximated by the DO norm, $|\Phi_{FI}|^2$, only. Most of the published papers use the SA for the prediction of the intensities of the combination transitions relative to the intensities of main lines. However, the accuracy of the predicted intensity ratios between different main transitions occurring at high excitation energies has been questioned in Refs. 28 and 60.

III. COMPUTATIONAL DETAILS

The spectra were calculated for two test systems, i.e., gas phase water and the $[Fe(H_2O)_6]^{2+}$ complex mimicking the Fe^{2+} ion within its first solvation shell in aqueous solution. Thus the following processes were studied:

$$H_2O^0 \longrightarrow H_2O^+ + e^-,$$
$$[Fe(H_2O)_6]^{2+} \longrightarrow [Fe(H_2O)_6]^{3+} + e^-.$$
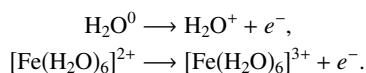
The geometry of water was optimized at the density functional theory level with the B3LYP functional[61,62] together with the 6-311G(d) basis set.[63,64] For the $[Fe(H_2O)_6]^{2+}$ complex, the geometry was first optimized using the MP2 method with the cc-pVTZ basis set.[65–67] Then, the Fe − O bond lengths were set to the CASPT2($10e^-$, 12MO)/ANO-RCC values obtained in Ref. 68. All geometry optimizations were done with Gaussian 09 program package.[69]

For state-averaged RASSCF calculations of water, the full valence RAS2 active space additionally including the 1s core orbital of oxygen was chosen (Fig. 2). For the iron complex, the active space included the 3d orbitals of iron in the RAS2 space and allowed single electron excitations from the iron 2p core orbitals in the RAS1 space. This results in the singly core-excited or ionized states, having full flexibility in the valence 3d manifold. This active space corresponds to that used for the study of X-ray absorption and resonant inelastic scattering spectra[53] providing interpretation on the same footing. The wave function was first optimized for the ground state and then all orbitals apart from the active ones were kept frozen.

The (8s4p3d)/[3s2p1d] ANO-RCC basis on hydrogen and (14s9p4d3f)/[5s4p3d2f] basis on oxygen[70] were employed for water, which corresponds to quadruple-zeta
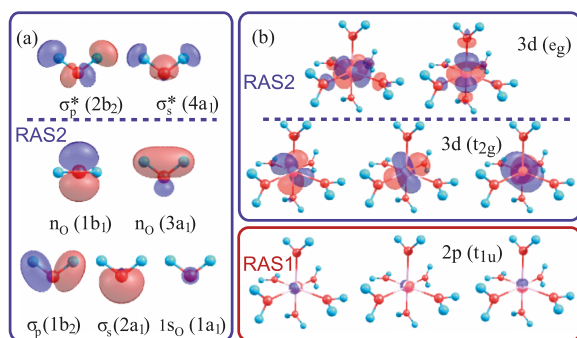
FIG. 2. Active spaces used for RASSCF calculations of (a) water and (b) $[Fe(H_2O)_6]^{2+}$.

quality. For Fe^{2+} the contractions (21s15p10d6f)/[6s5p3d2f], (14s9p4d3f)/[4s3p2d1f], and (8s4p)/[2s1p] were used for iron, oxygen, and hydrogen, respectively, corresponding to the triple-zeta level.

To account for dynamic correlation, the second order perturbation theory correction (RASPT2) was calculated[71,72] for the case of water. To avoid intruder state singularities, the imaginary level shift of 0.4 hartree was applied. Because of the much larger number of transitions, only RASSCF energies were calculated for the iron complex.

To incorporate scalar relativistic effects, the Douglas-Kroll-Hess transformation[73,74] up to second order was utilized and all overlaps in Eq. (3) were calculated for the transformed orbitals. For the case of water, SOC was not taken into account and only transitions from the singlet ground state to the 490 doublet singly ionized final states were considered. This corresponds to one out of six possible branches in Fig. 1. In case of the iron complex, quintet ($S = 2$) and triplet ($S = 1$) initial states as well as sextet ($S = 5/2$), quartet ($S = 3/2$), and doublet ($S = 1/2$) final states were taken into account. Septet ($S = 3$) and octet ($S = 7/2$) states are not possible with the active space chosen here. However, it was shown that they play a very minor role for the X-ray absorption spectrum[53] and can be neglected. Thus, only five branches out of the seven in Fig. 1 were considered. In total, for $[Fe(H_2O)_6]^{2+}$ one initial ground and 1260 core-excited SOC states were included. Thermal population of the low lying initial states was neglected.

The RASSCF/RASPT2/RASSI calculations were done without any symmetry restriction using a locally modified MOLCAS 8.0 program package.[75]

The transition dipole matrix elements in Eq. (2) were calculated with the ezDyson 3.0 program[76] via numerical integration of the DO with the free electron wave function $\psi^{el}(\mathbf{k})$. Neglecting the interaction between the photoelectron and ionic remainder, one may express $\psi^{el}(\mathbf{k})$ as a plane wave expanded in a basis of spherical waves with spherical harmonics $Y_{l,m}(\mathbf{k})$ in $\mathbf{k}$-space as coefficients (see, e.g., Ref. 77). Further, the spherical waves are expanded in position space using spherical Bessel functions $j_l(k \cdot r)$, where $k = |\mathbf{k}|$, $r = |\mathbf{r}|$, and spherical harmonics $Y_{l,m}(\mathbf{r})$ yielding

$$\psi^{el}(\mathbf{k}) = \sum_{l=0}^{\infty} \sum_{m=-l}^{l} i^l \sqrt{\frac{2}{\pi}} j_l(k \cdot r) Y_{l,m}(\mathbf{r}) Y_{l,m}^*(\mathbf{k}). \quad (11)$$

This particular form of the plane wave has the advantage that one can truncate the infinite angular momentum expansion at some l_{max}, e.g., according to the dipole selection rule $\Delta l = \pm 1$. The natural choice of maximum angular momentum in the expansion, Eq. (11), corresponds to the $l_{max} = l_{bas} + 1$, where l_{bas} is maximum angular momentum included in the atomic basis set. However, due to lower than spherical symmetry of the molecules under study, sometimes a larger l_{max} needs to be selected, see Ref. 32 and Sec. V.

It should be noted that the representation of $\psi^{el}(\mathbf{k})$ in Eq. (11) is correct only in the asymptotic limit far from the ionic core.[32,78] Coulomb waves being the solution of the radial Schrödinger equation of an electron in a spherical Coulomb potential[79] could be more suitable to describe the

photoionization of neutral or positively charged molecules. In this case, the partial wave expansion can be longer than in Eq. (11).[32]

In case of water, $l_{max} = 7$, box with a side length of 10 Å and an equidistant grid of $300 \times 300 \times 300$ points for numerical integration of Eq. (2) ensures convergence of the DO norms with an accuracy of 10^{-5}. Since the intensity of transition scales quadratically with the norm of the DO, they have been evaluated only if the norm of the respective DO was larger than 10^{-3}. For the iron ion, only contributions from those DOs that have a norm larger than 10^{-2} were taken into account. Here $l_{max} = 5$, box size of 16 Å, and a grid of $480 \times 480 \times 480$ points was used for the numerical integration reproducing the norms of DOs with an accuracy of 10^{-4}.

As shown in Sec. II, the spin-coupled DO comprises contributions from different spin-states. Therefore, the total spin of the DO and outgoing electron is not well defined. The consequence is that the DO consists of both α and β spin wave functions,

$$\Phi_{FI}^{SO} = \Phi_{FI}^{SO}(\alpha) + \Phi_{FI}^{SO}(\beta), \qquad (12)$$

which are complex-valued due to the SOC. Here, we neglect spin-coherence and calculate the squared PES matrix element as

$$\left| D_{FI}^{SO} \right|^2 \approx \left| D_{FI}^{Re}(\alpha) \right|^2 + \left| D_{FI}^{Im}(\alpha) \right|^2 + \left| D_{FI}^{Re}(\beta) \right|^2 + \left| D_{FI}^{Im}(\beta) \right|^2, \qquad (13)$$

where Re and Im represent the real and imaginary parts of D_{FI}. The broadenings of the spectral lines were fitted to reproduce the experimental data and are discussed in Sec. V. No nuclear vibrational effects were taken into account. The PES matrix element was integrated over all possible outgoing directions of the photoelectron and averaged over all possible orientations of the molecules to mimic free tumbling in a gaseous or liquid phase.

IV. EXPERIMENTAL DETAILS

The PESs were measured from a 15 μm vacuum liquid jet[80,81] at the soft-X-ray U41 PGM undulator beamline of the Berlin synchrotron radiation facility, BESSY II, Berlin. The jet velocity was approximately 100 m s^{-1}, and the jet temperature was 6 °C. At operation conditions, the pressure in the interaction chamber is $\approx 1.5 \cdot 10^{-4}$ mbars. Electrons were detected normal to both the synchrotron-light polarization vector and the flow of the liquid jet. A 100 μm diameter orifice that forms the entrance to the hemispherical electron energy-analyzer (Specs Leybold EA10) is typically at approximately 0.5 mm distance from the liquid jet. Because of the small focal size ($12 \times 23 \ \mu m^2$) of the incident photon beam at the interaction point with the liquid jet, by moving the jet slightly out of focus the photoelectron spectrum from gas-phase water can be measured. The valence spectrum of the latter was obtained using 180 eV photon energy; the total energy resolution was better than 60 meV. For the aqueous phase Fe^{2+} 2p core-level spectrum, the photon energy was 925 eV, and the energy resolution was approximately 300 meV. The 2M iron aqueous solution (pH ≈ 2.5) was prepared by adding anhydrous FeCl$_2$ salt (98% purity, Sigma Aldrich) to highly demineralized (>17 MΩ cm^{-1}) water. The major species in this pale-lime colored aqueous solution are [Fe(H$_2$O)$_5$Cl]$^+$ ($\approx 77\%$) and [Fe(H$_2$O)$_6$]$^{2+}$ ($\approx 23\%$).[82]

V. RESULTS AND DISCUSSION

A. Water

The PES of water was chosen as a benchmark for the derived protocol for calculation of PES for two reasons. First, the water valence PES is well understood both experimentally and theoretically.[25,26,28,60,83,84] Second, water is not influenced by strong SOC and has mostly single-configurational character as long as only the lowest valence excitations are regarded. This substantially simplifies the calculation and analysis of the nature of transitions, since DOs represent mostly single MOs.

In Fig. 3, the experimental and theoretical PESs for the 180 eV energy of the incoming photon are shown. For convenience, the individual transitions are also given as a stick spectrum. The normalized intensity is plotted against binding energy $E_b = \mathcal{E}_F - \mathcal{E}_I$, where $\mathcal{E}_F$ and $\mathcal{E}_I$ are the energies of final and initial states, respectively. Additionally, the DOs corresponding to selected transitions are presented. The broadening of each transition was fitted to reproduce the experiments: peak (1) (see Fig. 3) Lorentzian lineshape FWHM = 0.17 eV, peaks (2) and (3) Gaussian lineshape with FWHM of 1.18 eV and 1.75 eV, respectively. For all other transitions contributing to peak (4), Gaussian profiles with widths 1.5 eV for $E_b < 35$ eV and 3.0 eV for $E_b > 35$ eV were applied. The absolute energy shift of -0.78 eV was chosen to align peak (1) with the experiment.

The calculated spectrum is in rather good agreement with the experimental data. There are slight variations of intensities of peaks (2) and (3) relative to (1) and the most notable discrepancies between theory and experiment are observed
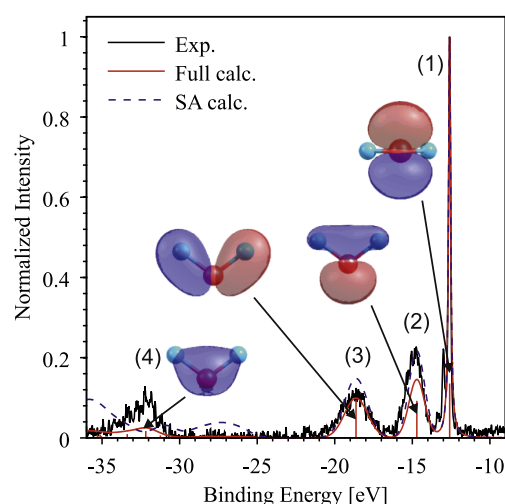

FIG. 3. Calculated and experimental PES of water in the gas phase for 180 eV excitation energy. Full calculation corresponds to numerical integration of PES matrix element, SA means sudden approximation.[41,42] Spin-free DOs of the selected transitions are also shown.

for peak (4). These deviations in the intensities and lineshapes could be ascribed to the fact that nuclear vibrational effects were not taken into account. However, the relative energetic positions of the peaks are predicted with very high accuracy. To note is the fact that RASPT2 correction is essential here to reproduce the transition energies. This stems from the fact that in RASSCF dynamic correlation is accounted for in an unbalanced way within the active space and may substantially change upon removal of one electron. To correct for this behavior a more complete treatment of correlation, such as RASPT2, is needed, see the supplementary material.[85]

It can be seen that SA predicts the relative intensities of peaks (1) to (3) with similar quality as the full calculation employing integration of the DO with the free electron wave function. But for peak (4) the agreement between SA and experiment is not even qualitative.

The assignment of peaks fully agrees with that established previously.[25,26,28,60,83,84] Peaks (1)-(3) correspond to ionizations from the lone pairs $n_O(1b_1)$ and $n_O(3a_1)$ and the $\sigma_p(1b_2)$ MO of water, respectively. The fourth peak consists of several transitions of different nature most of them having $\sigma_s(2a_1)$ character. This can be ascribed to the multi-configurational character of the wave function and appearance of combination transitions, see the supplementary material.[85] Interestingly, the DOs of a_1 symmetry resemble very closely the ground state Hartree-Fock MOs, but in fact they are linear combinations of the $\sigma_s(2a_1)$ and $n_O(3a_1)$ RASSCF active orbitals (cf. Fig. 2).

The water molecule has rather low point group symmetry and convergence of the series in Eq. (11) is quite slow. The contributions of the partial $\{l, m\}$ waves to intensities of peaks (1) and (3) are presented in Fig. 4. The DOs of transitions (1) and (2) represent almost pure 2p orbitals of oxygen and in accordance with the dipole selection rules ($\Delta l = \pm 1$) only contributions with $l = \{0, 2\}$ notably differ from zero. In contrast, the DOs for transitions (3) and (4) deviate strongly from atomic character, being rather delocalized MOs such that the series in Eq. (11) converges notably slower, approaching zero only for $l \geq 6$. In general, one can conclude that the more the DO is delocalized over the molecule and the less symmetric it is, the more terms have to be included in the photoelectron wave expansion (Eq. (11)), see also Ref. 32.

B. Fe²⁺ (aq.)

The calculated L-edge core PES of $[Fe(H_2O)_6]^{2+}$ at incoming photon energy of 925 eV is shown in Fig. 5(a) together with experimental results for a 2M aqueous solution of $FeCl_2$ at the same energy. The stick spectrum was broadened using the Voigt profile

$$V(x) = \int_{-\infty}^{\infty} G(\sigma, x')L(\gamma, x - x')dx, \quad (14)$$

with the Gaussian and Lorentzian lineshape functions $G(\sigma, x)$ and $L(\gamma, x)$. For the broadening of the L_3 peak ($E_b > -727.4$ eV), 0.5 eV and 0.7 eV were used for the Lorentzian and Gaussian FWHM, respectively. For the L_2 peak (below $E_b < -727.4$ eV), 0.7 eV for both Lorentzian and Gaussian widths in the Voigt profile was used. Additionally, the
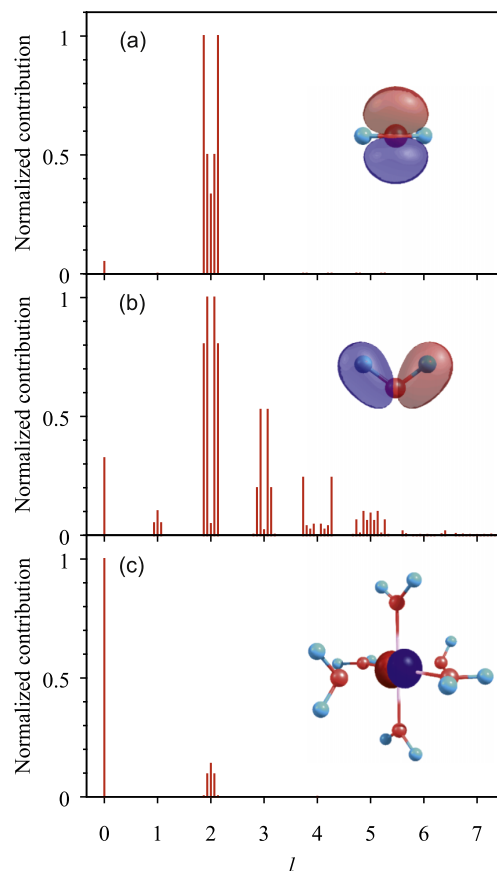
FIG. 4. Normalized contributions of different $\{l, m\}$ partial waves to the intensity of selected transitions: (a) and (b) transitions (1) and (3) of an isolated water molecule, respectively, see Fig. 3; (c) real part of β spin DO contribution of transition (2) of the $[Fe(H_2O)_6]^{2+}$ core PES, see Fig. 5. Each group of $2l + 1$ sticks corresponds to m-components, see Eq. (11). Corresponding DOs are shown as insets using different contour values for visual clarity.

calculated spectrum was shifted as a whole by +10.65 eV for better comparison with the experimental data.

The spectrum consists of two prominent bands called L_3 and L_2 which correspond to the SOC components of the created core-hole, i.e., 3/2 and 1/2 total angular momentum, respectively. Transitions to states $253 - 1000$ and $1001 - 1260$ of the $[Fe(H_2O)_6]^{3+}$ ion correspond to the L_3 and L_2 peaks, respectively, in the core PES shown in Fig. 5. The computed core PES with numerical integration according to Eq. (2) (full calculation) is in rather good agreement with the experiment. Our method reproduces well the L_2/L_3 energy splitting, intensity ratio, and the general asymmetric shape of the bands with the long tails at the low energy sides. Almost all of the 1260 transitions have notable intensity, hence the bands and corresponding tails are formed by hundreds of lines, most of them being combination transitions. The small discrepancies, e.g., the small peak at -722.9 eV and the minimum at -720.5 eV, also originate from a large number of transitions of different origins, which hinders a detailed analysis. In principle, they could be ascribed to the lack of dynamic correlation (no RASPT2 correction) and to the presence of
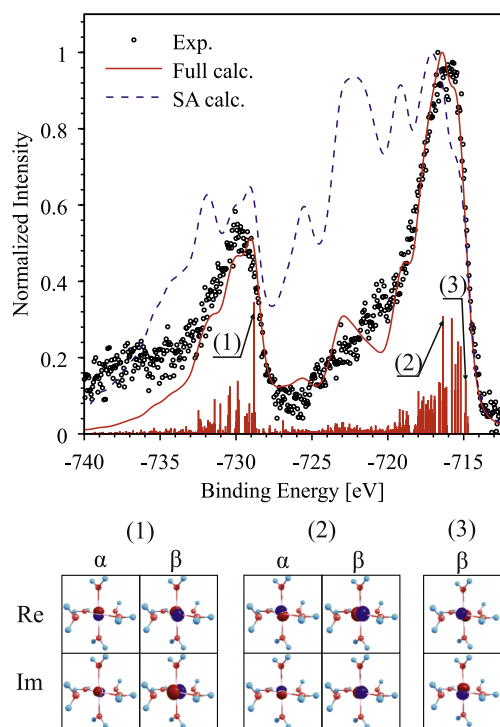
FIG. 5. (a) Experimental (2M FeCl$_2$ aqueous solution) and calculated (for [Fe(H$_2$O)$_6$]$^{2+}$ cluster) core PES for incoming photon energy of 925 eV. Full calculation corresponds to numerical integration of PES matrix element, SA means sudden approximation.[41,42] (b) Real and imaginary parts of α and β spin contributions to the DOs for selected transitions.

different species in solution. Note that ionization only from [Fe(H$_2$O)$_6$]$^{2+}$ was considered in computations. Further, the averaging over several thermally populated electronic initial states could be necessary. Finally, due to the high density of states, the tails of the L_2 and L_3 peaks are very sensitive to the wings of the lineshape function. Therefore, an inclusion of more than two different sets of broadening parameters might be necessary as well.

The wave functions of the final states of [Fe(H$_2$O)$_6$]$^{3+}$ are much more complex in comparison to those of water. First of all, the core-ionized final states do not have a leading contribution from one configuration and represent a combination of many configurations with comparable weights in Eq. (6). To illustrate this issue, the weights of the three most important configuration state functions for the quartet final states of [Fe(H$_2$O)$_6$]$^{3+}$ are shown in the supplementary material.[85] For other spin manifolds, the dependences look similar and are not shown. Second, due to strong SOC for the core-ionized states, a pronounced spin-mixing of states within the LS-coupling scheme applied here is observed. More details of this mixing are given in the supplementary material.[85] This implies that the spin of the final states is not well defined and their wave functions represent linear combinations of the sextet, quartet, and doublet spin-states (Eq. (8)). The complex structure of the wave function is reflected in the DOs (Fig. 5(b)). Here, most transitions correspond to DOs, where the real and imaginary parts of the α and β spin contributions

are of comparable magnitude. Thus, a calculation of only real DOs with definite spin would produce erroneous intensities. An exception occurs at the rising flank of L_3 (DO (3) in Fig. 5(b)) which can be ascribed to nearly pure quintet-sextet transitions and thus corresponds to photoelectrons with β spin. The β electron is easily removed because of the pairing (exchange) energy.

The DOs for different transitions of both the L_2 and L_3 bands are combinations of pure atomic 2p orbitals of iron and differ in the absolute and relative magnitude of real and imaginary α and β components. This corresponds to the fact that the electron is removed from the core 2p orbitals and, in contrast to water, the series in Eq. (11) converge to zero very quickly for all transitions. One example is shown in Fig. 4(c) for the most intense L_3 transition. Since only atomic 2p$_{Fe}$ orbitals are contributing to the DOs, the dipole selection rules hold strictly.

In Fig. 5 we also show the SA results, where the intensities of the transitions are approximated as the norms of DO and thus the computationally demanding integration in Eq. (2) is avoided. Apparently, the SA gives a PES which substantially deviates from both the experiment and the full calculation, most notably it shows rather intense tails of L_3 and L_2 bands. These deviations cannot be eliminated by the fitting of broadenings; note that in Fig. 5 the same broadening parameters as for the full calculation are used. This result shows that although this approximation is intensively used in CI[26,29] and LFM calculations of core PES[1] and in RASSCCF/RASSI calculations of valence PES of heavy elements,[36] it cannot be considered as being generally accurate. This holds especially if the kinetic energy of the ejected electron is relatively low. Thus, to obtain accurate L-edge core PES the integration of the DO with the free electron wave function is required. Commonly, the SA is used when the photoelectron momentum angular distribution is not of interest. Our results point to the failure of the SA even in such cases.

VI. CONCLUSIONS

We have presented a multi-reference approach to core and valence photoelectron spectra of transition metal complexes, taking into account the essential effects due to the multi-configurational character of the wave function and spin-orbit coupling. This method is an extension of the Dyson orbital formalism, previously applied with TDDFT[30,31] and EOM-CCSD[32,33] techniques, to RASSCF/RASSI wave functions. Thereby, an essential point for efficient computation of the Dyson orbitals is the biorthonormal MO basis transformation.[59] The proposed protocol includes the numerical integration of the matrix elements, resulting in more reliable intensities as compared with the widely used sudden approximation.

This present approach is complementary to the theoretical X-ray spectroscopic techniques, which have been recently reported for absorption, fluorescence, and inelastic scattering spectra.[50–57] Having the method describing photon-out and electron-out events on the same footing provides additional tools to address the electronic structure of transition metal complexes.

The computational protocol has been demonstrated for two examples, i.e., the valence PES of gaseous water and L-edge core PES of the $[Fe(H_2O)_6]^{2+}$ cluster as a model for the Fe^{2+} ion in aqueous solution. In both cases, the agreement between theory and experiment was rather good. In particular, for the aqueous ion the RASSCF/RASSI wave function has a rather complex structure. This is reflected in the DO, i.e., due to spin-mixing the Dyson orbitals for core-ionization of $[Fe(H_2O)_6]^{2+}$ contain complex-valued α and β contributions. This immediately implies that the usage of real DOs with definite spin would give erroneous spectra.

We have contrasted our results with those of the widely used sudden approximation. The latter shows for relatively low excitation energies notable deviations from experimental spectra for the aqueous Fe^{2+} ion. Hence, in general the numerical integration of the Dyson orbitals with the free electron wave function should not be dismissed.

ACKNOWLEDGMENTS

[1] F. M. F. de Groot and A. Kotani, *Core Level Spectroscopy of Solids*, Advances in Condensed Matter Science Vol. 6 (CRC Press, Boca Raton, 2008).

[2] C. Milne, T. Penfold, and M. Chergui, Coord. Chem. Rev. **277-278**, 44 (2014).

[3] A. Stolow, A. E. Bragg, and D. M. Neumark, Chem. Rev. **104**, 1719 (2004).

[4] B. Winter, Nucl. Instrum. Methods Phys. Res., Sect. A **601**, 139 (2009).

[5] D. Yepes, R. Seidel, B. Winter, J. Blumberger, and P. Jaque, J. Phys. Chem. B **118**, 6850 (2014).

[6] R. Seidel, S. Thürmer, J. Moens, P. Geerlings, J. Blumberger, and B. Winter, J. Phys. Chem. B **115**, 11671 (2011).

[7] J. Moens, R. Seidel, P. Geerlings, M. Faubel, B. Winter, and J. Blumberger, J. Phys. Chem. B **114**, 9173 (2010).

[8] S. Thürmer, R. Seidel, W. Eberhardt, S. E. Bradforth, and B. Winter, J. Am. Chem. Soc. **133**, 12528 (2011).

[9] J. F. da Silva and R. Williams, *The Biological Chemistry of the Elements: The Inorganic Chemistry of Life* (Oxford University Press, New York, 1991).

[10] D. Wöhrle and A. D. Pomogailo, *Metal Complexes and Metals in Macromolecules: Synthesis, Structure and Properties* (Wiley-VCH, 2003).

[11] J.-H. Guo, Y. Luo, A. Augustsson, J.-E. Rubensson, C. Såthe, H. Ågren, H. Siegbahn, and J. Nordgren, Phys. Rev. Lett. **89**, 137402 (2002).

[12] U. Bergmann, D. Nordlund, P. Wernet, M. Odelius, L. G. M. Pettersson, and A. Nilsson, Phys. Rev. B **76**, 024202 (2007).

[13] K. M. Lange, M. Soldatov, R. Golnak, M. Gotz, N. Engel, R. Könnecke, J.-E. Rubensson, and E. F. Aziz, Phys. Rev. B **85**, 155104 (2012).

[14] P. Ball, Chem. Rev. **108**, 74 (2008).

[15] D. S. Goodsell, *The Machinery of Life* (Springer, New York, 1993).

[16] T. Körzdörfer, S. Kümmel, N. Marom, and L. Kronik, Phys. Rev. B **79**, 201205 (2009).

[17] T. Körzdörfer and S. Kümmel, Phys. Rev. B **82**, 155206 (2010).

[18] C.-O. Almbladh and U. von Barth, Phys. Rev. B **31**, 3231 (1985).

[19] L. S. Cederbaum and W. Domcke, in *Advances in Chemical Physics*, edited by I. Prigogine and S. A. Rice (John Wiley, New York, London, 1977), Vol. XXXVI, pp. 205–344.

[20] J. Schirmer, L. S. Cederbaum, and O. Walter, Phys. Rev. A **28**, 1237 (1983).

[21] M. Pernpointner and L. S. Cederbaum, J. Chem. Phys. **122**, 214302 (2005).

[22] N. V. Kryzhevoi and L. S. Cederbaum, J. Chem. Phys. **130**, 084302 (2009).

[23] R. Santra, N. V. Kryzhevoi, and L. S. Cederbaum, Phys. Rev. Lett. **103**, 013002 (2009).

[24] M. Pernpointner, T. Rapps, and L. S. Cederbaum, J. Chem. Phys. **131**, 044322 (2009).

[25] R. Sankari, M. Ehara, H. Nakatsuji, A. D. Fanis, H. Aksela, S. Sorensen, M. Piancastelli, E. Kukk, and K. Ueda, Chem. Phys. Let. **422**, 51 (2006).

[26] A. Lisini, G. Fronzoni, and P. Decleva, J. Phys. B **21**, 3653 (1988).

[27] P. Decleva, G. Fronzoni, A. Kivimäki, J. Álvarez Ruiz, and S. Svensson, J. Phys. B **42**, 055102 (2009).

[28] R. Arneberg, J. Müller, and R. Manne, Chem. Phys. **64**, 249 (1982).

[29] A. Kivimäki, J. Álvarez Ruiz, M. Coreno, M. Stankiewicz, G. Fronzoni, and P. Decleva, Chem. Phys. **353**, 202 (2008).

[30] L. Kronik and S. Kümmel, in *First Principles Approaches to Spectroscopic Properties of Complex Materials*, edited by C. Di Valentin, S. Botti, and M. Cococcioni (Springer, Berlin, Heidelberg, 2014), Vol. 347, pp. 137–191.

[31] B. Mignolet, J. O. Johansson, E. E. B. Campbell, and F. Remacle, ChemPhysChem **14**, 3332 (2013).

[32] C. M. Oana and A. I. Krylov, J. Chem. Phys. **127**, 234106 (2007).

[33] C. M. Oana and A. I. Krylov, J. Chem. Phys. **131**, 124114 (2009).

[34] A. Ponzi, C. Angeli, R. Cimiraglia, S. Coriani, and P. Decleva, J. Chem. Phys. **140**, 204304 (2014).

[35] I. Josefsson, S. K. Eriksson, N. Ottosson, G. Öhrwall, H. Siegbahn, A. Hagfeldt, H. Rensmo, O. Björneholm, and M. Odelius, Phys. Chem. Chem. Phys. **15**, 20189 (2013).

[36] R. Klooster, R. Broer, and M. Filatov, Chem. Phys. **395**, 122 (2012).

[37] M. Barysz and Ł. Syrocki, Mol. Phys. **112**, 583 (2014).

[38] B. O. Roos, K. Andersson, M. P. Fülscher, P.-Å. Malmqvist, L. Serrano-Andrés, K. Pierloot, and M. Merchán, in *Advances in Chemical Physics New Methods in Computational Quantum Mechanics*, 1st ed., edited by I. Prigogine and S. A. Rice (John Wiley & Sons, Inc., New York, 1996), Vol. 93, pp. 219–332.

[39] F. M. F. de Groot, J. C. Fuggle, B. T. Thole, and G. A. Sawatzky, Phys. Rev. B **42**, 5459 (1990).

[40] K. Jänkälä, J. Schulz, and H. Aksela, J. Electron Spectrosc. Relat. Phenom. **161**, 95 (2007).

[41] R. Manne and T. Åberg, Chem. Phys. Lett. **7**, 282 (1970).

[42] T. Åberg, Phys. Rev. **156**, 35 (1967).

[43] B. T. Pickup, Chem. Phys. **19**, 193 (1977).

[44] K. L. Reid, Annu. Rev. Phys. Chem. **54**, 397 (2003).

[45] B. O. Roos and P. R. Taylor, Chem. Phys. **48**, 157 (1980).

[46] J. Olsen, B. O. Roos, P. Jörgensen, and H. J. A. Jensen, J. Chem. Phys. **89**, 2185 (1988).

[47] P.-Å. Malmqvist, A. Rendell, and B. O. Roos, J. Phys. Chem. **94**, 5477 (1990).

[48] P.-Å. Malmqvist, B. O. Roos, and B. Schimmelpfennig, Chem. Phys. Lett. **357**, 230 (2002).

[49] B. Schimmelpfennig, AMFI, An Atomic Mean-Field Spin-Orbit Integral Program, 1996.

[50] I. Josefsson, K. Kunnus, S. Schreck, A. Föhlisch, F. de Groot, P. Wernet, and M. Odelius, J. Phys. Chem. Lett. **3**, 3565 (2012).

[51] P. Wernet, K. Kunnus, S. Schreck, W. Quevedo, R. Kurian, S. Techert, F. M. F. de Groot, M. Odelius, and A. Föhlisch, J. Phys. Chem. Lett. **3**, 3448 (2012).

[52] E. Suljoti, R. Garcia-Diez, S. I. Bokarev, K. M. Lange, R. Schoch, B. Dierker, M. Dantz, K. Yamamoto, N. Engel, K. Atak *et al.*, Angew. Chem., Int. Ed. **52**, 9841 (2013).

[53] S. I. Bokarev, M. Dantz, E. Suljoti, O. Kühn, and E. F. Aziz, Phys. Rev. Lett. **111**, 083002 (2013).

[54] K. Atak, S. I. Bokarev, M. Gotz, R. Golnak, K. M. Lange, N. Engel, M. Dantz, E. Suljoti, O. Kühn, and E. F. Aziz, J. Phys. Chem. B **117**, 12613 (2013).

[55] N. Engel, S. I. Bokarev, E. Suljoti, R. Garcia-Diez, K. M. Lange, K. Atak, R. Golnak, A. Kothe, M. Dantz, O. Kühn *et al.*, J. Phys. Chem. B **118**, 1555 (2014).

[56] R. V. Pinjari, M. G. Delcey, M. Guo, M. Odelius, and M. Lundberg, J. Chem. Phys. **141**, 124116 (2014).

[57] P. Wernet, K. Kunnus, I. Josefsson, I. Rajkovic, W. Quevedo, M. Beye, S. Schreck, S. Grübel, M. Scholz, D. Nordlund *et al.*, Nature **520**, 78 (2015).

[58] B. Ritchie, J. Chem. Phys. **64**, 3050 (1976).

[59] P.-Å. Malmqvist, Int. J. Quantum Chem. **30**, 479 (1986).

[60] A. Palma, E. González, and O. Goscinski, Int. J. Quantum Chem. **18**, 237 (1980).

[61] A. D. Becke, J. Chem. Phys. **98**, 5648 (1993).

[62] C. Lee, W. Yang, and R. G. Parr, Phys. Rev. B **37**, 785 (1988).

[63] A. D. McLean and G. S. Chandler, J. Chem. Phys. **72**, 5639 (1980).

[64] R. Krishnan, J. S. Binkley, R. Seeger, and J. A. Pople, J. Chem. Phys. **72**, 650 (1980).

[65]T. H. Dunning, J. Chem. Phys. **90**, 1007 (1989).

[66]D. E. Woon and T. H. Dunning, J. Chem. Phys. **100**, 2975 (1994).

[67]N. B. Balabanov and K. A. Peterson, J. Chem. Phys. **123**, 064107 (2005).

[68]K. Pierloot and S. Vancoillie, J. Chem. Phys. **125**, 124303 (2006).

[69]M. J. Frisch, G. W. Trucks, H. B. Schlegel, G. E. Scuseria, M. A. Robb, J. R. Cheeseman, G. Scalmani, V. Barone, B. Mennucci, G. A. Petersson *et al.*, 09, Revision D.01, Gaussian, Inc., Wallingford, CT, 2009.

[70]B. O. Roos, R. Lindh, P.-Å. Malmqvist, V. Veryazov, and P.-O. Widmark, J. Phys. Chem. A **109**, 6575 (2005).

[71]P.-Å. Malmqvist, K. Pierloot, A. R. M. Shahi, C. J. Cramer, and L. Gagliardi, J. Chem. Phys. **128**, 204109 (2008).

[72]K. Andersson, P. Malmqvist, B. O. Roos, A. J. Sadlej, and K. Wolinski, J. Phys. Chem. **94**, 5483 (1990).

[73]M. Douglas and N. M. Kroll, Ann. Phys. **82**, 89 (1974).

[74]B. A. Hess, Phys. Rev. A **33**, 3742 (1986).

[75]F. Aquilante, L. De Vico, N. Ferré, G. Ghigo, P.-Å. Malmqvist, P. Neogrády, T. B. Pedersen, M. Pitoňák, M. Reiher, B. O. Roos *et al.*, J. Comput. Chem. **31**, 224 (2010).

[76]S. Gozem and A. I. Krylov, ezDyson 3.0, 2015, URL http://iopenshell.usc.edu/downloads/ezdyson.

[77]J. J. Sakurai, *Modern Quantum Mechanics*, 2nd ed. (Addison-Wesley, Boston, 2011).

[78]H. Park and R. N. Zare, J. Chem. Phys. **104**, 4554 (1996).

[79]L. D. Landau and E. M. Lifshitz, *Quantum Mechanics: Non-Relativistic Theory* (Pergamon, Oxford, 1977).

[80]B. Winter and M. Faubel, Chem. Rev. **106**, 1176 (2006).

[81]R. Seidel, S. Thürmer, and B. Winter, J. Phys. Chem. Lett. **2**, 633 (2011).

[82]C. Heinrich and T. Seward, Geochim. Cosmochim. Acta **54**, 2207 (1990).

[83]B. Winter, R. Weber, W. Widdra, M. Dittmar, M. Faubel, and I. V. Hertel, J. Phys. Chem. A **108**, 2625 (2004).

[84]M. S. Banna, B. H. McQuaide, R. Malutzki, and V. Schmidt, J. Chem. Phys. **84**, 4739 (1986).

[85]See supplementary material at http://dx.doi.org/10.1063/1.4928511 for comparison of RASSCF and RASPT2 results for water, weights of most important CSFs for water and iron complex, and spin-contributions to the wave function of iron complex.

Multi-reference approach to the calculation of photoelectron spectra including spin-orbit coupling

Gilbert Grell,[1] Sergey I. Bokarev,[1, a)] Bernd Winter,[2] Robert Seidel,[2] Emad F. Aziz,[2, 3] Saadullah G. Aziz,[4] and Oliver Kühn[1]

[1] *Institut für Physik, Universität Rostock, Universitätsplatz 3, 18055 Rostock, Germany*

[2] *Joint Laboratory for Ultrafast Dynamics in Solutions and at Interfaces (JULiq), Institute of Methods for Material Development, Helmholtz-Zentrum Berlin für Materialien und Energie, Albert-Einstein-Strasse 15, 12489 Berlin, Germany*

[3] *Department of Physics, Freie Universität zu Berlin, Arnimalle 14, 14159 Berlin, Germany*

[4] *Chemistry Department, Faculty of Science, King Abdulaziz University, 21589 Jeddah, Saudi Arabia*

(Dated: July 28, 2015)

X-ray photoelectron spectra provide a wealth of information on the electronic structure. The extraction of molecular details requires adequate theoretical methods, which in case of transition metal complexes has to account for effects due to the multi-configurational and spin-mixed nature of the many-electron wave function. Here, the Restricted Active Space Self-Consistent Field method including spin-orbit coupling is used to cope with this challenge and to calculate valence and core photoelectron spectra. The intensities are estimated within the frameworks of the Dyson orbital formalism and the sudden approximation. Thereby, we utilize an efficient computational algorithm that is based on a biorthonormal basis transformation. The approach is applied to the valence photoionization of the gas phase water molecule and to the core ionization spectrum of the $[Fe(H_2O)_6]^{2+}$ complex. The results show good agreement with the experimental data obtained in this work, whereas the sudden approximation demonstrates distinct deviations from experiments.

---

a) Electronic mail: sergey.bokarev@uni-rostock.de

1
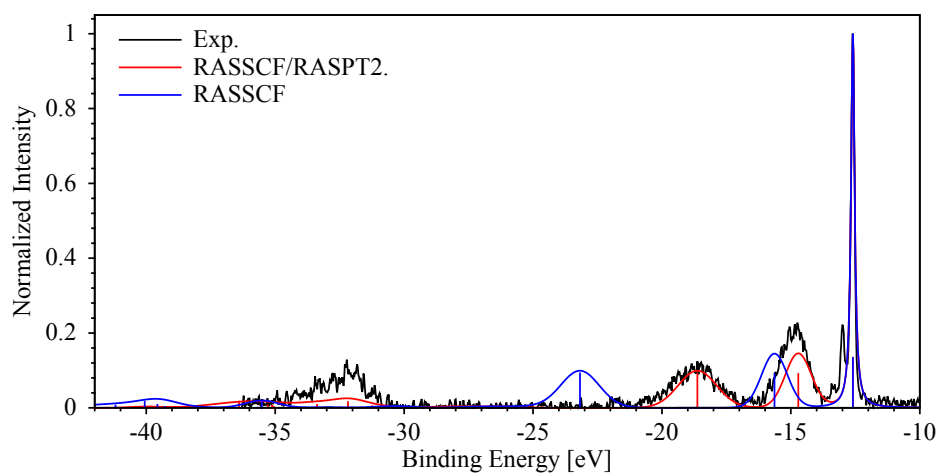
Figure 1. Comparison of RASSCF and RASPT2 results for the valence photoelectron spectrum of of gas phase water.
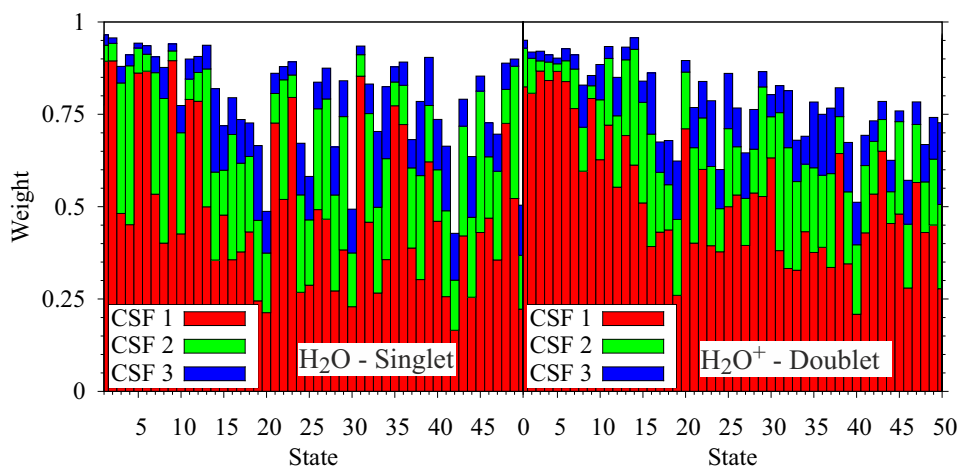
Figure 2. Weights of the three most important configuration state functions (CSF) for the 50 lowest singlet (left panel) and doublet singly ionized (right panel) states of the water molecule in the gas phase as predicted by the RASSCF method. The white space corresponds to the contribution of all other configurations.
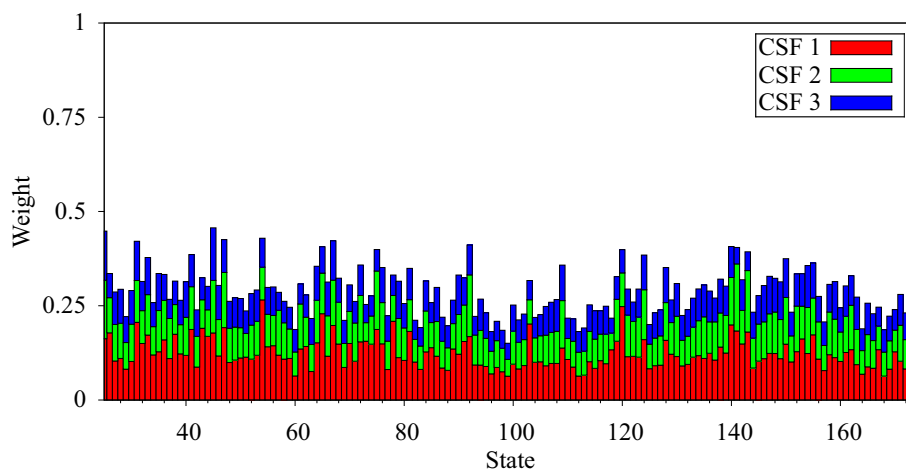
Figure 3. Weights of the three most important CSFs for the quartet core-excited states of $[Fe(H_2O)_6]^{3+}$. The white space corresponds to the contribution of all other configurations. For other spin manifolds of $[Fe(H_2O)_6]^{2+}$ and $[Fe(H_2O)_6]^{3+}$ the dependence looks similar.
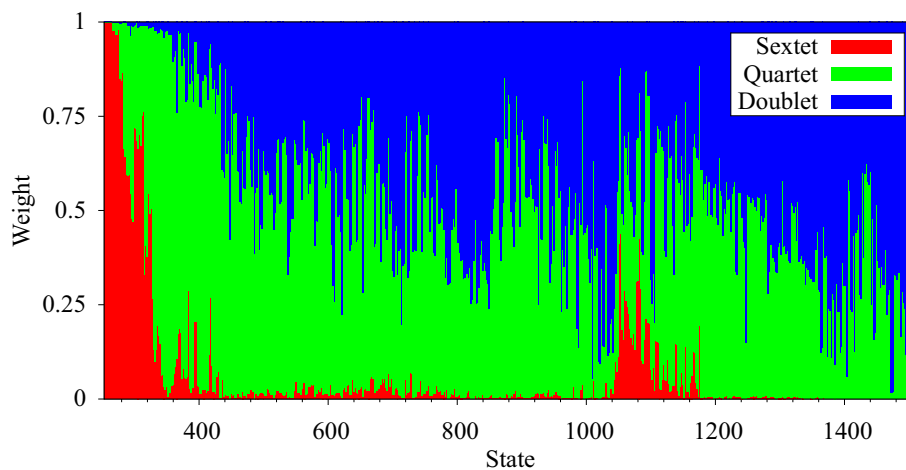
Figure 4. Collective weights of sextet, quartet and doublet spin contributions to the core excited spin-coupled states of $[Fe(H_2O)_6]^{3+}$.

4
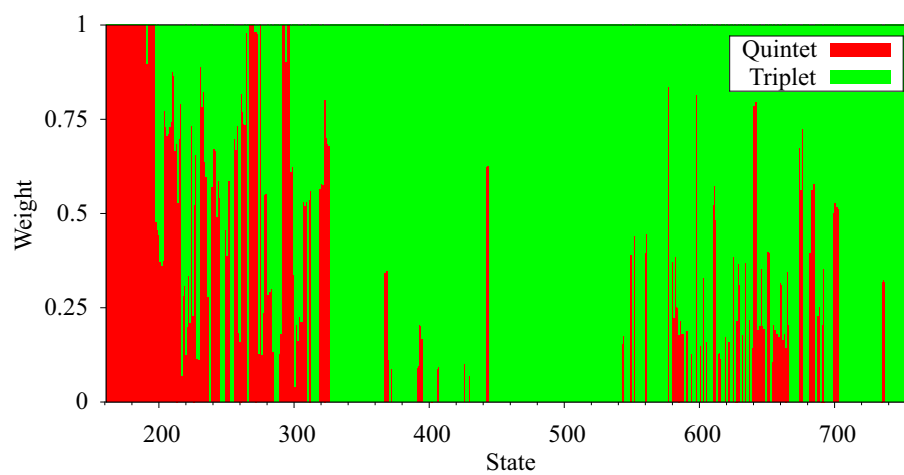
Figure 5. Collective weights of quintet and triplet spin contributions to the core excited spin-coupled states of $[\text{Fe}(\text{H}_2\text{O})_6]^{2+}$.

Erratum: "Multi-reference approach to the calculation of photoelectron spectra including spin-orbit coupling" [J. Chem. Phys. 143, 074104 (2015)]

Gilbert Grell,[1] Sergey I. Bokarev,[1,a)] Bernd Winter,[2] Robert Seidel,[2] Emad F. Aziz,[2,3]
Saadullah G. Aziz,[4] and Oliver Kühn[1]
[1]*Institut für Physik, Universität Rostock, Albert-Einstein-Str. 23-24, 18059 Rostock, Germany*
[2]*Helmholtz-Zentrum Berlin für Materialien und Energie, Methods for Material Development,*
Albert-Einstein-Strasse 15, 12489 Berlin, Germany
[3]*Department of Physics, Freie Universität zu Berlin, Arnimalle 14, 14159 Berlin, Germany*
[4]*Chemistry Department, Faculty of Science, King Abdulaziz University, 21589 Jeddah, Saudi Arabia*

[http://dx.doi.org/10.1063/1.4961314]

In Ref. 1 we have presented a novel first principles approach to the calculation of photoelectron spectra (PES) and a comparison with the widely used sudden approximation (SA)[2–4] has been performed. Two mistakes have been made in Ref. 1 which are corrected in this erratum. First, within the SA the intensity of a transition is proportional to the absolute square of the Dyson orbital (DO) norm

$$\sigma(\mathcal{E}_k) \propto \left| \langle \Psi_F^{N-1} | \hat{a} \Psi_I^N \rangle \right|^2. \tag{1}$$

However, in Figs. 2 and 5 of Ref. 1, the DO norm was not squared. Second, Eq. (10) from the original publication contained a typo and should read

$$\left| D_{FI}^{\mathrm{SA}} \right|^2 = \left| \langle \Psi_F^{N-1} \psi^{\mathrm{el}}(\mathbf{k}) \left| \hat{\mathbf{d}} \right| \Psi_I^N \rangle \right|^2 \approx \left| \langle \Psi_F^{N-1} | \hat{a} \Psi_I^N \rangle \right|^2. \tag{2}$$

Taking the square alters the discussion on the applicability of the SA to the calculation of X-ray PES of transition metal compounds. We emphasize that the main results of Ref. 1, i.e., the PES obtained via the numerical integration of the DO with the ionized electron wave function, are not affected.

The corrected SA PES are presented in Fig. 1 together with the full calculation results. In contrast to what is claimed in Ref. 1, Fig. 1 shows that the SA predicts the intensities of all peaks with an accuracy that is comparable to the full calculation.
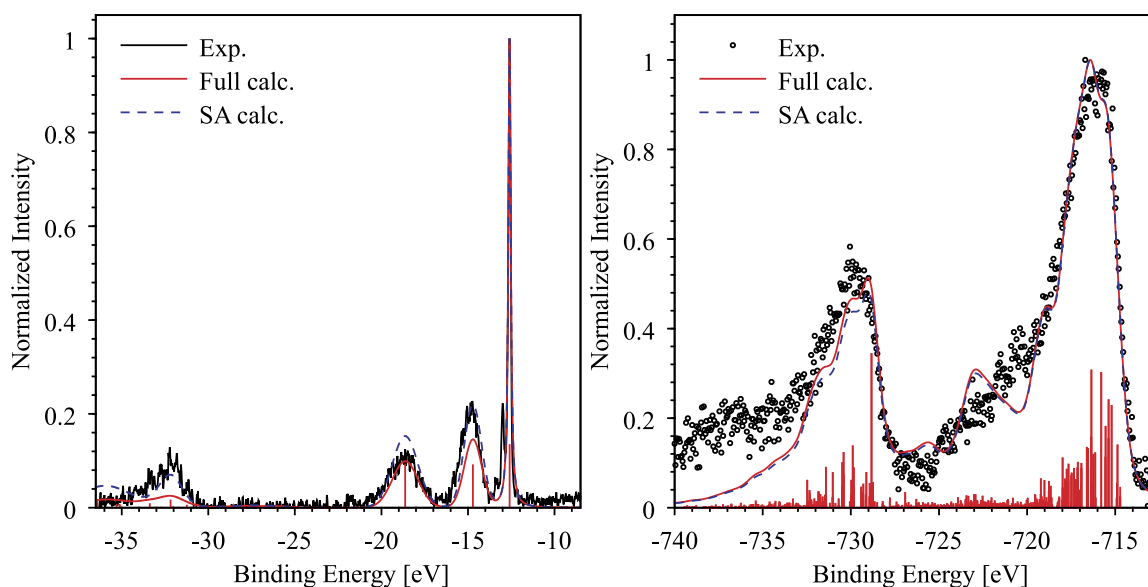
FIG. 1. (Left panel) Calculated and experimental PES of the gas-phase water for 180 eV photon energy. (Right panel) Experimental (2M FeCl$_2$ aqueous solution) and calculated (for the [Fe(H$_2$O)$_6$]$^{2+}$ cluster) core PES for 925 eV photon energy.

a)Electronic mail: sergey.bokarev@uni-rostock.de

145, 089901-1

Thus, the SA provides a good approximation to the full calculation of L-edge core PES of $[Fe(H_2O)_6]^{2+}$ where the kinetic energy of the outgoing electron is quite high and all transitions have the same character, i.e., being ionizations from the 2p orbitals.

Although the results obtained within the SA for the L-edge PES of $[Fe(H_2O)_6]^{2+}$ are quite accurate, the SA should be used with caution. If the spectrum contains transitions involving DOs of different character, e.g., localized on metal and ligands, or the kinetic energy of the outgoing electron is low, the applicability of the SA should be investigated on a case to case basis. We would like to stress that the protocol proposed in Ref. 1 that utilizes the numerical integration for the matrix elements allows us to obtain reliable intensities also in cases, where the widely used SA cannot be applied.

[1]G. Grell, S. I. Bokarev, B. Winter, R. Seidel, E. F. Aziz, S. G. Aziz, and O. Kühn, J. Chem. Phys. **143**, 074104 (2015).
[2]R. Manne and T. Åberg, Chem. Phys. Lett. **7**, 282 (1970).
[3]B. T. Pickup, Chem. Phys. **19**, 193 (1977).
[4]T. Åberg, Phys. Rev. **156**, 35 (1967).

[GG2]   Ultrafast Spin Crossover in [Fe^{II}(bpy)$_3$]$^{2+}$: Revealing Two Competing Mechanisms by Extreme Ultraviolet Photoemission Spectroscopy

Alexandre Moguilevski, Martin Wilke, Gilbert Grell, Sergey I. Bokarev, Saadullah G. Aziz, Nicholas Engel, Azhr A. Raheem, Oliver Kühn, Igor Yu. Kiyan, and Emad F. Aziz

Ultrafast Spin Crossover in [Fe^II(bpy)$_3$]$^{2+}$: Revealing Two Competing Mechanisms by Extreme Ultraviolet Photoemission Spectroscopy

Alexandre Moguilevski,[a] Martin Wilke,[a] Gilbert Grell,[b] Sergey I. Bokarev,*[b] Saadullah G. Aziz,[c] Nicholas Engel,[a] Azhr A. Raheem,[a] Oliver Kühn,[b] Igor Yu. Kiyan,*[a] and Emad F. Aziz*[a, d, e]

Photoinduced spin-flip in Fe^{II} complexes is an ultrafast phenomenon that has the potential to become an alternative to conventional processing and magnetic storage of information. Following the initial excitation by visible light into the singlet metal-to-ligand charge-transfer state, the electronic transition to the high-spin quintet state may undergo different pathways. Here we apply ultrafast XUV (extreme ultraviolet) photoemission spectroscopy to track the low-to-high spin dynamics in the aqueous iron tris-bipyridine complex, [Fe(bpy)$_3$]$^{2+}$, by monitoring the transient electron density distribution among excited states with femtosecond time resolution. Aided by first-principles calculations, this approach enables us to reveal unambiguously both the sequential and direct de-excitation pathways from singlet to quintet state, with a branching ratio of 4.5:1.

Light-induced spin crossover (SCO) in transition-metal complexes[1,2] is an effect, which is of fundamental interest in biology[3,4] and finds applications in magnetic data storage and molecular devices.[5–7] However, tracking the non-adiabatic dynamics following photoexcitation, required for mechanistic understanding of this process, poses high requirements for the experimental methods due to the large number of involved excited states and possible relaxation channels as well as the ultrashort time scale. This challenge might lead to ambiguous interpretations on the basis of absorption and fluorescence spectroscopies. A prominent example is the singlet-to-quintet transition in the iron tris-bipyridine complex, [Fe(bpy)$_3$]$^{2+}$. Photoexcitation of [Fe(bpy)$_3$]$^{2+}$ at 400–580 nm leads to the resonant population of a singlet metal-to-ligand charge-transfer state, ^{1}MLCT,[8,9,14–16] with a lifetime below 100 fs.[17,18] The pathway from the ^{1}MLCT to the metastable quintet state (Q$_1$) can be sequential, involving intermediate triplet states T$_n$ (^{1,3}MLCT→T$_n$→Q$_1$, Model I), or direct (^{1,3}MLCT→Q$_1$, Model II). Since the latter transition involves the spin-flip of two electrons, the direct pathway was argued to be unlikely by both theory[17] and experiment.[9] However, Auböck and Chergui have recently proposed the direct mechanism involving non-totally-symmetric vibrational modes,[8] opening the discussion again. Here, we demonstrate that by making use of high-order harmonic generation (HHG),[13] ultrafast XUV photoemission spectroscopy (PES)[10,11] (Figure 1a) aided by first principles calculations[12] is capable to track the sub-100 fs population dynamics of the excited electronic states. Mapping the transient states to the continuum on the absolute energy scale (Figure 1b), we show that both pathways I and II are possible and reveal their contributions to the low-to-high spin transition.

The PES study is performed on a 50 mM aqueous solution of [Fe(bpy)$_3$]Cl$_2$ by using a time-of-flight electron spectrometer and a liquid micro-jet technique. We employ a femtosecond Ti:sapphire laser system to generate pump pulses of 530 nm wavelength (2.34 eV photon energy) and probe pulses of 32.55 eV photon energy with the use of our HHG setup.[19] Since the pump and probe pulses are intrinsically synchronized, a high temporal resolution of ≈60 fs was achieved, which is superior to the resolution of free electron laser facilities.[9,16] For experimental details, see the Supporting Information (SI).

Figure 1c shows a spectrum obtained when applying the XUV probe beam only. The spectral peaks arising from ionization of liquid and gaseous water, [Fe(bpy)$_3$]$^{2+}$, and the chloride counter ion are designated in the figure. For convenience, the origin of energy scale is assigned below to the emission peak of the iron-localized Fe 3d(t$_{2g}$) orbitals instead of the vacuum level.

[a] A. Moguilevski, M. Wilke, N. Engel, A. A. Raheem, Dr. I. Yu. Kiyan, Prof. E. F. Aziz
Joint Laboratory for Ultrafast Dynamics in Solutions and at Interfaces (JULiq)
Institute of Methods for Material Development
Helmholtz-Zentrum Berlin
Albert-Einstein-Str. 15, 12489 Berlin (Germany)
E-mail: igor.kiyan@helmholtz-berlin.de
emad.aziz@helmholtz-berlin.de

[b] G. Grell, Dr. S. I. Bokarev, Prof. O. Kühn
Institute of Physics, University of Rostock
Albert-Einstein-Str. 23–24
18059 Rostock (Germany)
E-mail: sergey.bokarev@uni-rostock.de

[c] Prof. S. G. Aziz
Chemistry Department, Faculty of Science
King Abdulaziz University
21589 Jeddah (Saudi Arabia)

[d] Prof. E. F. Aziz
Department of Physics, Freie Universität Berlin
Arnimallee 14, 14195 Berlin (Germany)

[e] Prof. E. F. Aziz
School of Chemistry, Monash University
Clayton 3800, VIC (Australia)
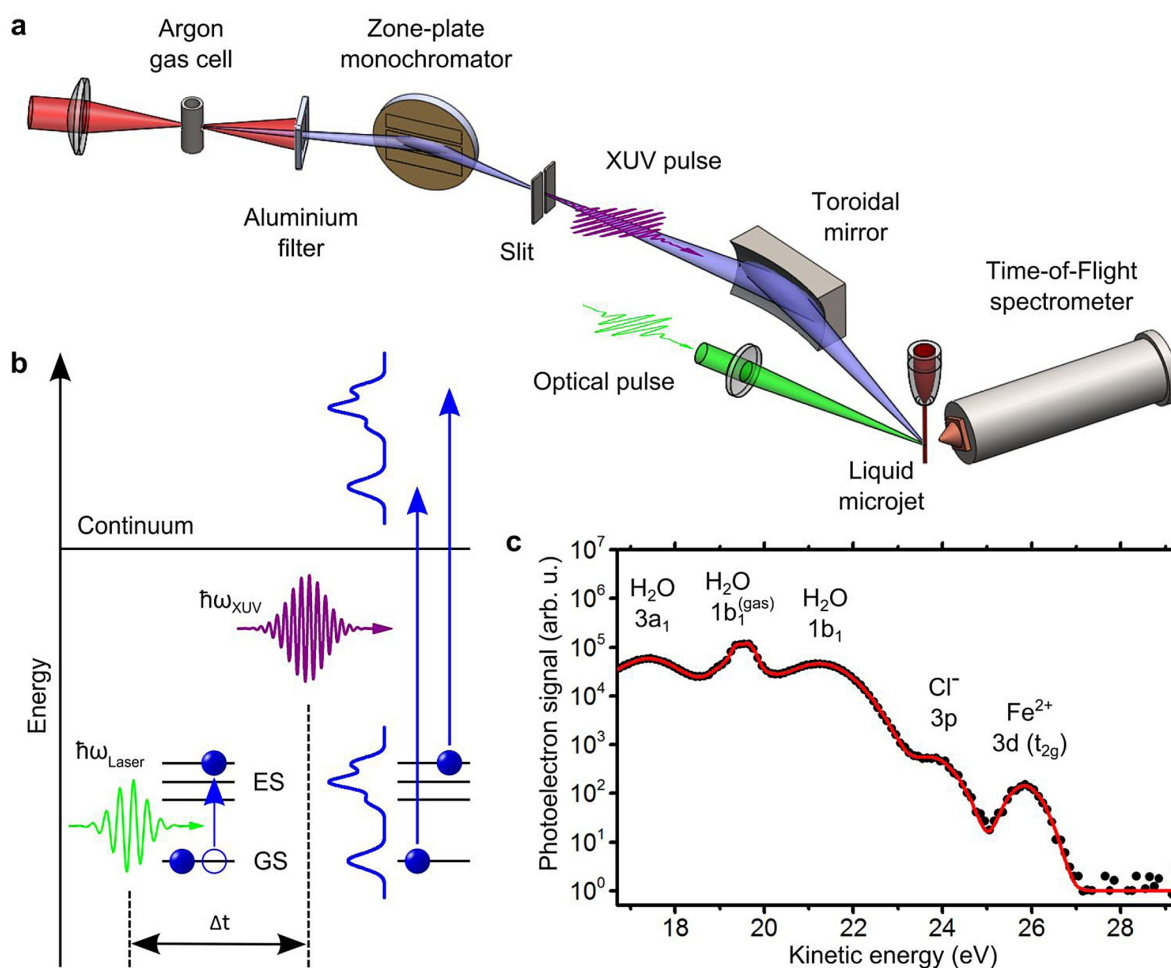
Figure 1. Overview of the transient PES experiment: a) Experimental setup including generation of the optical pump and XUV probe beams, time-of-flight electron spectrometer, and liquid micro-jet. b) Principle of transient PES: the pump pulse excites the system from the initial ground state (GS) to an excited state (ES); applied at a variable time delay Δt, the XUV probe pulse maps the spectrum of bound states (blue curve) to the kinetic energy spectrum of photoelectrons. c) PES obtained by the probe XUV beam. Spectral peaks are attributed to ionization from the iron-center-localized Fe $3d(t_{2g})$ orbitals, Cl$^-$ 3p, and the $1b_1$ and $3a_1$ water orbitals. The red curve represents a fit to a superposition of the corresponding Gaussian profiles.

A series of pump–probe XUV spectra was recorded at different time delays in the range between −150 and 750 fs (SI, Figure S1). The transient signal (TS) was derived by subtracting a negative-delay spectrum as a background from pump–probe spectra. The 2D plot in Figure 2 a shows the TS dependency on the electron energy and the time delay. The negative TS value at 0 eV is due to the depletion of the ground state by the pump beam. The analysis of the experimental results was carried out by making a global fit to different models and the fit results were compared with predictions by theory based on multi-configurational first-principles RASSCF/RASSI electronic structure calculations combined with the Dyson orbital formalism.[12] The theory was applied to describe PES originating from the ground singlet state, S_0, and a number of triplet and quintet states, whereas the doublet, quartet, and sextet states of [Fe(bpy)$_3$]$^{3+}$ were considered as final states of XUV ionization. Changes in the electronic structure caused by intersystem crossings and internal conversion as well as geometrical relaxation and vibrational cooling lead to different signatures in the photoelectron spectra, building a basis to reveal the individual contributions from the transient states.

The possibility of both the sequential and direct transition to the quintet state (models I and II discussed above) was considered in the data analysis. By applying a statistical F-test (see SI), we have found that an additional short-lived transient state needs to be considered in the SCO mechanism, as compared to the sequential[9] (I) and direct[8] (II) mechanisms. Different extended models were considered, where this state was involved in a parallel relaxation channel or contributed as an additional step in the cascade decay. For both extended models, the global fit yielded rather similar results for the decay time constants of the three short-lived states (SI, Table S1). The values 16±13, 35±10, and 70±20 fs were obtained for the model with parallel relaxation, which is presented in detail below.
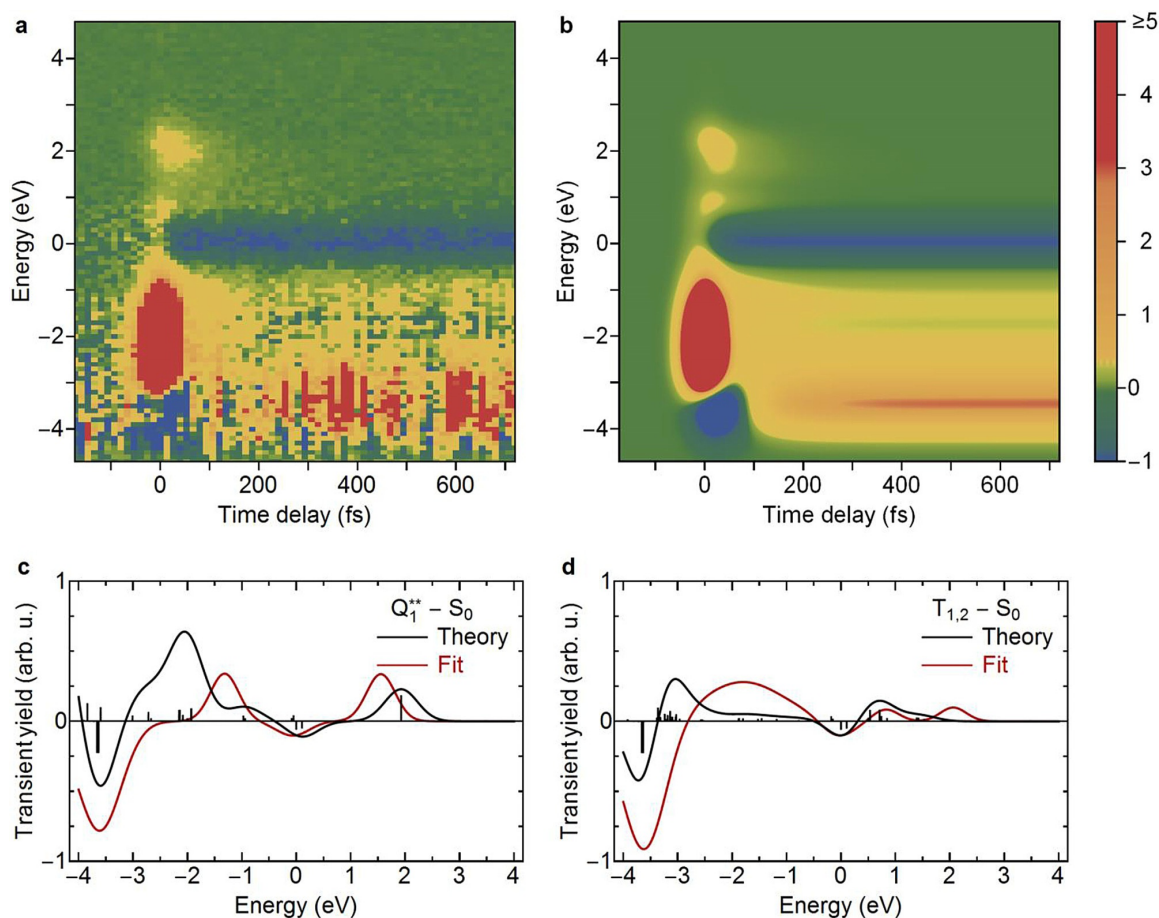
Figure 2. Transient photoemission signal: a) Measured TS as a function of the electron energy and the time delay. b) The result of a global fit that assumes parallel transition from the ^{1,3}MLCT to the Q_1^{**} and $T_{1,2}$ states. c,d) Comparison of the PES of the Q_1^{**} and $T_{1,2}$ states obtained from the global fit with the spectra predicted by theory (a 0.7 eV Gaussian broadening is applied).

One should note that the measurement of time constants considerably shorter than the laser pulse duration is possible if the precise time zero is known.[20] In this study, the time zero is inferred from the position of the cross-correlation signal which dominates in the TS between −3 and −1 eV (SI, Figure S4). Since the photo-emission yield from different transient states is maximal at different electron energies, the global fit of the energy-resolved TS enables determination of time constants shorter than the laser pulse duration. A contribution from the long-lived quintet state is also apparent in the TS at energies between −4 and −2.5 eV. Its life time of 650 ± 50 ps was inferred from an additional measurement in the nanosecond range (SI, Figure S2). The signal attributed to ionization from the quintet state exhibits oscillations, which one can distinguish despite a low signal-to-noise ratio (SI, Figure S3). As discussed in detail in the SI, these oscillations are due to two modes with periods of 265 ± 11 and 125 ± 4 fs. They appear immediately after the pump and are analogous to the oscillations reported previously,[8,15] where they had been assigned to impulsively excited vibrational spectator modes. However, a detailed dis-

cussion of the wave packet dynamics lies beyond our consideration.

The final choice of the extended model was made with the aid of theoretical calculations (see SI), since it cannot be done based solely on the F-test results. In the kinetic model, which is in agreement with theory, both the sequential (I) and direct (II) transitions from the MLCT to the quintet state are considered to occur simultaneously. This model can be depicted as [Eq. (1)]:

$$
S_0 \xrightarrow{\hbar\omega} {}^{1,3}\mathrm{MLCT}
\begin{array}{l}
\xrightarrow{\mathrm{I}} T_{1,2} \longrightarrow Q_1^* \\
\xrightarrow{\mathrm{II}} Q_1^{**} \longrightarrow Q_1^*
\end{array}
$$
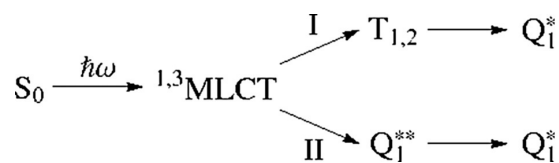
To simplify the consideration of the species with symmetry different from the octahedral one, we label the states according to their multiplicity and cardinal number. Two lowest triplet

states, T_1 and T_2, and the vertically populated vibrationally hot Q_1^{**} and adiabatically cooled but not yet equilibrated Q_1^* quintet states were found to be relevant to the present study. The transition from the singlet to the triplet MLCT state is fast (≈ 20 fs)[18] and their bands overlap on the energy scale. We do not resolve the individual contributions of these states in the TS and, therefore, they are treated together as one state, ^{1,3}MLCT, in the global fit. Further, as the internal conversion of T_2 to T_1 is expected to be ultrafast[17] these states are also treated as a single state.

The TS decomposition at a few chosen excitation energies is shown in the SI (Figure S4). The transient signal with the shortest lifetime of 16 ± 13 fs lies at ≈ 2.3 eV. This energy matches the applied photon energy and, thus, this band is assigned to the initially populated MLCT state. The assignment of the two other short-lived transient states was made on the basis of first principles calculations. These reveal that the PES from the transient state with 35 ± 10 fs lifetime is due to the vertically populated quintet state Q_1^{**} whereas the transient of 70 ± 20 fs lifetime originates from ionization of the triplet states T_1 and T_2.

The global fit results obtained with the use of the model described above are shown in Figure 2b, demonstrating a very good agreement with the experimental data. The emission spectra of the $T_{1,2}$ and Q_1^{**} states inferred from the fit are compared in Figure 2c and d with the corresponding spectra predicted by the theory (the S_0 emission spectrum was subtracted for consistency with the TS plot). One can see that the theory qualitatively reproduces the spectral band structure originating from a superposition of ionization channels leading to the formation of $[Fe(bpy)_3]^{3+}$ with different electronic configurations and multiplicities. One should note that the theoretical method can contain possible systematic errors, for example, due to the incomplete account for dynamic correlations, which can result in energy shifts of the photoelectron features of the order of 0.5 eV.[21,22] Thus, results presented in Figure 2c and d demonstrate a reasonable compromise between the fit stability and the accuracy of the reference theoretical data.

The branching ratio between channels I and II was found to be $4.5^{+4.8}_{-1.5}$ (see SI), indicating that the population of intermediate triplet states dominates the relaxation dynamics. However, our results also evidence the possibility of the direct transition from the excited ^{1,3}MLCT states to the quintet state with a time constant smaller than previously reported values,[9,14] thus, partially supporting the conclusion by Auböck and Chergui.[8] Note that the depletion of the ground state gives rise to negative TS also at energies between -4.2 and -3.2 eV. This feature disappears within < 100 fs due to the formation of the Q_1^* state contributing to the spectrum in the same energy interval. This provides additional evidence that the SCO transition occurs on a sub-100 fs time scale. It is worth to revise the issue of the unity quantum yield of the low-to-high spin transition, which was discussed in Ref. [8]. Taking into account the branching ratio of 4.5:1 between channels I and II and using the predicted value of 1:13 for the branching ratio between the deactivation $T_{1,2} \rightarrow S_0$ and the SCO $T_{1,2} \rightarrow Q_1^*$ channels (see Table 7 in Ref. [17]), we find that the quantum yield is approximately 94%. This value is, indeed, close to unity, and it is

a challenging task to detect the repopulation of 6% of the ground state in the experiment.

Summarizing, the present study demonstrates that the sensitivity of previously applied spectroscopies, such as transient absorption and X-ray fluorescence spectroscopy, allowed revealing of only one of the possible SCO channels, whereas the ultrafast PES applied here provides insight into the entire electron dynamics and is capable to detect both the direct and the cascade low-to-high spin transitions. The present tabletop methodology is a robust and convenient tool for detailed characterization of the ultrafast electron dynamics what suggests wide applications in photochemistry, photophysics, and photobiology.

[1] A. Hauser, *Coord. Chem. Rev.* **1991**, *111*, 275–290.
[2] P. Gütlich, Y. Garcia, H. A. Goodwin, *Chem. Soc. Rev.* **2000**, *29*, 419–427.
[3] J. N. Harvey, *Faraday Discuss.* **2004**, *127*, 165–177.
[4] R. Weiss, A. Gold, J. Terner, *Chem. Rev.* **2006**, *106*, 2550–2579.
[5] O. Kahn, C. J. Martinez, *Science* **1998**, *279*, 44–48.
[6] A. Bousseksou, G. Molnár, L. Salmon, W. Nicolazzi, *Chem. Soc. Rev.* **2011**, *40*, 3313–3335.
[7] M. A. Halcrow, *Spin-Crossover Materials: Properties and Applications*, Wiley, **2013**.
[8] G. Auböck, M. Chergui, *Nat. Chem.* **2015**, *7*, 629–633.
[9] W. Zhang, R. Alonso-Mori, U. Bergmann, C. Bressler, M. Chollet, A. Galler, W. Gawelda, R. G. Hadt, R. W. Hartsock, T. Kroll, K. S. Kjær, K. Kubiček, H. T. Lemke, H. W. Liang, D. A. Meyer, M. M. Nielsen, C. Purser, J. S. Robinson, E. I. Solomon, Z. Sun, D. Sokaras, T. B. van Driel, G. Vankó, T.-C. Weng, D. Zhu, K. J. Gaffney, *Nature* **2014**, *509*, 345–348.
[10] M. Faubel, K. R. Siefermann, Y. Liu, B. Abel, *Acc. Chem. Res.* **2012**, *45*, 120–130.
[11] R. Al-Obaidi, M. Wilke, M. Borgwardt, J. Metje, A. Moguilevski, N. Engel, D. Tolksdorf, A. Raheem, T. Kampen, S. Mähl, I. Yu, Kiyan, E. F. Aziz, *New J. Phys.* **2015**, *17*, 093016.
[12] G. Grell, S. I. Bokarev, B. Winter, R. Seidel, E. F. Aziz, S. G. Aziz, O. Kühn, *J. Chem. Phys.* **2015**, *143*, 074104.
[13] F. Krausz, M. Ivanov, *Rev. Mod. Phys.* **2009**, *81*, 163–234.
[14] C. Bressler, C. Milne, V.-T. Pham, A. ElNahhas, R. M. van der Veen, W. Gawelda, S. Johnson, P. Beaud, D. Grolimund, M. Kaiser, C. N. Borca, G. Ingold, R. Abela, M. Chergui, *Science* **2009**, *323*, 489–492.
[15] A. Cannizzo, C. J. Milne, C. Consani, W. Gawelda, C. Bressler, F. van Mourik, M. Chergui, *Coord. Chem. Rev.* **2010**, *254*, 2677–2686.
[16] H. T. Lemke, C. Bressler, L. X. Chen, D. M. Fritz, K. J. Gaffney, A. Galler, W. Gawelda, K. Haldrup, R. W. Hartsock, H. Ihee, J. Kim, K. H. Kim, J. H. Lee, M. M. Nielsen, A. B. Stickrath, W. Zhang, D. Zhu, M. Cammarata, *J. Phys. Chem. A* **2013**, *117*, 735–740.
[17] C. Sousa, C. de Graaf, A. Rudavskyi, R. Broer, J. Tatchen, M. Etinski, C. M. Marian, *Chem. Eur. J.* **2013**, *19*, 17541–17551.
[18] W. Gawelda, A. Cannizzo, V.-T. Pham, F. van Mourik, C. Bressler, M. Chergui, *J. Am. Chem. Soc.* **2007**, *129*, 8199–8206.

83

[19] J. Metje, M. Borgwardt, A. Moguilevski, A. Kothe, N. Engel, M. Wilke, R. Al-Obaidi, D. Tolksdorf, A. Firsov, M. Brzhezinskaya, A. Erko, I. Yu, Kiyan, E. F. Aziz, *Opt. Express* **2014**, *22*, 10747.

[20] T. Hertel, E. Knoesel, M. Wolf, G. Ertl, *Phys. Rev. Lett.* **1996**, *76*, 535 – 538.

[21] S. I. Bokarev, O. S. Bokareva, O. Kühn, *J. Chem. Phys.* **2012**, *136*, 214305.

[22] M. Kepenekian, V. Robert, B. Le Guennic, *J. Chem. Phys.* **2009**, *131*, 114702.

84

CHEMPHYSCHEM

Supporting Information

Ultrafast Spin Crossover in [Fe^{II}(bpy)$_3$]$^{2+}$: Revealing Two Competing Mechanisms by Extreme Ultraviolet Photoemission Spectroscopy

Alexandre Moguilevski,[a] Martin Wilke,[a] Gilbert Grell,[b] Sergey I. Bokarev,*[b] Saadullah G. Aziz,[c] Nicholas Engel,[a] Azhr A. Raheem,[a] Oliver Kühn,[b] Igor Yu. Kiyan,*[a] and Emad F. Aziz*[a, d, e]

cphc_201601396_sm_miscellaneous_information.pdf

Ultrafast spin crossover in [Fe$^{\text{II}}$(bpy)$_3$]$^{2+}$: revealing two competing mechanisms by means of XUV photoemission spectroscopy

Alexandre Moguilevski, Martin Wilke, Gilbert Grell, Sergey I. Bokarev,[*]

Saadullah G. Aziz, Nicholas Engel, Azhr A. Raheem, Oliver Kühn,

Igor Yu. Kiyan,[*] and Emad F. Aziz[*]

E-mail: sergey.bokarev@uni-rostock.de; igor.kiyan@helmholtz-berlin.de; emad.aziz@helmholtz-berlin.de

SUPPORTING INFORMATION

1

Experimental procedure.

The XUV photoemission spectroscopy (PES) measurements were performed on a 50 mM aqueous solution of $[Fe(bpy)_3]^{2+}$ with the use of pump-probe technique. The XUV pulses were produced with the use of our high-order harmonic generation (HHG) setup.[1] The Ti:sapphire laser system (Coherent) delivers linearly polarized pulses of 800 nm central wavelength, 5 kHz repetition rate, 2.4 mJ pulse energy, and 25 fs duration. The laser output was split into two beams so that a pulse energy of 1.4 mJ was available to pump the HHG process and a pulse energy of 1 mJ was applied to pump an optical parametric amplifier (OPA). The pump power for HHG could be tuned by using a half-wave plate in combination with a thin-film polarizer. In the experiment, the HHG pump energy was set to 1 mJ per pulse. The HHG process was induced in a cell filled with Argon gas of ~ 25 mbar pressure. The residual pump laser beam was filtered out from the XUV beam with the use of a 150 nm thin aluminum foil. The 21st harmonic of 32.55 eV photon energy was spectrally selected for the experiment by using a zone-plate monochromator.

The pump pulses of 530 nm wavelength were generated in a commercial OPA (Coherent/Light Conversion). Because of the use of dispersive optics in both 800 nm beam paths, a negative group velocity dispersion (GVD) was applied in the pulse compressor of the laser system.[2] The difference in the GVD between the HHG and OPA beam lines was compensated by using of a pair of BK7 wedges in the former line. The chirp of the 800 nm pump pulses was optimized to achieve the shortest 530 nm pulse, which was controlled by an autocorrelator, and to maximize the HHG output monitored by a photodiode behind the zone-plate monochromator. The polarization of both OPA pump and XUV probe beams was kept parallel to the electron spectrometer axis. The focus spot size of 155 and 75 μm of the optical and XUV beams, respectively, was measured by scanning a razor blade across the beam and recording the light intensity behind the blade with a photodiode. The pump beam was attenuated by using a thin neutral density filter to obtain an energy flux of ~ 88 W/cm^2 in the interaction region. A motorized optical delay stage was used in the pump beam path to vary the time delay between the pump and the probe pulses.

The liquid microjet technique was applied to facilitate achieving the high-vacuum conditions in the experimental chamber. A syringe pump was used to deliver the liquid sample to the interaction region through a quartz nozzle of 18 μm orifice with a constant flow rate of 0.4 ml/min. With this setup, a microjet of cylindrical shape was created with a laminar flow of a few millimeters length. The optical pump and the XUV probe beams intersected each other on the microjet surface in the region of the laminar flow in front of the skimmer of the

2

time-of-flight (TOF) electron spectrometer. The microjet was oriented perpendicular to the XUV beam and to the TOF spectrometer axis. The pump and probe beams were merged in the interaction region at a small angle of $\sim 1°$. This was achieved by reflecting the optical beam with the use of an aluminum mirror positioned in vacuum close to the path of the XUV beam.[3] The spectrometer was equipped with a conical skimmer of 400 μm aperture. A small distance of approximately 0.5 mm between the microjet and the skimmer was applied to reduce scattering of photoelectrons by the residual gas molecules. The sample solution, which was introduced into the interaction chamber during the experiment, was collected in a cryogenic trap filled with liquid nitrogen. This experimental procedure enabled to maintain the residual gas pressure in the interaction region below 2×10^{-5} mbar.

The temporal overlap between the pump and probe pulses and the experimental time resolution were determined from the cross-correlation measurements carried out on the liquid jet during the experiment. The cross-correlation signal arises from laser-assisted XUV ionization and was previously reported in the studies on gas[4] and solid-state[5] samples. This effect leads to the appearance of sidebands in the XUV photoelectron spectrum, shifted on the kinetic energy scale by the optical photon energy. The photoemission yield integrated over the region of the sidebands and recorded as a function of the time delay characterizes cross-correlation between the optical and XUV pulses. The integration range was chosen between the kinetic energies of 23 and 24 eV, where the first laser-assisted sideband of XUV ionization of water is most pronounced in the spectrum. The cross-correlation signal recorded in each time-resolved measurement was used to account in the data processing for the drift of the zero time delay. The cross-correlation width was varying between 51 and 60 fs during the experiment (see Figure S5 for illustration). Maximization of the cross-correlation signal was implemented for fine adjustment of the spatial overlap between the laser and XUV beams on the microjet.

A commercial TOF spectrometer provided by SPECS[6] was used for the data acquisition. In the steady-state measurements, the spectrometer was operated in the drift mode, corresponding to the classical field-free design with an electron acceptance angle of $\pm 1°$. In this mode the kinetic energy scale is not limited, which allows to record spectra in a wide kinetic energy range involving XUV ionization contributions from both $[Fe(bpy)_3]^{2+}$ and water. For time-resolved measurements, the wide-angle mode was applied. In this mode the spectrometer employs a predefined non-uniform electrostatic field, which allows increasing of the electron acceptance angle to $\pm 15°$ in a given limited spectral range. The larger acceptance angle enables reducing the acquisition time while achieving a high signal-to-noise ratio.

3

This is a crucial issue for the experiments with liquid samples, where the data acquisition needs to be fast because of instabilities in the experimental conditions. In the time-resolved measurements, XUV spectra were recorded in a spectral range of 9 eV width, centered at the energy peak originating from ionization of the iron-center-localized Fe $3d(t_{2g})$ orbital of $[Fe(bpy)_3]^{2+}$. The data acquisition was broken in a sequence of time-delay scans in the range between -100 and 700 fs. Each scan was carried out within 15 minutes with a delay increment of 13.3 fs.

The spectral characteristics of the XUV beam were inferred from steady-state photoelectron spectra of Argon. The central XUV photon energy and the bandwidth were obtained from a fit of the Argon spectra to a sum of two Gaussian profiles, associated with the formation of two spin-orbit states of the residual Ar^+ ion. The bandwidth of ~ 250 meV was obtained from the measurement when operating the spectrometer in the drift mode. The measurement on Ar also showed that the neighboring harmonics were discriminated in the monochromator below 0.07%.

Data processing.

The individual time-delay scans were added together prior the data analysis. While combining the series, the data sets were corrected for the energy shift and the drift of the zero time delay. The energy shift was caused by the space-charge effect induced by the pump beam in the liquid sample. This shift was shown to be dependent on the time delay between the pump and probe pulses.[3] Therefore, each spectrum of a given series needed to be corrected separately. The ionization signal from the Fe $3d(t_{2g})$ orbital, giving rise to a well distinguished energy peak in each XUV spectrum, was used as a reference since less than 20% of the $[Fe(bpy)_3]^{2+}$ molecules were excited by the pump beam. A Gaussian fit was used to determine the central energy of this peak and the origin of the kinetic energy scale was assigned to the fit value. The drift of the zero time delay was caused by changes in the environmental conditions in the lab and could reach a value of ~ 160 fs during the day. This drift was corrected according to the center position of the cross-correlation signal in each time-delay scan. The spectra recorded at negative time delays below -80 fs were combined together and used as a background which was subtracted from the pump-probe spectra of a given time-delay scan. This subtraction yielded the transient signal (TS) which was analyzed in terms of kinetic models.

4

Kinetic models.

A global fit of different kinetic models was carried out to analyze the experimental data. By applying a statistical F-test, we have found that an additional short-lived transient sate needs to be considered in the SCO mechanism, as compared to the sequential[7] (I) and direct[8] (II) mechanisms discussed in literature. Both model I and II, involving population of one intermediate state in the de-excitation pathway from the ^{1,3}MLCT states to the relaxed quintet state Q_1^*, can be expressed as:

$$S_0 \xrightarrow{P(t)} {}^{1,3}\text{MLCT} \xrightarrow{k_1} X \xrightarrow{k_2} Q_1^* \, , \tag{1}$$
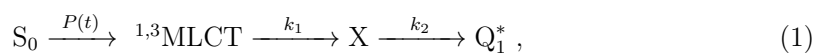
where $P(t)$ denotes the photoexitation rate of the ^{1,3}MLCT states from the ground S_0 state, X represents the triplet state T_2 in model I and the vibrationally hot quintet state Q_1^{**} in model II, respectively, and k_i are the corresponding transition rates. Equation (1) describes a 'nested' model for the two extended models considered below. In one of those, we consider that the ^{1,3}MLCT state relaxes to the quintet state via a cascade population of two triplet intermediate states, as described in Ref.[9]:

$$S_0 \xrightarrow{P(t)} {}^{1,3}\text{MLCT} \xrightarrow{k_1} T_1 \xrightarrow{k_2} T_2 \xrightarrow{k_3} Q_1^* \, . \tag{2}$$
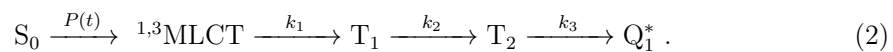
Another model assumes two relaxation channels occurring simultaneously:

$$S_0 \xrightarrow{P(t)} {}^{1,3}\text{MLCT} \begin{array}{c} \xrightarrow{k_1} T_{1,2} \xrightarrow{k_3} Q_1^* \\ \xrightarrow{k_2} Q_1^{**} \xrightarrow{k_4} Q_1^* \end{array} \tag{3}$$
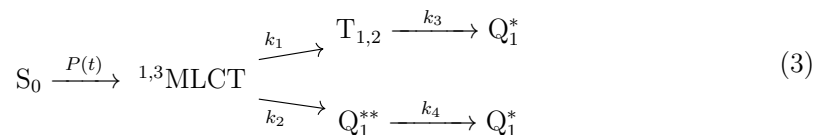
where the two triplet states are treated as a single $T_{1,2}$ state because of their ultrafast internal conversion.[9]

The global fit routine (see details in a separate section) was applied to fit the TS signal at 96×68 data points on the energy and time scale, respectively. To compare the extended and the 'nested' models, the F statistic is calculated, given by

$$F = \frac{(\chi_n^2 - \chi_e^2)(n - p_e)}{\chi_e^2(p_e - p_n)} \, , \tag{4}$$

where χ_e^2 and χ_n^2 are the χ^2 values of the extended and 'nested' model, respectively, p_e and p_n are the corresponding numbers of fit parameters, and n is the number of data points. The

5

extended model yields always a better (or at least equal quality) fit. The smaller χ_e^2 value is statistically significant if the F statistic exceeds a critical value defined by the F-distribution function. When the criterion $F_c < F$, $F_c = F(p_e - p_n, n - p_e)$ is satisfied, the simpler 'nested' model can be rejected with greater than 95% confidence. This criterion is well satisfied when comparing both the cascade (equation (2)) and the parallel (equation (3)) model with the 'nested' model. The corresponding inequalities are $2.6 < 89.1$ and $3.0 < 133.6$, pointing to the significance of the additional transient state in both extended models. This is illustrated in Figure S6 which shows the residuals for the best fit by different models. The domain where the 'nested' model is deficient in reproducing the experimental data is marked in panel (a) by white rectangles. The decay time constants (inverse values of the transition rates) obtained for different kinetic models are summarized in Table S1.

Based merely on the F-test results, we cannot judge which extended model is the proper one. Both model I and II yield approximately the same χ^2 value of 2846.5 and 2846.6, respectively, which is smaller than the value of 2965.6 of the 'nested' model. The choice of the model is, therefore, made with the aid of theory. The comparison of predictions with the fit results of the parallel and cascade models are shown in Figure 3(c,d) (see the main article) and in Figure S7, respectively. Whereas the theory reproduces well the emission band structure of the $T_{1,2}$ and Q_1^{**} states populated in the parallel relaxation process, only the T_2 emission spectrum can be reproduced in the cascade model. For the T_1 state, the fit results disagree with the predictions in the energy range below the Fe $3d(t_{2g})$ peak. Therefore, we reject the cascade relaxation mechanism.

Global fit routine.

The global fit routine is presented below for the case of parallel relaxation mechanism (equation (3)). Its modification for fitting the 'nested' (equation (1)) and cascade (equation (2)) model is straightforward. The following system of differential equations describes the population dynamics of the initially $(t \to -\infty)$ unpopulated ^{1,3}MLCT, $T_{1,2}$, Q_1^{**}, and Q_1^{*} states:

$$
\begin{aligned}
\frac{d\left[^{1,3}\text{MLCT}\right]}{dt} &= P(t) - (k_1 + k_2)\left[^{1,3}\text{MLCT}\right] \\
\frac{d\left[T_{1,2}\right]}{dt} &= k_1\left[^{1,3}\text{MLCT}\right] - k_3\left[T_{1,2}\right] \\
\frac{d\left[Q_1^{**}\right]}{dt} &= k_2\left[^{1,3}\text{MLCT}\right] - k_4\left[Q_1^{**}\right] \\
\frac{d\left[Q_1^{*}\right]}{dt} &= k_3\left[T_{1,2}\right] + k_4\left[Q_1^{**}\right] - k_r\left[Q_1^{*}\right]
\end{aligned}
\tag{5}
$$

6

where k_r denotes the relaxation rate of the metastable quintet state Q_1^* to the ground S_0 state. The value of k_r is rather small, so that the Q_1^* relaxation is negligible on the subpicosecond time scale considered here. Taking into account that the excitation rate of the ^{1,3}MLCT states is proportional to the pump intensity and assuming a Gaussian temporal envelope of the pump pulse, we have

$$P(t) = B \exp \left(-\frac{t^2}{\tau_{\text{pump}}^2} - \frac{\sqrt{\pi}}{2} B\tau_{\text{pump}} \left(1 + \text{erf} \left(\frac{t}{\tau_{\text{pump}}} \right) \right) \right) , \qquad (6)$$

where the second term of the exponential function argument describes the depletion of the initial ground state by the pump pulse, τ_{pump} is the pulse width, $\text{erf}(x)$ is the error function of argument x, B is a constant defined by a product of the photoexcitation cross section and the pump laser intensity, and the initial population of the ground state is normalized to unity. The system of differential equations (5) was solved numerically.

The fit function describing the dependency of the transient signal on the time delay t and the photoelectron kinetic energy E_{kin} has the form

$$T(E_{\text{kin}}, t) = \sum_{\text{J}} T_{\text{J}}(E_{\text{kin}}) [\text{J}]^*(t) - T_{S_0}(E_{\text{kin}}) (1 - [S_0]^*(t)) + T_{\text{c}}(E_{\text{kin}}, t) , \qquad (7)$$

where $T_{\text{J}}(E_{\text{kin}})$ represents the emission spectrum from the transient state J (J $=^{1,3}$MLCT, $T_{1,2}$, Q_1^{**}, Q_1^*), $T_{S_0}(E_{\text{kin}})$ is the emission spectrum from the ground state S_0, $[\text{J}]^*(t)$ is the transient population of state J convolved with the Gaussian temporal envelope of the XUV probe pulse:

$$[\text{J}]^*(t) = \frac{1}{\sqrt{\pi}\tau_{\text{probe}}} \int_{-\infty}^{+\infty} \exp \left(-\frac{(t-t')^2}{\tau_{\text{probe}}^2} \right) [\text{J}](t')dt', \qquad (8)$$

τ_{probe} is the probe pulse width, $[S_0]^*(t)$ is the time-dependent (due to the depletion) population of the ground state convolved with the temporal envelope of the probe pulse:

$$[S_0]^*(t) = \frac{1}{\sqrt{\pi}\tau_{\text{probe}}} \int_{-\infty}^{+\infty} \exp \left(-\frac{(t-t')^2}{\tau_{\text{probe}}^2} - \frac{\sqrt{\pi}}{2} B\tau_{\text{pump}} \left(1 + \text{erf} \left(\frac{t'}{\tau_{\text{pump}}} \right) \right) \right) dt , \qquad (9)$$

and $T_{\text{c}}(E_{\text{kin}}, t)$ is the cross-correlation yield:

$$T_{\text{c}}(E_{\text{kin}}, t) = T_{\text{c}}(E_{\text{kin}}) \exp(-t^2/(\tau_{\text{pump}}^2 + \tau_{\text{probe}}^2)) . \qquad (10)$$

7

The fit algorithm employs the matrix formalism introduced in Ref.[11], which improves significantly the computational efficiency. Following this approach, the TS is represented at the number of $N \times M$ data points on the energy and time scale by the matrix product:

$$T = A \, D^T \, , \tag{11}$$

where the matrix $A(N, s)$ describes the emission spectra of s transient states at the set of N data points on the energy scale whereas the matrix $D(M, s)$ describes the population of these states at the set of M data points on the time scale. The cross correlation signal (equation (10)) is treated as a transient state as well. Thus, in the model of parallel relaxation the number of states is $s = 6$ (4 transient states, the ground state, and the cross correlation). For a given set of rate constants k_i and the constant B, representing the fit parameters, the matrix D is defined via the solution of differential equations (5) and from equations (8), (9), and (10). The fit algorithm can be deduced to minimize the χ^2 value defined by[11]

$$\chi^2 = \|T_{\mathrm{exp}} - T_{\mathrm{exp}} D^T (DD^T)^{-1} D\|^2 \, , \tag{12}$$

where T_{exp} represents the 2D array of the experimental TS. Thus, this fit procedure finds the best values of fit parameters which describe the kinetics, whereas the spectral amplitudes can be found by applying the projection of T_{exp} on D. This approach was rather efficient in conducting the F-test.

To refine the band structure of photoemission spectra, another fit routine was applied where $T_{\mathrm{J}}(E_{\mathrm{kin}})$ were represented by superpositions of Gaussian profiles and the Gaussian amplitudes, positions, and widths were also treated as fit parameters. The lifetimes of the ^{1,3}MLCT, $T_{1,2}$, and Q_1^{**} states were calculated as $(k_1 + k_2)^{-1}$, k_3^{-1}, and k_4^{-1}, yielding the values of 16 ± 13, 70 ± 20, and 35 ± 10 fs, respectively (see also Table S1). The branching ratio of $4.5^{+4.8}_{-1.5}$ between the relaxation channels of the ^{1,3}MLCT state to the $T_{1,2}$ and Q_1^{**} states, respectively, was inferred from the ratio of k_1 to k_2. The asymmetric error bar was inferred from the dependency of χ^2 as a function of k_1/k_2.

Wave packet dynamics in the quintet state.

For a given population of transient state, the periodic nuclear motion leads to modulations in the XUV emission yield due to the periodic changes in the Franck-Condon conditions of the ionization transition. To account for these oscillations in the probe step, the transient

8

population of the quintet state $[Q_1^*](t)$ was convoluted as

$$[Q_1^*]^*(t) = \int_{-\infty}^{+\infty} \exp\left(-\frac{(t-t')^2}{\tau_{\text{probe}}^2}\right)\left(1 + \sum_j a_j\left(1 + \cos(\omega_j(t-t') + \phi_j)\right)\right)[Q_1^*](t')dt', \quad (13)$$

where j is the index of the oscillation mode of frequency ω_j, amplitude a_j, and phase ϕ_j. An F-test was carried out to reveal the significance of adding successively one, two, and three modes in the parallel relaxation model. For the first two modes, the criterion $F_c < F$ was found to be well satisfied: $2.6 < 129.8$ and $2.6 < 50.8$, respectively. However, an opposite inequality $2.6 > 0.3$ was obtained when adding the third mode, indicating that only two modes need to be considered. Figure S8 demonstrates the improvement in reproduction of the experimental data when one and two oscillation modes are taken into account. Their oscillation periods inferred from the global fit are 265 ± 11 and 125 ± 4 fs. Figure S3 shows the appearance of these oscillations in the population dynamics of the quintet state.

Additional measurements.

The depletion of the S_0 ground-state population was measured as a function of the energy flux of the optical pump beam in the range between 15 and 130 W/cm^2. The depletion coefficient was calculated as $D = (I_0 - I)/I_0$, where I_0 and I represent photoelectron yields from the Fe $3d(t_{2g})$ orbital at a negative and a small positive time delays, respectively. This measurement reveals a linear dependency of the excitation yield on the pump beam intensity (see Figure S9). This proves that the ^{1}MLCT state is excited in a one-photon transition.

The relaxation of the electron population to the ground S_0 state was measured by scanning the pump-probe time delay over 1.2 ns with a delay increment of 6.7 ps. The energy flux of 110 W/cm^2 of the optical pump was applied in this measurement. The integrated photoelectron yield from the Fe $3d(t_{2g})$ orbital shows an exponential relaxation into the S_0 state with a time constant of ~ 650 ps (see Figure S2). This result is in a good agreement with the previously reported value.[10]

Computational details.

The photoelectron (PE) spectra have been calculated for the isolated $[\text{Fe}(\text{bpy})_3]^{2+}$ (bpy = 2,2'-bipyridine) complex. The molecular geometries have been optimized for the singlet ground electronic state, S_0, and lowest quintet state, Q_1, with the density functional theory (DFT) employing the range-separated LC-BLYP functional,[12] where the range separation

9

parameter was optimized according to a ΔSCF procedure as described in detail in Ref.[13]. For these two states the optimal values of this parameter were found to be 0.14 bohr^{-1} and 0.15 bohr^{-1}, respectively. All DFT calculations have been performed using the GAUSSIAN 09 package[14] with the cc-pVTZ basis set.[15,16] The optimized geometry for the S_0 state (low-spin d^6 system) is of D_3 point group symmetry, whereas the quintet state equilibrium geometry has the C_2 symmetry due to Jahn-Teller distortion of this high-spin d^6 system.

To interpret the experimental spectra, the ground (S_0), two lowest excited triplet (T_1 and T_2), and quintet (Q_1) electronic states were taken into account as the states populated after the pump pulse prior to photoionization. One should note that both triplet as well as quintet states have near triple degeneracy and in previous studies[8,9] were denoted as $^3T_{1g}$, $^3T_{2g}$, and $^5T_{1g}$, respectively, as if the symmetry were octahedral. To simplify the consideration of the species with symmetry different from octahedral one, we label the states according to their multiplicity and cardinal number, with the labels T_1, T_2, Q_1, each representing a triple of near degenerate states.

For most of the calculations, the initial states populated in the Franck-Condon region (S_0 equilibrium geometry) were considered. In the main text, the vibrationally hot quintet state vertically populated by the direct mechanism is denoted as Q_1^{**}. To account for vibrational cooling and geometric relaxation the ionization from the Q_1 equilibrium configuration was also considered. However, the vibrational relaxation of the quintet state occurs on a time scale exceeding 1 ps[8] and, thus, ionization from the not yet equilibrated Q_1^* state contributes to the emission spectra at the time delays applied in the experiment. The 1600 doublet (S=1/2), 1440 quartet (S=3/2) and 265 sextet (S=5/2) electronic states of the residual $[Fe(bpy)_3]^{3+}$ ion, created in the process of XUV ionization from the S_0, $T_{1,2}$, and Q_1 initial states, have been considered as final states. The wave functions of initial and ionized states have been optimized at the restricted active space self-consistent field and state interaction (RASSCF/RASSI) level.[17,18] In the state averaged RASSCF procedure, three non-bonding 3d (t_{2g}) and two antibonding σ^*(3d) (e_g) orbitals were included in the RAS2 space with full CI flexibility. Additionally, three π(bpy) and π^*(bpy) orbitals have been included in the RAS1 and RAS3 spaces allowing one hole and one electron, respectively. Such an active space allows describing the ligand field and the lowest charge-transfer initial states of the system as well as the final states after the electron removal from both, the metal center and the ligands. The RASSCF/RASSI calculations have been carried out using a locally modified version of the MOLCAS 8.0 program package.[19] The ANO-RCC basis set[20,21] has been used with the contractions (21s15p10d6f)/[6s5p3d2f], (14s9p4d3f)/[4s3p2d1f], (8s4p)/[2s1p]

10

for the iron, nitrogen, carbon, and hydrogen atoms, corresponding to the triple zeta quality. Scalar relativistic effects have been taken into account by utilizing the second order Douglas-Kroll-Hess transformation.[22,23]

The PE intensities, f_{FI}, were calculated by employing a Dyson orbital (DO) approach.[24,25] Using the sudden ionization and strong orthogonality approximations (i.e. vanishing overlap of the photoelectron ψ^{el} and the bound orbitals ϕ_l^k wave functions: $\langle \psi^{\mathrm{el}} | \phi_l^k \rangle = 0$, $k = 1, ..., N$), the ionization intensities are represented by

$$f_{FI} \propto |\langle \psi^{\mathrm{el}} | \hat{d} | \Phi_{FI} \rangle|^2 \ ,$$

where

$$\Phi_{FI} = \sqrt{N} \int \Psi_F^{N-1}(x_1, ..., x_{N-1})^* \, \Psi_I^N(x_1, ..., x_N) dx_1...dx_{N-1}$$

is the Dyson orbital for the transition between the initial N-electron state Ψ_I^N and the final $N-1$ electron state Ψ_F^{N-1}, and $\hat{d}$ is the dipole operator.

The numerical evaluation of the bound-continuum transition matrix elements has been performed by using the ezDyson v3.0 program.[26] The final state of the photoelectron is therein represented by a plane wave expanded in terms of spherical waves:[27]

$$\psi^{\mathrm{el}}(\mathbf{r}) = \sum_{l=0}^{\infty} \sum_{m=-l}^{l} i^l \sqrt{2/\pi} j_l(\mathbf{k} \cdot \mathbf{r}) Y_{l,m}(\mathbf{r}) Y_{l,m}^*(\mathbf{k}) \ ,$$

where $j_l(\mathbf{k} \cdot \mathbf{r})$ are spherical Bessel functions, l and m denote the angular momentum quantum numbers of the outgoing electron, and $Y_{l,m}(\mathbf{r})$, $Y_{l,m}^*(\mathbf{k})$ are the spherical harmonics in the position and the momentum space, respectively. The quantization axis of the angular momentum is chosen to coincide with the polarization axis of the applied electromagnetic field. The numerical integration was carried out on a three-dimensional uniform grid in a box with a side length of 20 Å and 600 grid points per dimension. The angular momentum of the photoelectron was truncated at $l_{\mathrm{max}} = 10$. The resulting relative integration error for the norms of the Dyson orbitals was at most 10^{-3}. Since the ionization intensities are proportional to the respective squared DO norms, they were calculated only if the DOs norms were larger than 10^{-4}.

11
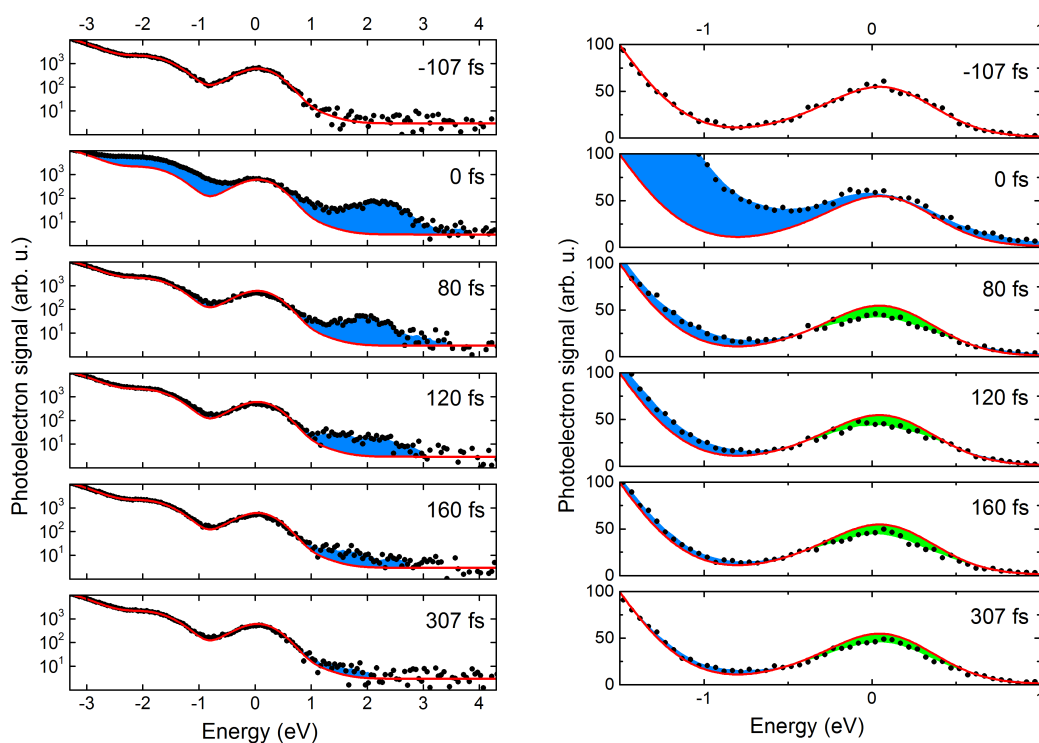
Figure S1. Photoelectron energy spectra shown on logarithmic (left panel) and linear (right panel) scales for a few selected time delays between the pump and probe pulses: -110, 0, 80, 120, 160, and 310 fs. The kinetic energy is given with respect to the emission peak of the Fe $3d(t_{2g})$ orbital. The red curve represents a fit to the XUV ionization yield when the pump beam is not applied. The transient emission signal is marked by blue color. At zero delay, a significant contribution to the spectrum arises from the cross-correlation yield of the pump and probe beams. The linear scale in the right panel enables to reveal in greater detail the transient signal at energies below the Fe $3d(t_{2g})$ peak and also the decrease (green color) of this peak due to depletion of the ground state of the metal complex by the pump beam.

12
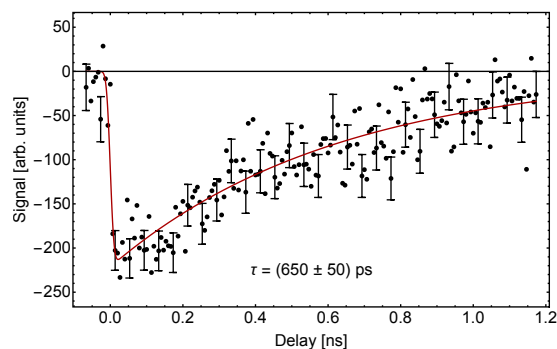
Figure S2. Depletion of the ground state as a function of the time delay. The red curve represents results of a fit where the initial depletion of the ground state by the pump beam and its re-population from the Q_1^* state during the photocycle are considered. The re-population is described by an exponential function with the fitted time constant of 650 ps.
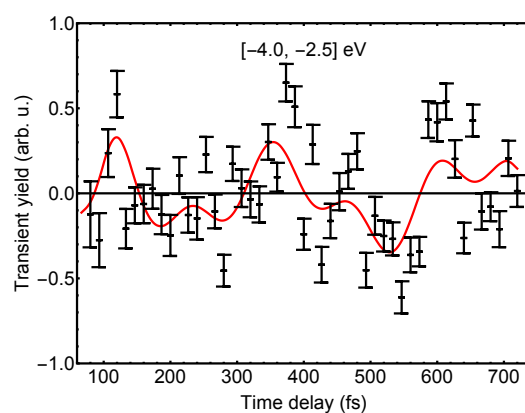
Figure S3. Oscillations in the transient signal from the ground quintet state Q_1^*. The vertical axis displays the difference between the results of experiment and the global fit by the model of parallel relaxation, normalized to the transient population of Q_1^* obtained from the fit. Note that the wave packet dynamics was disregarded in this kinetic model. The signal was integrated over the energy interval between -4 and -2.5 eV encompassing the emission band of Q_1^*. The red solid line shows the difference in the fit results when two oscillation modes are allowed for in the model. The oscillation periods of 265 ± 11 and 125 ± 4 fs were obtained from the global fit.

13
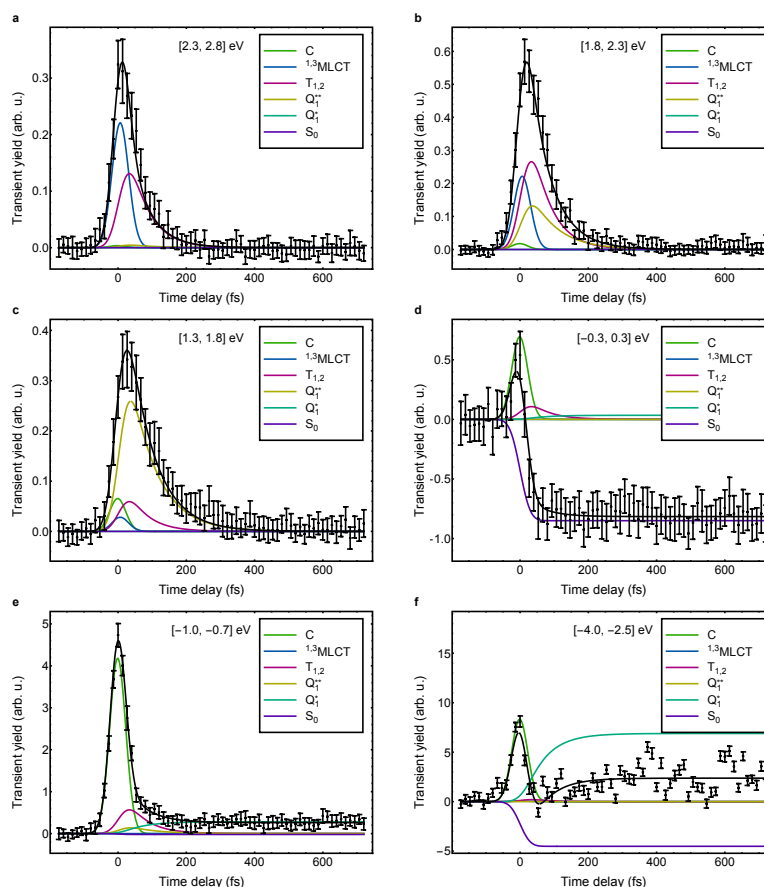
Figure S4. Time dependency of the transient signal at different excitation energies. **(a)** The signal integrated within the energy interval between 2.3 and 2.8 eV (dots with error bars). The black solid line represents the global fit result. The color lines show the signal decomposition to individual contributions from the ^{1,3}MLCT (blue), $T_{1,2}$ (red), Q_1^{**} (yellow), Q_1^* (cyan), and S_0 (violet) states as well as the cross correlation contribution C (green). **(b, c, d, e, f)** The same as in (a) shown for the energy intervals [1.8, 2.3] eV, [1.3, 1.8] eV, and [−0.3, 0.3] eV, [−1, −0.7] eV, and [−4, −2.5] eV, respectively. Note that the contribution from the S_0 state is of negative value due to the depletion of the ground state.

14
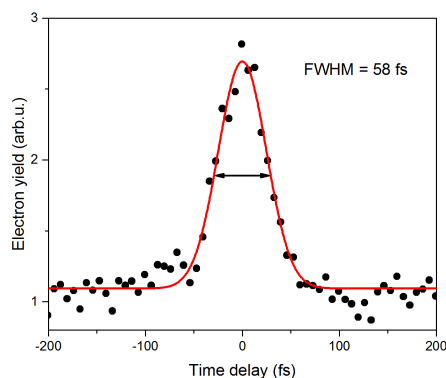
Figure S5. The cross correlation signal.
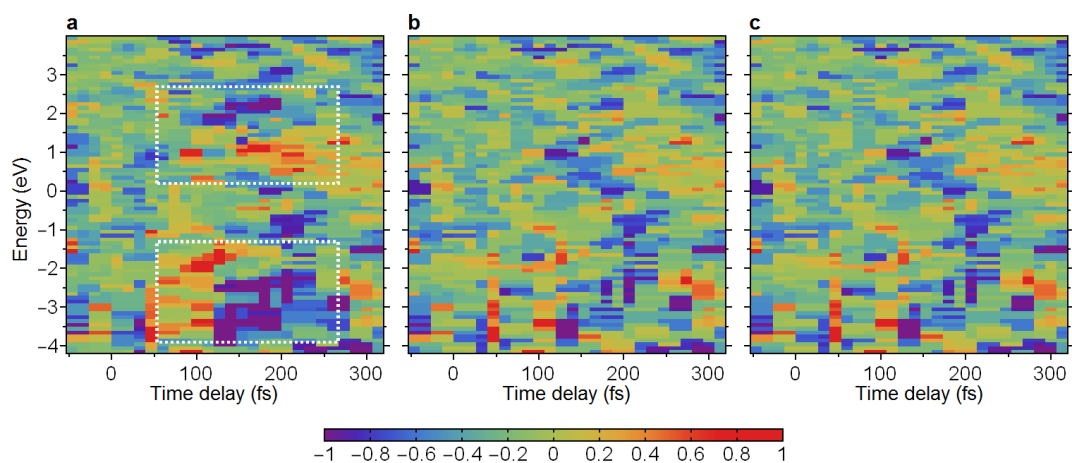
Figure S6. Residuals for the best fit by different models. The difference between the measured TS and the global fit results is shown for the 'nested' model (a), the model of parallel relaxation (b), and the cascade model (c). The data are shown in the range of time delays where the difference in residuals is most pronounced. The domain where the 'nested' model is deficient in reproducing the experimental data is marked in panel (a) by white rectangles.

15
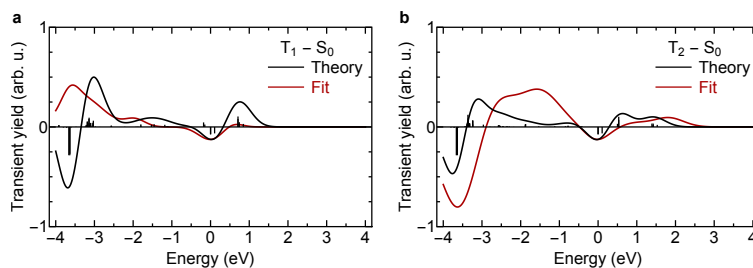
Figure S7. Comparison of theory and global fit results for the cascade model. Emission spectra of the triplet T_1 and T_2 states, considered in the cascade model, are shown. Note that the S_0 emission spectrum is subtracted for the sake of consistency with the TS plot in Fig. 3 (see the main article).
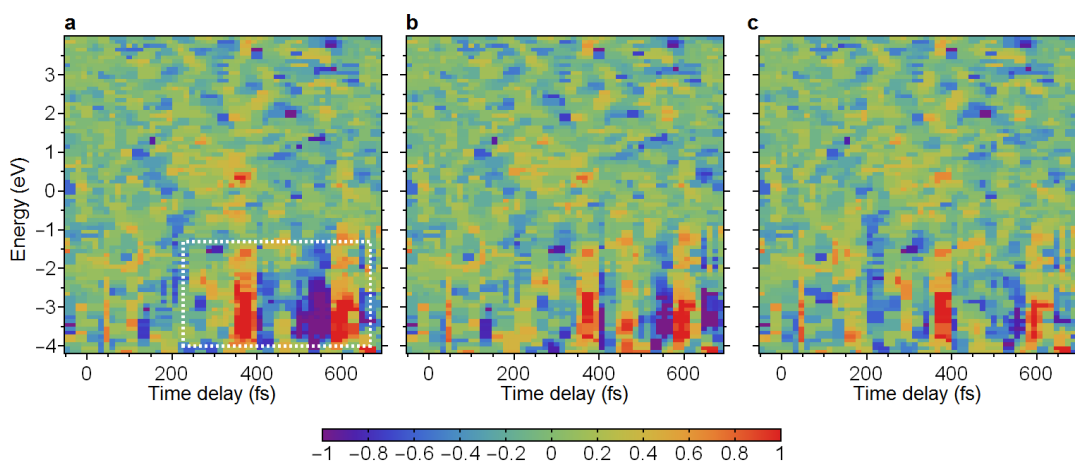
Figure S8. Residuals for the best fit by models allowing for the wave packet dynamics in the Q_1^* state. The difference between the measured TS and the global fit results is shown for the models of parallel relaxation: without taking the wave packet oscillations into account (a), allowing for one oscillation mode (b), and for two modes (c). The domain where the extended models improve significantly the fit to the experimental data is marked in panel (a) by the white rectangle.

16
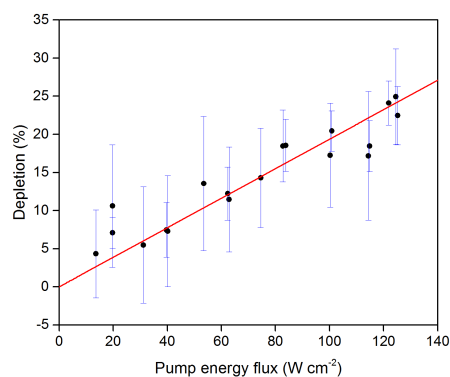
Figure S9. Depletion of the ground state as a function of the pump energy flux.

Table S1. Fitted model parameters. Time constants, representing inverse values of the corresponding transition rates, obtained from the global fit to different kinetic models. In the 'nested' model, the state X represents either the T_2 state (according to Ref.[7]) or the Q_1^{**} state (according to Ref.[8]).

Extended Model: parallel relaxation			
Transition	$^{1,3}MLCT \rightarrow T_{1,2}$	$^{1,3}MLCT \rightarrow Q_1^{**}$	$T_{1,2} \rightarrow Q_1^*$	$Q_1^{**} \rightarrow Q_1^*$
Lifetime (fs)	20 ± 20	90 ± 25	70 ± 20	35 ± 10
Extended Model: cascade relaxation			
Transition	$^{1,3}MLCT \rightarrow T_1$	$T_1 \rightarrow T_2$	$T_2 \rightarrow Q_1^*$	
Lifetime (fs)	25 ± 20	30 ± 20	80 ± 30	
'Nested' Model			
Transition	$^{1,3}MLCT \rightarrow X$	$X \rightarrow Q_1^*$		
Lifetime (fs)	13 ± 10	72 ± 10		

17

References

(1) J. Metje, M. Borgwardt, A. Moguilevski, A. Kothe, N. Engel, M. Wilke, R. Al-Obaidi, D. Tolksdorf, A. Firsov, M. Brzhezinskaya, A. Erko, I. Yu. Kiyan, E. F. Aziz, *Opt. Express* **2014**, *22*, 10747.

(2) V. Kozich, A. Moguilevski, K. Heyne, *Opt. Commun.* **2012**, *285*, 4515–4518.

(3) R. Al-Obaidi, M. Wilke, M. Borgwardt, J. Metje, A. Moguilevski, N. Engel, D. Tolksdorf, A. Raheem, T. Kampen, S. Mähl, I. Yu. Kiyan, E. F. Aziz, *New J. Phys.* **2015**, *17*, 093016.

(4) T. E. Glover, R. W. Schoenlein, A. H. Chin, C. V. Shank, *Phys. Rev. Lett.* **1996**, *76*, 2468–2471.

(5) L. Miaja-Avila, C. Lei, M. Aeschlimann, J. L. Gland, M. M. Murnane, H. C. Kapteyn, G. Saathoff, *Phys. Rev. Lett.* **2006**, *97*, 113604.

(6) See the website http://www.specs.de/.

(7) W. Zhang, R. Alonso-Mori, U. Bergmann, C. Bressler, M. Chollet, A. Galler, W. Gawelda, R. G. Hadt, R. W. Hartsock, T. Kroll, K. S. Kjær, K. Kubiček, H. T. Lemke, H. W. Liang, D. A. Meyer, M. M. Nielsen, C. Purser, J. S. Robinson, E. I. Solomon, Z. Sun, D. Sokaras, T. B. van Driel, G. Vankó, T.-C. Weng, D. Zhu, K. J. Gaffney, *Nature* **2014**, *509*, 345–348.

(8) G. Auböck, M. Chergui, *Nat. Chem.* **2015**, *7*, 629–633.

(9) C. Sousa, C. de Graaf, A. Rudavskyi, R. Broer, J. Tatchen, M. Etinski, C. M. Marian, *Chem. Eur. J.* **2013**, *19*, 17541–17551.

(10) W. Gawelda, A. Cannizzo, V.-T. Pham, F. van Mourik, C. Bressler, M. Chergui, *J. Am. Chem. Soc.* **2007**, *129*, 8199–8206.

(11) P. Fita, E. Luzina, T. Dziembowska, Cz. Radzewicz, A. Grabowska, *J. Chem. Phys.* **2006**, *125*, 184508.

(12) H. Iikura, T. Tsuneda, T. Yanai, K. Hirao, *J. Chem. Phys.* **2001**, *115*, 3540–3544.

(13) O. S. Bokareva, G. Grell, S. I. Bokarev, O. Kühn, *J. Chem. Theory Comput.* **2015**, *11*, 1700–1709.

18

(14) M. J. Frisch, G. W. Trucks, H. B. Schlegel, G. E. Scuseria, M. A. Robb, J. R. Cheeseman, G. Scalmani, V. Barone, B. Mennucci, G. A. Petersson, H. Nakatsuji, M. Caricato, X. Li, H. P. Hratchian, A. F. Izmaylov, J. Bloino, G. Zheng, J. L. Sonnenberg, M. Hada, M. Ehara, K. Toyota, R. Fukuda, J. Hasegawa, M. Ishida, T. Nakajima, Y. Honda, O. Kitao, H. Nakai, T. Vreven, J. A. Montgomery, Jr., J. E. Peralta, F. Ogliaro, M. Bearpark, J. J. Heyd, E. Brothers, K. N. Kudin, V. N. Staroverov, R. Kobayashi, J. Normand, K. Raghavachari, A. Rendell, J. C. Burant, S. S. Iyengar, J. Tomasi, M. Cossi, N. Rega, J. M. Millam, M. Klene, J. E. Knox, J. B. Cross, V. Bakken, C. Adamo, J. Jaramillo, R. Gomperts, R. E. Stratmann, O. Yazyev, A. J. Austin, R. Cammi, C. Pomelli, J. W. Ochterski, R. L. Martin, K. Morokuma, V. G. Zakrzewski, G. A. Voth, P. Salvador, J. J. Dannenberg, S. Dapprich, A. D. Daniels, Ö. Farkas, J. B. Foresman, J. V. Ortiz, J. Cioslowski, D. J. Fox, „Gaussian09 Revision D.01", gaussian Inc. Wallingford CT **2009**.

(15) T. H. Dunning, *J. Chem. Phys.* **1989**, *90*, 1007–1023.

(16) N. B. Balabanov, K. A. Peterson, *J. Chem. Phys.* **2005**, *123*, 064107.

(17) P. Å. Malmqvist, A. Rendell, B. O. Roos, *J. Phys. Chem.* **1990**, *94*, 5477–5482.

(18) P. Å. Malmqvist, B. O. Roos, B. Schimmelpfennig, *Chem. Phys. Lett.* **2002**, *357*, 230–240.

(19) G. Karlström, R. Lindh, P.-Å. Malmqvist, B. O. Roos, U. Ryde, V. Veryazov, P.-O. Widmark, M. Cossi, B. Schimmelpfennig, P. Neogrdy, L. Seijo, *Comp. Mater. Sci.* **2003**, *28*, 222–239.

(20) B. O. Roos, R. Lindh, P.-Å. Malmqvist, V. Veryazov, , P.-O. Widmark, *J. Phys. Chem. A* **2004**, *108*, 2851–2858.

(21) B. O. Roos, R. Lindh, P.-Å. Malmqvist, V. Veryazov, P.-O. Widmark, *J. Phys. Chem. A* **2005**, *109*, 6575–6579.

(22) M. Douglas, N. M. Kroll, *Ann. Phys.* **1974**, *82*, 89–155.

(23) B. A. Hess, *Phys. Rev. A* **1986**, *33*, 3742.

(24) C. M. Oana, A. I. Krylov, *J. Chem. Phys.* **2009**, *131*, 124114.

19

(25) G. Grell, S. I. Bokarev, B. Winter, R. Seidel, E. F. Aziz, S. G. Aziz, O. Kühn, *J. Chem. Phys.* **2015**, *143*, 074104.

(26) S. Gozem, A. I. Krylov, „ezDyson“, **2015**.

(27) L. D. Landau, E. M. Lifshitz, *Quantum Mechanics: Non-Relativistic Theory*, Pergamon, Oxford, **1977**.

20

[GG3]   Photoelectron shake-ups as a probe of molecular symmetry: 4d XPS analysis of I_3^- in solution

Jesper Norell, Gilbert Grell, Oliver Kühn, Michael Odelius, and Sergey I. Bokarev

Check for updates

Photoelectron shake-ups as a probe of molecular symmetry: 4d XPS analysis of I_3^- in solution†

Jesper Norell, [ID] *[a] Gilbert Grell, [ID] [b] Oliver Kühn, [ID] [b] Michael Odelius [ID] [a] and Sergey I. Bokarev [ID] [b]

A combination of multi-configurational restricted active space calculations with a Dyson orbital formalism has been applied for accurate simulations of 4d photo-electron spectra of the I_3^- molecular ion. The analysis based on the occupation numbers of natural orbitals allowed to predict and rationalize the spectral fingerprints of solvent-induced nuclear asymmetry. In particular, it demonstrates how the nuclear asymmetry directly causes an increase of shake-up intensity. The relative intensity of shake-up and main features of the I 4d XPS spectrum could therefore serve as a simplified experimental observable of structural asymmetry, complementary to changes in the shape of the main spectral features.

1 Introduction

Photoelectron spectroscopy is one of the most powerful and widely applied experimental methods for studies of electronic structure of matter, which in the X-ray regime (XPS), by targeting of core-levels, constitutes an element-specific local probe around distinct atomic sites in molecules and complex materials.[1] With the development of new delivering systems such as liquid jets combined with improved X-ray sources, XPS studies in the liquid phase have become increasingly viable to investigate the effects of solute–solvent interactions in *e.g.* electrolyte solutions[2,3] and at liquid interfaces.[4] Robust and detailed analysis of such experiments, however, often demands comparison to accurate theoretical simulations of spectra. Here, a crucial point is to predict and identify spectral signatures that are characteristic and yet readily detected in measurements, in addition to assigning ;and rationalizing the spectral features to facilitate an understanding of the underlying chemical and spectroscopic mechanisms.

As an important component in dye-sensitized solar cells, the electronic, structural and dynamic properties of I_3^- in solution have been studied in great detail both with experimental[5–7] and theoretical methods.[8–12] These studies all demonstrate how the

structure of the molecular ion and, in particular, its degree of nuclear asymmetry can be directly correlated with the varied strength of solvent–solute interaction in different solutions. In aqueous solution, the strong hydrogen bonding drives large amplitude asymmetrical stretches and charge localization, leading to an electronic structure more akin to an $I_2 \cdots I^-$ configuration. The influence of hydrogen bonding is less pronounced in, *e.g.*, ethanol and acetonitrile where the charge stays fairly delocalized over the whole moiety, $[I–I–I]^-$, and structural symmetry is comparatively preserved. In previous work[11,12] it has been demonstrated how the solvent-induced nuclear asymmetry may be evidenced from altered features of the main signal in 4d XPS measurements. Thus, I_3^- constitutes an ideal model system to explore not only the possible effects of nuclear asymmetry on electrochemical functionality, but also its interplay with XPS intensities.

Due to a recent implementation by Grell *et al.*[13] both main and shake-up XPS intensities can now be simulated within a Dyson orbital formalism with orbitals derived from the multi-configurational second order perturbation theory restricted active space method (RASPT2)[14,15] that can account for the multitude of effects that may influence spectral intensities such as: various types of chemical bonding, multi-configurational character of states, dynamic correlation, scalar relativistic effects, and spin–orbit coupling. The development thereby directly enables extension of previous I_3^- studies, with simulations of XPS spectra at an accuracy level that motivates theoretical predictions for possible future approval by experimental measurements. Complementarily, we also demonstrate in the current work how a framework for assignment and analysis, based on the multi-configurational Dyson orbital, may be conveniently formulated in terms of occupation numbers of the natural orbitals, to rationalize the predicted spectral trends.

[a] Department of Physics, AlbaNova University Center, Stockholm University, SE-106 91 Stockholm, Sweden. E-mail: jesper.norell@fysik.su.se
[b] Institut für Physik, Universität Rostock, Albert-Einstein-Str. 23-24, 18059 Rostock, Germany

† Electronic supplementary information (ESI) available: Motivation of sudden approximation *via* ezDyson 3.0 integration, extended definition of occupation numbers, multiplicity-decomposed spectrum, and the full set of relevant molecular orbitals. See DOI: 10.1039/c8cp02530d

19916 | *Phys. Chem. Chem. Phys.*, 2018, **20**, 19916–19921

This journal is © the Owner Societies 2018

2 Computational details

2.1 Molecular geometries

To study the principal influence of nuclear asymmetry on I_3^- 4d XPS, spectral simulations were performed and compared for a symmetric and an asymmetrically stretched geometry. The symmetric geometry (representing $[I–I–I]^-$ as in *e.g.* EtOH solution) with 2.91 Å I–I bond lengths corresponds to a CASPT2(16,9) I_3^-(g) optimization.[7] The linear asymmetric geometry (representing $I_2 \cdots I^-$) with I–I bonds of 3.37 Å and 2.82 Å was chosen to have the largest asymmetric stretch among structures found in a number of previous molecular dynamic simulations of aqueous LiI_3 solution.[11]

2.2 Electronic structure calculations

The electronic wave functions of the initial electronic state of I_3^- and the final core-ionized states of the neutral I_3 were calculated on the RASSCF[14] and RASPT2[15] levels, as implemented in the Molcas 8.0 program package.[16] A RAS(15, 3; 34 e^-, 1 h^+) active space was employed as illustrated in Fig. 1, *i.e.* 15 orbitals in the RAS1 space (one hole is allowed) and 3 orbitals in the RAS2 space (full CI) with a total of 34 active electrons (33 for the final states). The calculations were performed without explicit use of symmetry, a separate orbital constraint was, however, applied to the 15 4d orbitals to exclude orbital rotation with other occupied valence orbitals. Thereby, we ensure core-rather than valence-excitations in
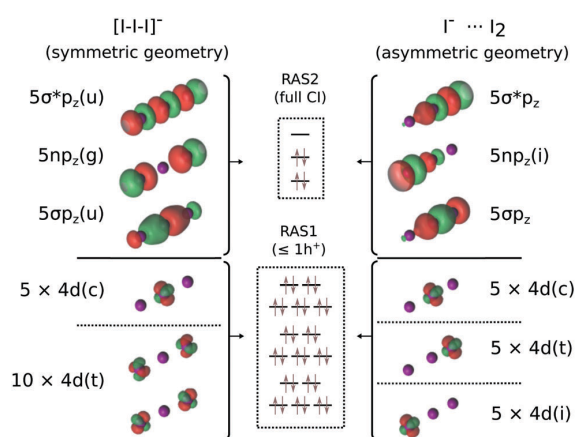
Fig. 1 Active space of the RAS(15, 3; 34 e^-, 1 h^+) calculations and representative multi-state RASPT2 natural orbitals as obtained for the I_3^- singlet species. One electron hole (h^+) in RAS1 allows for core-ionization (core-excitation in the neutral I_3 species) out of the 15 × 4d core orbitals; the RAS2 space allows for simultaneous valence-excitations and correlation within the 3 × $5p_z$ orbitals. The orbitals obtained for the symmetric geometry can be naturally grouped as 10 × terminal (t) and 5 × central (c) 4d core orbitals, in addition to 3 × $5p_z$ valence orbitals of bonding (σ), non-bonding (n) and anti-bonding (σ*) character. The $5p_z$ orbitals are further characterized by their inversion symmetry parity: gerade (g) and ungerade (u). The orbitals obtained for the asymmetric geometry are instead naturally grouped as 5 × ionic (i), 5 × terminal (t) and 5 × central (c) 4d core orbitals, in addition to 3 × $5p_z$ valence orbitals that are bonding (σ) and anti-bonding (σ*) on the I_2 moiety and of non-bonding (n) character on the I^- ion (i).

the final state calculation. Solvent effects, beyond their impact on the nuclear geometry, were not included in the calculations; previous work has, however, demonstrated the effects of explicit water solvation to mainly result in additional broadening and altered absolute shift of the XPS spectrum.[11]

For the molecular ion I_3^- (*i.e.* the initial states of the XPS process), both the singlet ground state and the first triplet spin-free (pure multiplicity) states were calculated. For the neutral molecule I_3 (*i.e.* the final states of the XPS process), all possible spin-free states were calculated within the state averaging formalism, namely 143 doublets (135 core-ionized) and 46 quartets (45 core-ionized). Subsequent multi-state RASPT2 calculations were carried out with an imaginary shift of 0.2 Hartree to accelerate convergence. For the doublet I_3^- calculations of the asymmetric geometry, the 10 states with highest energy were excluded from the multi-state RASPT2 due to the intruder states problems; this does not significantly affect the results as these states anyway fall outside the XPS energy range analyzed in the current work. Scalar relativistic effects were included *via* a Douglas–Kroll (DK) Hamiltonian[17,18] and the relativistically contracted ANO-RCC-VTZP[19] basis set. Spin–orbit coupling was included through the restricted active space state interaction (RASSI) method,[20,21] *via* atomic mean field integrals[22] with the electron repulsion integrals approximated through a density-fitting procedure.[23–25]

2.3 XPS intensities

XPS intensities were obtained within a Dyson orbital (DO) formalism, as described in detail in previous work.[13] In short, for the initial state i and final bound state of the ionized system f with the respective N and $N-1$-electron wave functions Ψ_i^N and Ψ_f^{N-1}, the photo-electron matrix element can be written as

$$D_{fi} = \langle \Psi_f^{N-1} \psi^{el}(\mathbf{k}) | \hat{d} | \Psi_i^N \rangle = \langle \psi^{el}(\mathbf{k}) | \hat{d} | \phi_{fi}^{DO} \rangle. \qquad (1)$$

Here, $\psi^{el}(\mathbf{k})$ is the photo-electron wave function ($\mathbf{k}$ its momentum), $\hat{d}$ the electronic dipole operator, and ϕ_{fi}^{DO} stands for the one-electron DO

$$\phi_{fi}^{DO}(\mathbf{x}_N) = \sqrt{N} \int \Psi_f^{N-1}(\mathbf{x}_1, \mathbf{x}_2, \ldots, \mathbf{x}_{N-1}) \\ \times \Psi_i^N(\mathbf{x}_1, \mathbf{x}_2, \ldots, \mathbf{x}_N) d\mathbf{x}_1 d\mathbf{x}_2 \ldots d\mathbf{x}_{N-1} \qquad (2)$$

that (after normalization) formally corresponds to the wave function of the photo-electron prior to the ionization. With ϕ_{fi}^{DO} obtained from the quantum chemical calculation the spectral intensity of the transition i → f is proportional to $|D_{fi}|^2$.

The results of the current work are all obtained within the sudden approximation (SA) where the energy (and thus $\mathbf{k}$) dependence of $\psi^{el}(\mathbf{k})$ is neglected to obtain

$$|D_{fi}|^2 = |\langle \psi^{el}(\mathbf{k}) | \hat{d} | \phi_{fi}^{DO} \rangle|^2 \propto \|\phi_{fi}^{DO}\|^2 \qquad (3)$$

where the proportionality constant is taken to be the same for all transitions.

The SA is well justified for our present comparison to experiments performed with 600 eV photon energies as shown

This journal is © the Owner Societies 2018

Phys. Chem. Chem. Phys., 2018, **20**, 19916–19921 | **19917**

109

PCCP

in ESI,† Section S1. This fact allowed us to avoid the most demanding step of computing transition matrix elements with continuum functions. We emphasize, however, that the approximation cannot be trivially assumed to hold equally well for other systems and binding energy ranges. Therefore, we advocate a case by case validation also in future studies.

All XPS transitions were shifted by 2.9 eV (1.5 eV at RASSCF level) and rescaled to align the main feature of the spectrum for the symmetric geometry to the experiment. The discrete XPS intensities from the calculations were convoluted with a Gaussian function with full-width-half-maximum of 1.1 eV, previously shown to yield good agreement with experiments.[11]

2.4 Assignment and analysis

The DO formalism constitutes a convenient framework for assigning XPS transitions within a molecular orbital picture. The multi-configurational DO carries information both about the photo-electron and shake-up excitations in the molecular system, as may be expressed in terms of occupation numbers of the natural orbitals. For a multi-configurational state Ψ_j, an occupation vector

$$\mathbf{n}_j = (\mathrm{occ}_j(\varphi_1), \mathrm{occ}_j(\varphi_2), \ldots, \mathrm{occ}_j(\varphi_M)) \quad (4)$$

may be defined from the occupation numbers of the M active molecular orbitals $\{\varphi_l\}$, where the components sum to the total number of active electrons. Similarly, an occupation-like vector

$$\mathbf{n}_{\mathrm{fi}}^{\mathrm{DO}} = (|\langle \phi_{\mathrm{fi}}^{\mathrm{DO}} | \varphi_1 \rangle|, |\langle \phi_{\mathrm{fi}}^{\mathrm{DO}} | \varphi_2 \rangle|, \ldots, |\langle \phi_{\mathrm{fi}}^{\mathrm{DO}} | \varphi_M \rangle|) \quad (5)$$

may be defined for the normalized DO, which carries information about the contributions of different active orbitals $\{\varphi_l\}$ to the photo-electron prior to the ionization, where the components instead sum to one. In other words, in a description accounting for electron correlation, the normalized DO corresponds to a

quasiparticle, with a wave function being a superposition of initial state active molecular orbitals. Due to electron correlation (*i.e.* multi-configurational character of the initial and/or final states), ionization may additionally be accompanied by electronic shake-up (and shake-down) excitations in the molecular system as expressed in the residual occupation vector

$$\mathbf{n}_{\mathrm{fi}}^{\mathrm{res}} = \mathbf{n}_f^{N-1} + \mathbf{n}_{\mathrm{fi}}^{\mathrm{DO}} - \mathbf{n}_i^N. \quad (6)$$

In a frozen-orbital approximation, the residual occupation is the zero vector for main lines (single-electron ionization). In contrast, for shake-up transitions it contains the occupation change due to the electronic excitations accompanying one-electron ionization. In the present case, with a multi-configurational self-consistent field method, both the DO and residual occupations are additionally affected by the orbital relaxation upon photo-ionization, *i.e.* the basis of orbitals $\{\varphi_l\}$ may differ for the initial and final states. Consequently, occupation number analysis is complicated by the possible differences in orbital bases for the I_3^- and I_3 species. As shown below, this effect is mainly seen for the asymmetric geometry.

3 Results and discussion

3.1 Comparison to experimental spectra

In Fig. 2(a), the spectra of the symmetric and asymmetric geometries simulated at the RASPT2 level are compared to the reported experimental I_3^- 4d signal in EtOH solution.[11] Firstly, comparison of the symmetric geometry and the experiment shows that the simulation protocol accurately reproduces both the main and shake-up features. Secondly, comparison of the XPS for symmetric and asymmetric geometries indicates the influence of solvent-induced nuclear asymmetry: while the peak positions are quite similar for both geometries, the asymmetry manifests itself in the changes in shape of the main
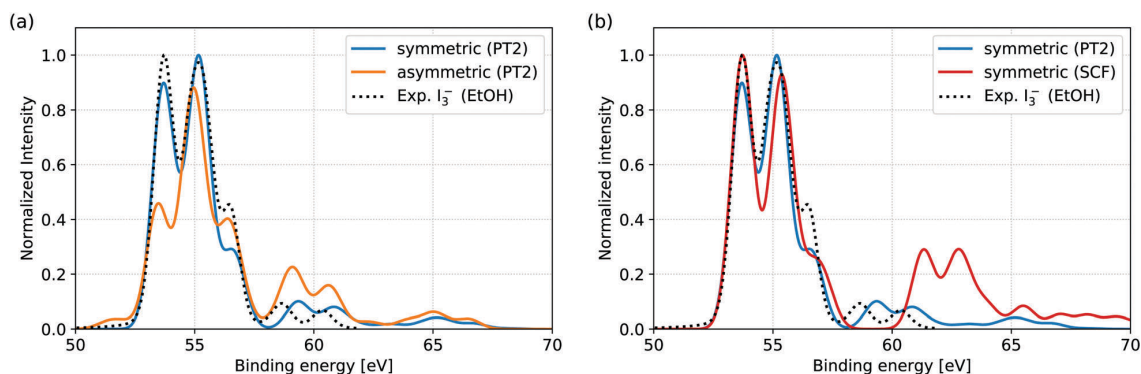
Fig. 2 Comparison of simulated XPS spectra to experimental reference of I_3^- in EtOH solution. The experimental spectrum represents the isolated I_3^- 4d signal, obtained after subtraction of the Li^+ 1s counter ion signal from the total measured spectrum.[11] (a) RASPT2 level simulations for the symmetric and asymmetric geometries. The experimental spectrum is well reproduced from the symmetric geometry, both for main lines (from 50 eV to 57.5 eV) and shake-up features (above 57.5 eV). In comparison, the asymmetric geometry results in both altered main line spectral shape and appreciably increased shake-up intensities. Note that the smaller energy range of the measurement (49.1 eV to 61.8 eV) excludes some of the features (near 65 eV) found in the simulations. (b) Comparison of RASPT2 and RASSCF level simulations for the symmetric geometry. While the main line features are very similar for the two computational levels, the intensity of the shake-up features and their energy splitting from the main features are both clearly overestimated at RASSCF level.

Paper

features and the increased shake-up intensity. The spectral features are assigned and the observed trends are rationalized through occupation number analysis in Section 3.2.

In the available experimental studies for EtOH and aqueous solutions aiming at the analysis of the main signal,[11] Li^+ was used as a counter ion. As the Li 1s direct ionization spectrally overlaps with the I_3^- 4d shake-up features, the Li^+ 1s signal had to be subtracted from the total measured spectrum to obtain the I 4d signal, as presented for EtOH in Fig. 2. In aqueous solution, further subtraction of I^- and $I_2(g)$ signal components was also necessary. This leaves too large uncertainties for a quantitative comparison, as indicated by the highly differing spectra obtained through different subtraction schemes.[11] We therefore refrain from direct comparison of our simulations to aqueous solution and hope that potential future experiments, aimed also at shake-up analysis, may be performed under more stable circumstances enabled by, *e.g.*, a different choice of counter ion and I_2/I^- ratio.

For comparison to the RASPT2 results, XPS spectra were also simulated directly from the RASSCF electronic states; the results for the symmetric geometry are shown in Fig. 2(a). While the main features of the spectra are nearly identical at the two levels of theory, the shake-up features are highly over-estimated both in terms of intensity and energetic distance from the main features. The effect can therefore be ascribed to the limited account for electron correlation provided by the active space. However, the current RASSCF calculations cannot be straightforwardly improved through inclusion of further valence orbitals, due to the already high computational cost of the setup with $15 \times 4d$ core-orbitals that is necessary to describe the XPS process. The accurate simulation and analysis of shake-up features is thereby directly enabled by the multi-configurational second order perturbation theory and would not be possible at reduced computational level.

3.2 XPS assignment and occupation number analysis

The XPS features obtained at RASPT2 level for the symmetric and asymmetric geometry are assigned and rationalized through occupation number analysis, as visualized in Fig. 3. The DO ($\mathbf{n}_{fi}^{DO}$) and residual occupations ($\mathbf{n}_{fi}^{res}$) (see eqn (6)) are shown in the panels in the left (a and c) and right (b and d) columns, respectively. Upper row of panels (a and b) corresponds to the symmetric and lower row (c and d) to the asymmetric geometries. In each panel, the respective occupation vector for a particular transition energy (*x*-axis) represents a vertical slice. Different segments of these slices (*y*-axis) correspond to the active molecular orbitals.

Important for the analysis of spectral changes is to distinguish between different types of orbitals. The $15 \times 4d$ orbitals can be grouped together based on their atomic site localization, with representative examples shown in Fig. 1. We denote them as $10 \times$ central 4d(c) and $5 \times$ terminal 4d(t) for the symmetric geometry. For the asymmetric geometry there are instead $5 \times$ ionic orbitals 4d(i) localized on I^-, and $5 \times$ central 4d(c) and $5 \times$ terminal 4d(t) orbitals of I_2. Crucial for the current work is also an understanding of shake-up effects due to $5p \rightarrow 5p$

valence excitations. Three combinations of symmetrized 5p orbitals are present for the symmetric geometry, which we denote as bonding $5\sigma p_z(u)$, non-bonding $5np_z(g)$, and anti-bonding $5\sigma^*p_z(u)$. Note that the inversion symmetry parity labels 'g' and 'u' are only applicable for the symmetric geometry. For the asymmetric geometry, the $5p_z$ orbitals instead form a non-bonding orbital $5np_z(i)$ on the I^- ion, and the bonding $5\sigma p_z$ and anti-bonding $5\sigma^*p_z$ combinations for the I_2 moiety.

For the symmetric geometry, the main features of the 4d spectrum can be assigned to ionization from orbitals localized mainly on either the terminal 4d(t) or central 4d(c) sites in accordance with previous calculations.[11,12] Each type of orbital gives rise to two features separated by spin–orbit splitting of 1.6 eV between the $4d_{3/2}$ and $4d_{5/2}$ levels, seen as two parallel vertical lines in the occupations (Fig. 3a) near -53.6 eV and -55.2 eV (terminal) and, respectively, near -55.1 eV and -56.7 eV (central). The overlap of transitions near -55 eV gives effectively rise to three main features in the spectrum. Further, two distinct shake-up features are found near -59.3 eV and -60.8 eV. As can be seen from the DO occupations (Fig. 3a), only ionization from the terminal sites is involved in these transitions; their intrinsic energy splitting is the same spin–orbit splitting as for the main features, while their distance from the main peaks is the result of the $5np_z(g)$ (HOMO) to $5\sigma^*p_z(u)$ (LUMO) shake-up excitation that can be confidently assigned from the clear transfer of occupation between these two orbitals in the associated residual occupations (Fig. 3b). The assignment can be rationalized through an inversion-symmetry argument previously given for the I 3d XPS spectrum of triiodide by Arbman *et al.*[26] that emphasizes the crucial impact of nuclear and electronic symmetry on shake-up features: shake-up excitation from gerade to ungerade orbitals is symmetry forbidden to occur together with ionization from central site orbitals, due to their gerade symmetry. The shake-up excitation is, however, allowed in combination with core-ionization at the terminal sites, as localization of the core-hole to either terminal site breaks the electronic symmetry in the final state. Shake-up features associated with central site ionization are instead seen at much lower intensity near -65.1 eV and -66.7 eV, *i.e.* at energies associated with the $5\sigma p_z(u)$ (HOMO−4) to $5\sigma^*p_z(u)$ (LUMO) excitation of parity-conserving ungerade to ungerade character.

Main feature assignments at the asymmetric geometry are also well described by the previous grouping of 4d orbitals. Assignment from the DO occupations (Fig. 3c) evidences dominant photo-ionization from the ionic site 4d(i) at 1.3 eV to 2.0 eV higher (-53.4 eV and -55.0 eV) rather than from the terminal 4d(t) (-54.8 eV and -56.3 eV) and central site 4d(c) (-55.4 eV and 56.9 eV), as explained by localization of surplus negative charge on the I^- site.[11,12] The single exception is a weak feature (less than 0.05 of maximal intensity) near -51.6 eV, ascribed to ionization from the central site 4d(c), rationalized in ESI,† Section S2.3. We note that while the characters and the order of the $5p_z$ orbitals are essentially preserved upon ionization in the symmetric geometry, this is not the case for the asymmetric geometry. Hence, we conclude that the frozen orbital approximation (initially assumed

PCCP

Paper
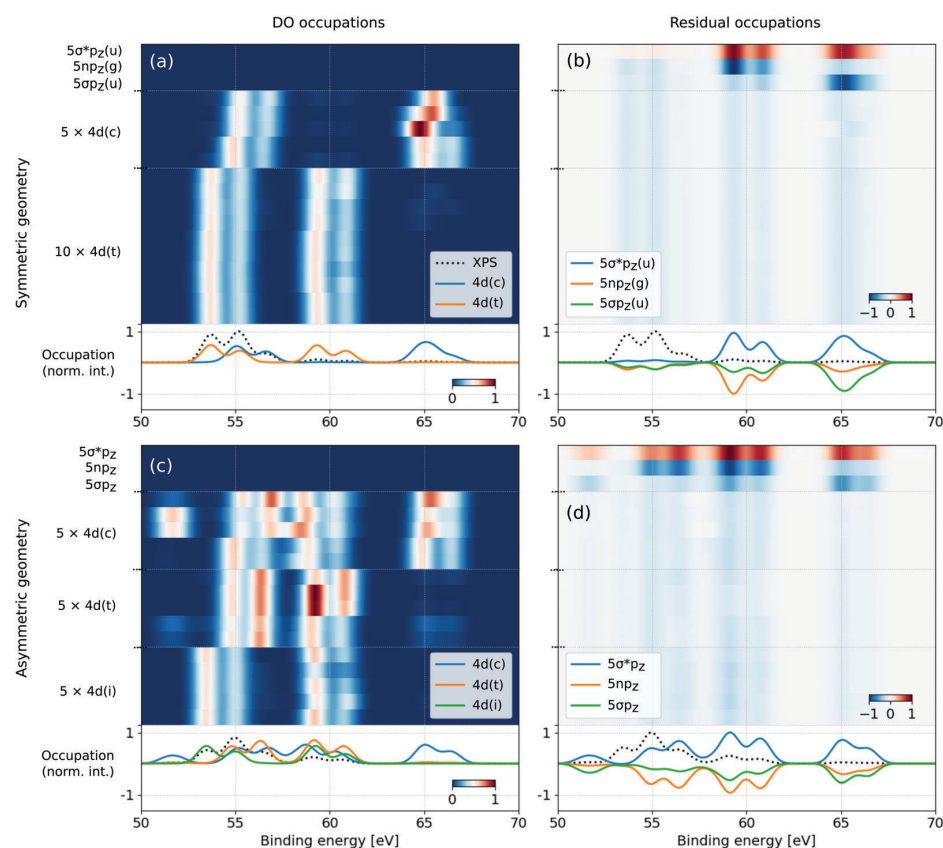
Fig. 3 Occupation number analysis of the multi-state RASTP2 natural orbitals for main ionization and shake-up transitions in the I_3^- 4d XPS spectra. DO ($\mathbf{n}_{fi}^{DO}$) and residual ($\mathbf{n}_{fi}^{res}$) occupation numbers (see eqn (6)) are given in the left (a and c) and right (b and d) columns of panels, respectively. Rows of panels correspond to the symmetric (upper, a and b) and asymmetric (lower, c and d) geometries. In each panel, the respective occupation vector for a particular transition energy (x-axis) represents a vertical slice. Different segments of these slices (y-axis) correspond to the active molecular orbitals. Occupation numbers are only shown for transitions with intensities larger than 0.05 of the most intense transition to filter out a large number of spectroscopically irrelevant transitions. The occupation numbers have been convoluted along the binding energy axis in the same way as the spectral intensities to facilitate visual comparison. For each panel the occupation numbers were subsequently renormalized to a range of −1 to 1. The lower part of each panel shows the occupation numbers averaged over the different orbital types as compared to the normalized XPS spectrum (dashed lines), thereby indicating the contributions from the different orbital types.

for occupation number analysis) is clearly violated. This is a crucial aspect for the assignment of the shake-up excitations. As can be seen from the full set of orbitals for both the I_3^- and I_3 species shown in the ESI,† Section S1 and Fig. S3, the ionic $5np_z(i)$ (HOMO) and bonding $5\sigma p_z$ (HOMO−7) orbitals permute their order, and the ionic orbital relaxes from an anti-bonding to bonding character towards the I_2 part, upon photo-ionization. This type of difference in orbital bases invalidates a straightforward comparison of initial and final states, and thereby makes simple characterization of shake-ups transitions in terms of e.g. HOMO, LUMO, etc impossible. The effect is clearly seen in the residual occupations (Fig. 3d), with strong contributions present even within the nominal main peaks of the spectrum. Nevertheless, the intense shake-up features near −59.0 eV and −60.6 eV can be clearly associated with ionization from all three sites, based on their DO occupations (Fig. 3c), which are expressed exclusively in the initial state orbital basis. Thus, the

symmetry limitations introduced for these features in the symmetric geometry are lifted, which directly explains their increased absolute intensity.

Based on comparison and rationalization of the symmetric and asymmetric spectra, it is clear that the degree of nuclear asymmetry is directly reflected in the relative intensity of main and shake-up features: integrating the XPS intensities between −50 eV to −57.5 eV (main features) and, respectively, −57.5 eV to −62 eV (shake-up features) one obtains the two highly different ratios of 9.6% for shake-up-to-main intensity ratio in the symmetric spectrum and 24.2% in the asymmetric spectrum. This theoretical prediction thus suggests a single scalar observable evidencing solvent-induced nuclear asymmetry in the I_3^- ion. It could be conveniently extracted from experimentally measured 4d XPS spectra given an appropriate choice of counter ion. This simplifies the analysis otherwise often based on a complete comparison of spectral features.

19920 | *Phys. Chem. Chem. Phys.*, 2018, **20**, 19916–19921

This journal is © the Owner Societies 2018

4 Conclusion

In summary, our RASPT2 calculations combined with a DO formalism can accurately reproduce I_3^- 4d XPS spectra, which allows us to predict the influence of nuclear asymmetry on XPS intensities and, in particular, shake-up features. Based on an analysis of natural orbital occupation numbers, we assign an increased shake-up intensity upon asymmetric stretching to result from the break-down of inversion-symmetry dependent selection rules for XPS transitions. The ratio of shake-up-to-main feature intensities could thereby serve as a simple scalar quantity to measure nuclear asymmetry in I_3^- with 4d XPS. This example demonstrates how the high accuracy of RASPT2 calculations can be utilized for theoretical predictions of XPS spectra, and motivates future experimental measurements of I_3^- in solution to further elucidate the influence of solvent-induced symmetry breaking.

Conflicts of interest

There are no conflicts of interest to declare.

Acknowledgements

References

1 K. Siegbahn, C. Nordling and A. Fahlman, *ESCA, atomic, molecular and solid state structure studied by means of electron spectroscopy*, Almqvist and wiksell technical report, 1967.

2 B. Winter and M. Faubel, *Chem. Rev.*, 2006, **106**, 1176–1211.

3 R. Golnak, S. I. Bokarev, R. Seidel, J. Xiao, G. Grell, K. Atak, I. Unger, S. Thürmer, S. G. Aziz, O. Kühn, B. Winter and E. F. Aziz, *Sci. Rep.*, 2016, **6**, 24659.

4 O. Björneholm, M. H. Hansen, A. Hodgson, L.-M. Liu, D. T. Limmer, A. Michaelides, P. Pedevilla, J. Rossmeisl, H. Shen, G. Tocci, E. Tyrode, M.-M. Walz, J. Werner and H. Bluhm, *Chem. Rev.*, 2016, **116**, 7698–7726.

5 A. E. Johnson and A. B. Myers, *J. Phys. Chem.*, 1996, **100**, 7778–7788.

6 K. H. Kim, J. H. Lee, J. Kim, S. Nozawa, T. Sato, A. Tomita, K. Ichiyanagi, H. Ki, J. Kim, S.-i. Adachi and H. Ihee, *Phys. Rev. Lett.*, 2013, **110**, 165505.

7 S. K. Eriksson, I. Josefsson, N. Ottosson, G. Öhrwall, O. Björneholm, H. Siegbahn, A. Hagfeldt, M. Odelius and H. Rensmo, *J. Phys. Chem. B*, 2014, **118**, 3164–3174.

8 C. Margulis, D. Coker and R. Lynden-Bell, *Chem. Phys. Lett.*, 2001, **341**, 557–560.

9 F. S. Zhang and R. M. Lynden-Bell, *Phys. Rev. Lett.*, 2003, **90**, 185505.

10 C. Margulis, D. Coker and R. Lynden-Bell, *J. Chem. Phys.*, 2001, **114**, 367–376.

11 I. Josefsson, S. K. Eriksson, N. Ottosson, G. Öhrwall, H. Siegbahn, A. Hagfeldt, H. Rensmo, O. Björneholm and M. Odelius, *Phys. Chem. Chem. Phys.*, 2013, **15**, 20189–20196.

12 N. K. Jena, I. Josefsson, S. K. Eriksson, A. Hagfeldt, H. Siegbahn, O. Björneholm, H. Rensmo and M. Odelius, *Chem. – Eur. J.*, 2015, **21**, 4049–4055.

13 G. Grell, S. I. Bokarev, B. Winter, R. Seidel, E. F. Aziz, S. G. Aziz and O. Kühn, *J. Chem. Phys.*, 2015, **143**, 074104.

14 P. A. Malmqvist, A. Rendell and B. O. Roos, *J. Phys. Chem.*, 1990, **94**, 5477–5482.

15 P. A. Malmqvist, K. Pierloot, A. R. M. Shahi, C. J. Cramer and L. Gagliardi, *J. Chem. Phys.*, 2008, **128**, 204109.

16 F. Aquilante, J. Autschbach, R. K. Carlson, L. F. Chibotaru, M. G. Delcey, L. De Vico, I. Fdez Galván, N. Ferré, L. M. Frutos, L. Gagliardi, M. Garavelli, A. Giussani, C. E. Hoyer, G. Li Manni, H. Lischka, D. Ma, P. Å. Malmqvist, T. Müller, A. Nenov, M. Olivucci, T. B. Pedersen, D. Peng, F. Plasser, B. Pritchard, M. Reiher, I. Rivalta, I. Schapiro, J. Segarra-Martí, M. Stenrup, D. G. Truhlar, L. Ungur, A. Valentini, S. Vancoillie, V. Veryazov, V. P. Vysotskiy, O. Weingart, F. Zapata and R. Lindh, *J. Comput. Chem.*, 2016, **37**, 506–541.

17 M. Douglas and N. M. Kroll, *Ann. Phys.*, 1974, **82**, 89–155.

18 B. A. Hess, *Phys. Rev. A: At., Mol., Opt. Phys.*, 1986, **33**, 3742–3748.

19 B. O. Roos, R. Lindh, P. Å. Malmqvist, V. Veryazov and P. O. Widmark, *J. Phys. Chem. A*, 2004, **108**, 2851–2858.

20 P.-Å. Malmqvist and B. O. Roos, *Chem. Phys. Lett.*, 1989, **155**, 189–194.

21 P. Å. Malmqvist, B. O. Roos and B. Schimmelpfennig, *Chem. Phys. Lett.*, 2002, **357**, 230–240.

22 B. A. Hess, C. M. Marian, U. Wahlgren and O. Gropen, *Chem. Phys. Lett.*, 1996, **251**, 365–371.

23 F. Aquilante, T. B. Pedersen and R. Lindh, *J. Chem. Phys.*, 2007, **126**, 194106.

24 F. Aquilante, P.-Å. Malmqvist, T. B. Pedersen, A. Ghosh and B. O. Roos, *J. Chem. Theory Comput.*, 2008, **4**, 694–702.

25 J. Boström, M. G. Delcey, F. Aquilante, L. Serrano-Andrés, T. B. Pedersen and R. Lindh, *J. Chem. Theory Comput.*, 2010, **6**, 747–754.

26 M. Arbman, S. Holmberg, M. Lundholm, H. Siegbahn, O. Gropen and U. Wahlgren, *Chem. Phys.*, 1983, **81**, 113–119.

113

PCCP

ARTICLE TYPE

Electronic Supplementary Information

S1   The sudden approximation

To investigate the effects of the sudden approximation on the obtained XPS intensities, numerical integration of equation 3 was carried out with the ezDyson 3.0 program[1].

The spatial plane wave is expanded in a basis of spherical waves with angular momentum $l = 0, 1, \ldots, l_{max}$. A rectangular numerical grid of 360 points from -6 to 6 Å along the molecular symmetry z-axis, and 180 points from -3 to 3 Å along the x- and y-axes was applied, with $l_{max} = 10$. To limit the computational cost, the integration was only performed for transitions with Dyson orbital norms $\|\phi_{fi}^{\mathrm{DO}}\| \geq 0.01$.

Fig. S1 displays the XPS results for the symmetric geometry at RASPT2 level and photon energies 600 eV, 200 eV and 100 eV. At 600 eV the spectrum is in good agreement with the results derived from the sudden approximation, as presented in the main manuscript, and the presented experimental reference. At reduced photon energies the shape of the main features is clearly affected. The XPS intensities would typically be expected to be more sensitive to the photon energy at low photon energies (due to the increased interaction between the ejected photo-electron and the local potential of the remaining molecular system). The nearly identical spectra for 100 eV and 200 eV photon energies thereby suggests that the applied numerical integration is not sufficient to accurately describe the XPS at lowered photon energies.

While the accuracy of the ezDyson integration could likely be improved through different choice of parameters, we note that the current setup already results in a total computational cost (per spectrum) that is comparable to the expensive RASPT2 step of the simulations. Further testing is thereby not motivated in the current work, since good agreement to experiment is already obtained within the sudden approximation. The analysis is consequently, in the main manuscript, most safely and efficiently performed for comparison of the sudden approximation (theory) and 600 eV photon energies (experiment).
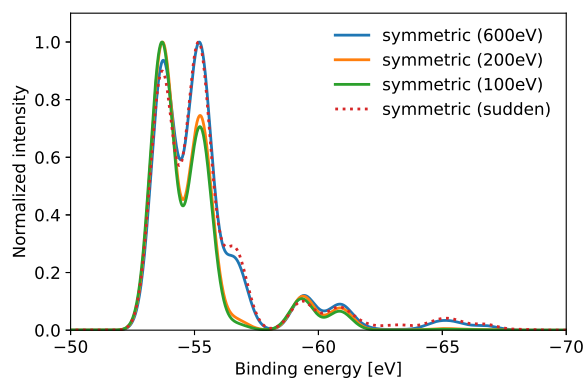
Fig. S1 Photon energy effects on the I_3^- 4d XPS intensities obtained from numerical integration with ezDyson. For 600 eV photon energy the results are in good agreement with the sudden approximation results presented in the main manuscript and the experimental reference. At reduced photon energy the spectral shape of the main features is clearly affected.

S2 Occupation number analysis

S2.1 Spin-orbit effects

Inclusion of spin-orbit coupling for I_3^- 4d XPS simulations is essential to describe the 4d core-hole, as seen from e.g. the 1.7 eV splitting between features with $4d_{3/2}$ and $4d_{5/2}$ level ionization respectively. This could, in principle, affect the occupation number analysis in a similar way as the final state molecular orbital relaxation, as both the initial and final spin-orbit coupled states are expressed in two bases of molecular orbitals obtained from calculations of spin-free states with pure multiplicities (singlet and triplet for initial states, doublet and quartet for final states). However, the spin-free triplet state basis has no influence on the spectrum, as the initial spin-orbit coupled state (with no core-hole) is a pure singlet. Fig. S2b shows a histogram of the spin-orbit coupled final states sorted according their total weights in terms of spin-free doublet states. While essentially pure doublet spin-orbit coupled states are by far most common, it is clear that states exist in the whole range from pure doublets to pure quartets. Shown in Fig. S2a, however, is also a decomposition of the XPS spectrum into contributions from spin-free doublet and quartet states, respectively, which makes clear that the spectral influences of the spin-free quartet states is nearly negligible. Consequently, spin-orbit coupling with relevance for the spectrum is only the doublet-doublet coupling, and we need only consider the I_3^- singlet and I_3 doublet molecular orbital bases for the occupation number analysis.

S2.2 Molecular orbitals

The full set of molecular orbitals obtained for both initial (singlet) and final (doublet) states are, as an extension of Fig. 1 from the main manuscript, shown in Fig. S3.

S2.3 Assignment of the additional weak central site ionization feature for the asymmetric geometry

While the orbital relaxation upon photo-ejection prohibits definitive molecular orbital assignments, the residual occupations in Fig. 3c indicates that the low intensity feature near -51.6 eV associated with central site ionization can be tentatively rationalized as charge-transfer excitation from I^- to I_2^+ in the final state, as compared to direct ionization. This explains both the lower energy (as the charge-transfer counteracts the charge imbalance caused by photo-ionization from the neutral I_2) and the low intensity (low orbital overlap between I^- and I_2^+) as compared to the strong feature at 54.9 eV. As the active orbitals 19 and 20 are both fully occupied (1.98 and 1.95 occupation respectively)

in the initial state, we ascribe the residual occupation of the feature to CI excitation in the final state I_3 from orbital 19 to 20 in its orbitals basis, which as shown in Fig. S3 indeed constitutes a charge-transfer excitation from the I^- to the I_2^+ site.

References

1 C. Melania Oana and A. I. Krylov, *The Journal of chemical physics*, 2007, **127**, 234106.
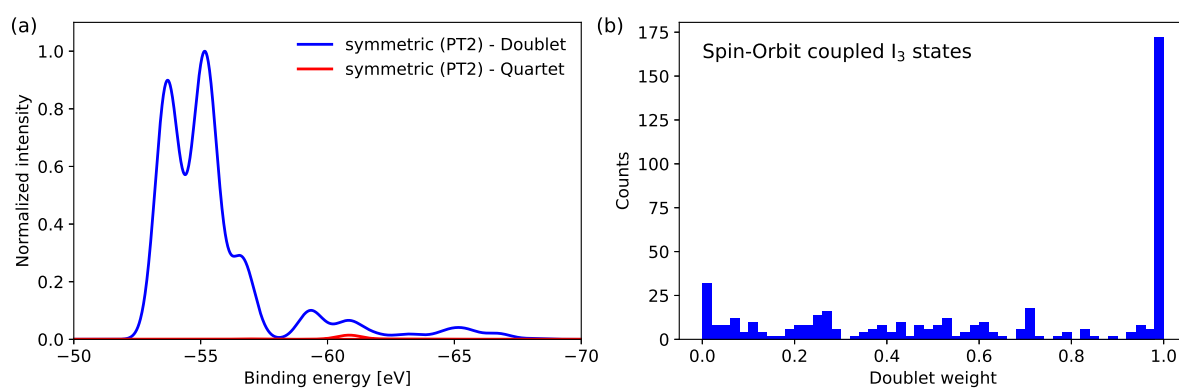
Fig. S2 Spin-orbit effects in the I_3 final states. **(a)** The RASPT2 level sudden spectrum obtained from the spin-orbit coupled states, decomposed into contributions from spin-free states with doublet and quartet multiplicities. **(b)** Histogram of the spin-orbit coupled neutral I_3 final states sorted according to their total weights of spin-free doublet states.

117
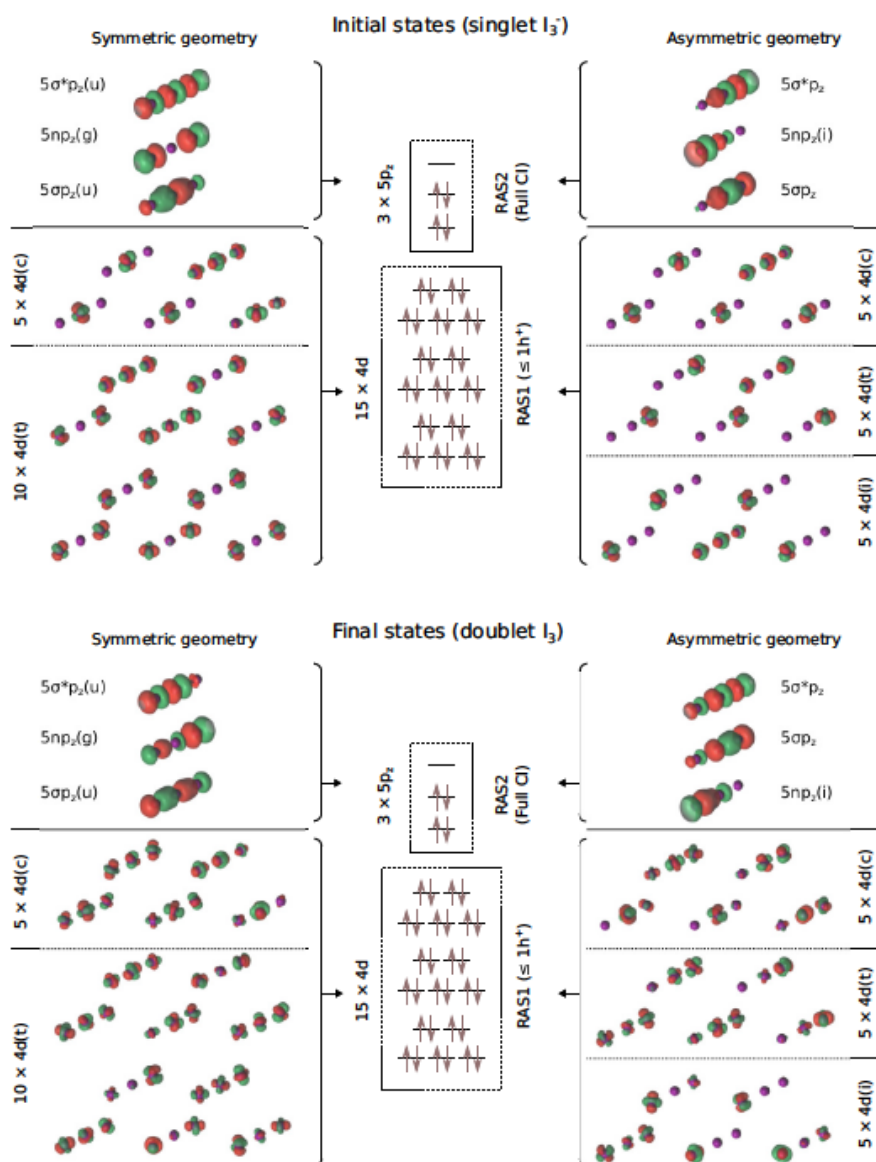
Fig. S3 Extended version of Fig. 1 from the main manuscript: Active space of the RAS(15, 3; 34 e⁻, 1 h⁺) calculations and multi-state RASPT2 natural orbitals obtained for the initial state singlet I₃⁻ species (above) and final state doublet I₃ species (below) for the spectrum simulations.

118

[GG4]   multi-reference quantum chemistry protocol for simulating autoionization spectra: Test of ionization continuum models for the neon atom

Gilbert Grell, Oliver Kühn, and Sergey I. Bokarev

Multireference quantum chemistry protocol for simulating autoionization spectra: Test of ionization continuum models for the neon atom

Gilbert Grell ⬤, Oliver Kühn ⬤, and Sergey I. Bokarev ⬤[*]

Institut für Physik, Universität Rostock, Albert-Einstein-Strasse 23-24, 18059 Rostock, Germany

In this paper we present a protocol to evaluate partial and total Auger decay rates combining the restricted active space self-consistent field electronic structure method for the bound part of the spectrum and numerically obtained continuum orbitals in the single-channel scattering theory framework. Additionally, the two-step picture is employed to evaluate the partial rates. The performance of the method is exemplified for the prototypical Auger decay of the neon $1s^{-1}3p$ resonance. Different approximations to obtain the continuum orbitals, the partial rate matrix elements, and the electronic structure of the bound part are tested against theoretical and experimental reference data. It is demonstrated that the partial and total rates are most sensitive to the accuracy of the continuum orbitals. For instance, it is necessary to account for the direct Coulomb potential of the ion for the determination of the continuum wave functions. The Auger energies can be reproduced quite well already with a rather small active space. Finally, perspectives of the application of the proposed protocol to molecular systems are discussed.

I. INTRODUCTION

Ionization triggered by photon absorption occurs along two pathways. In direct photoionization, the energy is transferred to an ejected electron. Alternatively, the system can be first put into a metastable state by a resonant excitation and afterwards decay via an autoionization mechanism. Autoionization can be approximately understood as a two-step process [1], in which the decay can be considered independently from the excitation process and interferences between direct and autoionization are neglected. For example, let us consider an atomic species, such as a neon atom that is prepared in a highly excited state $|\Psi_i\rangle$ above the continuum threshold at $E = 0$ eV (Fig. 1). This state spontaneously decays into the continuum state $|\Psi_\alpha\rangle$ consisting of the discrete state $|\Psi_f^+\rangle$ of the ion and the emitted electron, $|\psi_\alpha\rangle$, carrying the excess energy $\varepsilon_\alpha = \mathcal{E}_i - \mathcal{E}_f$. The system's electronic structure is thus encoded into the kinetic-energy spectrum of the ionized electrons. Photoelectron spectroscopy (PES) and autoionization spectroscopy (AIS) map bound states to the continuum, which makes them less sensitive to selection rule suppression and more informative than spectroscopies involving optical transitions between bound states [2–4].

Autoionization processes, predominantly Auger decay [5] but also interatomic Coulombic decay (ICD) [6] and electron transfer mediated decay (ETMD) [7], are particularly interesting on their own. Due to their correlated nature, they not only probe but also initiate or compete with intricate ultrafast electronic and nuclear dynamics (see, e.g., [8–12]). Additionally, they provide the main channel for the decay of core vacancies [13] and play a key role in biological radiation damage,

creating highly charged cations while a cascade of highly reactive low-energy electrons is emitted [11,14–17]. Further, in free-electron laser experiments operating with ultrashort intense x-ray pulses, autoionization after multiple photoionization induces the Coulomb explosion of the target, which limits the achievable spectroscopic and temporal resolution [18]. Due to this wealth of applications, autoionization and especially the local Auger effect have been studied extensively both theoretically and experimentally since their discovery by Meitner [5] and description by Wentzel [1].

Remarkably, AIS simulations of molecular systems remain challenging today, although the fundamental theory has been known for decades [19–21]. For atoms, methods combining highly accurate four-component multiconfigurational Dirac-Fock (MCDF) calculations with multichannel scattering theory are publicly available [22], whereas no such general purpose code exists for molecules. The main complication of the molecular case lies in the construction of molecular continuum states $|\Psi_\alpha\rangle$. The approaches to the simulation of AIS published during the last decades can be classified into two families—those that circumvent the continuum orbital problem and those that treat the continuum orbital explicitly.

The first family consists of the following approaches. The simplest method that allows one to assign experimental AIS is to evaluate the energetic peak positions [23–25]. Additionally, simple estimates for the partial decay rates can be obtained based on an electron population analysis [26]. More advanced approaches rely on an implicit continuum representation with Stieltjes imaging [27], a Green's-function operator [28,29], or a propagator formalism [30,31]. From this group, the Fano-Stieltjes algebraic diagrammatic construction (Fano-ADC) method [32] has been used to evaluate Auger, ICD, and ETMD decay rates of van der Waals clusters [33], first row hydrides [34], and the $[Mg(H_2O)_6]^{2+}$ cluster [11].

---

*sergey.bokarev@uni-rostock.de

042512-1
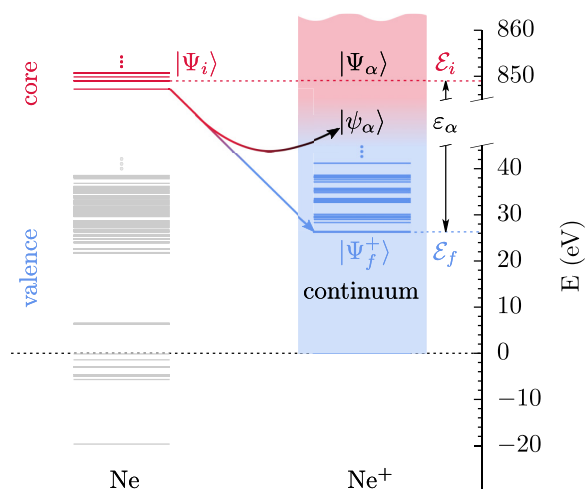
FIG. 1. Autoionization scheme for the neon atom. The core vacancy state $|\Psi_i\rangle$ with energy $\mathcal{E}_i$ (red/dark gray) decays isoenergetically into the continuum state $|\Psi_\alpha\rangle$ (black) composed of the ionic bound state $|\Psi_f^+\rangle$ with energy $\mathcal{E}_f$ (blue/gray) and the continuum orbital $|\psi_\alpha\rangle$ of the outgoing electron with the excess energy ε_α. States that do not contribute to the process are depicted in light gray; the singly ionized continuum is denoted by the color gradient/shaded area.

Therein, the continuum is approximately represented with spatially confined basis functions. However, the description of Auger electrons with kinetic energies of several hundred electronvolts requires large basis sets leading to computationally demanding simulations.

The second family, relying on an explicit representation of the continuum wave function, consists of the following approaches. The one-center approximation uses atomic continuum functions centered at the vacancy-bearing atom to describe the outgoing electron in the evaluation of partial decay rates [35–38]. This approximation can be applied on top of high-level electronic structure methods [39]. It is also applied in the XMOLECULE package [40,41], which is based on very cost efficient electronic structure calculations and atomic continuum functions. This allows for the evaluation of ionization cascades but may limit the applicability for strongly correlated systems, e.g., systems possessing a multiconfigurational character. Further, the influence of the molecular field may be taken into account perturbatively [42,43] or in a complete manner with, e.g., the single-center approach, where the whole molecular problem is projected onto a single-centered basis [44–49].

Finally, multichannel scattering theory methods that combine finite multicentered basis sets with the appropriate boundary conditions to represent the molecular continuum have been developed [50] and applied to the AIS of a variety of small systems [50–52]. For instance, the recently developed XCHEM approach [53] has been applied to simulate PES and AIS of atoms [54] and small molecular systems [55]. These techniques represent the most general and accurate quantum-mechanical treatment of the problem, thus potentially serving

as a high-level reference, although connected to substantial computational effort.

Summarizing, most of the above-mentioned methods have been applied only to simple diatomics, first row hydrides, halogen hydrides, and small molecules consisting of not more than two heavy atoms. Studies of larger molecular systems, such as tetrahedral molecules, small aldehydes, and amides [56,57]; solvated metal ions [11]; and polymers [58] are very scarce. In fact, the FANO-ADC [32,33] and the XMOLECULE [40,41] approaches are the only publicly available tools that allow one to simulate AIS for a variety of systems without restricting the molecular geometry. Further, both methods are not suited to treat systems possessing multiconfigurational wave functions. This puts studies of some chemically interesting systems having near degeneracies, e.g., transition-metal compounds, or of photodynamics in the excited electronic states, e.g., near conical intersections, out of reach. To keep up with the experimental advancements, the development of a general purpose framework to evaluate autoionization decay rates (Auger, ICD, and ETMD) for molecular systems is warranted. Such a framework should be kept accessible, transferable, and easy to use; i.e., it should be based on widespread robust and versatile quantum chemistry (QC) methods.

Here, we present a protocol that combines multiconfigurational restricted active space (RAS) self-consistent field (SCF) (RASSCF) bound-state wave functions with single-centered numerical continuum orbitals in the single-channel scattering theory framework [59]. We have chosen the RASSCF approach since it is known to yield reliable results for core-excited states [60], needed in the simulation of x-ray absorption [61,62], resonant inelastic scattering [63,64], and photoemission spectra [65–67], suggesting its application to AIS.

Although the ultimate goal is to investigate molecules, this proof-of-concept paper focuses on the simulation of the prototypical neon $1s^{-1}3p$ Auger electron spectrum (AES) to calibrate the approach, since highly accurate reference data are available from both theory [68] and experiment [69–72]. Special attention is paid to the representation of the radial continuum waves, which is investigated herein by a thorough test of different approximations. Note that our implementation allows one to calculate molecular AIS as well as PES, which will be presented elsewhere.

We commence this paper with an introduction to the underlying theory and further give important details of our implementation. The paper continues with the computational details and the benchmark of our results against theoretical and experimental references. Finally, we conclude the discussion and present perspectives for the molecular application.

II. THEORY

The approach for the calculation of partial autoionization rates consists of the following approximations.

(1) The two-step model [1] is employed; i.e., excitation and decay processes are assumed to be decoupled and interference effects between photoionization and autoionization are neglected (Fig. 1). Within this approximation, the partial

autoionization rate for the decay $i \rightarrow \alpha$ reads [19]

$$\Gamma_{i\alpha} = 2\pi |\langle \Psi_\alpha | \mathcal{H} - \mathcal{E}_i | \Psi_i \rangle|^2. \tag{1}$$

Atomic units are used throughout, unless explicitly stated otherwise.

(2) We require that all bound-state wave functions have the form of configuration interaction (CI) expansions in terms of N-electron Slater determinants:

$$|\Psi\rangle = \sum_j C_j a_{j_1,\sigma_1}^\dagger \cdots a_{j_N,\sigma_N}^\dagger |0\rangle. \tag{2}$$

The $a_{i,\sigma_i}^\dagger$ are the usual fermionic creation operators in the spin-orbital basis $\{\varphi_{i,\sigma_i}\}$. In this paper, multiconfigurational bound-state wave functions for the unionized and ionized states $|\Psi_i\rangle$ and $|\Psi_f^+\rangle$ are obtained with the RASSCF or restricted active space second-order perturbation theory (RASPT2) method. However, the presented protocol can employ any CI-like QC method.

(3) The limit of weak relativistic effects is assumed; thus, the total spins S and S^+ and their projections onto the quantization axis M and M^+ of the bound un-ionized and ionized systems are good quantum numbers. Further, S and M are conserved during the autoionization process.

(4) The single-channel scattering theory framework is employed, disregarding interchannel coupling as well as correlation effects between the bound and outgoing electrons.

(5) The continuum orbitals are treated as spherical waves, subject to the spherically averaged potential $V_f(r)$ of the ionic state $|\Psi_f^+\rangle$. Hence, the continuum orbitals have the form

$$\psi_{\alpha,\sigma}(r,\vartheta,\phi) = \frac{1}{r} w_l^{fk}(r) Y_l^m(\vartheta,\phi) \zeta(\sigma), \tag{3}$$

with spherical harmonics $Y_l^m(\vartheta,\phi)$ being the angular part and $\zeta(\sigma)$ being the spin function. For brevity, $\zeta(\sigma)$ is generally omitted and present only when needed. The composite channel index $\alpha = (f,l,m,k)$ contains the index of the ionized state f, the orbital and magnetic quantum numbers l and m, and the wave number $k = \sqrt{2\varepsilon_\alpha}$ of the continuum orbital. This notation uniquely identifies the total energy $\mathcal{E}_\alpha = \mathcal{E}_f + \varepsilon_\alpha$ and the continuum orbital and bound state for each channel $|\Psi_\alpha\rangle$. Generally, indices i and f always refer to bound states of the un-ionized and ionized species and α denotes decay channels.

The radial part $w_l^{fk}(r)/r$ is determined by solving the radial Schrödinger equation:

$$\left[\frac{d^2}{dr^2} + 2\left(\frac{k^2}{2} - V_f(r)\right) - \frac{l(l+1)}{r^2} \right] w_l^{fk}(r) = 0. \tag{4}$$

With the assumptions 1–5, the N-electron ionized continuum states with conserved total spin and projection of the un-ionized states, S and M, can be written as

$$|\Psi_\alpha\rangle = \sum_{M^+=-S^+}^{S^+} \sum_{\sigma=-\frac{1}{2},\frac{1}{2}} C_{S^+,M^+;\sigma}^{S,M} |\Upsilon_\alpha^{\sigma M^+}\rangle, \tag{5}$$

where σ is the spin projection of the outgoing electron. The Clebsch-Gordan coefficients $C_{S^+,M^+;\sigma}^{S,M} = \langle S,M|S^+,M^+;\frac{1}{2},\sigma\rangle$ couple the channel functions $|\Upsilon_\alpha^{\sigma M^+}\rangle$. These are constructed by inserting an additional electron with the continuum orbital

$|\psi_{\alpha,\sigma}\rangle$ into the bound ionic state with spin projection M^+, retaining the antisymmetry:

$$|\Upsilon_\alpha^{\sigma M^+}\rangle = a_{\alpha,\sigma}^\dagger |\Psi_{f,M^+}^+\rangle. \tag{6}$$

Note that in contrast to the continuum state $|\Psi_\alpha\rangle$, which is an eigenstate of $\mathbf{S}^2$ and S_z, the $|\Upsilon_\alpha^{\sigma M^+}\rangle$ are not eigenfunctions of $\mathbf{S}^2$, but only of S_z.

III. DETAILS OF THE IMPLEMENTATION

A. Model potentials

We commence with the discussion of different approximations to the potential $V_f(r)$ in Eq. (4), which are central for the quality of the free-electron function. In this paper, we have used the following models:

$$V^{\text{free}} = 0, \tag{7a}$$

$$V^{\text{eff}}(r) = -\frac{Z_{\text{eff}}}{r}, \tag{7b}$$

$$V_f^{\text{scr}}(r) = -\frac{Z_f(r)}{r}, \tag{7c}$$

$$V_f^{\text{J}}(r) = -\frac{Z}{r} + J_f(r), \tag{7d}$$

$$V_f^{\text{JX}}(r) = -\frac{Z}{r} + J_f(r) + X_f^{\text{S}}(r). \tag{7e}$$

In words, we use (a) no potential; (b) an effective Coulomb potential with a fixed charge Z_{eff}; (c) the screened Coulomb potential of an ionic state f with the charge $Z_f(r)$ varying with distance; (d) the nuclear, $-Z/r$, and spherically averaged direct potential of the ionic state, $J_f(r)$; and (e) the potential of approach (d) augmented with Slater's exchange term $X_f^{\text{S}}(r)$ [73]. Details on the definition of $Z_f(r)$, $J_f(r)$, and $X_f^{\text{S}}(r)$ are given in Appendix A.

B. Continuum orbitals

The solutions to the radial Schrödinger equation, Eq. (4), using the potentials (7a)–(7e) can be understood as follows: In approach (a), assuming a free particle, we completely neglect any influence of the ion onto the outgoing electron. Here, the radial part of $\psi_{\alpha,\sigma}(r,\vartheta,\varphi)$ corresponds to spherical Bessel functions $j_l(kr)$ [74]:

$$\psi_{\alpha,\sigma}^{\text{free}}(r,\vartheta,\phi) = \sqrt{\frac{2}{\pi}} k j_l(kr) Y_l^m(\vartheta,\phi) \zeta(\sigma). \tag{8}$$

The prefactor $\sqrt{\frac{2}{\pi}}k$ ensures the correct normalization,

$$\langle \psi_{\alpha,\sigma} | \psi_{\alpha',\sigma'} \rangle = \delta_{ll'} \delta_{m_l m_l'} \delta_{\sigma\sigma'} \delta(\varepsilon_\alpha - \varepsilon_{\alpha'}), \tag{9}$$

which is exact only for the free-particle approach, and approximate for all other potentials, due to the long-range Coulomb distortion.

An effective Coulomb form [approach (b)] is the simplest approach to approximately account for the ionic potential. It has the advantage that the solutions to Eq. (4) are still analytically available in the form of regular Coulomb functions

F_l [74]:

$$\psi_{\alpha,\sigma}^{\text{eff}}(r,\vartheta,\phi) = \sqrt{\frac{2}{\pi k}} \frac{F_l(\eta,kr)}{r} Y_l^m(\vartheta,\phi)\zeta(\sigma), \qquad (10)$$

with $\eta = -Z_{\text{eff}}/2k$.

Approaches (c)–(e) employ numerically obtained potentials according to Eqs. (7c)–(7e) and thus require a numerical solution of the radial Schrödinger equation (4). It is done using Numerov's method and the numerically obtained radial waves are scaled so as to satisfy the asymptotic boundary conditions:

$$w_l^{fk}(r \to 0) = nr^{l+1}, \qquad (11a)$$

$$w_l^{fk}(r \to \infty) = \sqrt{\frac{2}{\pi k}}\Big[\cos\delta_l^f(k)F_l(\eta,kr) \\ + \sin\delta_l^f(k)G_l(\eta,kr)\Big]. \qquad (11b)$$

The scaling factors and phase shifts $\delta_l^f(k)$ are obtained by matching the numerical solutions and their first derivatives with a linear combination of the regular and irregular Coulomb functions F_l and G_l (see [74]). This matching is carried out in the asymptotic region, where the potential is well approximated by the Coulomb potential of the ions' net charge $V_f(r) \approx -Z_{\text{net}}/r$.

Since the screened Coulomb potential model, Eq. (7c), is an *ad hoc* assumption based on the simple idea that the nuclear charge is screened by the integrated electron density, the applicability of this model needs to be tested. In turn, approaches (d) and (e), employing the spherically averaged direct Coulomb and exchange terms according to Eqs. (7d) and (7e), in a sense correspond to the Hartree and Slater-X_α levels of accuracy, respectively.

The continuum orbitals obtained by any of these methods are not orthogonal to the bound orbitals, which is in contrast to the behavior that an exact continuum orbital would possess.

C. Continuum matrix elements

Using the decomposition of the continuum states in terms of channel functions in Eq. (5) and separating the Hamiltonian into its one- and two-electron parts $\mathcal{H} = \sum_u h_u + \sum_{u<v} 1/r_{uv}$, the partial decay rate becomes

$$\Gamma_{i\alpha} = 2\pi \Bigg| \sum_{M^+,\sigma} C_{S^+,M^+;\sigma}^{S,M} \Bigg[\sum_u \langle \Upsilon_\alpha^{\sigma M^+} | h_u | \Psi_i \rangle \\ + \sum_{u<v} \langle \Upsilon_\alpha^{\sigma M^+} | \frac{1}{r_{uv}} | \Psi_i \rangle - \mathcal{E}_i \langle \Upsilon_\alpha^{\sigma M^+} | \Psi_i \rangle \Bigg] \Bigg|^2. \quad (12)$$

Here, u and v are electron indices, h_u contains the electronic kinetic-energy and electron-nuclei attraction terms, and $1/r_{uv}$ is the electron repulsion.

The expressions for the overlap and one- and two-electron matrix elements in Eq. (12) are obtained by using Löwdin's-Slater determinant calculus [75]. Here one has to take into account that the un-ionized and ionized bound states are obtained in separate SCF calculations. Consequently, they have different sets of N_{orb} spin orbitals $\{\varphi_i\}$ and $\{\varphi_i^+\}$ that are not mutually orthogonal. The spin coordinates are implicitly assumed to be assigned as introduced in Eq. (2). Then, the

respective creation and annihilation operators are $a_i^\dagger$, a_i and $(a_i^+)^\dagger$, a_i^+.

With this, the overlap integral in Eq. (12) can be rearranged into the overlap of the continuum orbital and the Dyson orbital (DO) $|\Phi_{i\alpha}^{M^+}\rangle$:

$$\langle \Upsilon_\alpha^{\sigma M^+} | \Psi_i \rangle = \langle \psi_{\alpha,\sigma} | \Phi_{i\alpha}^{M^+} \rangle. \qquad (13)$$

The DO is generally defined as the $N-1$ particle overlap of the un-ionized and ionized states $|\Psi_i\rangle$ and $|\Psi_{f,M^+}^+\rangle$ that are associated with the channel α and can be expressed in second quantization form as a linear combination of the spin orbitals $\{\varphi_s\}$ of the un-ionized species, with the coefficients $\phi_{\alpha,s}^{M^+}$:

$$|\Phi_{i\alpha}^{M^+}\rangle = \sum_{s=1}^{N_{\text{orb}}} \underbrace{\langle \Psi_{f,M^+}^+ | a_s | \Psi_i \rangle}_{\phi_{\alpha,s}^{M^+}} |\varphi_s\rangle. \qquad (14)$$

Staying on this route, the one- and two-electron transition matrix elements in Eq. (12) can be expressed as

$$\sum_u \langle \Upsilon_\alpha^{\sigma M^+} | h_u | \Psi_i \rangle = \langle \psi_{\alpha,\sigma} | h | \Phi_{i\alpha}^{M^+} \rangle + \langle \psi_{\alpha,\sigma} | \tilde{\Phi}_{i\alpha}^{1,M^+} \rangle \quad (15)$$

and

$$\sum_{u<v} \langle \Upsilon_\alpha^{\sigma M^+} | \frac{1}{r_{uv}} | \Psi_i \rangle = \sum_{q=1}^{N_{\text{orb}}} \langle \psi_{\alpha,\sigma} \varphi_q^+ | \frac{1}{r_{12}} | \Xi_{i\alpha}^{M^+,q} \rangle \\ + \langle \psi_{\alpha,\sigma} | \tilde{\Phi}_{i\alpha}^{2,M^+} \rangle. \qquad (16)$$

Here, $|\Xi_{i\alpha}^{M^+,q}\rangle$ is the two-electron reduced transition density

$$|\Xi_{i\alpha}^{M^+,q}\rangle = \sum_{s_1 \neq s_2}^{N_{\text{orb}}} \langle \Psi_{f,M^+}^+ | (\hat{a}_q^+)^\dagger \hat{a}_{s_1} \hat{a}_{s_2} | \Psi_i \rangle | \varphi_{s_1} \varphi_{s_2} \rangle, \qquad (17)$$

and $|\tilde{\Phi}_{i\alpha}^{n,M^+}\rangle$ are the one- and two-electron conjugated Dyson orbitals for $n = 1$ and 2, respectively [see Eqs. (B3) and (B4)]. A simpler formulation of the non-orthogonal (NO) terms proposed in [76] is not used herein, because in practice it is not always strictly equivalent to our approach (see Sec. II of Supplemental Material [77] for details).

The strong orthogonality (SO) approximation, i.e., the assumption that the overlaps of the continuum and all un-ionized orbitals are zero, $\langle \psi_{\alpha,\sigma} | \varphi_{i,\sigma_i} \rangle = 0$, implies that the overlap integrals between the continuum and the ordinary and conjugated Dyson orbitals in Eqs. (13), (15), and (16) vanish. Since the evaluation of the conjugate DOs can be quite involved, SO approximation substantially simplifies the computation.

A similar effect is achieved by using the Gram-Schmidt (GS) orthogonalization to project the orbitals of the ionized system out of the continuum functions and enforce $\langle \psi_{\alpha,\sigma}^{\text{GS}} | \varphi_{i,\sigma_i}^+ \rangle = 0$. This approach has been tried before, e.g., in [44], and will be tested herein as well.

In the following, we will use the labels SO, NO, and GS to indicate that the overlap terms in Eqs. (13), (15), and (16) have been neglected (SO) or fully included (NO) and that GS orthogonalized continuum functions have been used to evaluate the partial rates including the NO terms as well. Further, we also compare the results of the "full" Hamiltonian

TABLE I. QC setups and number of states used in the state-averaged RASSCF calculations.

QC	Basis set	Active space	States Ne/Ne$^+$	X2C
I	$[7s6p3d2f]$	RAS(8; 1, 1)	41/132	No
II	$[22s6p3d2f]$-rcc	RAS(8; 1, 1)	41/132	Yes
III	$[9s8p5d4f]$	RAS(26; 1, 1)	131/420	No

coupling against the popular choice to account only for the two-electron terms in Eq. (12), denoting them as $\mathcal{H}$ and r^{-1} coupling, respectively. The combination of matrix elements corresponding to each approach is detailed in Appendix B.

To sum up, the present paper reports on the influence of different combinations of the introduced approximations to the potentials, transition matrix elements, and continuum orbitals on the partial Auger decay rates of the exemplary neon $1s^{-1}3p$ resonance. As a shorthand notation for the combination of the different approximations we will use the (coupling)-(potential)-(nonorthogonality) notation, where applicable. For instance, $\mathcal{H}$-$V_f^{\mathrm{JX}}(r)$-NO denotes partial rates obtained using the $\mathcal{H}$ coupling, with radial waves corresponding to the $V_f^{\mathrm{JX}}(r)$ potential and including the overlap terms.

IV. COMPUTATIONAL DETAILS

A. Quantum chemistry for bound states

The wave functions of the bound neutral and ionic states have been obtained in separate state-averaged RASSCF calculations with a locally modified version of MOLCAS 8.0 [78]. To prevent mixing of different angular momentum basis functions into one orbital, the "atom" keyword has been employed. The QC schemes used to evaluate the bound states $|\Psi_i\rangle$ and $|\Psi_f^+\rangle$ are presented in Table I. The RAS formalism is a flexible means to select electronic configurations. Therein, the AS is subdivided into three subspaces RAS1, RAS2, and RAS3. The RAS notation that is used throughout the paper is to be understood as follows. In all spaces, the $1s$ orbital forms the RAS1 subspace and the $2s$ and $2p$ orbitals build up the RAS2 one. The occupation of the $2s$ and $2p$ orbitals in RAS2 is not restricted, while only h electrons may be removed from RAS1. Finally the RAS3 subspace contains v virtual orbitals that can be occupied by at most p electrons. Thus, we can herein uniquely specify each AS as RAS($v; h, p$). The ASs used in this paper are as follows: RAS(8; 1, 1), containing $3s$, $3p$, $4s$, and $4p$ orbitals in the RAS3; RAS(26; 1, 1), enlarging RAS3 by the $3d$, $4d$, $5s$, $5p$, $6s$, and $6p$ orbitals; and RAS(33; 1, 1), adding the $4f$ orbitals. The number of configurations possible with each AS is shown in Table II. For all QC schemes (see Table I) all states are included in the RASSCF procedure for

TABLE II. Maximum number of configurations for each AS.

RAS	RAS(8; 1, 1)	RAS(26; 1, 1)	RAS(33; 1, 1)
Ne	41	131	166
Ne$^+$	197	629	797

the Ne wave functions, while the core excited states have been excluded for the calculations of Ne$^+$.

Atomic natural orbital (ANO) type basis sets have been employed using a $(22s17p12d11f)$ primitive set. It was constructed by supplementing the ANO exponents for neon [79] in each angular momentum with eight Rydberg exponents generated according to the scheme proposed by Kaufmann *et al.* [80]. The contractions were then obtained with the GENANO module [81] of OPENMOLCAS [82] using density matrices from state averaged RASSCF calculations for Ne and Ne$^+$ with the RAS(33; 1, 1) AS. All 166 possible states for Ne have been taken into account, but for Ne$^+$ the core excited manifold has been excluded, leading to 532 states. To get the final basis set, the sets obtained for Ne and Ne$^+$ have been evenly averaged. In this paper, we use the following contractions: $[7s6p3d2f]$, obtained by the procedure described above; $[9s8p5d4f]$, corresponding to $[7s6p3d2f]$ supplemented with Rydberg contractions that resulted from the GENANO procedure using the "rydberg" keyword; and $[22s6p3d2f]$-rcc, similiar to $[7s6p3d2f]$ but with uncontracted s functions and scalar relativistic corrections according to the exact two component decoupling (X2C) scheme [83] (see Supplemental Material [77]).

All energies have been corrected using the single state RASPT2 method [84] with an imaginary shift of 0.01 a.u. To be consistent with the basis set generation, scalar relativistic effects have only been included for QC II. The RAS state interaction [85] module of MOLCAS was used to compute the biorthonormally transformed orbital and CI coefficients [86] for the atomic and ionic states: $\{\varphi_i\}, \{C_j\} \rightarrow \{\tilde{\varphi}_i\}, \{\tilde{C}_j\}$ such that $\langle \tilde{\varphi}_i^+ | \tilde{\varphi}_j \rangle = \delta_{ij}$, while the total wave functions remain unchanged. This biorthonormal basis is used in the evaluation of the Dyson orbitals [Eqs. (14), (B3), and (B4)] and two-electron reduced transition densities [Eq. (17)].

B. Matrix elements in the atomic basis

The matrix elements between bound orbitals occurring in Eqs. (12), (15), and (16) are evaluated by transforming the orbitals to the atomic basis and calculating the atomic basis integrals with the LIBCINT library [87]. The most time consuming part in the computation of the partial decay rates using Eq. (12) is the estimation of the two-electron continuum-bound integrals. Transforming the two-electron reduced transition densities and the orbitals to the atomic basis $\{\chi_i\}$ and neglecting the spin integration, the two-electron continuum-bound integrals used in the practical evaluation of Eq. (16) read as

$$\langle \alpha a | bc \rangle = \int \psi_\alpha^*(\mathbf{r}_1) \chi_b(\mathbf{r}_1) \underbrace{\left[\int \frac{\chi_a^*(\mathbf{r}_2) \chi_c(\mathbf{r}_2)}{r_{12}} d\mathbf{r}_2^3 \right]}_{f_{ac}(\mathbf{r}_1)} d\mathbf{r}_1^3. \tag{18}$$

The function $f_{ac}(\mathbf{r}_1)$ is similar to an atomic nuclear attraction integral and is evaluated as a function of $\mathbf{r}_1$ using the LIBCINT library [87]. An important point is to exploit the fact that the kinetic energy of the continuum electron is only encoded in its radial part. Transforming to spherical coordinates $\mathbf{r} \rightarrow (r, \Omega)$ centered at the origin of the outgoing electron allows one to

separate off the radial integration:

$$
\langle \alpha a | bc \rangle = \int_0^\infty r w_l^{fk}(r)
$$
$$
\times \underbrace{\left[\int_\Omega Y_l^m(\Omega) \chi_b(\mathbf{r}(r, \Omega)) f_{ac}(\mathbf{r}(r, \Omega)) d\Omega \right]}_{F_{abc}(r)} dr.
$$
(19)

The angular integral in $F_{abc}(r)$ is determined numerically by using the adaptive two-dimensional integration routine CUHRE from the CUBA 4.2 library [88]. To reduce the number of points at which $F_{abc}(r)$ is evaluated, an adaptive spline interpolation is used, which was developed by us and implemented in our code. Therein, the grid spacing is adjusted such that the absolute error estimate of the interpolation is kept lower than 10^{-6} a.u. on each region with a different spacing. Note that the $F_{abc}(r)$ are determined only once, while the final radial integration in Eq. (19) needs to be evaluated for every transition $i \to \alpha$. The radial integration in Eq. (19) is carried out using the Simpson rule. For the one-electron continuum-bound integrals that are needed in the evaluation of the one-electron matrix elements in Eq. (12), an analogous approach has been implemented. This protocol has been developed aiming for the application to molecular systems. Hence, it does not exploit that the atomic orbitals are eigenstates of angular momentum operators, which would be usual in a purely atomic approach.

V. RESULTS AND DISCUSSION

Here, we perform a thorough benchmark of the approaches to evaluate AES presented in Sec. II on the exemplary Auger decay of the neon $1s^{-1}3p$ resonance. First, in Sec. V A, we compare the AES modeled with our protocol against data obtained from an atomic MCDF calculation [68], which serves as a high level theoretical reference. Second, in Sec. V B, we undertake the comparison to experimental results. The comparison against both theory and experiment is needed since no uniform and highly resolved experimental data covering the full energy range discussed herein have been published to date.

A. Benchmark of theoretical models

Panel (a) of Fig. 2 shows neon AESs, resulting from the autoionization of the $1s^{-1}3p$ states, obtained using bound-state wave functions from QC scheme I (see Table I) with radial waves corresponding to the spherically averaged direct-exchange potential $V_f^{JX}(r)$ [Eq. (7e)]. The partial rates have been evaluated using the full $\mathcal{H}$ coupling as well as the approximate r^{-1} coupling in Eq. (12). Further, the nonorthogonality of the continuum and bound orbitals was accounted for by including the overlap terms, NO [see Eqs. (13), (15), and (16)]. A spectrum employing r^{-1} coupling at the MCDF level, obtained by Stock *et al.* [68] with the RATIP package [22], serves as a theoretical benchmark. Therein, the atomic structure was obtained with a configuration space including single-electron excitations from the $1s$, $2s$, and $2p$ to the np up to $n = 7$ and $3d$ orbitals. The four-component continuum

orbitals have been obtained as distorted waves within the potential of the respective ionized atomic state.

All spectra have been constructed by assigning a Gaussian line shape with a full width at half maximum (FWHM) of $\gamma = 0.1$ eV to each channel:

$$
\text{AES}_{1s^{-1}3p}(\varepsilon) = \sum_\alpha \Gamma_{1s^{-1}3p\alpha} G(\varepsilon - \varepsilon_\alpha, \gamma),
$$
(20)

where $G(\varepsilon, \gamma) = \sqrt{\ln 2/(\pi \gamma)} \exp(-4 \ln 2 \varepsilon^2 / \gamma^2)$, ε is the kinetic energy of the emitted electrons, and $\varepsilon_\alpha = \mathcal{E}_{1s^{-1}3p} - \mathcal{E}_f$ is the Auger electron energy of the channel $|\Psi_\alpha\rangle$. The spectra were normalized to the peak height at 811.5 eV, and shifted globally by -5.35 eV (QC I) and -2.45 eV (MCDF) such that the peak at 811.5 eV is aligned to the experimental data taken from Kivimäki *et al.* [69] (see Fig. 4). In addition, the dominant continuum orbital angular momentum contribution to the intensity is indicated for each peak. This shows that the regions 743–765, 765–800, and 800–825 eV correspond almost exclusively to the emission of s, p, and d waves, respectively, with the exception that the peaks at 803 and 808 eV lie in the d region but are due to s-wave emission. Hence, we will refer to these regions as s, p, and d, rather than using the energies, in what follows.

It is evident from Fig. 2(a) that the normalized AESs obtained for the $\mathcal{H}$ and r^{-1} couplings are almost indistinguishable in the s and d regions. In contrast, the features in the p region at 771 and 776 eV are enhanced by 10%, while the small bands in the range 783–788 eV are reduced by about 40%, if the $\mathcal{H}$ coupling terms are included. The overall effect on the spectrum, however, is still rather small and neglecting the contributions beyond the r^{-1} coupling in the partial rate evaluation seems to be justified in this case. The comparison with the MCDF data in the d region shows that the Auger energies and relative intensities are overall quite well reproduced by our approach. Only the intensities of two small satellite peaks at 803 and 809 eV are overestimated and three tiny features around 805.5–807.5 eV are not present when using our approach. The latter deficiency can be safely attributed to the smaller configuration space employed in the QC I scheme as compared to the one used to obtain the MCDF results in [68]. Looking at the s and p regions, the Auger energies from the QC model I become slightly but increasingly blueshifted with respect to the MCDF ones at the lower-energy flank of the spectrum. The intensities in turn are considerably overestimated by factors of about 5 and 2 for the s and p regions, respectively. Note that very similar spectra are obtained if the RASPT2 energy correction is not used (see Supplemental Material [77] Fig. S1).

Panels (b) and (c) of Fig. 2 show the integrated decay rates for the s, p, and d regions evaluated using QC model I with the r^{-1} (b) and $\mathcal{H}$ (c) couplings, comparing different approaches to compute the partial decay rates. The respective spectra are given in Supplemental Material [77] Figs. S2–S7. The rates were obtained for all combinations of potential models in Eqs. (7a)–(7e) with the different nonorthogonality approaches SO, NO, and GS for the continuum orbitals. Since no absolute rates for the MCDF results are available, these have been scaled to the total decay rate obtained using the r^{-1}-$V_f^{JX}(r)$-NO treatment. The data in panels (b) and (c) show
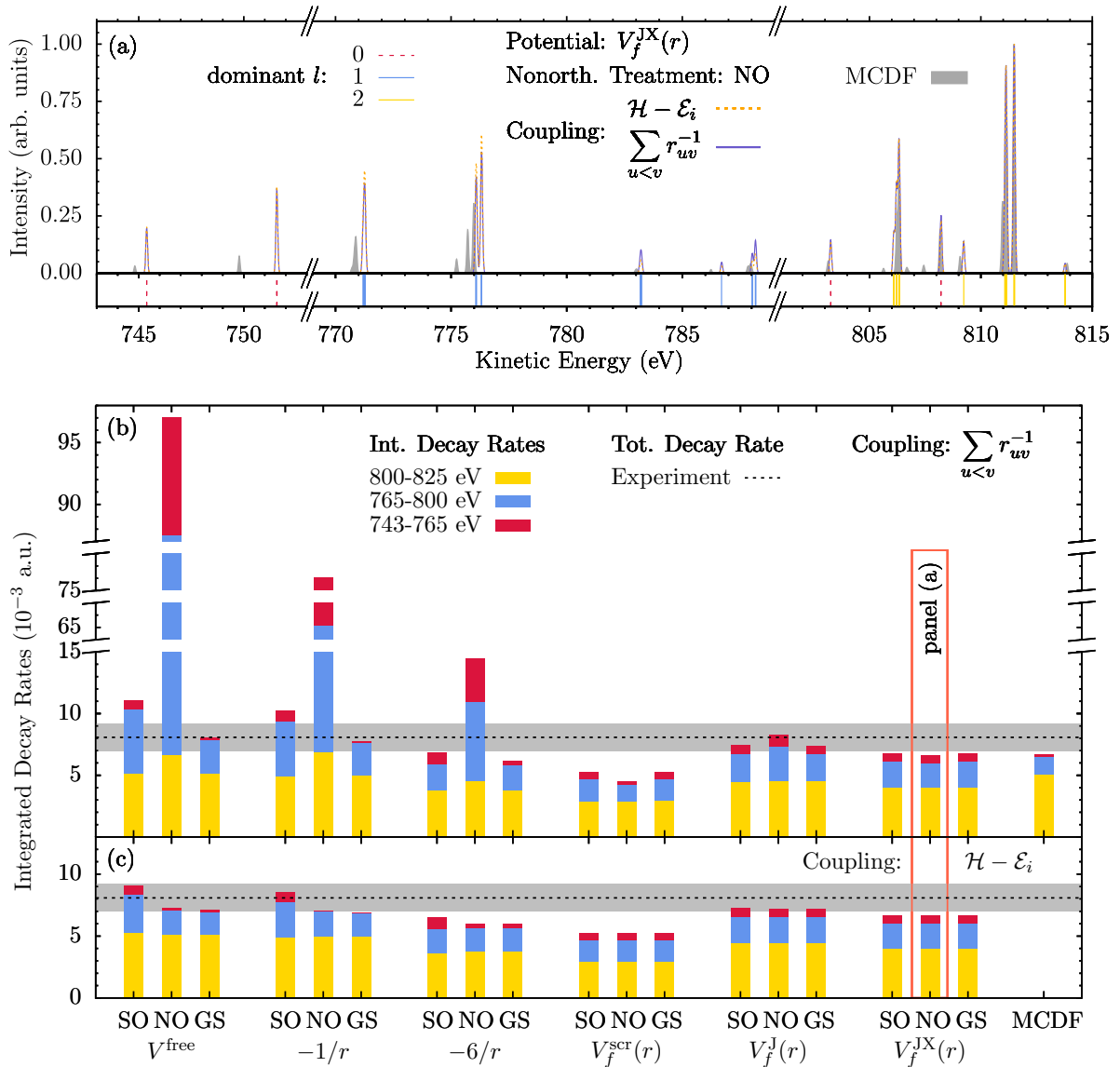
FIG. 2. (a) Neon $1s^{-1}3p$ AES obtained with the r^{-1} and $\mathcal{H}$ couplings and the NO approach using continuum orbitals generated by the $V_f^{\text{JX}}(r)$ potential are shown in comparison to the MCDF results reported by Stock *et al.* [68]. All spectra are broadened using a Gaussian profile with an FWHM of 0.1 eV, normalized to the peak at 811.5 eV, and shifted globally to align the 811.5-eV peak with experimental data [69]. The spectra from panel (a) correspond to the NO histograms of the $V_f^{\text{JX}}(r)$ potential in panels (b) and (c). The vertical lines at the bottom of panel (a) indicate the predominant continuum orbital angular momentum (l) contribution to each peak. (b), (c) Auger decay rates integrated over the given energy ranges corresponding to distinct l contributions. The decay rates have been evaluated based on QC model I for the r^{-1} (b) and $\mathcal{H}$ (c) couplings. The radial continuum functions correspond to the depicted potentials. Nonorthogonality of the continuum and bound orbitals was treated with the SO, NO, and GS approaches (see text). The MCDF data have been scaled such that the total decay rate matches the one obtained for the r^{-1}-$V_f^{\text{JX}}(r)$-NO approach. For reference, the experimentally determined total rate of $8.08 \pm 1.1 \times 10^{-3}$ a.u. $(0.22 \pm 0.03$ eV) [89] is depicted as a horizontal dashed line. The gray region indicates the experimental uncertainty.

that the decay rates corresponding to the s, p, and d spectral regions converge for both couplings as the quality of the potential is increased from the free-particle approximation V^{free} to the spherically averaged direct-exchange potential $V_f^{\text{JX}}(r)$. The $s:p:d$ ratio obtained from the MCDF spectrum,

however, is not matched. Our approaches systematically overestimate the decay rates due to the s and p channels, in line with the mismatch of intensities unveiled in panel (a).

Prominently, using the approximate r^{-1} coupling together with the NO overlap terms leads to an overestimation of the

s and p regions with respect to the SO results by an order of magnitude for V^{free} and $-1/r$, and by factors of 4 and 3 for $-6/r$. In contrast, employing the SO approximation or GS orthogonalized continuum orbitals results in more realistic decay rates. Here, the GS rates reproduce the SO ones for the d region but are considerably smaller in the s and p regions. However, when either of the more physically sound potentials $V_f^{\text{scr}}(r)$, $V_f^{\text{J}}(r)$, or $V_f^{\text{JX}}(r)$ is used, the choice of the nonorthogonality treatment has only a weak influence on the integrated decay rates. This characteristic is due to the continuum-bound orbital overlaps that decrease if more realistic potentials are chosen, causing the NO overlap terms in Eqs. (13), (15), and (16) as well as the effect of the GS orthogonalization to become negligible. Adding to this, the general insensitivity of the d region to the nonorthogonality treatment is explained by the fact that the overlap of the d continuum waves with the bound orbitals vanishes independently of the potential model. The overlap integrals are given in Supplemental Material [77] Table S1.

Generally, the inclusion of the $\mathcal{H}$ coupling, Fig. 2(c), yields mostly smaller total decay rates and less pronounced differences between the SO, NO, and GS results. The SO decay rates are usually the largest when $\mathcal{H}$ coupling is applied, while the NO and GS ones are smaller, underestimating the s and p regions for V^{free}, $-1/r$, and $-6/r$, with respect to SO. Noteworthy, the huge overestimation due to the combination of r^{-1} coupling and NO terms is mitigated completely. The reason is that the NO contribution to the matrix element is determined by cancellation effects between different one- and two-electron NO terms rather than their individual magnitude. Neglecting the one-electron contributions in r^{-1} coupling prohibits this error cancellation, leading to the immense overestimation observed for V^{free}, $-1/r$, and $-6/r$. Similarly, the agreement between the GS and NO results for these potentials is not because the effect of the GS orthogonalization is minute, but again due to the cancellation.

We conclude the discussion of this figure with the observation that the total rates obtained with the $V_f^{\text{J}}(r)$ and $V_f^{\text{JX}}(r)$ potentials reproduce the experimentally observed decay rate [89]. Independent of the chosen approach, the best match is obtained with the $V_f^{\text{J}}(r)$ potential, whereas the $V_f^{\text{JX}}(r)$ potential leads to slightly underestimated total rates, which can be attributed to the inclusion of the attractive exchange term, Eq. (A5). Similarly, we assign the considerable underestimation of the total decay rates by the $V_f^{\text{scr}}(r)$ potential to the fact that it is more attractive in the core region than $V_f^{\text{JX}}(r)$ (see Fig. 3). The $-6/r$ potential yields total rates and spectra that are in approximate agreement with those obtained for $V_f^{\text{J}}(r)$ and $V_f^{\text{JX}}(r)$ apart from the case when r^{-1} coupling and the NO terms are used (spectra in Supplemental Material [77] Figs. S2–S7). Notably, the total rates obtained in $\mathcal{H}$ coupling with the effective potentials V^{free} and $-1/r$ agree well with the experimental reference. However, despite the good agreement in the total rates the spectra for these approaches deviate in the p region considerably from the ones obtained for the more accurate potentials (see Supplemental Material [77] Figs. S5–S7), indicating that this agreement is rather accidental.

To shed light on the influence of different potentials on the total decay rates and spectra obtained with QC model

I, $\mathcal{H}$ coupling, and the NO approach, potentials, radial continuum functions, and spectra are presented in Fig. 3. Panel (a) contains the normalized AESs obtained using the potentials $-1/r$, $-6/r$, $V_f^{\text{scr}}(r)$, and $V_f^{\text{JX}}(r)$. The spectra have been shifted vertically for the sake of clarity. Shifts and broadening parameters are the same as in Fig. 2(a). The d region is represented very well with all potential models, with the exclusion that the satellite bands at 803 and 808 eV are barely present when using the $-1/r$ potential. In contrast, the relative intensities of the s and p regions of the spectra are strongly affected by the choice of the potential. Here, the p region consists of two peak groups with different character. Using the $V_f^{\text{JX}}(r)$ results as a reference for this discussion, the peaks around 771 and 776 eV are overestimated by 30% with $V_f^{\text{scr}}(r)$, almost reproduced with $-6/r$ and underestimated by a factor of 4 when using $-1/r$. In contrast, the bands between 783 and 788 eV behave in an inverse manner. Namely, they are underestimated by 50% with $V_f^{\text{scr}}(r)$ and overestimated by 50% and a factor of 4 with $-6/r$ and $-1/r$, respectively. This behavior of the screened and the effective Coulomb potentials is caused by the fact that $V_f^{\text{scr}}(r)$ is more attractive and $-1/r$ as well as $-6/r$ are less attractive than $V_f^{\text{JX}}(r)$, as depicted in panels (b)–(d). This trend is solely dictated by the potential but not the coupling or nonorthogonality treatment; note the exception of the r^{-1}-NO combination (see Supplemental Material [77] Figs. S2–S7). Finally, in the s region, the tighter potential results in larger intensities: $-1/r$ and $-6/r$ lead to an underestimation by an order of magnitude and 35%, respectively, whereas $V_f^{\text{scr}}(r)$ yields an overestimation by 25%.

For each region, the radial waves and respective potentials, including the angular momentum term, are shown in panels (b)–(d) corresponding to the characteristic peaks denoted in panel (a). Note that the V^{free} and $V_f^{\text{J}}(r)$ cases are very similar to the $-1/r$ and $V_f^{\text{JX}}(r)$ ones, respectively, and have been excluded from the discussion of this figure. The respective spectra are given in Supplemental Material [77] Fig. S7. One might understand the differences in the sensitivity of the s, p, and d spectral regions to the potential by comparing the short-range behavior of the radial waves $w_l^{fk}(r)/r$ [Eq. (11a)] with the electron density that is sharply peaked in the core region. This suggests that the matrix elements in Eq. (12) are very sensitive to the description of the continuum orbitals in this region. It is well known that only the s waves have a considerable contribution at the core, since the radial functions tend to zero as r^l. In fact, the effective radial potential at the core is dominated by the angular momentum term for $l > 0$, meaning that the influence of the present potential models on the total rates should decrease with increasing l. Regarding the relative changes of the integrated decay rates within each region, this is true for $\mathcal{H}$ and r^{-1} coupling, when the NO overlap terms are included, irrespective of whether the GS orthogonalization is used in addition or not [Figs. 2(b) and 2(c)]. However, under the SO approximation for r^{-1} coupling, the p spectral region is more sensitive to variations in the potential model than the s region. In fact, for the s waves it is seen that only the potentials $V_f^{\text{scr}}(r)$ and $V_f^{\text{JX}}(r)$ lead to similar radial waves, the slight differences being due to the fact that the screening model is too attractive in the core region.
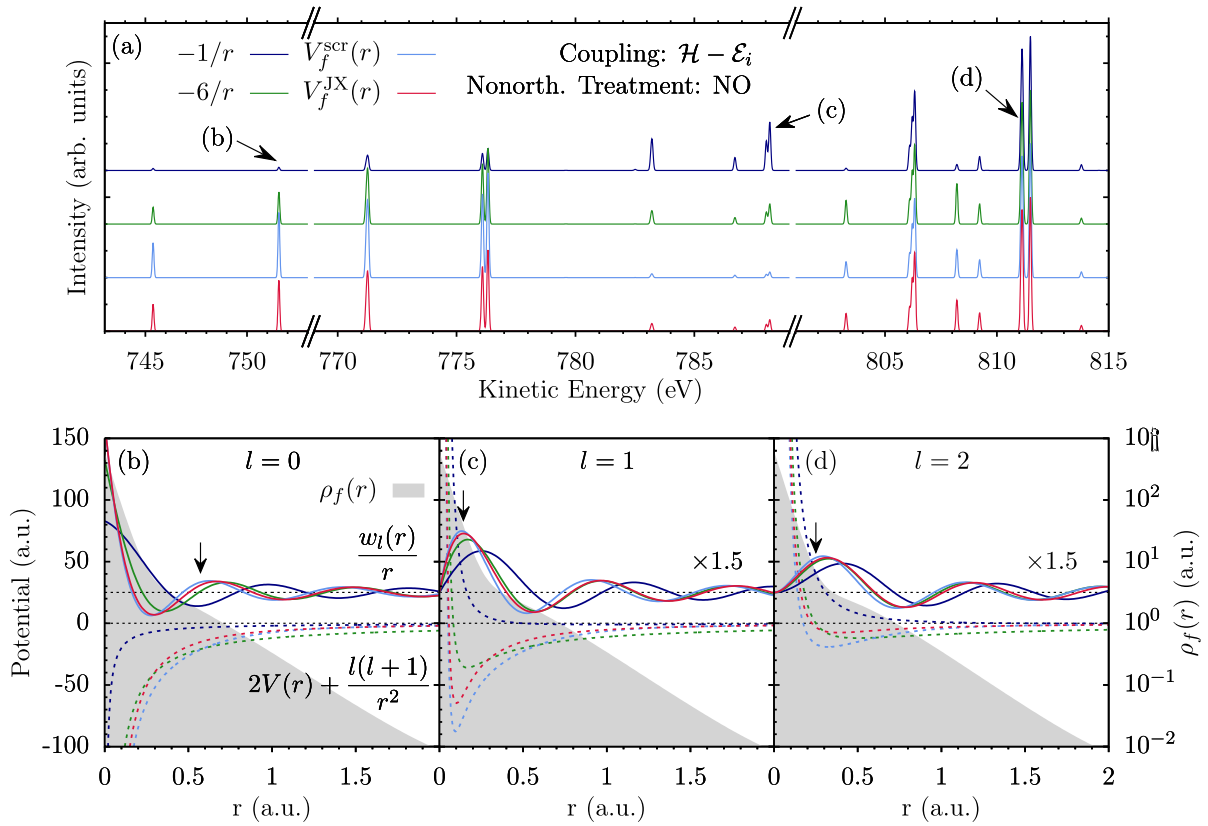
FIG. 3.   (a) Neon $1s^{-1}3p$ AES evaluated using QC scheme I, $\mathcal{H}$ coupling, and the NO nonorthogonality treatment with radial continuum functions corresponding to the given potentials. The spectra are normalized to the peak at 811.5 eV, broadened using a Gaussian FWHM of 0.1 eV, and shifted globally by -5.35 eV. In addition, they have have been shifted vertically by 2.0 [$V_f^{\mathrm{scr}}(r)$], 4.0 ($-6/r$), and 6.0 ($-1/r$) units to enhance the visibility. (b–d) Effective radial potentials (dashed) and continuum functions (solid) corresponding to the dominant angular momentum contribution $l = 0, 1, 2$ of the peaks (b)–(d) in panel (a) are shown together with the spherically averaged electron densities $\rho_f(r)$ of the respective ionized states. The colors of the radial waves and potentials correspond to the spectra shown in panel (a). At the positions indicated by the arrows in panels (b)–(d), the radial waves correspond to (top to bottom) $V_f^{\mathrm{scr}}(r)$, $V_f^{\mathrm{JX}}(r)$, $-6/r$, and $-1/r$. In the region of potential minima, the effective potentials are ordered (from top to bottom) as $-1/r$, $-6/r$, $V_f^{\mathrm{JX}}(r)$, and $V_f^{\mathrm{scr}}(r)$.

Notably, these slight deviations lead to an underestimation of the total decay rates obtained with the $V_f^{\mathrm{scr}}(r)$ potential by about 25% in comparison to those obtained for $V_f^{\mathrm{JX}}(r)$ (see Fig. 2), underlining the sensitivity of the total decay rates to the choice of the model potential.

The effective Coulomb potential $-1/r$ provides a qualitatively incorrect description in both the core and outer regions, whereas the $-6/r$ potential leads to a sort of compromise in accuracy. It describes the core region much better than the $-1/r$ potential but as a tradeoff has an incorrect asymptotic behavior in the valence region. For all but the r^{-1}-NO approaches this suffices to predict spectra that are in qualitative agreement with the ones obtained for $V_f^{\mathrm{JX}}(r)$, whereas using the $-1/r$ potential is only justified for the main features of the d region (see Supplemental Material [77] Figs. S2–S7). If one is interested in the full spectrum, one should use a model taking into account the electronic potential of the ionized core, such as $V^{\mathrm{scr}}(r)$, $V_f^{\mathrm{J}}(r)$, or $V_f^{\mathrm{JX}}(r)$.

Summarizing the discussion up to this point, it seems that satisfactory total decay rates and AESs are only obtained with the potentials $V_f^{\mathrm{J}}(r)$ and $V_f^{\mathrm{JX}}(r)$. Further, employing r^{-1} coupling and the SO approximation seems to be very well justified for these models and we will use these in the comparison against experimental data below. Generally, special caution has to be taken with the inclusion of the NO overlap terms for simple potential models. While the results obtained using $\mathcal{H}$ coupling greatly profit from error cancellation, this is not the case for r^{-1} coupling, where the NO terms strongly emphasize the deficiencies of an approximate potential. In addition, it remains to be clarified whether these cancellation effects are a general feature or a peculiarity of the neon $1s^{-1}3p$ AES.

B. Comparison to experimental data

In this section, the comparison of our theoretical results to the experimental data in the full spectral range is presented. In addition, to unravel the influence of the underlying QC onto
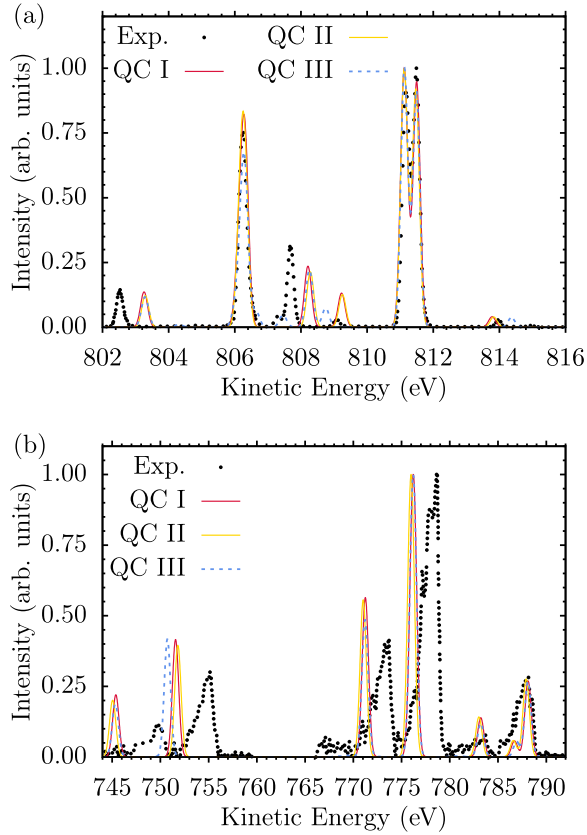
FIG. 4. Comparison of experimental and theoretical neon $1s^{-1}3p$ AES obtained based on the QC schemes I–III with the r^{-1}-$V_f^{JX}(r)$-SO method. The spectra obtained with QC I, II, and III have been shifted by -5.35, -4.75, and -5.18 eV, respectively, to align the peak at 811.5 eV with the experimental data in panel (a). To account for the different line shapes of the experimental spectra that have been digitalized from [69] (a) and [70] (b), broadening with a Gaussian FWHM of 0.25 and 0.77 eV was used in panels (a) and (b), respectively. Further, the spectra have been normalized individually to the peaks at 811.5 eV (a) and 776 eV (b).

the AES, we discuss spectra obtained with the QC schemes I–III as described in Table I. The QC model II, which is more sophisticated than QC I, contains an uncontracted s basis and accounts for scalar relativistic effects, whereas QC III employs an active space larger than in QC I.

To the best of our knowledge, no experimental Auger emission spectrum of the neon $1s^{-1}3p$ resonance that covers the full spectral range presented in Figs. 2 and 3 has been published to date. Hence, in Fig. 4 the spectra obtained with the QC models I–III and the r^{-1}-$V_f^{JX}(r)$-SO approach are compared against experimental data taken from Kivimäki *et al.* [69], for the d region (a), and Yoshida *et al.* [70], for the s and p regions (b). Note that the $\mathcal{H}$-V_f^{JX}-NO approach does not lead to a considerable improvement of the agreement with the experimental data, as shown in Supplemental Material [77] Fig. S9. The spectra have been shifted by -5.35, -4.75, and

-5.18 eV for QC models I, II, and III to align the peaks at 811.5 eV. In panel (a), the spectra have been broadened using a Gaussian profile with an FWHM of 0.25 eV, corresponding to the line shape of the peak at 806.5 eV in the experimental spectrum. Further, in panel (b) a Gaussian FWHM of 0.77 eV was chosen to represent the shape of the high-energy flank of the asymmetric peak at 778.5 eV in the experimental spectrum. Additionally, the spectra have been normalized to the heights of the main peaks at 811.5 eV (a) and 776 eV (b). Finally, the experimental data have been recorded at angles of $54.7°$ (a) and $56°$ (b) to the polarization vector. Data for these angles have been chosen to rule out anisotropy effects, which makes the comparison with our angle integrated spectra easier.

Panel (a) shows that the agreement between the experimental and the theoretical spectra is fairly good. In fact, the relative energetic positions and intensities of the main peaks are reproduced quite well. However, smaller satellite peaks at 803 and 808.2 eV are blueshifted by about 0.5 eV. Generally, the agreement between theory and experiment is worse for the smaller features, although an unambiguous assignment is still possible. Using the uncontracted s basis and including scalar relativistic effects in QC II does not influence the resulting spectrum. In turn, the larger active space incorporated in the QC scheme III leads to a better reproduction of some tiny features at 806.4, 807.5, and 808.8 eV. The blueshifts of the peaks already present with QC I and II are not affected, when employing QC III.

The comparison of the spectra covering the s and p regions with the experimental data is shown in panel (b). Here, the overall agreement is worse than in panel (a) concerning both the relative intensities and energetic positions of the peaks. Regarding the offset in energies, the low-energy part corresponds to transitions to the highest excited states of the ionic manifold, the energies of which are progressively overestimated. This is a typical situation when a smaller part of the electron correlation is recovered for the higher-lying states. Specifically, the positions of the peaks around 783 and 788 eV are reproduced well by all methods, while the intensity of the former, small peak is overestimated. Further, the peaks at 771 and 776 eV are redshifted by about 2 eV, and the relative intensity of the former is overestimated by approximately 30% (QC I and II) and 15% (QC III). Finally, the peaks at 745 eV and around 751 eV, corresponding to the s region, are redshifted by 5 eV (QC I–III) and 4 eV (QC I and II) or 5 eV (QC III), respectively. The intensities of these peaks are overestimated by about 30% with respect to the experimental data. Hence, in the s and p regions, our results agree better with the experimental reference than with the MCDF spectrum. The total decay rates, however, are not visibly altered by the choice of either of the QC schemes I, II, or III (see Supplemental Material [77] Fig. S8).

To wrap up this discussion, we conclude that the RASSCF and RASPT2 electronic structure method combined with the r^{-1}-V_f^{JX}-SO approach to construct continuum orbitals and evaluate the transition matrix elements provides Auger energies and intensities for the decay of the neon $1s^{-1}3p$ resonance of a similar quality as those obtained in [68] with the MCDF approach. In particular, a straightforward assignment of experimental results is possible. Further, the inclusion of scalar relativistic effects into the one-component electronic

structure of the bound states has no notable influence on the spectra, while a large active space is necessary only to reproduce minor satellite features.

VI. CONCLUSIONS AND OUTLOOK

In this paper, we have demonstrated an approach to the evaluation of autoionization rates on the example of the Auger decay from the neon $1s^{-1}3p$ resonance. The suggested protocol is based on the RASSCF and RASPT2 methods to evaluate the bound-state wave functions and energies, supplemented by a single-channel scattering model for the outgoing electron. Here, the single-center approximation is introduced to reduce the continuum orbital problem to the radial dimension by averaging over the angular structure of the ionized electron density. To model the true radial potential, six different models, V^{free}, $-1/r$, $-6/r$, $V_f^{\text{scr}}(r)$, $V_f^{\text{J}}(r)$, and $V_f^{\text{JX}}(r)$, have been discussed. Further, three different ways to account for the nonorthogonality of the continuum and bound orbitals, SO, NO, and GS, as well as the effect of using complete, $\mathcal{H}$, or approximate, r^{-1}, coupling in the partial rate evaluation have been investigated. All combinations of these sum up to 36 different variants to evaluate partial autoionization rates for an underlying bound-state QC calculation and have been implemented in a stand-alone program.

Here we compared all these approaches with respect to their ability to reproduce the experimental [69,70] as well as theoretical AES obtained at the fully relativistic MCDF level [68]. The applied quantum chemistry protocol allows for a fairly good reproduction of the transition energies if compared to the theoretical reference and experiments. However, intensities are more difficult to reproduce. Here, the quality of the continuum orbital was shown to be the most important issue as it strongly influences the obtained AESs. Especially the core part of the ionic potential is of importance for AES. The effect of the potential is closely connected to the angular momentum of the outgoing electron as it governs the extent of the continuum orbital into the core region. For instance, we found that the d region of the spectrum is rather insensitive to the choice of the model potential, whereas the s and p regions require one to use one of the potentials $V_f^{\text{scr}}(r)$, $V_f^{\text{J}}(r)$, and $V_f^{\text{JX}}(r)$. Still, the MCDF intensities can only be reproduced in the d region of the spectrum, while they are overestimated in the s and p parts. Further, the free-particle model and the asymptotic Coulomb potential $-1/r$ fail to reproduce the complete spectrum. Interestingly, inclusion of the NO terms in addition to using r^{-1} coupling in the SO approximation does not in general lead to improved spectra, but rather strongly emphasizes the deficiencies of the V^{free}, $-1/r$, and $-6/r$ potentials. Due to pronounced error cancellation, however, this is diminished to a large extent if the $\mathcal{H}$ coupling is used with the NO terms. Remarkably, the effective $-6/r$ potential yields qualitative agreement with the spectra obtained using the more accurate potentials for all approaches but the aforementioned combination of r^{-1} coupling and NO terms. In contrast, the spectra obtained with $V_f^{\text{scr}}(r)$, $V_f^{\text{J}}(r)$, and $V_f^{\text{JX}}(r)$ are weakly affected by the choice of both the coupling and nonorthogonality treatment. Since it remains unclear whether the cancellation effects observed

when using $\mathcal{H}$ coupling with the NO terms are a general feature, or a peculiarity of the neon AES, the NO terms should only be employed with caution. Generally, they should only be used if the descriptions of the potential and radial waves are sufficiently accurate. When dealing with approximate potentials, however, our results suggest to employ the SO or GS approaches, that seem to be less sensitive to the quality of the continuum orbital. In addition, due to the computational simplicity, the SO approximation could be preferred.

The comparison with experimentally obtained spectra using the r^{-1}-$V_f^{\text{JX}}(r)$-SO approach demonstrated the ability of the present method to accurately predict the neon $1s^{-1}3p$ AES, allowing a straightforward assignment of the experimental data. Interestingly, the general structure of the spectrum can be already reproduced quite well using a rather small active space, and is not sensitive to the inclusion of scalar relativistic effects. The best agreement with the experimental data is achieved by using a larger active space, including additional excitations to $3d$, $5s$, $5p$, $6s$, and $6p$ orbitals together with the spherically averaged direct exchange potential $V_f^{\text{JX}}(r)$. In addition our approach not only reproduces the experimentally measured AESs but the total decay rates of the neon $1s^{-1}3p$ resonance as well, when the potentials $-6/r$, $V_f^{\text{J}}(r)$, and $V_f^{\text{JX}}(r)$ are used. Since using the screened charge potential $V_f^{\text{scr}}(r)$ leads to notably underestimated absolute rates and is not computationally cheaper than using either $V_f^{\text{J}}(r)$ or $V_f^{\text{JX}}(r)$, providing a better accuracy, the latter two should be preferred.

Molecular systems can be treated with the presented method as well; however, in this case the molecular continuum has to be approximated by a single-centered spherically symmetric model. To keep the errors due to this approximation as small as possible, our findings suggest to use the r^{-1} coupling together with the SO approximation to evaluate molecular AIS. The potentials should be modeled using either the direct $V_f^{\text{J}}(r)$ or direct-exchange $V_f^{\text{JX}}(r)$ variant. The applicability of these approximations has to be tested for the molecular case.

Currently our code is interfaced to the MOLCAS/OPENMOLCAS as well as to the GAUSSIAN program packages, allowing one to evaluate PES and AIS based on bound-state calculations conducted with the RASSCF and RASPT2 [65] as well as the linear-response time-dependent density functional theory method [90]. A paper discussing the applicability of the present models to treat molecular systems will follow.

APPENDIX A: OBTAINING THE MODEL POTENTIALS

For the state-dependent models, Eqs. (7c)–(7e), the central quantity is the spherically averaged electron density of the

ionized state:

$$\rho_f(r) = \frac{1}{4\pi} \int_0^{4\pi} \rho_f(\mathbf{r}) \, d\Omega. \tag{A1}$$

It determines the potentials in the following way. The screened charge $Z_f(r)$ in Eq. (7c) is evaluated as the difference between the nuclear charge Z and the integrated number of electrons present in a sphere with radius r around the atom:

$$Z_f(r) = Z - \int_0^r \rho_f(r') r'^2 dr'. \tag{A2}$$

Further, the direct Coulomb potential of the ionized states in Eqs. (7d) and (7e) is the electrostatic potential of the

spherically averaged electron density $\rho_f(r)$:

$$J_f(r) = J_f(0) - \frac{4\pi}{r} \int_0^r dr' \int_0^{r'} r'' \rho_f(r'') dr''. \tag{A3}$$

$J_f(0)$ is defined by the asymptotic value of the integral over r'' in Eq. (A3):

$$\frac{J_f(0)}{4\pi} = \lim_{r' \to \infty} \int_0^{r'} r'' \rho_f(r'') dr''. \tag{A4}$$

Finally, a radial Slater-type exchange [73],

$$X_f^S(r) = -3 \left(\frac{3}{8\pi} \rho_f(r) \right)^{\frac{1}{3}}, \tag{A5}$$

is employed.

APPENDIX B: COUPLING MATRIX ELEMENTS

The total Auger transition matrix element $A_{i\alpha}^{\sigma M^+} = \langle \Upsilon_\alpha^{\sigma M^+} | \mathcal{H} - \mathcal{E}_i | \Psi_i \rangle$ reads

$$A_{i\alpha}^{\sigma M^+} = \langle \psi_{\alpha,\sigma} | h | \Phi_{i\alpha}^{M^+} \rangle + \overbrace{\sum_{q=1}^{N_{\text{orb}}} \langle \psi_{\alpha,\sigma} \varphi_q^+ | \frac{1}{r_{12}} | \Xi_{i\alpha}^{M^+,q} \rangle}^{r^{-1} \text{ coupling}} + \langle \psi_{\alpha,\sigma} | \tilde{\Phi}_{i\alpha}^{1,M^+} \rangle + \overbrace{\langle \psi_{\alpha,\sigma} | \tilde{\Phi}_{i\alpha}^{2,M^+} \rangle}^{r^{-1} \text{ coupling}} - \mathcal{E}_i \langle \psi_{\alpha,\sigma} | \Phi_{i\alpha}^{M^+} \rangle. \tag{B1}$$

Here the contributions corresponding to the SO approximation, the NO terms, and the r^{-1} coupling have been indicated. If the GS approach is used, $|\psi_{\alpha,\sigma}\rangle$ is replaced by

$$\left| \psi_{\alpha,\sigma}^{\text{GS}} \right\rangle = \left| \psi_{\alpha,\sigma} \right\rangle - \sum_{i=1}^{N_{\text{orb}}} \langle \varphi_{i,\sigma_i}^+ | \psi_{\alpha,\sigma} \rangle \left| \varphi_{i,\sigma_i}^+ \right\rangle. \tag{B2}$$

The conjugated one- and two-electron Dyson orbitals are defined as

$$\left| \tilde{\Phi}_{i\alpha}^{1,M^+} \right\rangle = \sum_{q,s,t}^{N_{\text{orb}}} \langle \varphi_q^+ | h | \varphi_s \rangle \langle \Psi_{f,M^+}^+ | (a_q^+)^\dagger a_s a_t | \Psi_i \rangle \left| \varphi_t \right\rangle \tag{B3}$$

and

$$\left| \tilde{\Phi}_{i\alpha}^{2,M^+} \right\rangle = \sum_{q_1 < q_2}^{N_{\text{orb}}} \sum_{s_1 < s_2,t}^{N_{\text{orb}}} \left(\langle \varphi_{q_1}^+ \varphi_{q_2}^+ | \frac{1}{r_{12}} | \varphi_{s_1} \varphi_{s_2} \rangle - \langle \varphi_{q_1}^+ \varphi_{q_2}^+ | \frac{1}{r_{12}} | \varphi_{s_2} \varphi_{s_1} \rangle \right) \langle \Psi_{f,M^+}^+ | (a_{q_1}^+)^\dagger (a_{q_2}^+)^\dagger a_{s_2} a_{s_1} a_t | \Psi_i \rangle | \varphi_t \rangle. \tag{B4}$$

Note that the sum of both terms, which occurs when the $\mathcal{H}$ coupling is used, takes the simple form

$$\left| \tilde{\Phi}_{i\alpha}^{1,M^+} \right\rangle + \left| \tilde{\Phi}_{i\alpha}^{2,M^+} \right\rangle = \mathcal{E}_f \left| \Phi_{i\alpha}^{M^+} \right\rangle, \tag{B5}$$

as demonstrated in [76], if the Hamiltonian eigenvalue equation $\mathcal{H} | \Psi_{f,M^+}^+ \rangle = \mathcal{E}_f | \Psi_{f,M^+}^+ \rangle$ is used. However, as detailed in the Supplemental Material [77] Sec. II, both approaches are strictly equivalent only if the occupied spin orbitals of the bound ionized and un-ionized wave functions span the same space. This is generally also not fulfilled for RASSCF orbitals if separate SCF procedures are used to obtain ionized and un-ionized states since the respective transformation properties between orbitals from different subspaces are lost. Moreover, the formulation of [76] cannot be applied to the r^{-1} coupling case whereas our formulation can.

[1] V. G. Wentzel, Z. Phys. **43**, 524 (1927).

[2] P. Van der Heide, *X-Ray Photoelectron Spectroscopy: An In-troduction to Principles and Practices* (Wiley, New York, 2012).

[3] S. Hofmann, *Auger- and X-Ray Photoelectron Spectroscopy in Materials Science: A User-Oriented Guide*, Springer Series in Surface Sciences Vol. 49 (Springer, New York, 2013).

[4] S. Hüfner, *Photoelectron Spectroscopy: Principles and Applications* (Springer-Verlag, Berlin, 2003).

[5] L. Meitner, Z. Phys. **11**, 35 (1922).

[6] L. S. Cederbaum, J. Zobeley, and F. Tarantelli, Phys. Rev. Lett. **79**, 4778 (1997).

[7] J. Zobeley, R. Santra, and L. S. Cederbaum, J. Chem. Phys. **115**, 5076 (2001).

[8] P. Slavíček, N. V. Kryzhevoi, E. F. Aziz, and B. Winter, J. Phys. Chem. Lett. **7**, 234 (2016).

[9] P. Slavíček, B. Winter, L. S. Cederbaum, and N. V. Kryzhevoi, J. Am. Chem. Soc. **136**, 18170 (2014).

[10] M. A. Brown, M. Faubel, and B. Winter, Annu. Rep. Sect. C Phys. Chem. **105**, 174 (2009).

[11] V. Stumpf, K. Gokhberg, and L. S. Cederbaum, Nat. Chem. **8**, 237 (2016).

[12] H. Wang, T. Möhle, O. Kühn, and S. I. Bokarev, Phys. Rev. A **98**, 013408 (2018).

[13] F. de Groot and A. Kotani, *Core Level Spectroscopy of Solids* (CRC, Boca Raton, FL, 2008).

[14] R. W. Howell, Int. J. Radiat. Biol. **84**, 959 (2008).

[15] E. Alizadeh, T. M. Orlando, and L. Sanche, Annu. Rev. Phys. Chem. **66**, 379 (2015).

[16] R. F. Martin and L. E. Feinendegen, Int. J. Radiat. Biol. **92**, 617 (2016).

[17] A. Yokoya and T. Ito, Int. J. Radiat. Biol. **93**, 743 (2017).

[18] R. Neutze, R. Wouts, D. van der Spoel, E. Weckert, and J. Hajdu, Nature (London) **406**, 752 (2000).

[19] T. Åberg and G. Howat, in *Corpsucles and Radiation in Matter I*, edited by W. Mehlhorn, Encyclopedia of Physics Vol. 31 (Springer-Verlag, Berlin, 1982), p. 469.

[20] T. Åberg, Phys. Scr. **21**, 495 (1980).

[21] U. Fano, Phys. Rev. **124**, 1866 (1961).

[22] S. Fritzsche, Comput. Phys. Commun. **183**, 1525 (2012).

[23] H. Ågren, S. Svensson, and U. Wahlgren, Chem. Phys. Lett. **35**, 336 (1975).

[24] H. Ågren, J. Chem. Phys. **75**, 1267 (1981).

[25] I. Hillier and J. Kendrick, Mol. Phys. **31**, 849 (1976).

[26] M. Mitani, O. Takahashi, K. Saito, and S. Iwata, J. Electron Spectrosc. Relat. Phenom. **128**, 103 (2003).

[27] V. Carravetta, H. Ågren, O. Vahtras, and H. J. A. Jensen, J. Chem. Phys. **113**, 7790 (2000).

[28] B. Schimmelpfennig, B. Nestmann, and S. D. Peyerimhoff, J. Phys. B **25**, 1217 (1992).

[29] B. Schimmelpfennig, B. Nestmann, and S. Peyerimhoff, J. Electron Spectrosc. Relat. Phenom. **74**, 173 (1995).

[30] J. Oddershede, in *Advances in Chemical Physics*, edited by K. P. Lawley (Wiley, New York, 1987), pp. 201–239.

[31] C.-M. Liegener, Chem. Phys. Lett. **90**, 188 (1982).

[32] V. Averbukh and L. S. Cederbaum, J. Chem. Phys. **123**, 204107 (2005).

[33] P. Kolorenč, V. Averbukh, K. Gokhberg, and L. S. Cederbaum, J. Chem. Phys. **129**, 244102 (2008).

[34] P. Kolorenč and V. Averbukh, J. Chem. Phys. **135**, 134314 (2012).

[35] H. Siegbahn, L. Asplund, and P. Kelfve, Chem. Phys. Lett. **35**, 330 (1975).

[36] D. R. Jennison, Chem. Phys. Lett. **69**, 435 (1980).

[37] F. P. Larkins, L. C. Tulea, and E. Z. Chelkowska, Aust. J. Phys. **43**, 625 (1990).

[38] R. Fink, J. Electron Spectrosc. Relat. Phenom. **76**, 295 (1995).

[39] O. Travnikova, R. F. Fink, A. Kivimäki, D. Céolin, Z. Bao, and M. N. Piancastelli, Chem. Phys. Lett. **474**, 67 (2009).

[40] L. Inhester, K. Hanasaki, Y. Hao, S.-K. Son, and R. Santra, Phys. Rev. A **94**, 023422 (2016).

[41] Y. Hao, L. Inhester, K. Hansaki, and R. Santra, Struct. Dyn. **2**, 041707 (2015).

[42] K. Faegri and H. P. Kelly, Phys. Rev. A **19**, 1649 (1979).

[43] M. Higashi, E. Hiroike, and T. Nakajima, Chem. Phys. **68**, 377 (1982).

[44] K. Zähringer, H.-D. Meyer, and L. S. Cederbaum, Phys. Rev. A **45**, 318 (1992).

[45] P. V. Demekhin, D. V. Omel'yanenko, B. M. Lagutin, V. L. Sukhorukov, L. Werner, A. Ehresmann, K.-H. Schartner, and H. Schmoranzer, Opt. Spectrosc. **102**, 318 (2007).

[46] P. V. Demekhin, I. D. Petrov, V. L. Sukhorukov, W. Kielich, P. Reiss, R. Hentges, I. Haar, H. Schmoranzer, and A. Ehresmann, Phys. Rev. A **80**, 063425 (2009).

[47] P. V. Demekhin, A. Ehresmann, and V. L. Sukhorukov, J. Chem. Phys. **134**, 024113 (2011).

[48] L. Inhester, C. F. Burmeister, G. Groenhof, and H. Grubmüller, J. Chem. Phys. **136**, 144304 (2012).

[49] H. I. B. Banks, D. A. Little, J. Tennyson, and A. Emmanouilidou, Phys. Chem. Chem. Phys. **19**, 19794 (2017).

[50] R. Colle and S. Simonucci, Phys. Rev. A **39**, 6247 (1989).

[51] R. Colle and S. Simonucci, Phys. Rev. A **48**, 392 (1993).

[52] R. Colle, D. Embriaco, M. Massini, S. Simonucci, and S. Taioli, J. Phys. B **37**, 1237 (2004).

[53] C. Marante, M. Klinker, I. Corral, J. González-Vázquez, L. Argenti, and F. Martín, J. Chem. Theory Comput. **13**, 499 (2017).

[54] C. Marante, M. Klinker, T. Kjellsson, E. Lindroth, J. González-Vázquez, L. Argenti, and F. Martín, Phys. Rev. A **96**, 022507 (2017).

[55] M. Klinker, C. Marante, L. Argenti, J. González-Vázquez, and F. Martín, Phys. Rev. A **98**, 033413 (2018).

[56] J. V. Ortiz, J. Chem. Phys. **81**, 5873 (1984).

[57] N. Correia, A. Naves de Brito, M. P. Keane, L. Karlsson, S. Svensson, C.-M. Liegener, A. Cesar, and H. Ågren, J. Chem. Phys. **95**, 5187 (1991).

[58] K. Endo, S. Shimada, N. Kato, and T. Ida, J. Mol. Spectrosc. **1122**, 341 (2016).

[59] P. G. Burke, *R-Matrix Theory of Atomic Collisions: Application to Atomic, Molecular and Optical Processes*, Springer Series on Atomic, Optical, and Plasma Physics Vol. 61 (Springer-Verlag, Heidelberg, 2011).

[60] S. I. Bokarev and O. Kühn, Wiley Interdiscip. Rev. Comput. Mol. Sci. e1433 (2019), doi: 10.1002/wcms.1433.

[61] S. I. Bokarev, M. Dantz, E. Suljoti, O. Kühn, and E. F. Aziz, Phys. Rev. Lett. **111**, 083002 (2013).

[62] R. V. Pinjari, M. G. Delcey, M. Guo, M. Odelius, and M. Lundberg, J. Comput. Chem. **37**, 477 (2016).

[63] I. Josefsson, K. Kunnus, S. Schreck, A. Föhlisch, F. de Groot, P. Wernet, and M. Odelius, J. Phys. Chem. Lett. **3**, 3565 (2012).

[64] S. I. Bokarev, M. Khan, M. K. Abdel-Latif, J. Xiao, R. Hilal, S. G. Aziz, E. F. Aziz, and O. Kühn, J. Phys. Chem. C **119**, 19192 (2015).

[65] G. Grell, S. I. Bokarev, B. Winter, R. Seidel, E. F. Aziz, S. G. Aziz, and O. Kühn, J. Chem. Phys. **143**, 074104 (2015).

[66] R. Golnak, S. I. Bokarev, R. Seidel, J. Xiao, G. Grell, K. Atak, I. Unger, S. Thürmer, S. G. Aziz, O. Kühn, B. Winter, and E. F. Aziz, Sci. Rep. **6**, 24659 (2016).

[67] J. Norell, G. Grell, O. Kühn, M. Odelius, and S. I. Bokarev, Phys. Chem. Chem. Phys. **20**, 19916 (2018).

[68] S. Stock, R. Beerwerth, and S. Fritzsche, Phys. Rev. A **95**, 053407 (2017).

[69] A. Kivimäki, S. Heinäsmäki, M. Jurvansuu, S. Alitalo, E. Nõmmiste, H. Aksela, and S. Aksela, J. Electron Spectrosc. Relat. Phenom. **114**, 49 (2001).

[70] H. Yoshida, K. Ueda, N. M. Kabachnik, Y. Shimizu, Y. Senba, Y. Tamenori, I. Ohashi, I. Koyano, I. H. Suzuki, R. Hentges, J. Viefhaus, and U. Becker, J. Phys. B **33**, 4343 (2000).

[71] K. Ueda, M. Kitajima, A. De Fanis, Y. Tamenori, H. Yamaoka, H. Shindo, T. Furuta, T. Tanaka, H. Tanaka, H. Yoshida, R. Sankari, S. Aksela, S. Fritzsche, and N. M. Kabachnik, Phys. Rev. Lett. **90**, 153005 (2003).

[72] Y. Tamenori and I. H. Suzuki, J. Phys. B **47**, 145001 (2014).

[73] J. C. Slater, Phys. Rev. **81**, 385 (1951).

[74] *NIST Handbook of Mathematical Functions*, 1st ed., edited by F. W. J. Olver, D. W. Lozier, R. F. Boisvert, and C. W. Clark (Cambridge University, Cambridge, England, 2010).

[75] P.-O. Löwdin, Phys. Rev. **97**, 1474 (1955).

[76] R. Manne and H. Ågren, Chem. Phys. **93**, 201 (1985).

[77] See Supplemental Material at http://link.aps.org/supplemental/10.1103/PhysRevA.100.042512 for additional results, theoretical details, and the employed basis sets.

[78] F. Aquilante, J. Autschbach, R. K. Carlson, L. F. Chibotaru, M. G. Delcey, L. De Vico, I. F. Galván, N. Ferré, L. M. Frutos, L. Gagliardi, M. Garavelli, A. Giussani, C. E. Hoyer, G. Li Manni, H. Lischka, D. Ma, P. Å. Malmqvist, T. Müller, A. Nenov, M. Olivucci, T. B. Pedersen, D. Peng, F. Plasser, B. Pritchard, M. Reiher, I. Rivalta, I. Schapiro, J. Segarra-Martí,

M. Stenrup, D. G. Truhlar, L. Ungur, A. Valentini, S. Vancoillie, V. Veryazov, V. P. Vysotskiy, O. Weingart, F. Zapata, and R. Lindh, J. Comput. Chem. **37**, 506 (2016).

[79] P.-O. Widmark, P. Å. Malmqvist, and B. O. Roos, Theor. Chim. Acta **77**, 291 (1990).

[80] K. Kaufmann, W. Baumeister, and M. Jungen, J. Phys. B **22**, 2223 (1989).

[81] J. Almlöf and P. R. Taylor, J. Chem. Phys. **86**, 4070 (1987).

[82] I. F. Galván, M. Vacher, A. Alavi, C. Angeli, J. Autschbach, J. J. Bao, S. I. Bokarev, N. A. Bogdanov, R. K. Carlson, L. F. Chibotaru, J. Creutzberg, N. Dattani, M. G. Delcey, S. S. Dong, A. Dreuw, L. Freitag, L. M. Frutos, L. Gagliardi, F. Gendron, A. Giussani, L. González, G. Grell, M. Guo, C. E. Hoyer, M. Johansson, S. Keller, S. Knecht, G. Kovačević, E. Källman, G. Li Manni, M. Lundberg, Y. Ma, S. Mai, J. P. Malhado, P. Å. Malmqvist, P. Marquetand, S. A. Mewes, J. Norell, M. Olivucci, M. Oppel, Q. M. Phung, K. Pierloot, F. Plasser, M. Reiher, A. M. Sand, I. Schapiro, P. Sharma, C. J. Stein, L. K. Sørensen, D. G. Truhlar, M. Ugandi, L. Ungur, A. Valentini, S. Vancoillie, V. Veryazov, O. Weser, P.-O. Widmark, S. Wouters, J. P. Zobel, and R. Lindh, J. Chem. Theory Comput. (2019), doi: 10.1021/acs.jctc.9b00532.

[83] D. Peng and M. Reiher, Theor. Chem. Acc. **131** (2012).

[84] P. Å. Malmqvist, K. Pierloot, A. R. M. Shahi, C. J. Cramer, and L. Gagliardi, J. Chem. Phys. **128**, 204109 (2008).

[85] P. Å. Malmqvist, B. O. Roos, and B. Schimmelpfennig, Chem. Phys. Lett. **357**, 230 (2002).

[86] P. Å. Malmqvist, Int. J. Quantum Chem. **30**, 479 (1986).

[87] Q. Sun, J. Comput. Chem. **36**, 1664 (2015).

[88] T. Hahn, Comput. Phys. Commun. **168**, 78 (2005).

[89] L. Avaldi, G. Dawber, R. Camilloni, G. C. King, M. Roper, M. R. F. Siggel, G. Stefani, M. Zitnik, A. Lisini, and P. Decleva, Phys. Rev. A **51**, 5025 (1995).

[90] T. Möhle, O. S. Bokareva, G. Grell, O. Kühn, and S. I. Bokarev, J. Chem. Theory Comput. **14**, 5870 (2018).

Supplementary material:

Multi-reference quantum chemistry protocol for simulating autoionization spectra: Test of ionization continuum models for the neon atom

Gilbert Grell, Oliver Kühn, and Sergey I. Bokarev[*]

Institut für Physik, Universität Rostock,

Albert-Einstein-Str. 23-24, 18059, Rostock, Germany

(Dated: October 9, 2019)

Abstract

In this contribution we present a protocol to evaluate partial and total Auger decay rates combining the restricted active space self-consistent field electronic structure method for the bound part of the spectrum and numerically obtained continuum orbitals in the single-channel scattering theory framework. On top of that, the two-step picture is employed to evaluate the partial rates. The performance of the method is exemplified for the prototypical Auger decay of the neon $1s^{-1}3p$ resonance. Different approximations to obtain the continuum orbitals, the partial rate matrix elements, and the electronic structure of the bound part are tested against theoretical and experimental reference data. It is demonstrated that the partial and total rates are most sensitive to the accuracy of the continuum orbitals. For instance, it is necessary to account for the direct Coulomb potential of the ion for the determination of the continuum wave functions. The Auger energies can be reproduced quite well already with a rather small active space. Finally, perspectives of the application of the proposed protocol to molecular systems are discussed.

---

[*] sergey.bokarev@uni-rostock.de

1

I.   ADDITIONAL DATA

Here we supply data that were not included in the main text. All abbreviations and naming conventions that have been introduced in the main text are used here without further reiteration.

potential	(b), $l = 0$	(c), $l = 1$	(d), $l = 2$
V^{free}	7.46×10^{-6}	1.14×10^{-4}	7.38×10^{-27}
$-1/r$	7.45×10^{-6}	9.34×10^{-5}	1.43×10^{-26}
$-6/r$	2.65×10^{-6}	1.83×10^{-5}	6.39×10^{-27}
$V_f^{\text{scr}}(r)$	4.54×10^{-7}	3.90×10^{-6}	3.40×10^{-26}
$V_f^{\text{J}}(r)$	3.45×10^{-7}	3.38×10^{-6}	3.61×10^{-26}
$V_f^{\text{JX}}(r)$	1.05×10^{-8}	7.64×10^{-7}	3.79×10^{-26}

TABLE S1. Representative absolute values of continuum-bound overlap integrals for the peaks (b)-(d) from Fig. 3 of the main text. The data has been evaluated using QC scheme I. Shown are the overlap of the continuum orbitals corresponding to the indicated potentials and l quantum numbers with the Dyson orbitals for the respective transition. They have been evaluated as: $\sum_{m=-l}^{l} |\langle \psi_\alpha | \Phi_{i\alpha} \rangle|$; note that compound index α contains m in it. The summation over the spin projections has been dropped for clarity.
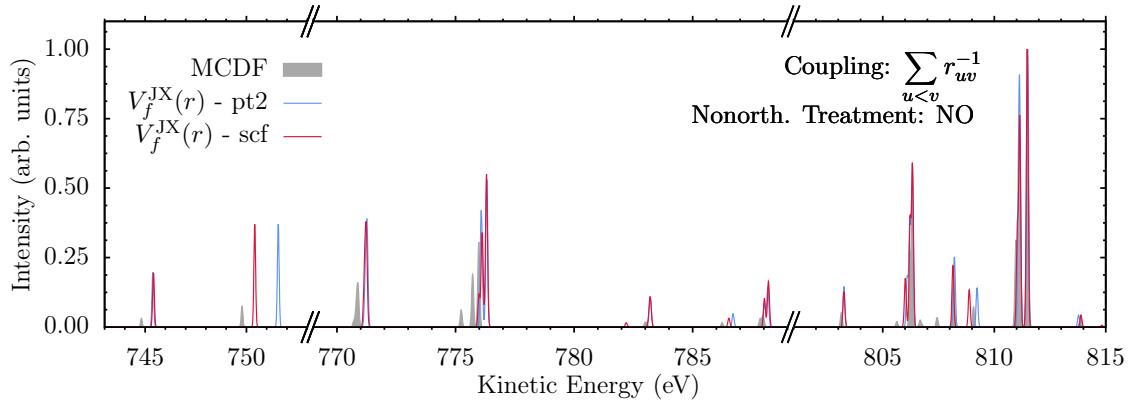
FIG. S1. Comparison of the r^{-1}-$V_f^{\text{JX}}(r)$-NO spectra evaluated using QC scheme I with the RASPT2 correction (pt2) and using the uncorrected RASSCF energies (scf). For reference the MCDF spectrum is shown as well. All spectra are broadened using a Gaussian with an FWHM of 0.1 eV, normalized to the peak at 811.5 eV and shifted globally by -5.35 eV (pt2), -6.75 eV (scf), and -2.45 eV (MCDF).

2
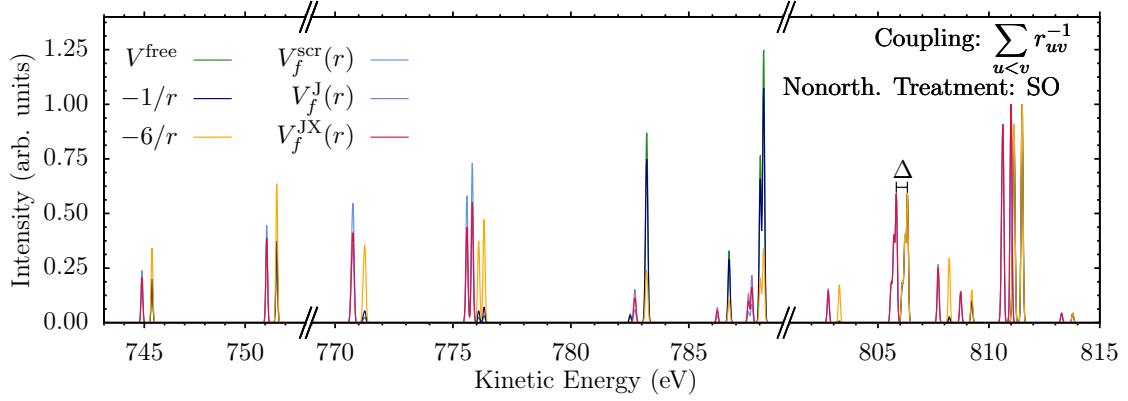
FIG. S2. Spectra obtained for the depicted potentials, using QC scheme I, r^{-1} coupling and the SO approximation. All spectra are broadened using a Gaussian with an FWHM of 0.1 eV, normalized to the peak at 811.5 eV and shifted globally by -5.35 eV. For clarity, the spectra obtained with the potentials $V_f^{\mathrm{scr}}(r)$, $V_f^{\mathrm{J}}(r)$, and $V_f^{\mathrm{JX}}(r)$ have been shifted additionally by $\Delta = -0.5$ eV with respect to the data corresponding to V^{free}, $-1/r$, and $-6/r$.
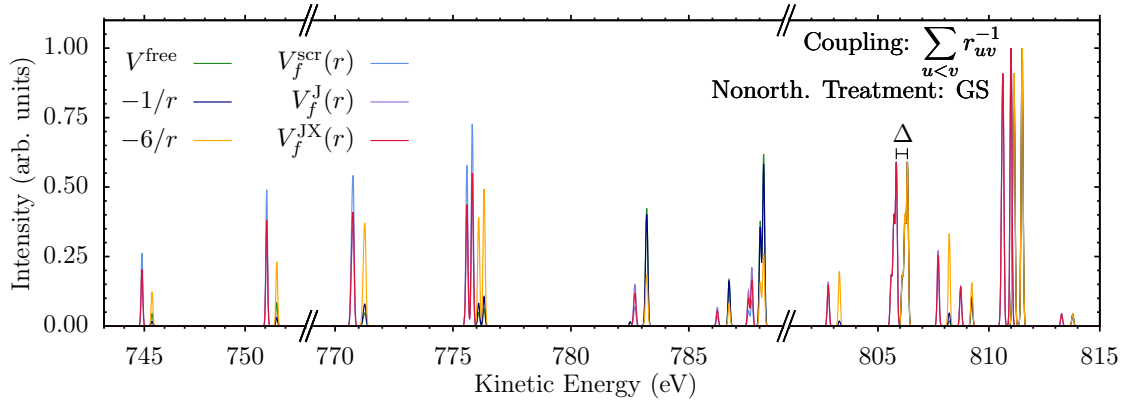
FIG. S3. Spectra obtained for the depicted potentials, using QC scheme I, r^{-1} coupling and the GS approach. All spectra are broadened using a Gaussian with an FWHM of 0.1 eV, normalized to the peak at 811.5 eV and shifted globally by -5.35 eV. For clarity, the spectra obtained with the potentials $V_f^{\mathrm{scr}}(r)$, $V_f^{\mathrm{J}}(r)$, and $V_f^{\mathrm{JX}}(r)$ have been shifted additionally by $\Delta = -0.5$ eV with respect to the data corresponding to V^{free}, $-1/r$, and $-6/r$.

3
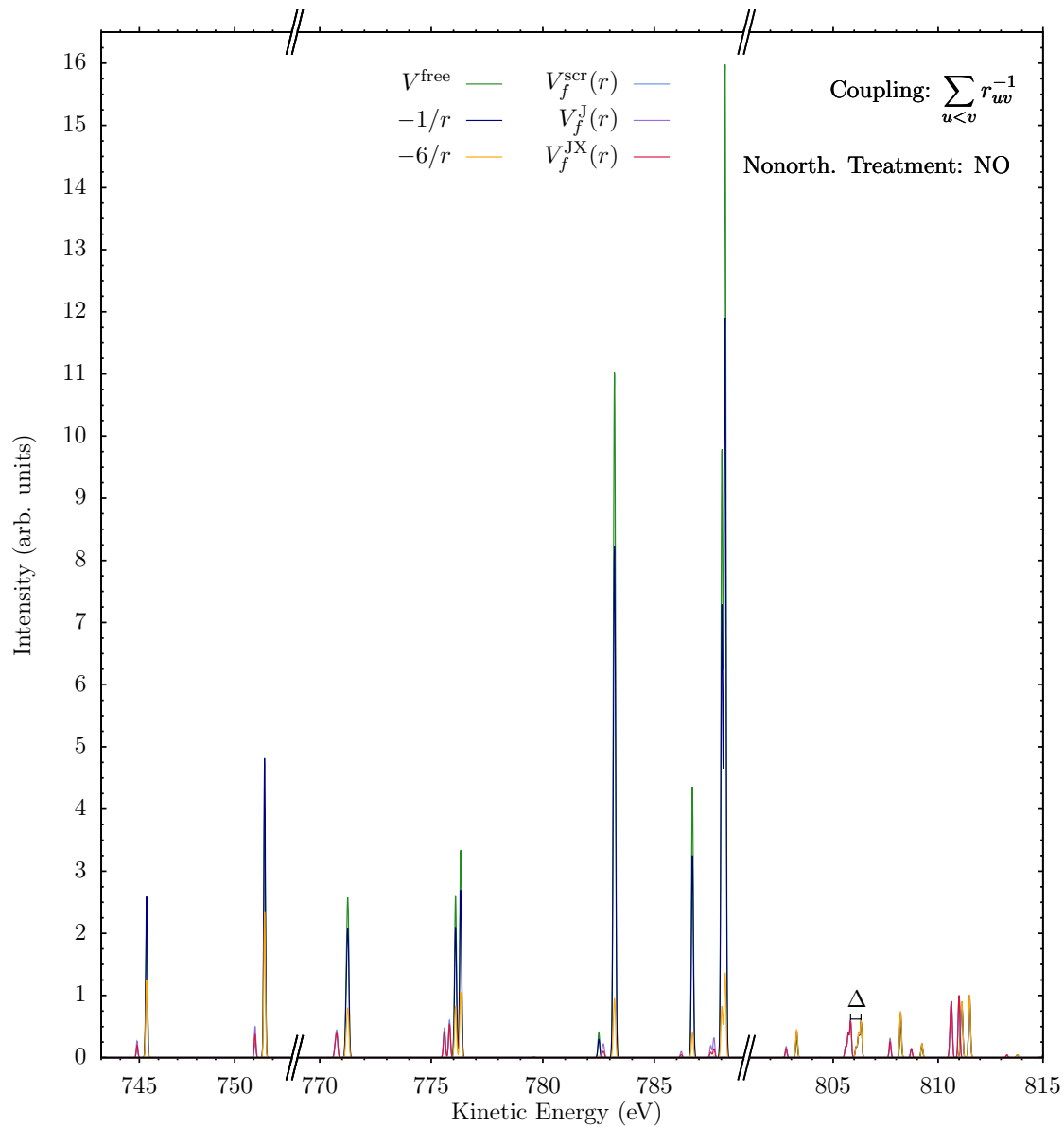
FIG. S4. Spectra obtained for the depicted potentials, using QC scheme I, r^{-1} coupling and the NO approach. All spectra are broadened using a Gaussian with an FWHM of 0.1 eV, normalized to the peak at 811.5 eV and shifted globally by -5.35 eV. For clarity, the spectra obtained with the potentials $V_f^{\text{scr}}(r)$, $V_f^{\text{J}}(r)$, and $V_f^{\text{JX}}(r)$ have been shifted additionally by $\Delta = -0.5$ eV with respect to the data corresponding to V^{free}, $-1/r$, and $-6/r$.

4

FIG. S5. Spectra obtained for the depicted potentials, using QC scheme I, $\mathcal{H}$ coupling and the SO approximation. All spectra are broadened using a Gaussian with an FWHM of 0.1 eV, normalized to the peak at 811.5 eV and shifted globally by -5.35 eV. For clarity, the spectra obtained with the potentials $V_f^{\text{scr}}(r)$, $V_f^{\text{J}}(r)$, and $V_f^{\text{JX}}(r)$ have been shifted additionally by $\Delta = -0.5$ eV with respect to the data corresponding to V^{free}, $-1/r$, and $-6/r$.
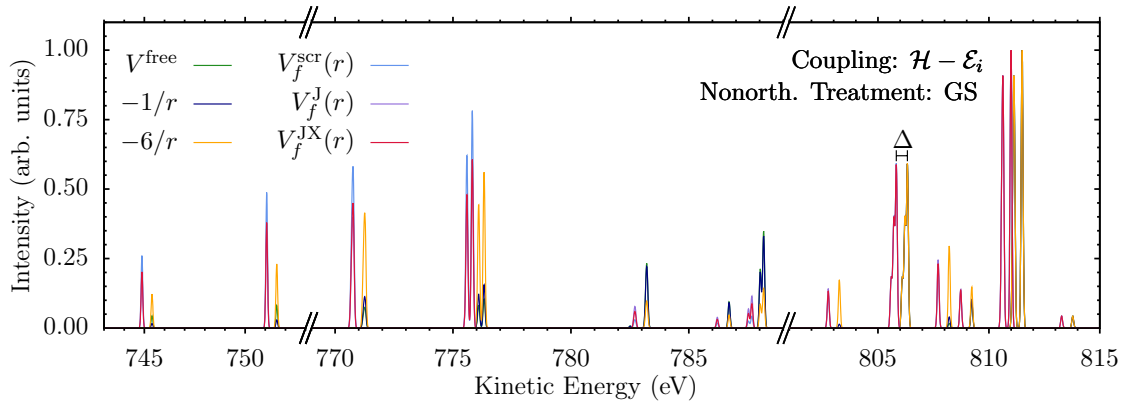
FIG. S6. Spectra obtained for the depicted potentials, using QC scheme I, $\mathcal{H}$ coupling and the GS approach. All spectra are broadened using a Gaussian with an FWHM of 0.1 eV, normalized to the peak at 811.5 eV and shifted globally by -5.35 eV. For clarity, the spectra obtained with the potentials $V_f^{\text{scr}}(r)$, $V_f^{\text{J}}(r)$, and $V_f^{\text{JX}}(r)$ have been shifted additionally by $\Delta = -0.5$ eV with respect to the data corresponding to V^{free}, $-1/r$, and $-6/r$.

5
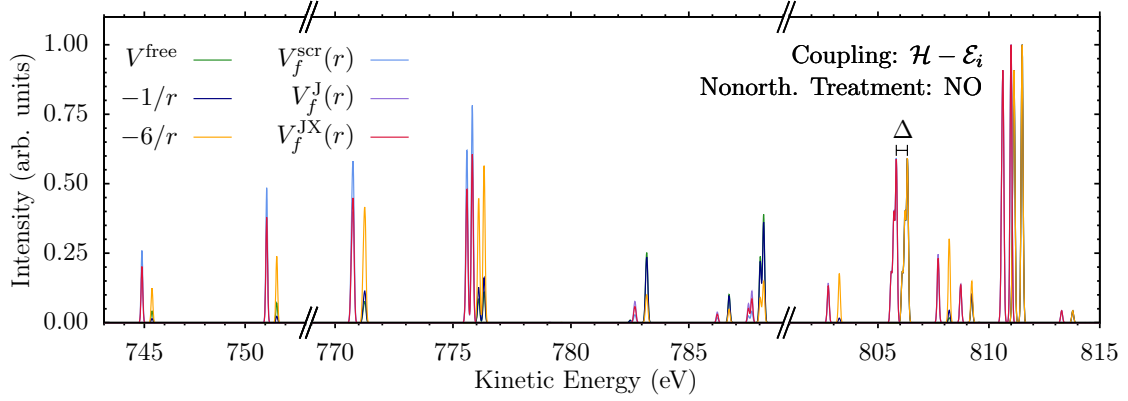
FIG. S7. Spectra obtained for the depicted potentials, using QC scheme I, $\mathcal{H}$ coupling and the NO approach. All spectra are broadened using a Gaussian with an FWHM of 0.1 eV, normalized to the peak at 811.5 eV and shifted globally by -5.35 eV. For clarity, the spectra obtained with the potentials $V_f^{\text{scr}}(r)$, $V_f^{\text{J}}(r)$, and $V_f^{\text{JX}}(r)$ have been shifted additionally by $\Delta = -0.5$ eV with respect to the data corresponding to V^{free}, $-1/r$, and $-6/r$.

FIG. S8. Comparison of the neon $1s^{-1}3p$ Auger decay rates integrated over the given spectral regions. The partial rates have been obtained based on the QC schemes I,II and III using the r^{-1} coupling, the $V_f^{\text{JX}}(r)$ potential, and either of the NO or SO nonorthogonality approaches. For reference, the experimental $(8.08 \pm 1.1 \times 10^{-3}$ a.u. [1]) value of the total Auger decay rate is given.
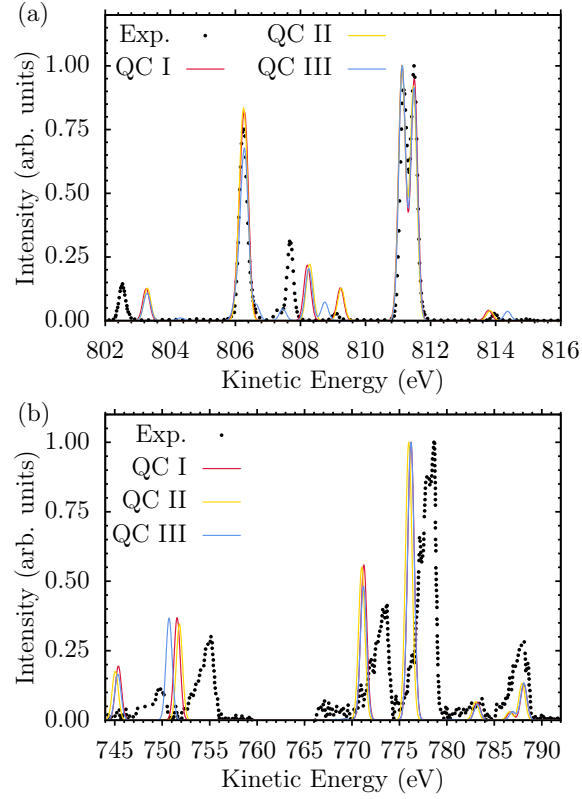
FIG. S9. Comparison of experimental and theoretical neon $1s^{-1}3p$ AES obtained based on the QC schemes I - III with the $\mathcal{H}\text{-}V_f^{\text{JX}}(r)$-NO method. The spectra obtained with QC I, II, and III have been shifted by -5.35 eV, -4.75 eV, and -5.18 eV, respectively, to align the peak at 811.5 eV with the experimental data in panel (a). To account for the different lineshapes of the experimental spectra that have been digitalized from [2], panel (a), and [3] in panel (b), broadening with a Gaussian FWHM of 0.25 eV and 0.77 eV was used in panels (a) and (b), respectively. Further, the spectra have been normalized individually to the peaks at 811.5 eV (a) and 776 eV (b).

7

II.   THE EVALUATION OF THE NO CORRECTION TERMS

In Ref. 4, Manne and Ågren have described a general way to compute the Auger transition matrix elements, based only on the fundamental assumption that the involved wave functions can be written as linear combinations of Slater determinants, that are in turn constructed out of a set of orthonormal orbitals. In brief, using the same notation as in the main text their results can be summarized as follows:

We start with the continuum state $|\Psi_\alpha\rangle$ being decomposed into the channel functions: $|\Psi_\alpha\rangle = \sum_{M^+=-S^+}^{S^+} \sum_{\sigma=-\frac{1}{2},\frac{1}{2}} C_{S^+,M^+;\sigma}^{S,M} \left|\Upsilon_\alpha^{\sigma M^+}\right\rangle$. These are defined by acting with the creation operator of the continuum orbital on the corresponding bound state of the ionized system, $\left|\Upsilon_\alpha^{\sigma M^+}\right\rangle = a_{\alpha,\sigma}^\dagger \left|\Psi_{f,M^+}^+\right\rangle$. We shall not discuss the summation of different spins here and thus drop the spin indices completely in what follows. The Auger matrix element for one channel function may then be expressed as :

$$A_{i\alpha} = \left\langle \Psi_f^+ \middle| a_\alpha (\mathcal{H} - \mathcal{E}_i) \middle| \Psi_i \right\rangle \tag{S1}$$

Employing the commutator $[a_\alpha, \mathcal{H}]$ Manne and Åberg proceed to express the matrix element as

$$A_{i\alpha} = \left\langle \Psi_f^+ \middle| [a_\alpha, \mathcal{H}] \middle| \Psi_i \right\rangle + \left\langle \Psi_f^+ \middle| (\mathcal{H} - \mathcal{E}_i) a_\alpha \middle| \Psi_i \right\rangle \tag{S2}$$

Now, they suppose that $\left\langle \Psi_f^+ \right|$ is indeed an eigenstate of the Hamiltonian and exploit the eigenvalue equation $\left\langle \Psi_f^+ \middle| \mathcal{H} = \left\langle \Psi_f^+ \middle| \mathcal{E}_f \right.$ together with the definition of the energy of the ionized electron $\varepsilon_\alpha = \mathcal{E}_i - \mathcal{E}_f$, which gives:

$$A_{i\alpha} = \left\langle \Psi_f^+ \middle| [a_\alpha, \mathcal{H}] \middle| \Psi_i \right\rangle - \varepsilon_\alpha \left\langle \Psi_f^+ \middle| a_\alpha \middle| \Psi_i \right\rangle \tag{S3}$$

To obtain a practically useful equation, the Hamiltonian and annihilation operator need to be expressed in the basis of the ionized and unionized states: These basis functions are the spin orbitals $\{\varphi_s\}$ and $\{\varphi_q^+\}$ corresponding to $|\Psi_i\rangle$ and $\left|\Psi_f^+\right\rangle$. In the RASSCF family of methods, these are defined as the eigenfunctions of effective Fockians $\mathcal{F}$ and $\mathcal{F}^+$, corresponding to the

8

unionized and ionized states:

$$\mathcal{F}\left|\varphi_s\right\rangle = \varepsilon_s\left|\varphi_s\right\rangle, \tag{S4}$$

$$\mathcal{F}^+\left|\varphi_q^+\right\rangle = \varepsilon_q^+\left|\varphi_q^+\right\rangle. \tag{S5}$$

To continue, one has to assume that the Fockians are constructed from a complete basis, and that their spectrum of eigenfunctions and eigenvalues comprises a bound and a continuous part. Given this, the annihilator may be expressed in the basis corresponding to the unionized state as:

$$a_\alpha = \sum_s \langle\psi_\alpha|\varphi_s\rangle\, a_s + \int \langle\psi_\alpha|\varphi(\beta)\rangle\, a(\beta)d\beta = \sum_s\!\!\!\!\!\!\int \langle\psi_\alpha|\varphi(s)\rangle\, a(s)ds. \tag{S6}$$

Where the greek and latin indices indicate the continuous and discrete part of the spectrum of $\mathcal{F}$. As a compromise, the abbreviated sum + integral notation employs the latin index in a functional dependence. Note that the discrete and continuous eigenfunctions can always be clearly distinguished, because the former are square integrable functions, while the latter are not, i.e. they fulfill the normalization relation:

$$\langle\varphi(r)|\varphi(s)\rangle = \delta(r,s) = \begin{cases} \delta_{rs} & \text{discrete spectrum} \\ \delta(\varepsilon_r - \varepsilon_s) & \text{continuous spectrum} \end{cases} \tag{S7}$$

Since both basis are complete and can be converted into each other, it is convenient to express the Hamiltonian by using the the basis $\{\varphi_i^+\}$ and $\{\varphi_i\}$ for the creation and annihilation operators, respectively:

$$\mathcal{H} = \sum\!\!\!\!\!\!\int \mathrm{d}q\mathrm{d}s\, h_1(q,s)\left(a^+(q)\right)^\dagger a(s) \tag{S8}$$

$$+ \frac{1}{2}\sum\!\!\!\!\!\!\int \mathrm{d}q_1\mathrm{d}q_2\mathrm{d}s_1\mathrm{d}s_2\, h_2(q_1,q_2;s_1,s_2)\left(a^+(q_1)\right)^\dagger\left(a^+(q_2)\right)^\dagger a(s_2)a(s_1) \tag{S9}$$

Where the operators act as $\left(a^+(q)\right)^\dagger|0\rangle = \left|\varphi^+(q)\right\rangle$ and $a^\dagger(s)|0\rangle = |\varphi(s)\rangle$, and

$$h_1(q,s) = \left\langle\varphi^+(q)\middle|h\middle|\varphi(s)\right\rangle \tag{S10}$$

$$h_2(q_1,q_2;s_1,s_2) = \left\langle\varphi^+(q_1)\varphi^+(q_2)\middle|\varphi(s_1)\varphi(s_2)\right\rangle \tag{S11}$$

9

Using the anticommutators

$$[a_\alpha, (a^+(q))^\dagger]_+ = \langle \psi_\alpha | \varphi^+(q) \rangle, \tag{S12}$$

$$[a_\alpha, a(q)]_+ = 0, \tag{S13}$$

$$[a(t), a(s)]_+ = 0, \tag{S14}$$

and Eq. (S8), the matrix element involving the commutator in Eq. (S3) can be expressed as:

$$\langle \Psi_f^+ | [a_\alpha, \mathcal{H}] | \Psi_i \rangle = \sum\!\!\!\!\!\!\int ds\, h_1(\alpha, s) \langle \Psi_f^+ | a(s) | \Psi_i \rangle \tag{S15}$$
$$+ \sum\!\!\!\!\!\!\int dq ds_1 ds_2 h_2(\alpha, q; s_1, s_2) \langle \Psi_f^+ | (a^+(q))^\dagger a(s_2) a(s_1) | \Psi_i \rangle$$

Finally, one uses the fact that by definition the states $|\Psi_i\rangle$ and $|\Psi_f^+\rangle$ are purely bound states. Consequently, any continuum annihilation operator applied to these states produces zeros, i.e. $a(s)|\Psi_i\rangle = 0$ and $\langle \Psi_f^+ | a_+(q)^\dagger = 0$, if the operators correspond to the continuum. This allows to disregard the continuum integration in Eq. (S15) and to express the full matrix element as

$$A_{i\alpha} = \sum_s^{N_{\rm orb}} \langle \psi_\alpha | h | \varphi_s \rangle \langle \Psi_f^+ | a_s | \Psi_i \rangle + \sum_q^{N_{\rm orb}} \sum_{s_1 \neq s_2}^{N_{\rm orb}} \langle \psi_\alpha \varphi_q^+ | \varphi_{s_1} \varphi_{s_2} \rangle \langle \Psi_f^+ | (a_q^+)^\dagger a_{s_2} a_{s_1} | \Psi_i \rangle \tag{S16}$$
$$- \varepsilon_\alpha \sum_s^{N_{\rm orb}} \langle \Psi_f^+ | a_s | \Psi_i \rangle \langle \psi_\alpha | \varphi_s \rangle,$$

where we have used the expansion (S6), again reduced to the discrete part. This is the celebrated result of Manne and Åberg [4]. Using the definitions for the Dyson orbital $|\Phi_{i\alpha}\rangle$ and the two-electron reduced transition density $|\Xi_{i\alpha}^q\rangle$ in Eqs. (15) and (18), the matrix element takes the form:

$$A_{i\alpha} = \langle \psi_\alpha | h | \Phi_{i\alpha} \rangle + \sum_q^{N_{\rm orb}} \langle \psi_\alpha \varphi_q^+ | \frac{1}{r_{12}} | \Xi_{i\alpha}^q \rangle - \varepsilon_\alpha \langle \psi_\alpha | \Phi_{i\alpha} \rangle. \tag{S17}$$

While this formulation is straightforwardly derived, subtle problems are encountered in the actual evaluation of the term that arises due to the nonorthogonality of the continuum

10

and bound orbitals of the unionized system, i.e. the NO term $\varepsilon_\alpha \langle \psi_\alpha | \Phi_{i\alpha} \rangle$. In our implementation, we derived all matrix elements in first quantization using Löwdin's calculus for transition matrix elements between Slater determinants in a nonorthogonal basis [5]. Naturally, this formalism cannot make use of elegant simplifications by using the commutation relations as in Eq. (S3) to reexpress the matrix elements. However, one can of course relate the determinant based first quantized formalism to the second quantized one as was done in the Theory section of this paper. It is possible to rearrange the NO-terms in such a way that a relation similiar to the second term in Eq. (S3) is obtained, namely:

$$A_{i\alpha}^{\mathrm{NO}} = \sum_t^{N_{\mathrm{orb}}^{\mathrm{occ}}} \langle \psi_\alpha | \varphi_t \rangle \tag{S18}$$

$$\times \langle \Psi_f^+ | \left(\underbrace{\sum_{q,s}^{N_{\mathrm{orb}}^{\mathrm{occ}}} \langle \varphi_q^+ | h | \varphi_s \rangle (a_q^+)^\dagger a_s + \frac{1}{2} \sum_{\substack{q_1 \neq q_2 \\ s_1 \neq s_2}}^{N_{\mathrm{orb}}^{\mathrm{occ}}} \langle \varphi_{q_1}^+ \varphi_{q_2}^+ | \frac{1}{r_{12}} | \varphi_{s_2} \varphi_{s_1} \rangle (a_{q_1}^+)^\dagger (a_{q_2}^+)^\dagger a_{s_2} a_{s_1}}_{\tilde{\mathcal{H}}} - \mathcal{E}_i \right) a_t | \Psi_i \rangle$$

$$\tag{S19}$$

Note that two first sums in the parentheses correspond to Hamiltonian matrix $\tilde{\mathcal{H}}$ in the mixed basis. Here, the limit $N_{\mathrm{orb}}^{\mathrm{occ}}$ indicates that the summation is carried out only over orbitals φ_s, φ_q^+ that may be occupied in the states $|\Psi_i\rangle$ and $|\Psi_f^+\rangle$, respectively. That is inactive and active ones within RASSCF formalism. To show the equivalence, i.e. that $A_{i\alpha}^{\mathrm{NO}} = \langle \Psi_f^+ | (\mathcal{H} - \mathcal{E}_i) a_\alpha | \Psi_i \rangle$, we need first to transform the Hamiltonian $\tilde{\mathcal{H}}$ to the basis of the ionized state $|\Psi_f^+\rangle$. This is achieved by expanding the annihilation operators a_s in the ionized basis:

$$a_s = \sum_q^{N_{\mathrm{orb}}} \langle \varphi_s | \varphi_q^+ \rangle a_q^+ \tag{S20}$$

Here, however, one has to take into account all, i.e. occupied and virtual orbitals: $N_{\mathrm{orb}} = N_{\mathrm{orb}}^{\mathrm{occ}} + N_{\mathrm{orb}}^{\mathrm{virt}}$. Second, the ket orbitals need to be contracted with the the overlap integrals using the completeness:

$$|\varphi_q^+\rangle = \sum_s^{N_{\mathrm{orb}}} \langle \varphi_s | \varphi_q^+ \rangle |\varphi_s\rangle \tag{S21}$$

11

In Eq. (S18), however, the summation spans only the space of the occupied unionized orbitals φ_s. Hence we can in generally not transform the operator $\tilde{\mathcal{H}}$ into a proper Hamiltonian

$$\mathcal{H}^+ = \sum_{q_1,q_2}^{N_{\text{orb}}^{\text{occ}}} \langle \varphi_{q_1}^+ | h | \varphi_{q_2}^+ \rangle (a_{q_1}^+)^\dagger a_{q_2}^+ + \frac{1}{2} \sum_{\substack{q_1 \neq q_2 \\ q_3 \neq q_4}}^{N_{\text{orb}}^{\text{occ}}} \langle \varphi_{q_1}^+ \varphi_{q_2}^+ | \frac{1}{r_{12}} | \varphi_{q_3}^+ \varphi_{q_4}^+ \rangle (a_{q_1}^+)^\dagger (a_{q_2}^+)^\dagger a_{q_4}^+ a_{q_3}^+ \qquad \text{(S22)}$$

that allows the exploitation of $\mathcal{H}^+ |\Psi_f^+\rangle = \mathcal{E}_f |\Psi_f^+\rangle$. The only exceptions to this rule are cases, when the occupied orbitals used for the ionized and unionized states span the same Hilbert space. Two particular cases, where this is true are Full-CI calculations and calculations in frozen orbital approximation, where the ionized wave functions are obtained using the unionized orbital basis, or vice-versa.

In brief this can by summarized in the following statements: Due to the fact that the wave functions for the bound ionized and unionized states are obtained in independent RASSCF calculations, these wave functions generally belong to different Hilbert spaces. A consequence of this is that the NO terms evaluated using the second quantization approach of Manne and Åberg [4], exploiting the eigenvalue equation $\mathcal{H} |\Psi_f^+\rangle = \mathcal{E}_f |\Psi_f^+\rangle$, deviate from the ones evaluated using the approach presented in the main text in Eqs. (12)-(18). These two approaches give equal results only, if wave functions actually span the same space, e.g., in full CI approach or using the frozen orbital approximation. Further, the eigenvalue equation can in principle only be used, if the coupling Hamiltonian is the same as the one used in the wave function optimization. This regards especially perturbative energetic corrections, or the inclusion of scalar relativistic effects, which are often included in the SCF procedures, but in our case not in the evaluation of the coupling matrix element. For the decay of the neon $1s^{-1}3p$ resonance, evaluated using QC scheme I with and without RASPT2 corrected energies, the difference between both approaches is indicated in Fig. S10. The integrated decay rates evaluated using the RASPT2 corrected and the original RASSCF state energies, do not visibly differ, indicating, that the pt2 terms can in this case be neglected from the coupling Hamiltonian.

12
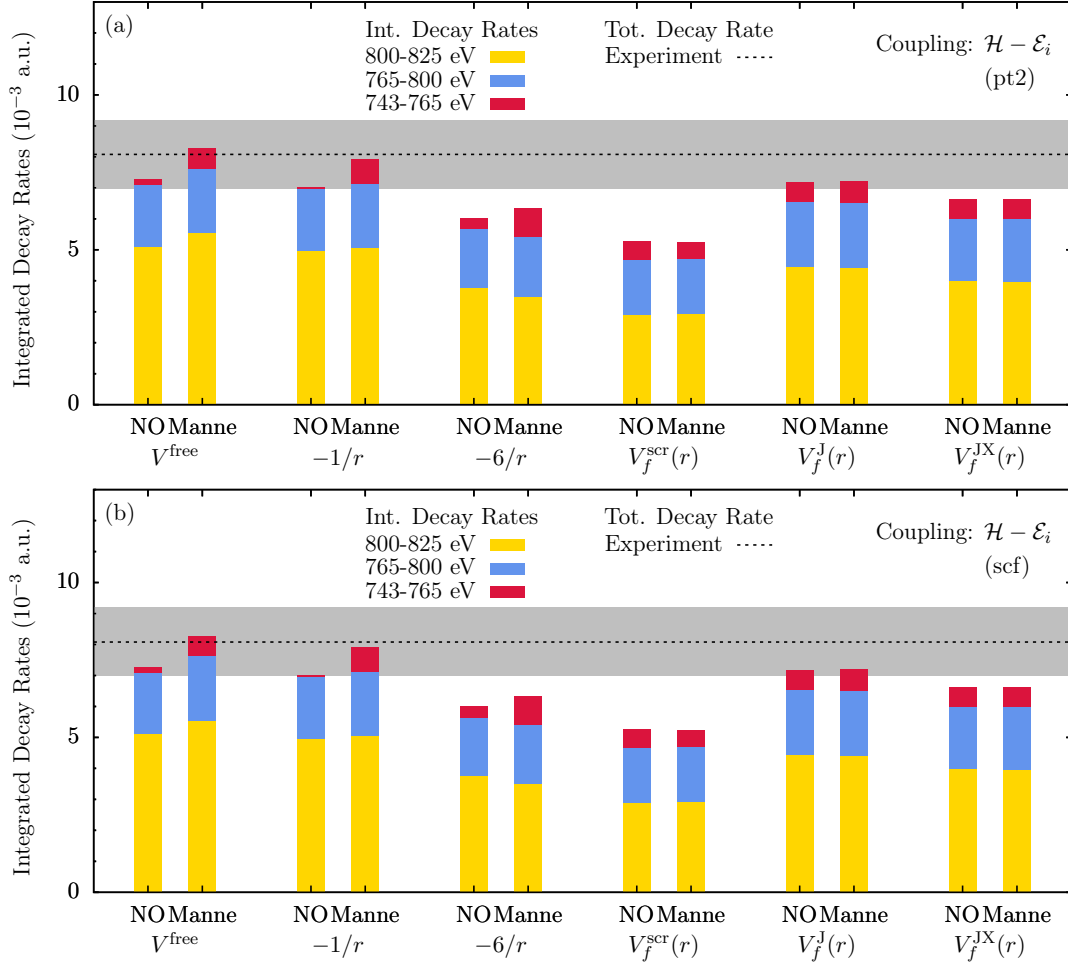
FIG. S10. Comparison of the neon $1s^{-1}3p$ Auger decay rates integrated over the given spectral regions. Data in(a) and (b) were obtained using the underlying QC scheme I, with and without the RASPT2 correction. The partial rates have been obtained using the $\mathcal{H}$ coupling, all potential models and either the NO approach as discussed in the main text of the paper and in Eq. (S18) (NO), or the one suggested in Ref. 4, corresponding to Eq. (S3) (Manne). For reference, the experimental ($8.08 \pm 1.1 \times 10^{-3}$ a.u. [1]) value of the total Auger decay rate is given.

13

III.   BASIS SETS

- QC I: $(22s17p12d11f)/[7s6p3d2f]$

```
     Ne S
166165.08      0.0000   -0.0000    0.0000   -0.0000    0.0000   -0.0000    0.0000
23107.524      0.0004   -0.0001    0.0000   -0.0000    0.0000   -0.0000    0.0000
5060.1539      0.0022   -0.0005    0.0001   -0.0000    0.0000   -0.0001    0.0001
1384.6123      0.0096   -0.0024    0.0004   -0.0001    0.0000   -0.0004    0.0004
436.51258      0.0351   -0.0089    0.0015   -0.0004    0.0001   -0.0015    0.0016
153.47148      0.1049   -0.0277    0.0046   -0.0012    0.0002   -0.0047    0.0049
59.389087      0.2385   -0.0693    0.0117   -0.0031    0.0006   -0.0120    0.0124
24.861967      0.3704   -0.1311    0.0220   -0.0057    0.0012   -0.0222    0.0230
11.015704      0.3054   -0.1662    0.0309   -0.0082    0.0017   -0.0325    0.0341
4.9651750      0.0832   -0.0071    0.0015   -0.0002    0.0000   -0.0008    0.0021
1.9365030      0.0033    0.4415   -0.0849    0.0220   -0.0045    0.0894   -0.0982
0.76572800     0.0007    0.5713   -0.1913    0.0547   -0.0118    0.2388   -0.2584
0.29553800    -0.0001    0.1218   -0.1230    0.0394   -0.0132    0.1114   -0.0841
0.10343800     0.0002   -0.0130    0.1017   -0.0460    0.0066   -0.7688    1.0169
0.06564559    -0.0002    0.0089    0.3612   -0.1964    0.0610   -0.8099    0.6778
0.02462393     0.0001   -0.0035    1.2334   -0.8336    0.8883    1.8774   -3.0894
0.01125334    -0.0001    0.0036   -0.6690    0.9454   -1.8079   -0.0414    1.6952
0.00585838     0.0002   -0.0040   -0.5411    0.9891   -1.3819   -0.9776    3.4980
0.00334597    -0.0002    0.0044    0.6793   -0.4056    2.9154    0.1501   -5.6430
0.00204842     0.0002   -0.0041   -0.0644    0.1257   -0.3728   -1.7904    1.0781
0.00132364    -0.0001    0.0023    0.0417   -0.0656    0.2021    2.0906    0.9034
0.00089310     0.0000   -0.0006   -0.0258    0.0241   -0.1583    0.1710    0.6692
     Ne P
234.94500      0.0018   -0.0002    0.0000   -0.0000    0.0004   -0.0003
55.077385      0.0143   -0.0017    0.0001   -0.0003    0.0028   -0.0026
17.389549      0.0653   -0.0081    0.0004   -0.0015    0.0129   -0.0121
6.3895370      0.1918   -0.0246    0.0011   -0.0045    0.0398   -0.0377
2.5420820      0.3494   -0.0492    0.0022   -0.0091    0.0823   -0.0793
1.0337640      0.3958   -0.0562    0.0025   -0.0101    0.0943   -0.0900
0.41878800     0.2048   -0.0311    0.0026   -0.0070    0.0292   -0.0140
0.16462700     0.0139    0.1027   -0.0123    0.0127   -0.3868    0.3837
0.05761900     0.0095    0.2481   -0.0285   -0.0296   -1.3944    1.3447
0.04233528    -0.0113    0.3076   -0.0647    0.2715    1.0749   -1.1970
0.01925421     0.0063    0.8708   -0.1525    0.5566    0.9404   -1.1293
0.00998821    -0.0075   -0.5514    0.4601   -1.5324   -0.4657    0.9914
0.00568936     0.0095   -0.1837    0.4750   -0.6211   -0.2237    1.3645
0.00347568    -0.0102   -0.1157    0.2575    1.2679    0.0567   -2.0164
0.00224206     0.0083    0.2662   -0.0324    0.5138   -0.6760   -0.0023
0.00151064    -0.0047   -0.0682    0.0319    0.2608   -0.1087   -0.6459
0.00105475     0.0013   -0.0217   -0.0090   -0.3426    1.2059    1.6974
     Ne D
6.4200000      0.0002   -0.0016    0.0020
2.2470000      0.0007   -0.0046    0.0058
0.78645000     0.0034   -0.0260    0.0340
0.275257500    0.0042   -0.0365    0.0489
0.16329773     0.0195   -0.1902    0.2497
0.06054020     0.0894   -0.5041    0.5975
0.02744569     0.3365   -0.1129   -0.1793
0.01420440     0.4900    0.0937   -0.5889
0.00807659     0.1965    0.1198   -0.1697
0.00492719     0.0129    0.2599    0.4914
0.00317481    -0.0284    0.2720    0.3012
0.00213712    -0.0158    0.1298    0.2098
     Ne F
4.1900000      0.0000   -0.0000
1.6760000      0.0001   -0.0002
0.67040000     0.0008   -0.0014
0.21400555     0.0121   -0.0225
0.07906987     0.0892   -0.1611
0.03576293     0.2559   -0.4308
0.01847779     0.3113   -0.3363
0.01049301     0.2119    0.1208
0.00639492     0.2212    0.4092
0.00411721     0.1148    0.2259
0.00276965     0.0981    0.1924
```

14

- QC II: (22s17p12d11f)/[22s6p3d2f]-rcc

```
Ne S
166165.08      1.0 0.0 0.0 0.0 0.0 0.0 0.0 0.0 0.0 0.0 0.0 0.0 0.0 0.0 0.0 0.0 0.0 0.0 0.0 0.0 0.0 0.0
23107.524      0.0 1.0 0.0 0.0 0.0 0.0 0.0 0.0 0.0 0.0 0.0 0.0 0.0 0.0 0.0 0.0 0.0 0.0 0.0 0.0 0.0 0.0
5060.1539      0.0 0.0 1.0 0.0 0.0 0.0 0.0 0.0 0.0 0.0 0.0 0.0 0.0 0.0 0.0 0.0 0.0 0.0 0.0 0.0 0.0 0.0
1384.6123      0.0 0.0 0.0 1.0 0.0 0.0 0.0 0.0 0.0 0.0 0.0 0.0 0.0 0.0 0.0 0.0 0.0 0.0 0.0 0.0 0.0 0.0
436.51258      0.0 0.0 0.0 0.0 1.0 0.0 0.0 0.0 0.0 0.0 0.0 0.0 0.0 0.0 0.0 0.0 0.0 0.0 0.0 0.0 0.0 0.0
153.47148      0.0 0.0 0.0 0.0 0.0 1.0 0.0 0.0 0.0 0.0 0.0 0.0 0.0 0.0 0.0 0.0 0.0 0.0 0.0 0.0 0.0 0.0
59.389087      0.0 0.0 0.0 0.0 0.0 0.0 1.0 0.0 0.0 0.0 0.0 0.0 0.0 0.0 0.0 0.0 0.0 0.0 0.0 0.0 0.0 0.0
24.861967      0.0 0.0 0.0 0.0 0.0 0.0 0.0 1.0 0.0 0.0 0.0 0.0 0.0 0.0 0.0 0.0 0.0 0.0 0.0 0.0 0.0 0.0
11.015704      0.0 0.0 0.0 0.0 0.0 0.0 0.0 0.0 1.0 0.0 0.0 0.0 0.0 0.0 0.0 0.0 0.0 0.0 0.0 0.0 0.0 0.0
4.9651750      0.0 0.0 0.0 0.0 0.0 0.0 0.0 0.0 0.0 1.0 0.0 0.0 0.0 0.0 0.0 0.0 0.0 0.0 0.0 0.0 0.0 0.0
1.9365030      0.0 0.0 0.0 0.0 0.0 0.0 0.0 0.0 0.0 0.0 1.0 0.0 0.0 0.0 0.0 0.0 0.0 0.0 0.0 0.0 0.0 0.0
0.76572800     0.0 0.0 0.0 0.0 0.0 0.0 0.0 0.0 0.0 0.0 0.0 1.0 0.0 0.0 0.0 0.0 0.0 0.0 0.0 0.0 0.0 0.0
0.29553800     0.0 0.0 0.0 0.0 0.0 0.0 0.0 0.0 0.0 0.0 0.0 0.0 1.0 0.0 0.0 0.0 0.0 0.0 0.0 0.0 0.0 0.0
0.10343800     0.0 0.0 0.0 0.0 0.0 0.0 0.0 0.0 0.0 0.0 0.0 0.0 0.0 1.0 0.0 0.0 0.0 0.0 0.0 0.0 0.0 0.0
0.06564559     0.0 0.0 0.0 0.0 0.0 0.0 0.0 0.0 0.0 0.0 0.0 0.0 0.0 0.0 1.0 0.0 0.0 0.0 0.0 0.0 0.0 0.0
0.02462393     0.0 0.0 0.0 0.0 0.0 0.0 0.0 0.0 0.0 0.0 0.0 0.0 0.0 0.0 0.0 1.0 0.0 0.0 0.0 0.0 0.0 0.0
0.01125334     0.0 0.0 0.0 0.0 0.0 0.0 0.0 0.0 0.0 0.0 0.0 0.0 0.0 0.0 0.0 0.0 1.0 0.0 0.0 0.0 0.0 0.0
0.00585838     0.0 0.0 0.0 0.0 0.0 0.0 0.0 0.0 0.0 0.0 0.0 0.0 0.0 0.0 0.0 0.0 0.0 1.0 0.0 0.0 0.0 0.0
0.00334597     0.0 0.0 0.0 0.0 0.0 0.0 0.0 0.0 0.0 0.0 0.0 0.0 0.0 0.0 0.0 0.0 0.0 0.0 1.0 0.0 0.0 0.0
0.00204842     0.0 0.0 0.0 0.0 0.0 0.0 0.0 0.0 0.0 0.0 0.0 0.0 0.0 0.0 0.0 0.0 0.0 0.0 0.0 1.0 0.0 0.0
0.00132364     0.0 0.0 0.0 0.0 0.0 0.0 0.0 0.0 0.0 0.0 0.0 0.0 0.0 0.0 0.0 0.0 0.0 0.0 0.0 0.0 1.0 0.0
0.00089310     0.0 0.0 0.0 0.0 0.0 0.0 0.0 0.0 0.0 0.0 0.0 0.0 0.0 0.0 0.0 0.0 0.0 0.0 0.0 0.0 0.0 1.0
Ne P
234.94500      0.0018637129    -0.0002325222     0.0000107091    -0.0000429907     0.0003738603    -0.0003517440
55.077385      0.0144368802    -0.0017603337     0.0000805393    -0.0003240015     0.0028269923    -0.0026522743
17.389549      0.0655455723    -0.0081059303     0.0003802324    -0.0015003783     0.0129611220    -0.0121016505
6.3895370      0.1919505918    -0.0246273668     0.0011183944    -0.0045294322     0.0398964111    -0.0377131548
2.5420820      0.3493936429    -0.0492170997     0.0022603113    -0.0091034183     0.0822657993    -0.0793181401
1.0337640      0.3956032309    -0.0561815168     0.0025468717    -0.0101499112     0.0943376692    -0.0899698274
0.41878800     0.2047389632    -0.0310120557     0.0026180533    -0.0069506079     0.0290727168    -0.0138380624
0.16462700     0.0138949272     0.1023512480    -0.0123569722     0.0126714756    -0.3869789499     0.3837973808
0.05761900     0.0093620053     0.2505761725    -0.0284266987    -0.0301358904    -1.3945339063     1.3434793957
0.04233528    -0.0111611841     0.3042531367    -0.0657160178     0.2725443581     1.0754321215    -1.1958775614
0.01925421     0.0061177004     0.8724225945    -0.1531717163     0.5562091504     0.9401891546    -1.1295873123
0.00998821    -0.0071209447    -0.5528054898     0.4603629211    -1.5319718069    -0.4659020697     0.9925670366
0.00568936     0.0091045317    -0.1798678725     0.4759377271    -0.6216710256    -0.2232771060     1.3622486397
0.00347568    -0.0097318352    -0.1189668097     0.2570227575     1.2685463019     0.0562993054    -2.0141040571
0.00224206     0.0079224405     0.2686353415    -0.0323894548     0.5133406889    -0.6755011942    -0.0041620579
0.00151064    -0.0044646463    -0.0696963916     0.0317415552     0.2609943268    -0.1088498576    -0.6447441951
0.00105475     0.0012792313    -0.0212088242    -0.0088902706    -0.3425688911     1.2056376298     1.6972415185
Ne D
6.4200000      0.0002327144    -0.0015610076     0.0020109806
2.2470000      0.0007463332    -0.0045587641     0.0057582120
0.78645000     0.0034266133    -0.0259142298     0.0340449112
0.27525750     0.0042948074    -0.0367084557     0.0484963240
0.16329773     0.0193393737    -0.1898629249     0.2501956316
0.06054020     0.0900242792    -0.5043133352     0.5972605729
0.02744569     0.3346702372    -0.1128353381    -0.1792156753
0.01420440     0.4932777735     0.0939364131    -0.5887038263
0.00807659     0.1921250090     0.1193953290    -0.1703931380
0.00492719     0.0170430431     0.2603482660     0.4920300727
0.00317481    -0.0309291251     0.2717510449     0.3008438462
0.00213712    -0.0150705742     0.1298422386     0.2098560362
Ne F
4.1900000      0.0000241701    -0.0000391518
1.6760000      0.0001347578    -0.0002504648
0.67040000     0.0007803298    -0.0013482270
0.21400555     0.0120397134    -0.0225258780
0.07906987     0.0893736617    -0.1608630787
0.03576293     0.2555265976    -0.4315122957
0.01847779     0.3118937733    -0.3352314194
0.01049301     0.2113443838     0.1197315048
0.00639492     0.2217027219     0.4102217040
0.00411721     0.1142746337     0.2249266115
0.00276965     0.0983741234     0.1929267171
```

15

- QC III: (22s17p12d11f)/[9s8p5d4f]

```
Ne S
166165.08    0.0000   -0.0000    0.0000   -0.0000    0.0000   -0.0000    0.0000    0.0000   -0.0000
23107.524    0.0004   -0.0001    0.0000   -0.0000    0.0000   -0.0000    0.0000    0.0000   -0.0000
5060.1539    0.0022   -0.0005    0.0001   -0.0000    0.0000   -0.0001    0.0001    0.0000   -0.0000
1384.6123    0.0096   -0.0024    0.0004   -0.0001    0.0000   -0.0004    0.0004    0.0000   -0.0000
436.51258    0.0351   -0.0089    0.0015   -0.0004    0.0001   -0.0015    0.0016    0.0001   -0.0001
153.47148    0.1049   -0.0277    0.0046   -0.0012    0.0002   -0.0047    0.0049    0.0003   -0.0003
59.389087    0.2385   -0.0693    0.0117   -0.0031    0.0006   -0.0120    0.0124    0.0009   -0.0008
24.861967    0.3704   -0.1311    0.0220   -0.0057    0.0012   -0.0222    0.0230    0.0016   -0.0014
11.015704    0.3054   -0.1662    0.0309   -0.0082    0.0017   -0.0325    0.0341    0.0024   -0.0023
4.9651750    0.0832   -0.0071    0.0015   -0.0002    0.0000   -0.0008    0.0021   -0.0003    0.0005
1.9365030    0.0033    0.4415   -0.0849    0.0220   -0.0045    0.0894   -0.0982   -0.0058    0.0047
0.76572800   0.0007    0.5713   -0.1913    0.0547   -0.0118    0.2388   -0.2584   -0.0199    0.0193
0.29553800  -0.0001    0.1218   -0.1230    0.0394   -0.0132    0.1114   -0.0841   -0.0056    0.0006
0.10343800   0.0002   -0.0130    0.1017   -0.0460    0.0066   -0.7688    1.0169    0.0540   -0.0178
0.06564559  -0.0002    0.0089    0.3612   -0.1964    0.0610   -0.8099    0.6778    0.1659   -0.2089
0.02462393   0.0001   -0.0035    1.2334   -0.8336    0.8883    1.8774   -3.0894   -0.4864    0.5907
0.01125334  -0.0001    0.0036   -0.6690    0.9454   -1.8079   -0.0414    1.6952   -0.5593    0.0109
0.00585838   0.0002   -0.0040   -0.5411    0.9891   -1.3819   -0.9776    3.4980    3.7655   -1.8740
0.00334597  -0.0002    0.0044    0.6793   -0.4056    2.9154    0.1501   -5.6430   -3.7723   -2.7701
0.00204842   0.0002   -0.0041   -0.0644    0.1257   -0.3728   -1.7904    1.0781   -1.8134   20.6876
0.00132364  -0.0001    0.0023    0.0417   -0.0656    0.2021    2.0906    0.9034    2.0417  -30.2943
0.00089310   0.0000   -0.0006   -0.0258    0.0241   -0.1583    0.1710    0.6692    1.1648   14.1291
Ne P
234.94500    0.0018   -0.0002    0.0000   -0.0000    0.0004   -0.0003    0.0000   -0.0000
55.077385    0.0143   -0.0017    0.0001   -0.0003    0.0028   -0.0026    0.0002   -0.0002
17.389549    0.0653   -0.0081    0.0004   -0.0015    0.0129   -0.0121    0.0007   -0.0008
6.3895370    0.1918   -0.0246    0.0011   -0.0045    0.0398   -0.0377    0.0022   -0.0022
2.5420820    0.3494   -0.0492    0.0022   -0.0091    0.0823   -0.0793    0.0042   -0.0047
1.0337640    0.3958   -0.0562    0.0025   -0.0101    0.0943   -0.0900    0.0051   -0.0044
0.41878800   0.2048   -0.0311    0.0026   -0.0070    0.0292   -0.0140    0.0031   -0.0059
0.16462700   0.0139    0.1027   -0.0123    0.0127   -0.3868    0.3837   -0.0293    0.0399
0.05761900   0.0095    0.2481   -0.0285   -0.0296   -1.3944    1.3447   -0.1268    0.0159
0.04233528  -0.0113    0.3076   -0.0647    0.2715    1.0749   -1.1970    0.1017    0.1029
0.01925421   0.0063    0.8708   -0.1525    0.5566    0.9404   -1.1293    0.2895   -0.7123
0.00998821  -0.0075   -0.5514    0.4601   -1.5324   -0.4657    0.9914   -0.0079    1.3222
0.00568936   0.0095   -0.1837    0.4750   -0.6211   -0.2237    1.3645   -1.6572   -2.1903
0.00347568  -0.0102   -0.1157    0.2575    1.2679    0.0567   -2.0164    1.8177    8.9400
0.00224206   0.0083    0.2662   -0.0324    0.5138   -0.6760   -0.0023    0.5743  -23.9575
0.00151064  -0.0047   -0.0682    0.0319    0.2608   -0.1087   -0.6459    0.5885   28.5560
0.00105475   0.0013   -0.0217   -0.0090   -0.3426    1.2059    1.6974   -2.1804  -12.3430
Ne D
6.4200000    0.0002   -0.0016    0.0020    0.0004   -0.0003
2.2470000    0.0007   -0.0046    0.0058    0.0011   -0.0009
0.78645000   0.0034   -0.0260    0.0340    0.0061   -0.0060
0.275257500  0.0042   -0.0365    0.0489    0.0093   -0.0043
0.16329773   0.0195   -0.1902    0.2497    0.0419   -0.0459
0.06054020   0.0894   -0.5041    0.5975    0.1196   -0.0823
0.02744569   0.3365   -0.1129   -0.1793   -0.0300   -0.0772
0.01420440   0.4900    0.0937   -0.5889   -0.3045    0.7403
0.00807659   0.1965    0.1198   -0.1697   -0.3555   -0.9664
0.00492719   0.0129    0.2599    0.4914    0.4717    2.4093
0.00317481  -0.0284    0.2720    0.3012    0.3991   -5.7700
0.00213712  -0.0158    0.1298    0.2098    0.4574    4.1147
Ne F
4.1900000    0.0000   -0.0000    0.0000   -0.0000
1.6760000    0.0001   -0.0002    0.0001    0.0001
0.67040000   0.0008   -0.0014    0.0002   -0.0008
0.21400555   0.0121   -0.0225    0.0045   -0.0021
0.07906987   0.0892   -0.1611    0.0286   -0.0487
0.03576293   0.2559   -0.4308    0.1041   -0.0358
0.01847779   0.3113   -0.3363    0.1124   -0.4500
0.01049301   0.2119    0.1208    0.1505    0.9052
0.00639492   0.2212    0.4092   -0.4570   -1.9310
0.00411721   0.1148    0.2259   -0.0127    4.5540
0.00276965   0.0981    0.1924   -0.7222   -3.3404
```

16

[1] L. Avaldi, G. Dawber, R. Camilloni, G. C. King, M. Roper, M. R. F. Siggel, G. Stefani, M. Zitnik, A. Lisini, and P. Decleva, Phys. Rev. A **51**, 5025 (1995).

[2] A. Kivimäki, S. Heinäsmäki, M. Jurvansuu, S. Alitalo, E. Nõmmiste, H. Aksela, and S. Aksela, J. Electron Spectrosc. Relat. Phenom. **114**, 49 (2001).

[3] H. Yoshida, K. Ueda, N. M. Kabachnik, Y. Shimizu, Y. Senba, Y. Tamenori, H. Ohashi, I. Koyano, I. H. Suzuki, R. Hentges, J. Viefhaus, and U. Becker, J. Phys. B At. Mol. Opt. Phys. **33**, 4343 (2000).

[4] R. Manne and H. Ågren, Chem. Phys. **93**, 201 (1985).

[5] P.-O. Löwdin, Phys. Rev. **97**, 1474 (1955).

17

9 Additional manuscripts

[GG5]   Multi-reference protocol for (auto)ionization spectra: application to molecules

GILBERT GRELL, and SERGEY I. BOKAREV

Reprinted from GILBERT GRELL, and SERGEY I. BOKAREV, *arXiv:* 1912.04139 [physics.chem-ph] (2019).

Multi-reference protocol for (auto)ionization spectra: application to molecules

Gilbert Grell[a)] and Sergey I. Bokarev

Institut für Physik, Universität Rostock, Albert-Einstein-Str. 23-24, 18059 Rostock, Germany

(Dated: December 10, 2019)

We present the application of the spherically averaged continuum model to the evaluation of molecular photoelectron and resonant Auger electron spectra. In this model, the continuum wave function is obtained in a numerically efficient way by solving the radial Schrödinger equation with a spherically averaged molecular potential. Different approximations to the Auger transition matrix element and, in particular, the one-center approximation are thoroughly tested against experimental data for the CH_4, O_2, NO_2, and pyrimidine molecules. In general, this approach appears to estimate the shape of the photoelectron and autoionization spectra as well as the total Auger decay rates with reasonable accuracy, allowing for the interpretation of experimental results.

I. INTRODUCTION

Photoionization and (resonant) autoionization processes encode the system's electronic structure into the kinetic energy of the ejected electrons, producing a Photoelectron Spectrum (PES) or a Resonant Auger Electron Spectrum (RAES), respectively. A particular advantage of these electron-out spectroscopies is that they map bound to continuum states and thus are not subject to selection rule suppression and are more flexible than optical spectroscopy.[1–3] For instance, the combination of X-ray valence PES and RAES has been used to unravel specific solute-solvent interactions of transition metal complexes in solutions.[4–6] In addition, these processes can probe, initiate, and couple to complex electronic and nuclear dynamics.[7–11] Moreover, they can cause biological radiation damage by a cascade of autoionization events.[12,13]

Often the resulting spectra are feature-rich and difficult to interpret based on the experimental data alone.[6,14] Hence, the development of theoretical methods for the simulation of PES and RAES has accompanied the experimental advancement during the last decades. Notably, modelling ionization processes remains challenging until today, although the fundamental theory is been known for decades.[15–18]

Here, the most general framework is the multi-channel scattering formalism,[17] treating continuum and bound states on the same level and including correlation effects between them.[19,20] At this level of accuracy, solving the bound and continuum problems in a B-spline basis,[21] specialized Gaussian basis sets,[22,23] or combination of both[24] has proven to be a versatile approach for atoms, diatomics, and first-row hydrides.[23,25–27]

More approximate approaches are usually obtained in the single-channel scattering formalism.[20] For example, the multi-centered B-spline static-exchange Density Functional Theory (DFT) method[28,29] has been applied to molecules reaching the size of small organometallic complexes.[29–32] Further, methods that project the molecular problem on a one-center expansion allow to evaluate PES and RAES of small molecular systems with remarkable accuracy.[33–35] A particular efficient scheme is obtained, if the molecular continuum orbital problem is approximated by an atomic one.[36–41] Here, the simplest approach is to model the outgoing electron as a free particle or a distorted wave corresponding to an effective Coulomb potential,[42–44] which has been in particular applied to PES studies of rather large molecules.[45–49] Finally, an entirely different set of methods relies on an implicit continuum representation with Stieltjes imaging[50–53] or a Green's operator formalism.[54] However, energies of several hundreds of eV, targeted in X-ray PES and RAES necessitate large basis sets leading to demanding computations.

In all these methods, there is a certain trade-off between the accuracy that can be afforded for modelling the bound states and the continuum part on the one side and the size of the system on the other. On the one pole, the multi-channel methods are residing which are highly accurate but computationally expensive and, thus, allow for treatment of only small systems. The other extreme is to neglect the multi-center molecular potential and use simplistic representations like the free-particle approach, sacrificing the accuracy in favor of computational feasibility. Moreover, most of the methods described above have a single reference character and are not suited to treat systems possessing multi-configurational wave functions, e.g., open-shell and transition metal compounds or dynamics near conical intersections.

In this article, we employ a multi-reference Quantum Chemistry (QC) protocol and present the Spherical Continuum for Ionization (SCI) approach for the evaluation of photoionization cross sections and partial Auger decay rates for the case of molecules. The central approximation in the protocol is that the angular structure of the molecular potential is averaged out, leading to spherically symmetric continuum orbitals that are obtained by numerically solving the radial Schrödinger equation.

Thus, it represents a compromise between the two extreme cases mentioned above. This work is a logical continuation of our previous benchmark of the protocol for the atomic case of RAES of the neon $1s^{-1}3p$ resonance, where it was shown to yield spectra and total decay rates in good agreement with experimental references.[55] Such an approach, being natural for atoms, requires a numerical justification for the non-spherically symmetric molecular case. As is demonstrated here, the SCI method indeed provides a valuable insight into the character of photoionization and autoionization molecular spectral features. In addition, we investigate the performance of the popular One-Center Approximation (1CA) to Auger decay,[36,39,40,56] neglecting contributions from atoms other than the core-hole bearing one.

Concerning the applicability of the SCI ansatz, the crucial role is expected to be played by the deviations of the molecular point symmetry from the spherical one. In this respect, highly symmetric molecules should in general be more suitable objects for SCI representation, whereas for highly non-spherical systems, e.g., linear or planar, SCI model might represent a quite crude approximation. Therefore, we start the discussion with the K-edge spectra of CH_4, being isoelectronic to neon studied previously,[55] which is the simplest system out of the selected series as it contains only one heavy atom and possesses a high symmetry. Increasing the complexity, we continue with the open shell molecules O_2 and NO_2, allowing for ionization channels corresponding to different spins of ionic remainder, and address the K-edges of oxygen and nitrogen, respectively. The largest object studied herein is the pyrimidine ($C_4H_4N_2$) which is an aromatic heterocyclic system, where we aim at description of nitrogen K-edge. For O_2 and pyrimidine, there is ambiguity in selecting the origin of the spherically symmetric continuum orbital because of presence of two equivalent atoms, which makes them also interesting objects for testing.

One should note that for such small molecules vibrational effects, showing up as, e.g. vibronic progressions in the (auto)ionization spectra, are of importance and alter the measured experimental spectrum.[56] Furthermore, they can lead to emergence of a measurable signal, even if a purely electronic transition is forbidden, due to vibronic interactions[57] or show up in new features appearing due to the ultrafast dissociation.[58] In this work, we considered only electronic effects since the main goal is to test our multi-reference protocol for the case of molecules. The full treatment, however, would require the inclusion of the nuclear motion into the consideration.

The article is organized as follows. First, we briefly recapitulate the theory behind our approach in Section II, which is presented in detail elsewhere,[55] and give the details of our computational setup in Section III. The X-ray Absorption Spectrum (XAS), RAES, and valence PES are discussed on a case to case basis for each molecule separately in Section IV. The overall summary across the series of molecules under study is given in Conclusions, Section V.

II. THEORY

In this section, we briefly present theory behind our method; the detailed description can be found in our recent article.[55] Atomic units (a.u.) are employed throughout this article, if not stated otherwise. We restrict ourselves to the limits of first order perturbation theory, dipole approximation, and length gauge for the absorption and photoionization cross sections σ_{gi} and $\sigma_{g\alpha}$. Further, the average over the molecular orientation with respect to the polarization vector of the incoming light is taken. Finally, the nonradiative decay rates $\Gamma_{i\alpha}$ are estimated within the two-step model,[59] neglecting the excitation process and the interference of decay and direct ionization pathways. The resulting expressions for XAS, PES, and RAES read

$$\sigma_{gi} = \frac{4\pi^2}{3c}\omega \left| \left\langle \Psi_i \middle| \boldsymbol{\mu} \middle| \Psi_g \right\rangle \right|^2, \tag{1}$$

$$\sigma_{g\alpha} = \frac{4\pi^2}{3c}\omega k \left| \left\langle \Psi_\alpha \middle| \boldsymbol{\mu} \middle| \Psi_g \right\rangle \right|^2, \tag{2}$$

$$\Gamma_{i\alpha} = 2\pi \left| \left\langle \Psi_\alpha \middle| \mathcal{H} - \mathcal{E}_i \middle| \Psi_i \right\rangle \right|^2, \tag{3}$$

respectively.[16,19,60] Here, $\left| \Psi_g \right\rangle$ denote the ground state, $\left| \Psi_i \right\rangle$ are intermediate core-excited states (resonances), and $\left| \Psi_\alpha \right\rangle$ are ionized continuum states (autoionization channels) of the system. Further, $\boldsymbol{\mu} = -\sum_{u=1}^{N} \mathbf{r}_u$ is the N-electron dipole operator, $\mathcal{H} = \sum_u h_u + \sum_{u<v} 1/r_{uv}$ is the molecular Hamiltonian, containing one-electron h_u and two-electron $1/r_{uv}$ parts respectively, and $\mathcal{E}_i$, ω, and k are the energies of $\left| \Psi_i \right\rangle$, of the incoming radiation as well as the wavenumber of the ionized electron, respectively. To ensure that the total spin and its projection onto the quantization axis for the unionized system, S and M, are conserved, the continuum states are constructed as

$$\left| \Psi_\alpha \right\rangle = \sum_{M^+=-S^+}^{S^+} \sum_{\sigma=-\frac{1}{2},\frac{1}{2}} C^{S,M}_{S^+,M^+;\sigma} \left| \Upsilon_\alpha^{\sigma M^+} \right\rangle, \tag{4}$$

where $\left| \Upsilon_\alpha^{\sigma M^+} \right\rangle = a_{\alpha,\sigma}^\dagger \left| \Psi_{f,M^+}^+ \right\rangle$ are channel functions corresponding to the bound cationic states $\left| \Psi_{f,M^+}^+ \right\rangle$ with an additional electron, created by $a_{\alpha,\sigma}^\dagger$, in the continuum orbital $\left| \psi_{\alpha,\sigma} \right\rangle$. The $C^{S,M}_{S^+,M^+;\sigma}$ are the Clebsch-Gordan coefficients; note that S^+ and M^+ correspond to the total spin and its quantization axis projection of the ionic remainder.

The central approximation of the SCI approach is to employ the spherically averaged molecular potential of the ion and thus spherically symmetric continuum orbitals

$$\psi_{\alpha,\sigma}(r,\Omega) = \frac{1}{r}w_l^{fk}(r)Y_l^m(\Omega)\zeta(\sigma), \tag{5}$$

where spherical harmonics $Y_l^m(\Omega)$, $\zeta(\sigma)$, and $w_l^{fk}(r)$ correspond to the angular, spin, and radial parts of the

wave function, respectively. The compound channel index $\alpha = (f, l, m, k)$ contains the index of the ionic bound state f, the angular and magnetic quantum numbers l and m, and the wave number $k = \sqrt{2\varepsilon_\alpha}$ of the outgoing electron. For the evaluation of the spectra, one needs to sum over all decay channels α and in particular l and m. The energy of the outgoing electron is

$$\varepsilon_\alpha = \begin{cases} \omega + \mathcal{E}_g - \mathcal{E}_f, & \text{direct ionization} \\ \mathcal{E}_i - \mathcal{E}_f, & \text{Auger decay} \end{cases} . \qquad (6)$$

In contrast to the atomic case,[55] for a molecule the origin of the continuum orbital, $\mathbf{r}_c$, and the molecular coordinate system in general differ. In fact, the location of $\mathbf{r}_c$ is often ambiguous. Thus $\mathbf{r}_s = \mathbf{r} - \mathbf{r}_c$ defines the reference frame for Eq. (5). The functions $w_l^{fk}(r)$ are numerical solutions to the radial Schrödinger equation with the spherically averaged direct Coulomb potential $V_f^{\mathrm{J}}(r) = V^{\mathrm{nuc}}(r) + J_f(r)$ of the cationic state $\left| \Psi_{f,M^+}^+ \right\rangle$ defined in spherical coordinates $\mathbf{r}_s = (r, \Omega)$ and containing nuclear $V^{\mathrm{nuc}}(r)$ and electronic $J_f(r)$ parts. They are computed using Numerov's method on a radial grid. Asymptotically the solutions are constructed such as to fulfill the conditions

$$w_l^{fk}(r \to 0) = nr^{l+1}, \qquad (7a)$$

$$w_l^{fk}(r \to \infty) = \sqrt{\frac{2}{\pi k}} \Big(\cos\delta_l^f(k) F_l(\eta, kr)$$
$$+ \sin\delta_l^f(k) G_l(\eta, kr) \Big). \qquad (7b)$$

Therein $\delta_l^f(k)$ are the scattering phases and F_l and G_l are the regular and irregular Coulomb functions,[61] respectively.

The nuclear part of $V_f^{\mathrm{J}}(r)$, corresponding to the nuclear charges being smeared out over a sphere around the photoelectron origin, resembles the classical potential of charged hollow spheres with the radii $R_{cA} = |\mathbf{r}_c - \mathbf{R}_A|$ and charge Z_A

$$V^{\mathrm{nuc}}(r) = \sum_A \begin{cases} -\frac{Z_A}{R_{cA}}, & r < R_{cA} \\ -\frac{Z_A}{r}, & r \geq R_{cA} \end{cases} . \qquad (8)$$

The electronic part $J_f(r)$, however, is the electrostatic potential of the spherically averaged electron density of the respective ionized state, which has to be determined numerically within the $\mathbf{r}_s$ reference frame.[55]

To keep this approach flexible with respect to the electronic structure method, we only require that the bound state wave functions are expressed as Configuration Interaction (CI) expansions built on the Molecular orbitals (MOs) expressed in terms of conventional Gaussian type orbital basis sets. Further, it is assumed that the neutral and cationic states have been obtained in separate calculations, comprising different relaxed sets of N_{orb} spin orbitals $\{\varphi_i\}$ and $\{\varphi_i^+\}$, respectively. Finally, the Strong Orthogonality (SO) approximation is employed throughout this work, since previous investigations[55] have shown

that quite reliable results can be obtained with it. Hence, the overlap between the continuum and bound orbitals is neglected.

For a particular ionization channel function this yields

$$\left\langle \Upsilon_\alpha^{\sigma M^+} \Big| \boldsymbol{\mu} \Big| \Psi_g \right\rangle \overset{\mathrm{SO}}{=} - \left\langle \psi_{\alpha,\sigma} \Big| \mathbf{r} \Big| \Phi_{g\alpha}^{M^+} \right\rangle, \qquad (9)$$

and the Auger decay matrix element reads

$$\left\langle \Upsilon_\alpha^{\sigma M^+} \Big| \mathcal{H} - \mathcal{E}_i \Big| \Psi_i \right\rangle \qquad (10)$$

$$\overset{\mathrm{SO}}{=} \left\langle \psi_{\alpha,\sigma} \Big| h \Big| \Phi_{i\alpha}^{M^+} \right\rangle + \underbrace{\sum_{q=1}^{N_{\mathrm{orb}}} \left\langle \psi_{\alpha,\sigma} \varphi_q^+ \Big| \frac{1}{r_{12}} \Big| \Xi_{i\alpha}^{M^+,q} \right\rangle}_{r^{-1} \text{ coupling}} .$$

Here, the matrix elements have been transformed to one and two-body integrals in terms of the corresponding Dyson orbitals $\left| \Phi_{n\alpha}^{M^+} \right\rangle$ $(n = i, g)$ and two-electron reduced transition densities $\left| \Xi_{i\alpha}^{M^+,q} \right\rangle$. Formal details and the numerical procedure to evaluate the continuum-bound matrix elements are elucidated in Ref. 55. A popular approximation to the full Auger matrix element ($\mathcal{H}$ coupling) is to disregard the one-electron terms, only accounting for the electronic Coulomb interaction (r^{-1} coupling). Further, the 1CA can be applied on top of the r^{-1} coupling to reduce the computational demands. Therein, the continuum orbital is placed on the core vacancy bearing atom and non-local contributions from all other atoms to the matrix element in Eq. 10 are neglected. The performance of the $\mathcal{H}$ and r^{-1} couplings as well as of the 1CA has been investigated here.

III. COMPUTATIONAL DETAILS

For the molecules apart from oxygen, the geometries have been obtained with the GAUSSIAN09[66] program at the B3LYP/aug-cc-pVTZ level. For oxygen, we have employed the experimentally determined equilibruum distance of $r = 1.208$ Å.[67] The molecular symmetry has been restricted to the T_d (CH_4) and C_{2v} (NO_2 and pyrimidine) point groups.

For the joint discussion of the XAS, PES and RAES on equal footing, the underlying electronic structure calculation needs to satisfy all the demands for the involved electronic states. In fact, this requires accurate predictions of the ground and core-excited states of the neutral species, as well as of the cationic valence-excited states. For this purpose we have selected the Restricted Active Space Self-Consistent Field (RASSCF)/Restricted Active Space Second Order Perturbation Theory (RASPT2)[68,69] approach. The active space is subdivided into the RAS1, RAS2, and RAS3 subspaces. The RAS1 contains o fully occupied orbitals, allowing for h holes at maximum. The occupation of the c orbitals within RAS2 is not restricted, corresponding to a full CI treatment within this subspace.

Table I. QC schemes used for the bound electronic structure calculations of the depicted molecules: employed basis set, active space, imaginary shift used in the respective PT2 calculation, and number of electronic states per charge/multiplicity of the molecule. The number of electrons in the active space corresponds to the neutral species. ANO-L[62] basis functions have been used in all cases.

	Basis Set	Active Space	δ_{PT2} [a.u.]	Nr. of States	Comment
CH_4	C: $[7s5p3d2f]^a$	$RAS(10, 1, 1; 1, 4, 19)$	0.01	$^1CH_4$: 96	SupSym^c
	H: $[3s2p1d]$	RAS1: $1a_1$, RAS2: $2a_1$, $1t_2$		$^2CH_4^+$: 308	
		RAS3: $3s(a_1)$, $3p(t_2)$, $3d(t_2)$, $3d(e)$,			
		$4s(a_1)$, $4p(t_2)$, $4d(t_2)$, $4d(e)$, $5s(a_1)$			
O_2	$[5s4p2d1f]$	$RAS(16, 2, 0; 2, 8, 0)$	0.1	$^3O_2$: 826	Linear^c
		RAS1: $1\sigma_u$, $1\sigma_g$		$^2O_2^+$: 1008	
		RAS2: $2\text{-}3\sigma_g$, $2\text{-}3\sigma_u$, $1\pi_u$, $1\pi_g$		$^4O_2^+$: 504	
NO_2	N: $[5s4p2d1f]$	$CAS(19; 11)$	0.3	$^2NO_2$: 430	O(1s) frozen
	O: $[5s4p2d1f]$	CAS: $2\text{-}6a_1$, $1a_2$, $1\text{-}2b_1$, $2\text{-}4b_2$		$^1NO_2^+$: 825	
				$^3NO_2^+$: 990	
$C_4H_4N_2$	N: $[4s3p2d1f]$	$RAS(34, 1, 1; 2, 15, 8)$	0.2	$^1C_4H_4N_2$: 137	SupSym^c
	C: $[4s3p2d1f]$	RAS1: $\sigma(1a_1)$, $\sigma(1b_2)$		$^2C_4H_4N_2^+$: 2297	C(1s) frozen
	H: $[3s2p1d]$	RAS2: $\sigma(5\text{-}10a_1)$, $\sigma(3\text{-}6b_2)$, $\pi_1(1b_1)$,			
		$\pi_2(1a_2)$, $\pi_3(2b_1)$, $n_{N_-}(7b_2)$, $n_{N_+}(11a_1)$			
		RAS3: $\pi^*(2a_2)$, $\pi^*(3\text{-}4b_1)$,			
		$\sigma^{Ryd}(12\text{-}13a_1)$, $\pi^{Ryd}(5\text{-}6b_1)$, $\pi^{Ryd}(3a_2)$			

^{a} ANO-L exponents[62] have been supplemented by $(8s6p6d4f)$ Rydberg exponents generated according to the procedure in Ref. 63. The $(22s15p10d7f)/[7s5p3d2f]$ contractions have been obtained with the GENANO module[64] of OPENMOLCAS.[65], see Supplement: Section III.
^{c} Keyword used in the RASSCF calculation in MOLCAS 8.0 to prevent mixing of orbitals from different symmetries during the Self-Consistent Field (SCF) procedure.

RAS3, however, contains v virtual orbitals occupied by at most p electrons. Herein, we denote the total number of active electrons as a, which allows to uniquely specify each active space as $RAS(a, h, p; o, c, v)$. If only the RAS2 space is used, it corresponds to the Complete Active Space Self-Consistent Field (CASSCF)[70] calculation. In this case, the active space is denoted as $CAS(a; c)$. Due to the restricted configuration space central to these methods, the wave functions are often lacking dynamic correlation effects. This is corrected to the second order of perturbation theory with the RASPT2[69] and CASPT2[71] methods. All calculations have been conducted with a locally modified version of MOLCAS 8.0.[72] The QC setups, i.e., the used basis sets, active spaces, number of states included in the state averaged SCF procedure, special keywords, and imaginary shifts within the PT2 correction are detailed for each system in Table I.

The Dyson orbitals and two-electron reduced transition densities in Eqs. (9) and (10) have been estimated using the biorthonormally transformed orbital and CI coefficients[73] for the neutral and cationic states.

IV. RESULTS AND DISCUSSION

We have chosen to present all ionization spectra with respect to the electronic binding energies rather than the kinetic energies. This introduces a common reference for PES and RAES irrespective of the photon energy at

which they have been obtained, simplifying the analysis. To allow for a uniform comparison, both the simulated results and the digitized experimental spectra have been aligned with respect to the lowest vertical Ionization Potentials (IPs) of each molecule, taken from Refs. 74–77. In case of methane, the $2a_1^{-1}$ IP has been used because the respective bands are narrower than the lowest $1t_2^{-1}$ ones. Note that for the open shell systems O_2 and NO_2 each ionization branch differing in the spin of the final ion was shifted individually in our simulated spectra. The calculated XAS have been shifted as well. All applied shifts are summarized in Table II. The broadening parameters for the XAS, PES, and RAES of all molecules, tuned for the best agreement between our theory and the reference, are detailed in Supplement: Section II.

A. Methane

CH_4 has been chosen because it is isoelectronic to the previously investigated neon atom[55] and thorough studies regarding its XAS, PES and RAES have been carried out both experimentally[57,78,79] and theoretically.[80,81] In addition, its tetrahedral symmetry with the central carbon atom closely resembles spherical symmetry, indicating that the SCI approach could be well suited to study ionization processes in this case. In Fig. 1, we compare our theoretical results for the XAS, PES, and RAES from various resonances to experimental reference data
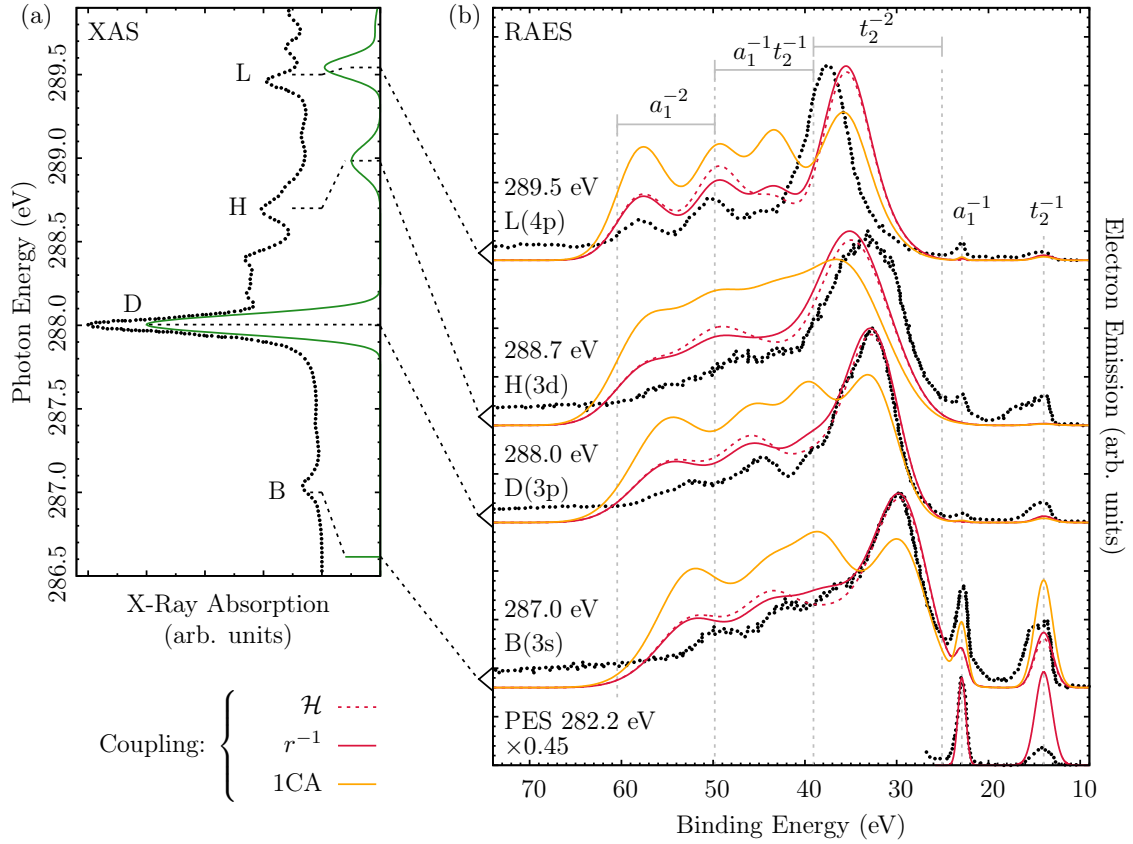
Figure 1. (a) Calculated XAS of methane at the carbon K-edge (green, solid) compared to the experimental result (black, dotted). The position of the dipole-forbidden excitation to the $3s(a_1)$ orbital at 286.6 eV is indicated by a single stick. The assignment of the experimental data follows Refs. 78 and 79 and has been connected to the corresponding core-excited states in our calculation (dashed). (b) RAES obtained with our method using the SCI model together with the respective measured spectra. The key for the coupling types is given under panel (a). All simulated spectra for one resonance have been normalized with the same constants to underline their differences. Dominant Rydberg contributions obtained in our calculation (in paranthesis) as well as the excitation energies used in the experiment are given for guidance. The experimental and theoretical valence PES taken at a photon energy of 282.2 eV are shown at the bottom as well. Note that all experimental data in this figure have been digitized from Kivimaeki et al.[57] Shifts and broadening parameters are detailed in Table II and the main text.

digitized from Kivimäki et al.[57] Therein, the ionization spectra have been recorded using a magic angle geometry,[82] eliminating angular anisotropy effects that have not been covered in our angle-integrated spectra.

a. *XAS* Fig. 1(a) contains the experimental[57] and calculated XAS. Both spectra are normalized to the D(3p) peak and the experimental data are shifted by 2 units of intensity for clarity. Below we use the notation of bands from Ref. 57. Note that we always omit the core orbital from the labeling of resonances here and in the following, unless explicitly required.

The experimental spectrum comprises a wealth of features. The assignment of them is complicated by the strong vibronic coupling especially for higher transition energies,[78,79] which is not included in our consideration.

For instance, the B(3s) peak is due to the dipole forbidden $3s(a_1)$ core excitation which becomes allowed due to a coupling to t_2 vibrational modes with a frequency of 0.374 eV.[79] This fits well to the offset of -0.4 eV in the resonance position predicted in our calculation. The remaining peaks have been assigned as follows. D(3p) corresponds to the $3p(t_2)$ resonance and according to the literature[78,79] should be free of vibrational effects. H(3d) is a $3d(t_2)$ resonance in accordance with Ref. 78 and is shifted by 0.3 eV with respect to the experiment. However, it may also be ascribed to a mixed $3d(t_2)$/vibrationally excited $3p(t_2)$ character which might explain the obtained shift.[57] Finally, L(4p) calculated with a slight offset of 0.1 eV is assigned to the $4p(t_2)$

Table II. The respective reference IPs and shifts (in eV) for the alignment of the theoretical and experimental ionization and absorption spectra. The experimental shifts have been applied to the indicated properties (see respective footnotes), whereas the theoretical ones have been uniformly applied to all PES and RAES for each system.

	vertical IP[a]	$\Delta_{\text{Theory}}^{\text{Ion}}$	$\Delta_{\text{Exp}}^{\text{Ion}}$	$\Delta_{\text{Theory}}^{\text{XAS}}$
CH$_4$	22.90[74] ($2a_1^{-1}$)	-0.670	0.110[b]	-0.850
			-0.260[c] (B)	
			-0.300[c] (D)	
			0.200[c] (H)	
			0.060[c] (L)	
O$_2$	12.33[75] (^{2}O$_2^+$)	-0.120	-0.100[b]	0.294
	16.70[75] (^{4}O$_2^+$)	-0.110	–[c]	
NO$_2$	11.25[76] (^{1}NO$_2^+$)	-0.056	0.125[b]	-0.938
	13.02[76] (^{3}NO$_2^+$)	-0.245	0.100[c]	
C$_4$H$_4$N$_2$	9.81[77]	0.200	–	2.680

[a] The final state of the ion is given in parentheses.
[b] PES
[c] RAES

resonance.[78,79] However, because of the aforementioned strong vibronic coupling other electronic states might contribute to this peak as well.[79] Generally, taking into account the absence of vibrational effects in our calculations, the relative energetic positions of the Rydberg resonances and their XAS intensities are in good agreement with the experiments.

b. PES and RAES Panel (b) of Fig. 1 shows the theoretical and experimental[57] RAES taken at the indicated resonance energies. Further, the valence PES, recorded at 282.20 eV are depicted. Complete, $\mathcal{H}$, and approximate, r^{-1}, couplings as well as the 1CA of the r^{-1} coupling were employed to evaluate the partial decay rates. To ensure convergence of the spectral intensities with respect to the continuum orbital angular momentum l, we took into account partial waves up to $l_{\max} = 5$ (1CA RAES) and $l_{\max} = 12$ (PES, $\mathcal{H}$, and r^{-1} RAES. This is natural, since the 1CA results correspond to matrix elements centered at one atom and thus converge faster in l.

Finally, the PES and RAES have been normalized to the a_1^{-1} and t_2^{-2} features, respectively. Note that the normalization constants determined for the r^{-1} RAES have been used for the 1CA and $\mathcal{H}$ spectra as well to underline their relative differences.

The valence PES contains two peaks corresponding to electron emission from the $2a_1$ and $1t_2$ valence orbitals, leading to single hole states depicted as a_1^{-1} and t_2^{-1}. Apparently, our model can not reproduce the relative PES intensities of these peaks correctly at this excitation energy and overestimates the intensity of the t_2^{-1} feature by a factor of 4. A study of the PES with different model potentials (Supplement: Fig. S1) has revealed that the spectrum depicted in Fig. 1, employing $V_f^J(r)$, yields in fact the best agreement possible within our present model. A

further improvement would require a non-spherical continuum model that accounts for the true molecular symmetry. However, the a_1^{-1} : t_2^{-1} intensity ratio is quite sensitive to the photon energy,[83,84] which suggests that this is a somewhat difficult case.

The RAES can roughly be divided into the participator and spectator decay regions, below and above 25 eV binding energy. Participator decay involves the excited electron in the decay process, leading to single hole states that are the main PES features as well. Here, the corresponding states are a_1^{-1} and t_2^{-1}, indicated by the dashed lines. Spectator decay, in contrast, leaves the excited electron intact and leads to states with two holes in the valence shell. Similar states result from normal Auger decay as well, albeit the additional electron introduces energetic shifts in the resonant case. The dominant character of the respective two hole states obtained in our calculation is indicated at the top of panel (b). Clearly the spectator decay is dominating the RAES. The main peak located in the range $25 - 40$ eV is due to t_2^{-2} target states for all resonances. The high energy tail however generally comprises three features for all but the H resonance, where vibrational effects lead to a stronger broadening that hides the detailed structure in the experimental data. With decreasing binding energy, the first feature may be assigned to a_1^{-2} states, while the latter two can be assigned to states of $a_1^{-1}t_2^{-1}$ character. The participator region is most prominent for the B(3s) resonance.

Fig. 1 (b) demonstrates that the theoretical spectra obtained with $\mathcal{H}$ and r^{-1} coupling reproduce the experimental RAES for all resonances with good accuracy. Note that using a simple effective Coulomb potential $-1/r$ to obtain the continuum orbitals leads to considerably worse agreement, see Supplement: Fig. S2. Further, employing an additional radial Slater exchange term into the potential does not improve the results, see Supplement: Fig. S3. With respect to the r^{-1} results, the $\mathcal{H}$ coupling introduces just a slight redistribution of intensity from the high energy flank of the t_2^{-2} peak to the center of the high energy tail (about 45-50 eV). In contrast, employing the 1CA leads to an overestimation of the tail (>40 eV) and participator regions, whereas the main feature is underestimated. Thus, it seems that nonlocal contributions from the hydrogen atoms can not be disregarded and the 1CA is not a suitable approximation when evaluating RAES of methane with the SCI approach. In the remainder of this section, we will only refer to the results obtained with $\mathcal{H}$ and r^{-1} coupling.

While the overall agreement for the $\mathcal{H}$ and r^{-1} couplings is very good, the following differences remain. For all resonances, the a_1^{-2} and $a_1^{-1}t_2^{-1}$ regions are slightly overestimated with respect to the main t_2^{-2} feature. Further, the features in the tail region are blue shifted by roughly 3.0 eV and 2.0 eV for the B(3s) and D(3p) resonances, while for the H(3d) resonance the whole spectrum appears to be blue shifted by 1.0 eV. In contrast for L(4p), the t_2^{-2} feature appears red shifted by 2.0 eV,

which decreases towards higher binding energies to 0.5 eV for the a_1^{-2} peak. We attribute these shifts to the fact that our active space does not allow to include enough electron correlation to represent the highly excited states of CH_4^+ with the same accuracy as the lower ones. In addition, the lack of nuclear effects prohibits the description of shifts due to vibronic coupling in the resonances as well as the ionized states. Finally, the a_1^{-1} and t_2^{-1} participator peaks are barely present for the H($3d$) and D($3p$) resonances and the a_1^{-1} peak seems to be generally underestimated with respect to the t_2^{-1} one. This discrepancy is most probably due to the two-step approach to resonant Auger emission employed herein, disregarding the excitation process and the interference between photoionization and the Auger decay terms. Further, the deficiencies of our SCI model to describe the correct a_1^{-1} : t_2^{-1} intensity ratio in the PES, might translate to the participator decay as well.

We conclude this discussion with the observation that the relative energetic positions and intensities of the features in the methane B($3s$), D($3p$), H($3d$), and L($4p$) RAES can be reproduced quite well with the SCI approach, using the $V_f^J(r)$ potential together with $\mathcal{H}$ or r^{-1} coupling, while vibrational effects can be disregarded in a first approximation. The 1CA, however, is not enough to reproduce the relative intensities. Further, an improved model of the continuum orbital seems to be required to recover the a_1^{-1} : t_2^{-1} intensity ratio in the PES at this energy.

B. Molecular oxygen

Being a biradical open shell system with triplet ground state multiplicity, molecular oxygen is an intriguing system, allowing for ionization into doublet and quartet spin states and being targeted by many studies. Especially the core-hole decay of O_2 has been subject to frequent investigation, since it is a textbook example of strong lifetime-vibrational interference effects.[86–88] The plethora of available experimental data regarding its XAS[85,89,90], PES[58,86] and RAES[58,86,90,91] allows for a detailed test of our approach.

The homonuclear linear geometry of O_2 suits to test the applicability of the spherically symmetric continuum orbital model that is central to our protocol. For instance, the $1s$ core hole might be delocalized over both atoms, whereas we expect our method to be more appropriate in the case of a localized hole. Further, it introduces some ambiguity regarding the coordinate origin of the continuum wave functions, see Section II, which might be placed either on one atom, $\mathbf{R}_O$, or at the interatomic center $\overline{\mathbf{R}}_{O_2}$. Both approaches have been tested here with respect to their ability to reproduce the PES and RAES of O_2.

a. XAS The comparison of the theoretical K-edge XAS of O_2 against experimental data that has been digitized from Ma et al.[85] is presented in Fig. 2 (a).

Both spectra were normalized to the dominating peak at 531 eV that corresponds to core excitations to the $1\pi_g$ orbitals.[85] The structured double peak at 539-545 eV has been assigned to two broad $3\sigma_u$ resonances that are exchange split by 2.3 eV and a series of Rydberg excitations.[85] We recover this characteristic in our theory, however the splitting is smaller being about 1.4 eV, which can be attributed to the missing Rydberg orbitals in our active space. In agreement with Ref. 85, we find the following assignment. The lower energy feature at 539.3 eV predominantly corresponds to the promotion of a spin-up (α) electron to the $3\sigma_u$ orbital, i.e., quartet spin coupling in the valence shell, which we denote as q-$3\sigma_u$ in the following. The higher energy peak at 540.7 eV comprises doublet spin coupling in the valence shell, labeled analogously as d-$3\sigma_u$. Further, a small feature at 535.5 eV is not found in the experimental data, while the one at 547.5 eV is already above the core ionization threshold.[92] The former corresponds to the shake-up excitation of 1.0 core and 0.6 valence electrons to the $1\pi_g$ orbitals, while the latter is due to states involving simultaneous excitations to the $1\pi_g$ and $3\sigma_u$ orbitals.

The photon energy of 530.8 eV at which Caldwell et al.[58] have recorded the RAES has been assigned to the $1\pi_g$ resonance. However, due to the bandwidth of ~ 2.7 eV in the experimental setup, the excitation at 540.0 eV involves both exchange-split q-$3\sigma_u$ and d-$3\sigma_u$ resonances. Notably, the evaluated core holes are $1\sigma_g^{-0.3}1\sigma_u^{-0.7}$ and $1\sigma_g^{-0.65}1\sigma_u^{-0.35}$ for the $1\pi_g$ and both $3\sigma_u$ resonances, respectively, i.e., they are delocalized in our calculation.

b. PES and RAES In Fig. 2(b), the computed PES and $1\pi_g$ as well as q-$3\sigma_u$ and d-$3\sigma_u$ RAES of O_2 are compared to the experimental data recorded under the pseudo magic angle of $57°$ by Caldwell et al.[58] The respective spectra have been normalized to the the heights of the features P1, R4, and S3. The continuum orbitals have been generated with the $V_f^J(r)$ potential, centered either at $\mathbf{R}_O$ or $\overline{\mathbf{R}}_{O_2}$. Further, the partial decay rates have been estimated using the complete, $\mathcal{H}$, and approximate, r^{-1}, couplings. Results obtained with the 1CA for the $\mathbf{R}_O$ origin are shown as well. Note the remarkably different convergence of the results with respect to highest angular momentum included in the photoelectron representation: it was necessary to include waves up to $l_{max} = 12$ for the PES, $l_{max} = 15$ for the RAES with $\mathcal{H}$ and r^{-1} couplings, and $l_{max} = 5$ in case of 1CA RAES.

The experimental RAES and PES are quite structured and feature-rich. Remarkably, the energetic positions of experimental PES features are reproduced almost exactly. Using the SCI approach we have been able to achieve quite good overall agreement with the experimental $1\pi_g$ RAES. Reproducing the $3\sigma_u$ spectrum is more problematic, because the q-$3\sigma_u$, d-$3\sigma_u$ and underlying Rydberg resonances,[85] which are not included here, are simultaneously excited in the experiment.

In the PES, P1 and P3 correspond to the $^2 1\pi_g^{-1}$ and $^2 3\sigma_g^{-1}$ ionic final states, respectively. P2, hav-
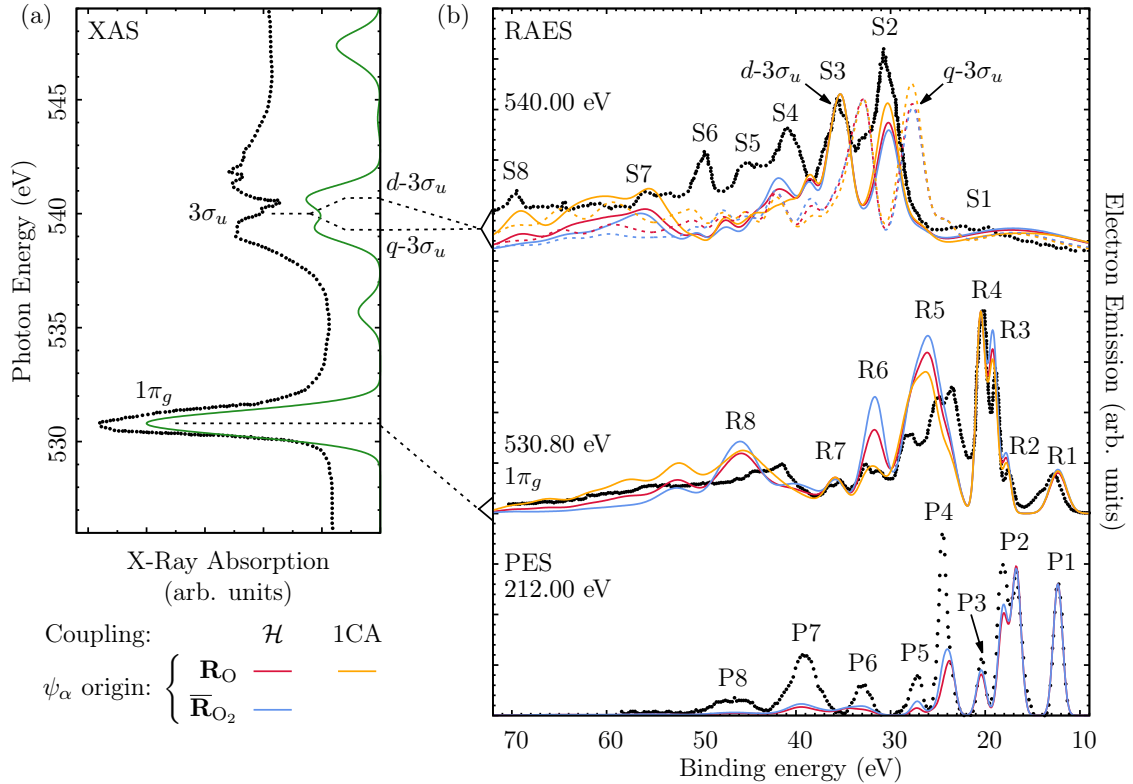
Figure 2. (a) Calculated K-edge XAS of O_2 (solid) compared against experimental results from Ma et al.[85] (dotted). The experimental excitation energies are connected to the theoretically found $1\pi_g$, $q\text{-}3\sigma_u$, and $d\text{-}3\sigma_u$ resonances in the XAS, as well as to the respective RAES in (b). Therein, the theoretical RAES and PES obtained with the SCI approach are presented together with the respective experimental data that has been digitized from Caldwell et al[58] (dotted). Note that due to the high bandwidth of ~ 2.5 eV, the whole exchange split $3\sigma_u$ double peak is excited by the incoming radiation at 540 eV. Hence, the theoretical RAES for the $q\text{-}3\sigma_u$ (dashed) and $d\text{-}3\sigma_u$ (solid) resonances are depicted in this case. The theoretical results have been obtained with continuum orbitals corresponding to the $V_f^J(r)$ potential originating either at one atom, $\mathbf{R}_O$, or at the molecular center, $\overline{\mathbf{R}}_{O_2}$, as well as with the indicated coupling approaches. All spectra have been normalized. The applied shifts and broadenings are detailed in Table II and Supplement: Table S2, respectively.

ing a double peak structure, is due to primarily quartet cationic states: $^41\pi_u^{-1}$ at 17 eV and $^43\sigma_g^{-1}$ with a smaller contribution from $^2\pi_u^{-1}$ at 18 eV, respectively. P4 contains already combination transitions with the leading states $^21\pi_u^{-1}$ and $^42\sigma_u^{-0.5}3\sigma_g^{-0.5}$ which are accompanied by excitations to the σ and π orbitals. P5 corresponds to the double hole states $^43\sigma_g^{-1}1\pi_u^{-0.75}1\pi_g^1$ and $^22\sigma_u^{-0.3}3\sigma_g^{-0.6}1\pi_u^{-0.5}1\pi_g^{0.5}$. The higher binding energy features increasingly correspond to states carrying multiple excitations that can hardly be assigned in the orbital picture. Note that our analysis is in accord with that of Ref. 75.

The calculated PES intensities quite well reproduce the experiment for P1-P3. However, P4-P8, involving multiple excitations become increasingly underestimated with rising binding energy. This might be due to the lack of

combination transitions in this energy region because of the limited active space. The integrated total cross sections, however, are considerably affected, being 0.30 and 0.14 a.u. for $\mathbf{R}_O$ and $\overline{\mathbf{R}}_{O_2}$, respectively.

The oxygen molecule represents a convenient object to discuss the dependence of total decay rates on the continuum origin. Moreover, it demonstrates the largest dependence of this kind among the molecules studied here and this comparison is supported by the available experimental value. The total decay rates of the $1\pi_g$, $q\text{-}3\sigma_u$, and $d\text{-}3\sigma_u$ resonances obtained with all approaches are compiled in Table III together with the experimentally determined lifetime width of the $1\pi_g$ resonance.[89] In the literature, it has been assumed that the $1\pi_g$ and $3\sigma_u$ resonances have approximately the same decay rate.[90,91] The computed total decay rates support this assumption for the results obtained within each model. Notably,

Table III. Computed total, doublet, and quartet autoionization rates in meV for the $1\pi_g$, q-$3\sigma_u$, and d-$3\sigma_u$ resonances of O_2 obtained with the indicated approaches. The experimental reference for the total decay width of the $1\pi_g$ resonance has been taken from Ref. 89.

		$\mathbf{R}_O$			$\overline{\mathbf{R}}_{O_2}$		
		$1\pi_g$	q-$3\sigma_u$	d-$3\sigma_u$	$1\pi_g$	q-$3\sigma_u$	d-$3\sigma_u$
$\mathcal{H}$	Total	126.0	125.9	125.0	120.2	122.5	121.2
	Quartet	25.2	104.8	30.2	35.7	95.6	40.6
	Doublet	100.7	21.1	94.8	84.5	26.9	80.6
r^{-1}	Total	169.0	167.8	165.2	186.6	187.9	184.4
	Quartet	48.9	132.4	52.8	69.4	140.1	73.6
	Doublet	120.1	35.4	112.4	117.2	47.8	110.8
1CA	Total	69.7	65.1	65.5			
	Quartet	7.5	57.5	56.0			
	Doublet	62.2	7.6	9.5			
Exp.	Total	149.5 ± 10					

the total decay rates of the q-$3\sigma_u$ and d-$3\sigma_u$ resonances demonstrate the expected preferential decay into quartet and doublet target states, respectively, corresponding to their valence spin coupling. The $1\pi_g$ resonance, however, favors decay into doublet states. Interestingly, this spin selectivity is less pronounced if the $\overline{\mathbf{R}}_{O_2}$ origin is used.

In absolute terms, the $\mathcal{H}$ coupling results recover approximately 80% of the experimental value.[89] The r^{-1} coupling in turn produces total decay rates larger than the reference by 13% and 25% for the $\mathbf{R}_O$ and $\overline{\mathbf{R}}_{O_2}$ origins, respectively. However, the 1CA decay rates are the smallest, providing only about 45% of the experimental result. This suggests that the 1CA misses important contributions in this case. The delocalization of the core hole, that we discussed earlier, could be an explanation for this behavior, since the 1CA excludes all contributions from one atom. Still, doubling the 1CA results recovers only about 80% of the full r^{-1} coupling result at the $\mathbf{R}_O$ origin, which is why we ascribe the remainder to non-local contributions. Although the $\mathcal{H}$ and r^{-1} couplings reproduce the experimental reference with similar absolute deviations, see Table III, we consider the $\mathcal{H}$ results to be in general more reliable. This is because our method does not include nuclear effects and therefore has less open decay channels. Thus it is rather likely that the present model indeed should underestimate the experimentally determined total decay rate. Further, the spectra obtained with $\mathcal{H}$ coupling agree better with the experimental $1\pi_g$ RAES and the r^{-1} results are more sensitive to the placement of the continuum origin, see Supplement: Fig. S4.

For the $1\pi_g$ resonance (Fig. 2(b)), the computed spectrum is in an overall good agreement with experiment, with the low binding energy features R1-4 being better reproduced. This region of the spectrum corresponds predominantly to participator decay into single hole states that constitute the PES as well. The following PES and participator RAES features can be assigned to the same single hole states: P1 and R1, the high energy part of P2 and R2, P3 and R4 (30% of participator character), and P4 constitutes the rising flank of R5. The remainder of the RAES is due to spectator decay to double hole and higher excited states, the representation of which might benefit from a larger active space. For O_2, the 1CA RAES agree quite well with those obtained with $\mathcal{H}$ coupling, in contrast to the behavior that we found for CH_4 in Fig. 1. Further, the choice of the continuum orbital origin only weakly affects the q-$3\sigma_u$ and d-$3\sigma_u$ spectra and the overall shape of the $1\pi_g$ one. Similar to the PES spectrum, the agreement gets worse for higher binding energies. For instance, the intensity of R5 is overestimated, it is less structured, and its onset is shifted to higher energies by 1.5 eV. The atom centered approach ($\mathbf{R}_O$) performs better, and moreover the best agreement especially for high-energy features is obtained within the 1CA. The R6 peak behaves similar, albeit the relative overestimation by the $\mathcal{H}$ coupling approaches, especially with $\overline{\mathbf{R}}_{O_2}$ is stronger. R7, however, is reproduced well with all approaches. Finally R8, i.e. the beginning of the tail region appears blue shifted by 2.5 eV. The intensity overestimation with the $\overline{\mathbf{R}}_{O_2}$ origin is due to the enhancement of the quartet decay branch, as indicated by the total decay rates in Table III.

For the $3\sigma_u$ resonance the agreement with the experiment is worse than for the $1\pi_g$ resonance. The q-$3\sigma_u$ and d-$3\sigma_u$ RAES appear to be shifted with respect to each other both due to exchange splitting in the core-excited states and preferential decay to different spin manifolds of O_2^+. In particular, the q-$3\sigma_u$ spectrum is shifted to lower binding energies by $\sim$ 2.5 eV relative to the experiment even after the alignment of all spectra to the reference IPs, see Table II. Further, the intensity of the features with a binding energy above 35 eV (S4-6) are considerably underestimated. This discrepancy may be attributed mainly to two reasons as discussed previously in experimental works.[85,90,91,93] As mentioned before, the $3\sigma_u$ band is overlaid by a manifold of Rydberg transitions in addition to the exchange splitting between q-$3\sigma_u$ and d-$3\sigma_u$ resonances.[85] Namely, within the excitation bandwidth of 2.7 eV,[58] Rydberg states of $np(\pi_u), n = 3$–7 and $ns(\sigma_g), n = 3$–5 character have been identified by Ma et al.[85] around 540 eV. This indicates that the measured spectrum contains contributions from all these resonances and in our calculation we consider only one at a time. Further, the $3\sigma_u$ states are dissociative and a fast bond elongation is expected to occur on the timescale of the Auger decay that has been claimed to lead to appearence of atomic features.[58,90,91] Our test calculations with a bond distance of 1.26 Å (0.05 Å elongation) show for q-$3\sigma_u$ an almost doubled energetic mismatch between theory and experiment of 4.5 eV (compare with 2.5 eV), indicating that a simple bond elongation might not explain the effect. To close this question, the one-step model for resonant Auger decay[19] has to be employed together with a larger active space that includes excitations to Rydberg orbitals. Finally, varying the excitation ratio of all these resonances might strongly influence the

result.

Summarizing, the total Auger decay rates, the $1\pi_g$ RAES as well as the PES are in quite good agreement with the experiment, whereas the $3\sigma_u$ RAES agrees slightly worse calling for more sophisticated treatment. In general, the full $\mathcal{H}$ coupling seems to yield the most stable spectra and total decay rates and the 1CA predicts spectra of the same quality as the full approaches, although the overall decay rates are underestimated. Finally, the choice of the continuum origin has no strong effect on the spectra and total decay rates, although the total photoionization cross sections vary by a factor of two.

C.   Nitrogen dioxide

NO_2, being a radical with multi-configurational character of the ground doublet state, represents an increase of complexity with respect to O_2. This fact makes it a convenient object to study the performance of our multi-reference protocol. Moreover, recent reference data for its XAS[94,96], PES[95], and RAES[95] taken at the nitrogen and oxygen K-edges are available for comparison. In this article, we focus on the nitrogen K-edge. This takes advantage of the fact that the origin of the spherically symmetric continuum functions can be unambiguously put on the nitrogen atom $\mathbf{R}_N$.

a.   XAS   The calculated XAS at the nitrogen K-edge of NO_2 is presented in Fig. 3 panel (a), together with the experimental reference that has been digitized from Gejo et al.[94] Both spectra have been normalized to the height of the $2b_1$ peak. The relative intensities of the $6a_1$ and $2b_1$ resonances are reproduced almost exactly, although the $6a_1$ peak is predicted slightly by 0.2 eV too high in energy. The features at higher energies correspond to excitations to the $7a_1$, $5b_2$, and Rydberg orbitals[94] that are not included in our active space. Thus, they are reproduced herein only to some extent.

The excitation energies of 402.86 eV and 403.73 eV used to obtain the RAES from the low and high energy flank of the $2b_1$ resonance[95] are indicated by the arrows. We have connected them to the positions of two core-excited states predicted by our calculations that correspond to the $2b_1$ resonance. Our calculation predicts a splitting of 0.34 eV for these states. Further, the oscillator strength obtained for the lower state is a factor of ~ 20 smaller than the one of the higher state. An analysis in terms of the occupation numbers of the state averaged orbitals obtained from the CASSCF procedure shows that both states are quite similar in character, bearing the $N(1s)$ core hole and the excitation to the $2b_1$ orbital. However, the analysis of the core-hole spin in our calculations does not support the assignment of this splitting to an exchange mechanism, in contrast to the experimental results for the $O(1s) \rightarrow 2b_1$ resonance.[95]

b.   PES and RAES   Panel (b) comprises the RAES corresponding to the low and high energy flanks of the

$2b_1$ resonance, as well as the direct PES taken at 399 eV below the edge. The experimental data has been digitized from Ref. 95. The PES and RAES have been normalized to the peaks 4 and 3, respectively. To converge the partial decay rates and the ionization cross sections it was necessary to include partial waves up to $l_{\max} = 9$ (r^{-1} coupling) and $l_{\max} = 4$ (1CA) as well as $l_{\max} = 15$ (PES), respectively. Note that we have used a Lorentzian lineshape with an Full Width at Half Maximum (FWHM) of 0.1 eV for peak 6 in the calculated PES. To have a common reference, the theoretical and experimental data have been aligned to reference values for the lowest singlet and triplet IPs as detailed in Table II. For the sake of clarity a common set of identifiers 1-7 is used for features in all spectra. The dashed lines denote features or groups thereof that predominantly correspond to direct photoionization, whereas those that are found in both, PES and RAES, are indicated with solid lines.

PES is found to be in fairly good agreement with experiment, although the feature 2 is overestimated by an approximate factor of 2. Further, the peak 4 is slightly overestimated and around 23.6 eV our simulation yields a feature that has no correspondence in the experimental data. Some of this deviations might be due to anisotropy effects present in the experimental data[95] which are not recovered in our angle integrated spectra. In addition, the valence PES is a rather non-local probe and thus might be more sensitive to the quality of the continuum orbital than RAES, which in this case seems to be an almost purely local process. An improvement could thus require a more elaborate model for the continuum electron, possibly involving a multi-centered approach.[24]

We address here different flanks of the $2b_1$ resonance which exhibits an exchange splitting of ~ 0.5 eV for the $O(1s)$ hole[94,95]. Piancastelli et al.[95] found that the low energy side of the $O(1s) \rightarrow 2b_1$ resonance favors decay to triplet ionized states whereas the higher energy side favors decay to singlet states, which is a trace of this splitting. A similar behavior can be expected for the $N(1s) \rightarrow 2b_1$ resonance, although the splitting is assumed to be smaller[95]. However, to the best of our knowledge no data regarding the splitting has been published yet and the experimental RAES results in Ref. 95 are inconclusive in this case. We attempt to shed light on this question in the following.

The results of the r^{-1} coupling are presented in Fig. 3 assuming the full molecular treatment and 1CA. Noteworthy, the RAES obtained within the 1CA closely resemble the ones that have been obtained by taking into account non-local contributions from the oxygen atoms as well. Adding to that, the calculated total decay widths of 92 meV and 98 meV corresponding to the 1CA and the full r^{-1} couplings agree with each other as opposed to oxygen case. Thus it seems that the decay of the $1b_2$ resonance can be described quite well as a purely local phenomenon, in contrast to our findings for CH_4 and O_2.

To unravel the relative contribution of the triplet and singlet decay pathways, we found T:S ratios of 1.0 and
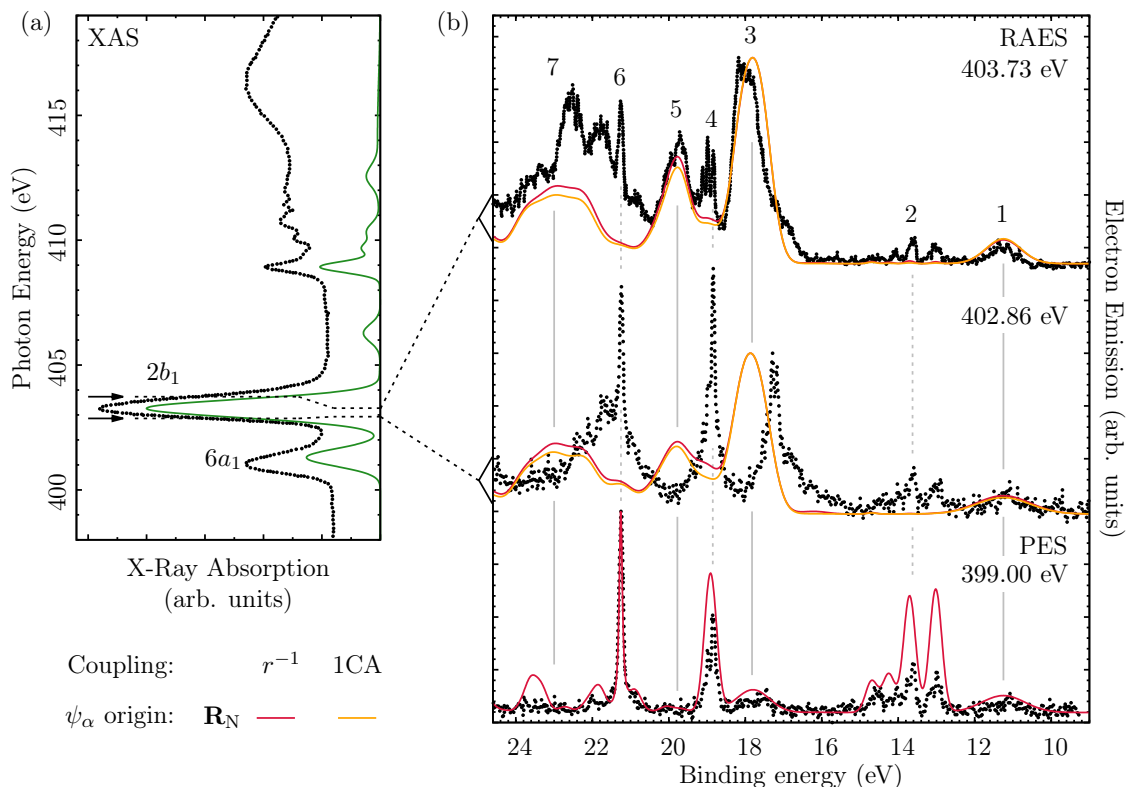
Figure 3. (a) Theoretical nitrogen K-edge XAS of NO_2 (green, solid) and the experimental reference digitized from Gejo et al.[94] (black, dotted). The arrows indicate the excitation energies used by Piancastelli et al.[95] to obtain the experimental RAES in panel (b). In addition, the dashed lines link the experimental excitations to the respective core-excited states predicted in our calculation and the corresponding RAES in (b). Therein, the decay spectra measured at the low and high energy sides of the $2b_1$ resonance as well as the PES taken at 399 eV below the edge[95] (dotted) are compared against our theoretical results (solid). The partial decay rates have been obtained using r^{-1} coupling and the 1CA. The vertical lines indicate corresponding features that are predominantly found in PES (dashed) and RAES (solid), respectively. The applied shifts and broadenings are detailed in Table II and in Supplement: Table S3.

1.2 for the the low and high energy $1b_2$ RAES. Thus there is no appreciable difference in the spin coupling of the respective core-excited states, supporting the result from the analysis of the respective core-hole spins, see the discussion of the XAS above. In contrast, the total photoionization cross section yields a T:S ratio of 2.5, i.e., the PES at this energy is dominated by the triplet branch. This behavior fits well with the fact that the $6a_1$ orbital is occupied in the NO_2 ground state, as well as in a large part of the triplet ionized states but only to lesser extent in the singlet states.

Concerning the analysis of the spectra, the comparison against the reference data[95] yields a very good agreement regarding the energetic positions of all features in the high energy RAES and the PES. The peaks 2, 4, and 6 are predominant PES features and their presence in the experimental RAES indicates that a considerable portion of the absorbed photon flux leads to a direct

ionization rather than to a resonant excitation of the molecule. To reproduce these effects theoretically, the one-step model[19] for resonant Auger decay must be employed.

The frontier orbital configurations for NO_2 as well as singlet and triplet NO_2^+ are $4b_2^2 1a_2^2 6a_1^1$, $4b_2^2 a_2^2 6a_1^0$, and $1a_2^2 4b_2^1 6a_1^1$, respectively. The $2b_1$ orbital however, is unoccupied in all ground states with given charge and multiplicity. Hence, core excitations to the $2b_1$ orbital can be expected to have a considerable participator decay contribution. In contrast, the peaks 3, 5, and 7 are predominant spectator Auger decay contributions having only small counterparts in the PES. Finally, the lowest energy peak, 1, corresponds to the singlet NO_2^+ ground state, i.e. the $^1 6a_1^{-1}$ ionization. It can be reached via direct ionization and participator decay of the $2b_1$ resonance and contributes equally to both, PES and RAES. In opposite to that, participator decay into the higher

lying single hole states contained in feature 2, i.e., $^{3}4b_2^{-1}$, $^{3}1a_2^{-1}$, $^{1}1a_2^{-1}$, and $^{1}4b_2^{-1}$ at 13 eV, 13.6 eV, 14.2 eV, and 14.6 eV, is suppressed, although this states contribute to the PES. We can confirm the statement of Ref. 95 that this is most likely due to the localization of the $1a_2$ and $4b_2$ orbitals on the oxygen atoms, whereas the $2b_1$ excitation is primarily localized on the nitrogen. Hence, the main part of the Auger decay of the $2b_1$ resonance at the N K-edge of NO_2 can be ascribed to spectator decay into double-hole or higher excited states, which appear only as satellites in the PES. This is a common situation and underlines the importance of the joint analysis of PES and RAES. The strong configuration mixing in the electronic structure calculation hinders a clear assignment of the remaining features, thus, we refer to the assignments in Refs. 97 and 76.

One can expect the Auger features to shift on the binding energy scale when changing the photon energy, the energetic position of the direct ionization PES features, however, should stay intact. The theoretically obtained RAES taken at the low-energy flank is rather similar to our high-energy result and does not recover the shift of the decay features 3, 5, and 7 by approximately 0.6 eV observed in the experimental spectrum. Judging by the relative contribution of the direct ionization (PES) features 2, 4, and 6 to the measured data, the resonant decay contribution is here much weaker than in the RAES taken at high-energy flank. In turn, feature 1 can be ascribed exclusively to direct photoionization that does not appear red-shifted in contrast to its participator decay counterpart that could be concealed within the noise due to its small intensity. Since our preliminary studies with a larger active space and basis set have not led to an improvement here, we tend to attribute this shift to difference in exciting photon energies and vibrational effects. Nevertheless, we do not exclude other possible explanations.

Finally, concerning the relative intensities. The overall agreement is good, with some exclusions. For instance in the high energy flank RAES, the relative intensities of the features 1, 3, and 5 are reproduced quite well, while the peak 7 is underestimated considerably and is less structured than in experiment. The situation is more delicate concerning the low energy RAES. In this case, the overall small magnitude of the decay features in the experimental spectrum could be due to the low oscillator strength of the corresponding core-excited state, as discussed in the XAS part. Further, the red shift of the resonant decay features by 0.6 eV increases the overlap between the direct photoionization peaks 4 and 6 with the decay features 5 and 7, respectively. Thus a disentanglement of direct and resonant contributions is hardly possible for these peaks. It seems that for a better reproduction of the experimental results for the low energy RAES, the one-step ansatz to RAES, allowing for interference between multiple resonant decay and direct ionization channels[19] as well as the inclusion of vibrational effects have to be considered.

In summary, the comparison to the experimental XAS has verified that our electronic structure is suitable to describe the $2b_1$ resonance at the nitrogen K-edge. Further, our theoretical data agree well with the experimental reference for the PES and the RAES recorded at the high energy flank of the resonance. In addition, the 1CA results closely resemble the spectra and total decay rates obtained when all atomic centers are included. However, the RAES stemming from the low energy side of the resonance probably requires a more involved treatment of the resonance decay within the one-step model as well as the inclusion of nuclear effects. Finally, our results do not indicate a difference in the spin coupling on the low and high energy flank of the $N(1s) \rightarrow 2b_1$ resonance, in contrast to previous findings for the $O(1s) \rightarrow 2b_1$ resonance.[95]

D. Pyrimidine

Finally, we benchmark the SCI approach for the pyrimidine molecule ($C_4H_4N_2$). Having six heavy atoms arranged in a C_{2v} symmetric ring, the theoretical study of its PES and RAES is considerably more involved than for the previous examples. Moreover, pyrimidine is interesting on its own, since the structures of the nucleic acids uracil, cytosine, and thymine are derived from it. Its ionization spectra are thus an important landmark on the route towards a better understanding of DNA radiation damage. Due to this, a number of experimental and theoretical investigations regarding its XAS[77,98], PES[77,99–102], normal[103] and resonant[77] Auger emission have been published during the last 20 years. Bolognesi et al.[77] have recently reported complete sets of XAS, PES, and RAES measurements at the carbon and nitrogen K-edges of pyrimidine, making this work a suitable reference for our simulations. Conveniently, the electrons have been collected at the pseudo magic angle, suppressing angular anisotropy effects.

We have chosen to focus on the nitrogen K-edge of pyrimidine, since the corresponding RAES are quite structured and it allows to incorporate only two instead of four core orbitals into the active space. However, the symmetric arrangement of the nitrogen atoms, Fig. 4, might lead to core-hole delocalization effects. Similar to the O_2 case, see Sec. IV B, the continuum orbital origin is also not well defined. Here, two options seem reasonable. First, it might be placed on one of the nitrogen atoms, denoted as $\mathbf{R}_N$, or in the geometric center of the ring, $\overline{\mathbf{R}}_{C_4N_2}$, which might be the most balanced choice if all atoms contribute to the continuum orbital.

a. XAS The calculated nitrogen K-edge XAS of pyrimidine is depicted in panel (a) of Fig. 4 together with the experimental reference;[77] the band labels are taken from this experiment. In case of pyrimidine, the agreement with the experimental XAS is less satisfactory than for the other molecules. In accord with previous findings,[77,104] we assign the main features to a $\pi^{*}(a_2)$ core
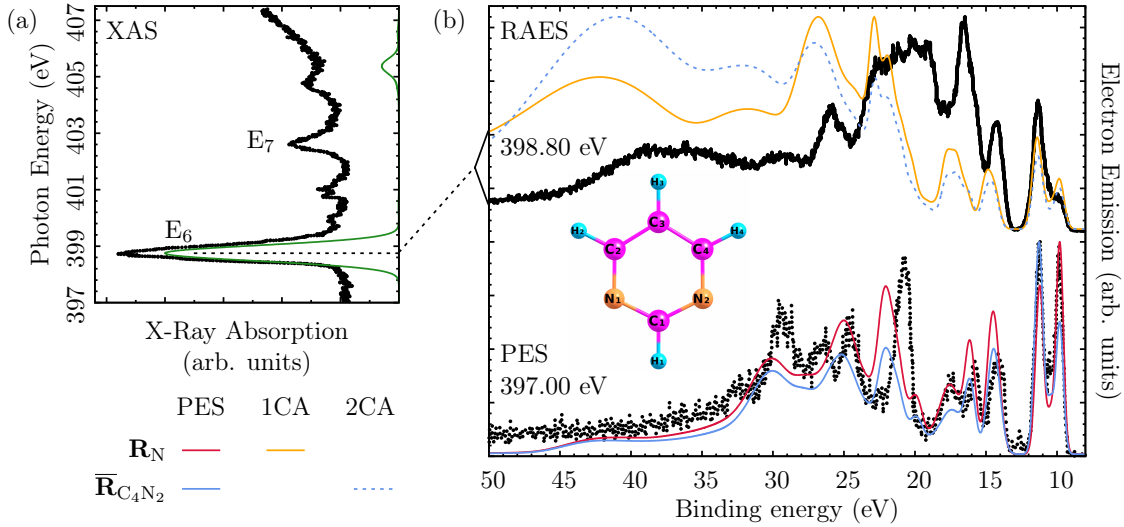
Figure 4. (a) Theoretical nitrogen K-edge XAS of pyrimidie (solid green) and the respective experimental measurement taken from Bolognesi et al.[77] (black dotted). (b) Theoretical and experimental[77] (black) RAES of the E6 resonance and the pre-edge PES obtained at the indicated energies. The continuum orbitals have been eevealuated using the $V_f^J(r)$ potential centered at one nitrogen atom, $\mathbf{R}_N$, or at the geometric center of the ring, $\overline{\mathbf{R}}_{C_4N_2}$. The RAES have been evaluated in the 1CA and 2CA, see text. The applied shifts and broadenings are detailed in Table II and Supplement: Table S4, respectively.

excitation (E6) and to transitions to the π - Rydberg mixed $\pi^{Ryd}(b_1)$ orbitals (~ 406 eV; E7). In contrast, the shoulder of E6 at 399.9 eV that has been attributed to $\pi^*(b_1)$ excitations[104] is missing in our results. In fact, the corresponding core-excited state is present at 400.4 eV, but its absorption is by a factor of ~ 500 lower than for the E6 one. A different theoretical study,[98] however, found this feature to be underestimated as well, but perceivable. Finally, the structure around 401 eV has been attributed to a contamination with N_2 molecules[104] and can be neglected in the discussion.

The energetic spacing between E6 and E7 is overestimated by about 2.8 eV in our calculations. This is an indication of the lack of electron correlation as well as Rydberg character in the active orbitals. However, including a higher level of CI and employing much larger Rydberg bases has not been feasible.

b. PES and RAES The predicted PES at 397 eV and the RAES obtained at the E6 resonance together with experimental data digitized from Bolognesi et al.[77] are compiled in Fig. 4 (b). All spectra have been normalized to their respective highest peaks. We focus here solely on the E6 resonance, because its spectrum yields more structure than the E7 one[77] and we deem our core-excited states to be more reliable for this lower lying resonance. The continuum orbitals used in the calculations have been constructed based on the $V_f^J(r)$ potential centered at the $\mathbf{R}_N$ and $\overline{\mathbf{R}}_{C_4N_2}$ origins, as depicted in Fig. 4. Due to the computational costs, the RAES have only been obtained in the nitrogen centered 1CA, as well as

the Two-Center Approximation (2CA). For the latter spectrum contributions from at most two different atoms of the C_4N_2 ring have been included in a two-center approximate fashion with the continuum orbitals being centered at $\overline{\mathbf{R}}_{C_4N_2}$. We have included partial waves up to $l_{max} = 15$ for the PES and 2CA RAES, which is the current maximum supported by our code. However, the contributions of the $l = 15$ term can for some transitions reach up to 15% and 25% for the $\overline{\mathbf{R}}_{C_4N_2}$ (PES and 2CA RAES) and $\mathbf{R}_N$ (PES) origins, respectively. Hence, partial waves with higher angular momenta might be needed to ensure complete convergence of the respective band intensities. However, for the 1CA decay spectrum, corresponding to the autoionization contribution from one nitrogen atom embedded in the molecular potential, the intensities converged already for $l = 4$, although $l_{max} = 9$ has been used.

At first glance, our simulations reproduce the experimental PES results very well, whereas the RAES intensities are matched to a lesser extent. For the detailed discussion, we follow Bolognesi et al.[77] in dividing the spectra into three regions, spanning binding energies up to 13 eV (1), 20 eV (2), and > 20 eV (3). We begin the discussion with the PES. Region (1) contains clearly distinguishable single hole states with the leading configurations $n_{N_-}(7b_2)^{-1}$ at 9.8 eV, $\pi_3(2b_1)^{-1}$ at 10.5 eV, $n_{N_+}(11a_1)^{-1}$ at 11.2 eV and $\pi_2(1a_2)^{-1}$ at 11.5 eV in Fig. 4 (b). This assignment agrees with the one obtained in Refs. 99,100, regarding the still controversial question of the ordering of the $n_{N_+}(11a_1)^{-1}$ and $\pi_2(1a_2)^{-1}$ fea-

tures[77] that are difficult to resolve experimentally. The region (2), marks the transition from single to double hole states. The feature around 14.5 eV comprises three states of dominant $\pi_1(1b_1)^{-1}$, $\sigma(10a_1)^{-1}$ and $\sigma(6b_2)$ nature with an admixture of up to 20% π^* character. The other two peaks, correspond dominantly to lower lying σ^{-1} states with up to 30% π^* character. Finally, in region (3), the density of the ionized states increases considerably and they are predominantly of two hole character. Here, multiple transitions contribute to each peak and an assignment in terms of orbitals is not possible anymore.

Concerning the intensities, in region (1), the height ratio of the double peak is not symmetric. The low and high energy parts are enhanced with the $\mathbf{R}_N$ and $\overline{\mathbf{R}}_{C_4N_2}$ origins, respectively. In region (2), $\overline{\mathbf{R}}_{C_4N_2}$ leads to a better agreement for the first two peaks, whereas using $\mathbf{R}_N$ resembles the part around 17.5 eV better. The experimental data in region (3) yields four distinct features around 21 eV, 25 eV, 26.5 eV, and 29.5 eV as well as an unresolved tail at higher energies. Our data reproduces the general structure, albeit the features appear blue shifted by 1.3 eV, 0.5 eV, 1.1 eV, and 0.8 eV, respectively. Further, the relative intensity of this region tends to be underestimated, in particular with the $\overline{\mathbf{R}}_{C_4N_2}$ origin. Especially the feature around 27.5 eV appears only as a small shoulder. Since the PES of O_2 demonstrated only minor variations for different origins, one might attribute the deviations observed here to the fact that the angular momentum expansion is not fully converged in this case.

Now concerning the RAES of the E6 resonance, Fig. 4 (b). Both, the 1CA and 2CA spectra show only a very approximate correspondence to the experimental data. In region (1) the theoretical RAES resembles the shape of the experimental reference. It can be assigned to pure participator decay into the single hole states that constitute the PES in this region as well. Already in region (2), we find that spectator decay is dominating and the number of final states increases to around 40 for the whole region. Here, our data yields two distinct peaks similar to the experimental result, but blue shifted by about 0.7 eV. The relative intensity of the one at 17.5 eV, which is the most prominent feature in the experimental data, however, is underestimated by a factor of 2.5 in the 1CA. Finally, region (3) comprises more than 250 mainly spectator transitions with appreciable intensities that in total constitute the spectrum. Here, the experimental data comprises 4 features. A broad one $(19.0 - 24.0\text{ eV})$ is only partially reproduced in the theoretical spectrum. It is too narrow, spanning only $21.5 - 23.5$ eV and its rising edge is blue shifted by approximately 3.0 eV. Next, a narrower peak around 26.0 eV is found in our data with a blue shift of 0.5 eV but too large in intensity. Furthermore, the two broad features around 29.0 eV and 37.0 eV in the experiment are represented with respective blue shifts of 3.0 eV and 5.0 eV. Generally, the tail region, > 25.0 eV carries too much intensity in our calculation, especially in the 2CA variant.

In comparison to our RAES results for O_2 and NO_2, we find the extent of the disagreement between the theoretical and experimental decay spectra surprising. This is especially striking, since the PES is represented quite well by our approach, indicating that the valence electronic structure of the cation is well described with the present active space and that the employed continuum model captures the most important effects. Unfortunately, a detailed scrutinization of this deviation is difficult since, to the best of our knowledge, references obtained on a higher level of theory are not available. Tentatively, the disagreement can be assigned to the exclusion of the hydrogen atoms within both, 1CA and 2CA, which might induce a similar characteristic as for methane, see Fig. 1. This line of argumentation is supported by the fact that region (2), with the greatest mismatch to the experimental reference, comprises ionized states bearing holes in the σ valence orbitals which contain a considerable hydrogen character. Further, the 2CA ansatz, that includes all "heavy" atoms does not improve the agreement with the experimental data in this region, although the total decay rates increase by a factor of 3.5 from 32.5 meV (1CA) to 114.7 meV (2CA). While this indicates that non-local contributions from the C and N atoms play a considerable role for the decay of the E6 resonance, it also shows that the inclusion of the hydrogen atoms might be necessary, to further improve the spectrum. Another reason could be that the active space used herein does in fact not describe the core-excited states well enough, as pointed out in the discussion of the XAS.

We conclude the discussion of this system with the following recapitulation. The pyrimidine molecule has been studied with a large active space, allowing one electron to be removed from the N(1s) orbitals, as well as a single electron to be excited into 8 valence orbitals. With this active space not all prominent XAS features can be be reproduced. However, irrespective of the continuum orbital origin, the experimental PES has been reproduced quite well with the SCI approach, although it is not fully converged at $l_{\max} = 15$. This also indicates that the valence electronic structure is described sufficiently accurate. Still, the simulated RAES of the E6 resonance obtained with our approach yield notable differences to the experimental reference[77] in the spectator decay region. We tentatively ascribe this to the exclusion of the hydrogen atoms within the employed 1CA and 2CA schemes, which might influence different spectral regions to a varying degree, thus altering the shape of the spectrum. Further studies including the hydrogen orbitals as well as involving an active space that covers more core-hole correlation need to be carried out to rule out these remaining uncertainties.

V. CONCLUSIONS AND OUTLOOK

In this article, we have presented the SCI approach for the evaluation of photoionization cross sections and

partial Auger decay rates for the case of molecules. It is a logical continuation of our previous benchmark of the protocol for the atomic case of RAES of the neon $1s^{-1}3p$ resonance, where it was shown to yield spectra and total decay rates in good agreement with experimental references.[55] The central approximation in the protocol is that the angular structure of the molecular potential is averaged out, leading to spherically symmetric continuum orbitals that are obtained by numerically solving the radial Schrödinger equation. As has been shown here, such an approach, being natural for atoms, in fact provides a valuable insight into the nature of molecular photoionization and autoionization spectral features as well.

The investigated molecules have been selected to represent different classes. To perform a thorough test of the protocol, the XAS, PES, and RAES at the carbon, oxygen and nitrogen K-edges of CH_4, O_2, and NO_2 as well as pyrimidine, respectively, have been evaluated and compared to the experimental data. Of course, accurate calculations of these molecules in the gas phase require the inclusion of vibrational effects, with the O_2 $3\sigma_u$ resonance being an extreme case. Here, they have been excluded and the discussion is focused on the purely electronic effects.

From the viewpoint of electronic structure calculations, this protocol can be applied together with any quantum chemistry method, allowing for a CI-like representation of the wave function. In particular, in the present article the bound electronic structure is obtained at the RASSCF/RASPT2 level. The analysis of the XAS has shown that this method with the respective active spaces is capable of capturing the most important effects in core-excited states of neutral systems with the exception of pyrimidine, possibly requiring a larger active space. Further, the energetic positions of lines in PES and RAES, characterizing the structure of the valence levels of the ionized system could be reproduced with an overall high accuracy. However, there is a tendency to overestimate the binding energies towards high-energy parts of the spectra.

Regarding the PES intensities, the SCI approach has lead to fairly good agreement with experiments for NO_2, pyrimidine, and the lower binding energy region of O_2, but in some cases discrepancies have been observed. For example, the high binding energy region of the O_2 PES bears too few intensity, which we attribute to the lack of combination transitions to Rydberg orbitals in the active space. In CH_4, the relative intensities of the a_1^{-1} and t_2^{-1} peaks PES at 282.2 eV can not be correctly described using our approach.

The SCI approach appears to produce in general reasonable RAES, for all resonances in methane, the $1\pi_g$ resonance of O_2, and the high-energy flank of the $2b_1$ resonance in NO_2. Those spectra which cannot be accurately reproduced generally correspond to cases when either vibronic effects are important, several resonances are overlaying, or the active space is too small. Nevertheless, this information can be still valuable for the

assignment of experimental spectra.

The $\mathcal{H}$ coupling has been applied only to CH_4 and O_2, where it has led to the best agreement. However, the approximate r^{-1} coupling produces very similar spectra for CH_4, whereas for O_2 the differences between both couplings are larger. Overall, the origin dependence of the spectra in both O_2 and pyrimidine cases has been found to be relatively small, especially when $\mathcal{H}$ coupling is applied. The One-Center Approximation (1CA) seems to be not applicable in all cases for the present method. Although it is very attractive from the computational viewpoint as it substantially reduces the numerical effort. For example, the CH_4 1CA results do not agree well to experiment, while for NO_2 they closely resemble the r^{-1} ones. However, for pyrimidine only the 1CA and 2CA, including two-center contributions from only heavy atoms, were feasible. Unfortunately, these approximations do not lead to good agreement with experiment in this case; we suppose that the deviations can be rather attributed to deficiencies of the quantum chemistry setup, exclusion of hydrogen contributions, or the SCI model itself.

Finally, some of the deviations between calculations and experiment can be mitigated if the one-step model is applied. This might be especially needed to describe spectral regions with notable participator decay character and cases with strong interference between different ionization pathways. Taking into account nuclear motion might also be highly advisable.

ACKNOWLEDGMENTS

REFERENCES

[1] A. Stolow, A. E. Bragg, and D. M. Neumark, Chem. Rev. **104**, 1719 (2004).

[2] S. Hofmann, *Auger- and X-Ray Photoelectron Spectroscopy in Materials Science: A User-Oriented Guide*, Springer Series in Surface Sciences No. 49 (Springer, Heidelberg , New York, 2013).

[3] S. Hüfner, *Photoelectron Spectroscopy: Principles and Applications* (Springer, Berlin, Heidelberg, 2003).

[4] D. Yepes, R. Seidel, B. Winter, J. Blumberger, and P. Jaque, J. Phys. Chem. B **118**, 6850 (2014).

[5] R. Golnak, S. I. Bokarev, R. Seidel, J. Xiao, G. Grell, K. Atak, I. Unger, S. Thürmer, S. G. Aziz, O. Kühn, B. Winter, and E. F. Aziz, Sci. Rep. **6**, 24659 (2016).

[6] S. I. Bokarev and O. Kühn, Wiley Interdiscip. Rev. Comput. Mol. Sci. , e1433 (2019).

[7] H. Wang, T. Möhle, O. Kühn, and S. I. Bokarev, Phys. Rev. A **98**, 013408 (2018).

[8] A. Rudenko, L. Inhester, K. Hanasaki, X. Li, S. J. Robatjazi, B. Erk, R. Boll, K. Toyota, Y. Hao, O. Vendrell, C. Bomme, E. Savelyev, B. Rudek, L. Foucar, S. H. Southworth, C. S. Lehmann, B. Kraessig, T. Marchenko, M. Simon, K. Ueda, K. R. Ferguson, M. Bucher, T. Gorkhover, S. Carron, R. Alonso-Mori, J. E. Koglin, J. Correa, G. J. Williams, S. Boutet, L. Young,

C. Bostedt, S.-K. Son, R. Santra, and D. Rolles, Nature **546**, 129 (2017).

[9] I. Unger, R. Seidel, S. Thürmer, M. N. Pohl, E. F. Aziz, L. S. Cederbaum, E. Muchová, P. Slavíček, B. Winter, and N. V. Kryzhevoi, Nat. Chem. **9**, 708 (2017).

[10] V. Stumpf, K. Gokhberg, and L. S. Cederbaum, Nat. Chem. **8**, 237 (2016).

[11] P. Slavíček, N. V. Kryzhevoi, E. F. Aziz, and B. Winter, J. Phys. Chem. Lett. **7**, 234 (2016).

[12] R. W. Howell, Int. J. Radiat. Biol. **84**, 959 (2008).

[13] A. Yokoya and T. Ito, Int. J. Radiat. Biol. **93**, 743 (2017).

[14] M. Nisoli, P. Decleva, F. Calegari, A. Palacios, and F. Martín, Chem. Rev. **117**, 10760 (2017).

[15] T. Åberg, G. Howat, L. Karlsson, J. A. R. Samson, H. Siegbahn, and A. F. Starace, *Corpsucles and Radiation in Matter I*, edited by W. Mehlhorn, Encyclopedia of Physics, Vol. 31 (Springer, Berlin, 1982).

[16] A. F. Starace, in *Corpsucles and Radiation in Matter I*, Encyclopedia of Physics, Vol. 31, edited by W. Mehlhorn and W. Mehlhorn (Springer, Berlin, 1982) pp. 1–121.

[17] U. Fano, Physical Review **124**, 1866 (1961), 10750.

[18] G. Breit and H. A. Bethe, Phys. Rev. **93**, 888 (1954).

[19] T. Åberg and G. Howat, in *Corpsucles and Radiation in Matter I*, Encyclopedia of Physics, Vol. 31, edited by W. Mehlhorn (Springer, Berlin, 1982) pp. 469–619.

[20] P. G. Burke, *R-Matrix Theory of Atomic Collisions: Application to Atomic, Molecular and Optical Processes*, Springer Series on Atomic, Optical, and Plasma Physics No. 61 (Springer, Heidelberg, 2011).

[21] H. Bachau, E. Cormier, P. Decleva, J. E. Hansen, and F. Martín, Rep. Prog. Phys. **64**, 1815 (2001).

[22] R. Colle and S. Simonucci, Phys. Rev. A **39**, 6247 (1989).

[23] R. Colle and S. Simonucci, Phys. Rev. A **48**, 392 (1993).

[24] C. Marante, M. Klinker, I. Corral, J. González-Vázquez, L. Argenti, and F. Martín, J. Chem. Theor. Comput. **13**, 499 (2017).

[25] F. Martín, J. Phys. B At. Mol. Opt. Phys. **32**, R197 (1999).

[26] R. Colle, D. Embriaco, M. Massini, S. Simonucci, and S. Taioli, J. Phys. B At. Mol. Opt. Phys. **37**, 1237 (2004).

[27] M. Klinker, C. Marante, L. Argenti, J. González-Vázquez, and F. Martín, Phys. Rev. A **98**, 033413 (2018).

[28] D. Toffoli, M. Stener, G. Fronzoni, and P. Decleva, Chemical Physics **276**, 25 (2002).

[29] D. Catone, M. Stener, P. Decleva, G. Contini, N. Zema, T. Prosperi, V. Feyer, K. C. Prince, and S. Turchini, Phys. Rev. Lett. **108**, 083001 (2012).

[30] M. Stener, D. Toffoli, G. Fronzoni, and P. Decleva, Theor Chem Account **117**, 943 (2007).

[31] F. Calegari, D. Ayuso, A. Trabattoni, L. Belshaw, S. D. Camillis, S. Anumula, F. Frassetto, L. Poletto, A. Palacios, P. Decleva, J. B. Greenwood, F. Martín, and M. Nisoli, Science **346**, 336 (2014).

[32] E. Plésiat, S. E. Canton, J. D. Bozek, P. Decleva, and F. Martín, J. Phys. Chem. A **123**, 1062 (2019).

[33] P. V. Demekhin, D. V. Omel'yanenko, B. M. Lagutin, V. L. Sukhorukov, L. Werner, A. Ehresmann, K.-H. Schartner, and H. Schmoranzer, Opt. Spectrosc. **102**, 318 (2007).

[34] P. V. Demekhin, I. D. Petrov, V. L. Sukhorukov, W. Kielich, P. Reiss, R. Hentges, I. Haar, H. Schmoranzer, and A. Ehresmann, Phys. Rev. A **80** (2009).

[35] H. I. B. Banks, D. A. Little, J. Tennyson, and A. Emmanouilidou, Phys. Chem. Chem. Phys. **19**, 19794 (2017).

[36] H. Siegbahn, L. Asplund, and P. Kelfve, Chem. Phys. Lett. **35**, 330 (1975).

[37] F. P. Larkins, L. C. Tulea, and E. Z. Chelkowska, Aust. J. Phys. **43**, 625 (1990).

[38] R. Fink, J. Electron Spectrosc. Relat. Phenom. **76**, 295 (1995).

[39] O. Travnikova, R. F. Fink, A. Kivimäki, D. Céolin, Z. Bao, and M. N. Piancastelli, Chem. Phys. Lett. **474**, 67 (2009).

[40] L. Inhester, K. Hanasaki, Y. Hao, S.-K. Son, and R. Santra, Phys. Rev. A **94**, 023422 (2016).

[41] Y. Hao, L. Inhester, K. Hansaki, and R. Santra, Struct. Dyn. **2**, 041707 (2015).

[42] C. M. Oana and A. I. Krylov, J. Chem. Phys. **131**, 124114 (2009).

[43] C. M. Oana and A. I. Krylov, J. Chem. Phys. **127**, 234106 (2007).

[44] G. Grell, S. I. Bokarev, B. Winter, R. Seidel, E. F. Aziz, S. G. Aziz, and O. Kühn, J. Chem. Phys **143**, 074104 (2015).

[45] B. Mignolet, J. O. Johansson, E. E. B. Campbell, and F. Remacle, ChemPhysChem **14**, 3332 (2013).

[46] A. O. Gunina and A. I. Krylov, J. Phys. Chem. A **120**, 9841 (2016).

[47] T. Möhle, O. S. Bokareva, G. Grell, O. Kühn, and S. I. Bokarev, J. Chem. Theor. Comput. **14**, 5870 (2018).

[48] A. Moguilevski, M. Wilke, G. Grell, S. I. Bokarev, S. G. Aziz, N. Engel, A. A. Raheem, O. Kühn, I. Y. Kiyan, and E. F. Aziz, ChemPhysChem **18**, 465 (2017).

[49] A. A. Raheem, M. Wilke, M. Borgwardt, N. Engel, S. I. Bokarev, G. Grell, S. G. Aziz, O. Kühn, I. Y. Kiyan, C. Merschjann, and E. F. Aziz, Struct. Dyn. **4**, 044031 (2017).

[50] V. Carravetta, H. Ågren, O. Vahtras, and H. J. A. Jensen, J. Chem. Phys. **113**, 7790 (2000).

[51] K. Gokhberg, V. Vysotskiy, L. S. Cederbaum, L. Storchi, F. Tarantelli, and V. Averbukh, J. Chem. Phys. **130**, 064104 (2009).

[52] P. Kolorenč, V. Averbukh, K. Gokhberg, and L. S. Cederbaum, J. Chem. Phys. **129**, 244102 (2008).

[53] M. Stener, P. Decleva, and A. Lisini, Journal of Electron Spectroscopy and Related Phenomena **74**, 29 (1995).

[54] B. Schimmelpfennig, B. Nestmann, and S. Peyerimhoff, J. Electron. Spectrosc. Relat. Phenom. **74**, 173 (1995).

[55] G. Grell, O. Kühn, and S. I. Bokarev, Phys. Rev. A **100**, 042512 (2019).

[56] F. Holzmeier, T. J. A. Wolf, C. Gienger, I. Wagner, J. Bozek, S. Nandi, C. Nicolas, I. Fischer, M. Gühr, and R. F. Fink, J. Chem. Phys. **149**, 034308 (2018).

[57] A. Kivimäki, M. Neeb, B. Kempgens, H. M. Köppe, and A. M. Bradshaw, J. Phys. B At. Mol. Opt. Phys. **29**, 2701 (1996).

[58] C. D. Caldwell, S. J. Schaphorst, M. O. Krause, and J. Jiménez-Mier, J. Electron Spectrosc. Relat. Phenom. **67**, 243 (1994).

[59] V. G. Wentzel, Z. Physik **43**, 524 (1927).

[60] B. H. Bransden and C. J. Joachain, *Physics of Atoms and Molecules*, 1st ed. (Longman Scientific & Technical, Essex, 1983).

[61] F. W. J. Olver, D. W. Lozier, R. F. Boisvert, and C. W. Clark, eds., *NIST Handbook of Mathematical Functions*, 1st ed. (Cambridge University Press, 2010).

[62] P.-O. Widmark, P. Å. Malmqvist, and B. O. Roos, Theor. Chim. Acta **77**, 291 (1990).

[63] K. Kaufmann, W. Baumeister, and M. Jungen, J. Phys. B At. Mol. Opt. Phys. **22**, 2223 (1989).

[64] J. Almlöf and P. R. Taylor, J. Chem. Phys. **86**, 4070 (1987).

[65] I. Fernández Galván, M. Vacher, A. Alavi, C. Angeli, F. Aquilante, J. Autschbach, J. J. Bao, S. I. Bokarev, N. A. Bogdanov, R. K. Carlson, L. F. Chibotaru, J. Creutzberg, N. Dattani, M. G. Delcey, S. S. Dong, A. Dreuw, L. Freitag, L. M. Frutos, L. Gagliardi, F. Gendron, A. Giussani, L. González, G. Grell, M. Guo, C. E. Hoyer, M. Johansson, S. Keller, S. Knecht, G. Kovačević, E. Källman, G. Li Manni, M. Lundberg, Y. Ma, S. Mai, J. P. Malhado, P. Å. Malmqvist,

P. Marquetand, S. A. Mewes, J. Norell, M. Olivucci, M. Oppel, Q. M. Phung, K. Pierloot, F. Plasser, M. Reiher, A. M. Sand, I. Schapiro, P. Sharma, C. J. Stein, L. K. Sørensen, D. G. Truhlar, M. Ugandi, L. Ungur, A. Valentini, S. Vancoillie, V. Veryazov, O. Weser, T. A. Wesołowski, P.-O. Widmark, S. Wouters, A. Zech, J. P. Zobel, and R. Lindh, J. Chem. Theory Comput. **15**, 5925 (2019).

[66] M. J. Frisch, G. W. Trucks, H. B. Schlegel, G. E. Scuseria, M. A. Robb, J. R. Cheeseman, G. Scalmani, V. Barone, B. Mennucci, G. A. Petersson, H. Nakatsuji, M. Caricato, X. Li, H. P. Hratchian, A. F. Izmaylov, J. Bloino, G. Zheng, J. L. Sonnenberg, M. Hada, M. Ehara, K. Toyota, R. Fukuda, J. Hasegawa, M. Ishida, T. Nakajima, Y. Honda, O. Kitao, H. Nakai, T. Vreven, J. J. A. Montgomery, J. E. Peralta, F. Ogliaro, M. Bearpark, J. J. Heyd, E. Brothers, K. N. Kudin, V. N. Staroverov, R. Kobayashi, J. Normand, K. Raghavachari, A. Rendell, J. C. Burant, S. S. Iyengar, J. Tomasi, M. Cossi, N. Rega, J. M. Millam, M. Klene, J. E. Knox, J. B. Cross, V. Bakken, C. Adamo, J. Jaramillo, R. Gomperts, R. E. Stratmann, O. Yazyev, A. J. Austin, R. Cammi, C. Pomelli, J. W. Ochterski, R. L. Martin, K. Morokuma, V. G. Zakrzewski, G. A. Voth, P. Salvador, J. J. Dannenberg, S. Dapprich, A. D. Daniels, O. Farkas, J. B. Foresman, J. V. Ortiz, J. Cioslowski, and D. J. Fox, "Gaussian 09, Revision D.01," Tech. Rep. (Gaussian Inc., Wallingfort, CT, 2009).

[67] K. P. Huber and G. Herzberg, in *Molecular Spectra and Molecular Structure* (Springer, Boston, MA, 1979) pp. 8–689.

[68] P.-Å. Malmqvist, A. Rendell, and B. O. Roos, J. Phys. Chem. **94**, 5477 (1990).

[69] P. Å. Malmqvist, K. Pierloot, A. R. M. Shahi, C. J. Cramer, and L. Gagliardi, J. Chem. Phys. **128**, 204109 (2008).

[70] B. O. Roos, P. R. Taylor, and P. Siegbahn, Chem. Phys. **48**, 157 (1980).

[71] K. Andersson, P. A. Malmqvist, B. O. Roos, A. J. Sadlej, and K. Wolinski, J. Phys. Chem. **94**, 5483 (1990).

[72] F. Aquilante, J. Autschbach, R. K. Carlson, L. F. Chibotaru, M. G. Delcey, L. De Vico, I. F. Galván, N. Ferré, L. M. Frutos, L. Gagliardi, M. Garavelli, A. Giussani, C. E. Hoyer, G. Li Manni, H. Lischka, D. Ma, P. Å. Malmqvist, T. Müller, A. Nenov, M. Olivucci, T. B. Pedersen, D. Peng, F. Plasser, B. Pritchard, M. Reiher, I. Rivalta, I. Schapiro, J. Segarra-Martí, M. Stenrup, D. G. Truhlar, L. Ungur, A. Valentini, S. Vancoillie, V. Veryazov, V. P. Vysotskiy, O. Weingart, F. Zapata, and R. Lindh, J. Comput. Chem. **37**, 506 (2016).

[73] P. Å. Malmqvist, Int. J. Quantum Chem. **30**, 479 (1986).

[74] G. Bieri and L. Åsbrink, J. Electron Spectrosc. Relat. Phenom. **20**, 149 (1979).

[75] O. Edqvist, E. Lindholm, L. E. Selin, and L. Åsbrink, Phys. Scr. **1**, 25 (1970).

[76] S. Katsumata, H. Shiromaru, K. Mitani, S. Iwata, and K. Kimura, Chemical Physics **69**, 423 (1982).

[77] P. Bolognesi, P. O'Keeffe, Y. Ovcharenko, L. Avaldi, and V. Carravetta, J. Chem. Phys. **136**, 154308 (2012).

[78] K. Ueda, M. Okunishi, H. Chiba, Y. Shimizu, K. Ohmori, K. Sato, E. Shigemasa, and N. Kosugi, Chem. Phys. Let. **236**, 311 (1995).

[79] J. Schirmer, A. B. Trofimov, K. J. Randall, J. Feldhaus, A. M. Bradshaw, Y. Ma, C. T. Chen, and F. Sette, Phys. Rev. A **47**, 1136 (1993).

[80] M. Higashi, E. Hiroike, and T. Nakajima, Chem. Phys. **68**, 377 (1982).

[81] O. M. Kvalheim, Chem. Phys. Lett. **86**, 159 (1982).

[82] J. Feldhaus, W. Erlebach, A. L. D. Kilcoyne, K. J. Randall, and M. Schmidbauer, Rev. Sci. Instrum. **63**, 1454 (1992).

[83] M. Banna and D. Shirley, Chem. Phys. Lett. **33**, 441 (1975).

[84] C. Backx and M. J. V. der Wiel, J. Phys. B: At. Mol. Phys. **8**, 3020 (1975).

[85] Y. Ma, C. T. Chen, G. Meigs, K. Randall, and F. Sette, Phys. Rev. A **44**, 1848 (1991).

[86] S. L. Sorensen, R. Fink, R. Feifel, M. N. Piancastelli, M. Bässler, C. Miron, H. Wang, I. Hjelte, O. Björneholm, and S. Svensson, Phys. Rev. A **64**, 012719 (2001).

[87] M. Neeb, J.-E. Rubensson, M. Biermann, W. Eberhardt, K. Randall, J. Feldhaus, A. Kilcoyne, A. Bradshaw, Z. Xu, P. Johnson, and Y. Ma, Chemical Physics Letters **212**, 205 (1993).

[88] T. X. Carroll and T. D. Thomas, J. Chem. Phys. **89**, 5983 (1988).

[89] M. Coreno, M. de Simone, K. C. Prince, R. Richter, M. Vondráček, L. Avaldi, and R. Camilloni, Chem. Phys. Lett. **306**, 269 (1999).

[90] P. Kuiper and B. I. Dunlap, The Journal of Chemical Physics **100**, 4087 (1994).

[91] S. Schaphorst, C. Caldwell, M. Krause, and J. Jiménez-Mier, Chemical Physics Letters **213**, 315 (1993).

[92] W. Wurth, J. Stöhr, P. Feulner, X. Pan, K. R. Bauchspiess, Y. Baba, E. Hudel, G. Rocker, and D. Menzel, Phys. Rev. Lett. **65**, 2426 (1990).

[93] D. Lapiano-Smith, E. Lee, C.-I. Ma, K. T. Wu, and D. M. Hanson, The Journal of Chemical Physics **93**, 2169 (1990).

[94] T. Gejo, Y. Takata, T. Hatsui, M. Nagasono, H. Oji, N. Kosugi, and E. Shigemasa, Chemical Physics **289**, 15 (2003).

[95] M. Piancastelli, V. Carravetta, I. Hjelte, A. De Fanis, K. Okada, N. Saito, M. Kitajima, H. Tanaka, and K. Ueda, Chem. Phys. Lett. **399**, 426 (2004).

[96] A. Jürgensen and R. G. Cavell, Chemical Physics **257**, 123 (2000).

[97] J. Schirmer, L. Cederbaum, and W. Von Niessen, Chemical Physics **56**, 285 (1981).

[98] G. Vall-llosera, B. Gao, A. Kivimäki, M. Coreno, J. Álvarez Ruiz, M. de Simone, H. Ågren, and E. Rachlew, The Journal of Chemical Physics **128**, 044316 (2008).

[99] D. Holland, A. Potts, L. Karlsson, M. Stener, and P. Decleva, Chemical Physics **390**, 25 (2011).

[100] P. O'Keeffe, P. Bolognesi, A. R. Casavola, D. Catone, N. Zema, S. Turchini, and L. Avaldi, Molecular Physics **107**, 2025 (2009).

[101] A. W. Potts, D. M. P. Holland, A. B. Trofimov, J. Schirmer, L. Karlsson, and K. Siegbahn, J. Phys. B: At. Mol. Opt. Phys. **36**, 3129 (2003).

[102] U. Lottermoser, P. Rademacher, M. Mazik, and K. Kowski, Eur. J. Org. Chem. **2005**, 522 (2005).

[103] L. Storchi, F. Tarantelli, S. Veronesi, P. Bolognesi, E. Fainelli, and L. Avaldi, The Journal of Chemical Physics **129**, 154309 (2008).

[104] P. Bolognesi, P. O'Keeffe, Y. Ovcharenko, M. Coreno, L. Avaldi, V. Feyer, O. Plekan, K. C. Prince, W. Zhang, and V. Carravetta, The Journal of Chemical Physics **133**, 034302 (2010).

Supplementary material:

Multi-reference protocol for (auto)ionization spectra: application to molecules

Gilbert Grell[a)] and Sergey I. Bokarev

Institut für Physik, Universität Rostock, Albert-Einstein-Str. 23-24, 18059 Rostock, Germany

(Dated: December 10, 2019)

In this contribution we present the application of the spherically averaged continuum model to the evaluation of molecular PES and AIS / AES

[a)]gilbert.grell@uni-rostock.de

1

I. ADDITIONAL DATA

Herein we present additional results for the methane and oxygen photoelectron spectrum (PES) and resonant Auger electron spectrum (RAES).

A. Methane CH_4

Below we show the PES and RAES of CH_4 obtained with continuum orbitals corresponding to different approximations to the spherically averaged potentials than the spherically averaged direct potential $V_f^J(r)$ that has been used throughout the main text. First, the dependence of the methane PES at 282.2 eV on the continuum orbital approximations is illustrated in Fig. S1. Therein the PES have been obtained using the same quantum chem-
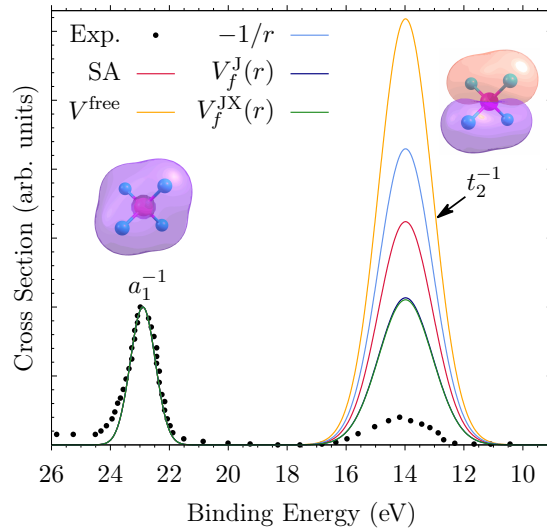

Figure S1. Theoretical results for the 282.2 eV methane valence PES obtained with continuum orbitals corresponding to the indicated potential models.[1] The experimental reference has been digitized from Kivimaeki et al.[2] In addition, the normalized Dyson orbitals for the respective a_1^{-1} and t_2^{-1} features are shown. As in the main text, the spectra have been aligned to the experimentally obtained value for the a_1^{-1} ionization potential of 22.90 eV[3]. The broadening is detailed in Table S1.

istry (QC) protocol, as described in the main text. However, results corresponding to the free-particle, effective Coulomb, direct, and direct-exchange potentials, V^{free}, $-1/r$, $V_f^J(r)$, and $V_f^{JX}(r)$, introduced in Ref. 1, are compared. Note that the $V_f^J(r)$ result corresponds to the PES shown in Fig 1. of the main text. Further, results obtained in sudden approxima-

2

tion $(SA)^4$, neglecting the continuum orbital treatment entirely, are depicted as well. In SA, the cross section of each transition is approximated by the squared norm of the respective Dyson orbital: $\sigma_{g\alpha} \approx ||\Phi_{g\alpha}||^2$. Note, that at this energy none of the potential models that have been devised by reproduces the correct intensity ratio of a_1^{-1} and t_2^{-1} features. However, the $V_f^{JX}(r)$ and $V_f^J(r)$ potentials yield the closest agreement with the experimental data.
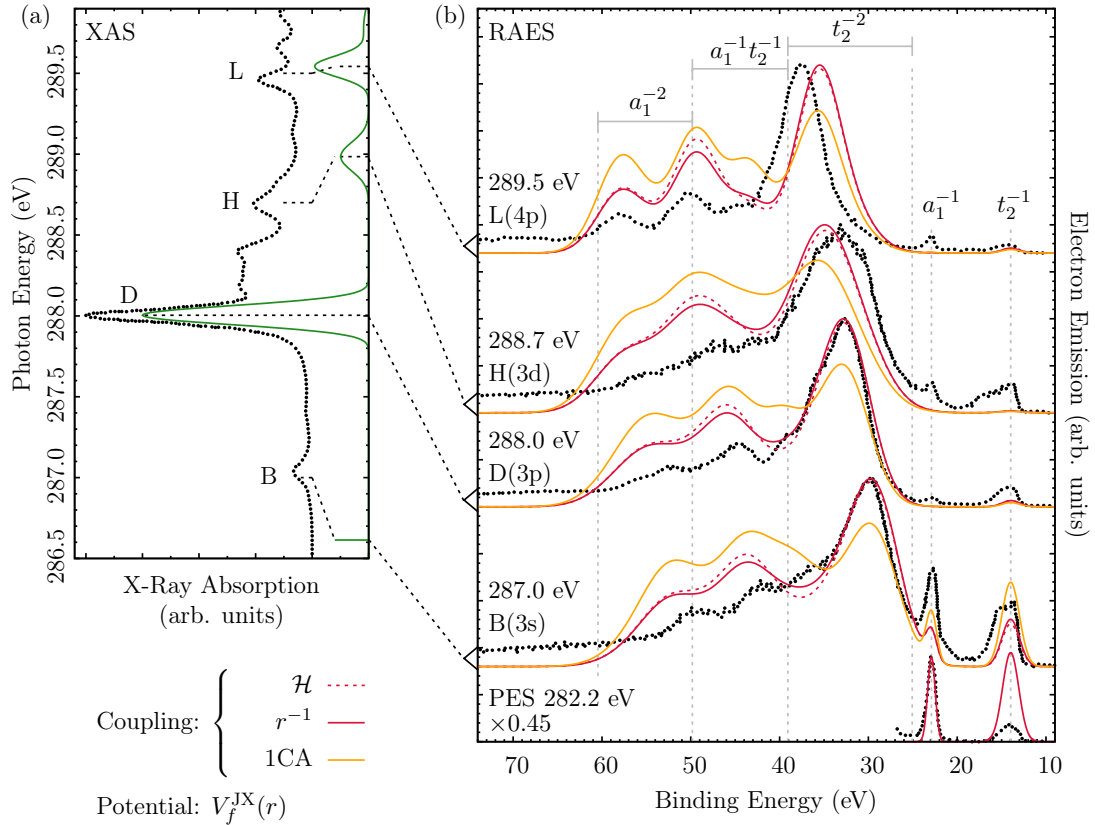

Figure S2.   All experimental data (dotted) have been digitized from Kivimaeki et al.[2] (a) Calculated (green) and experimental XAS of methane at the carbon K-edge. The dipole-forbidden $3s(a_1)$ excitation is indicated by a single stick. The assignment of the experimental spectrum[5,6] is connected to the corresponding calculated core-excited states of CH_4. (b) For each resonance depicted in (a) the RAES calculated using continuum orbitals corresponding to the direct-exchange $V_f^{JX}(r)$ potential and the indicated couplings are shown together with the measured results. The $\mathcal{H}$, r^{-1}, and 1CA spectra for one resonance have been normalized with the same constant. The respective calculated carbon Rydberg contributions are given in paranthesis for each resonance. Further, spectral regions have been assigned to different valence hole states of CH_4^+ (gray). The experimental and theoretical valence PES obtained at a photon energy of 282.2 eV are shown as well. Shifts: see main text; broadenings: see Table S1.
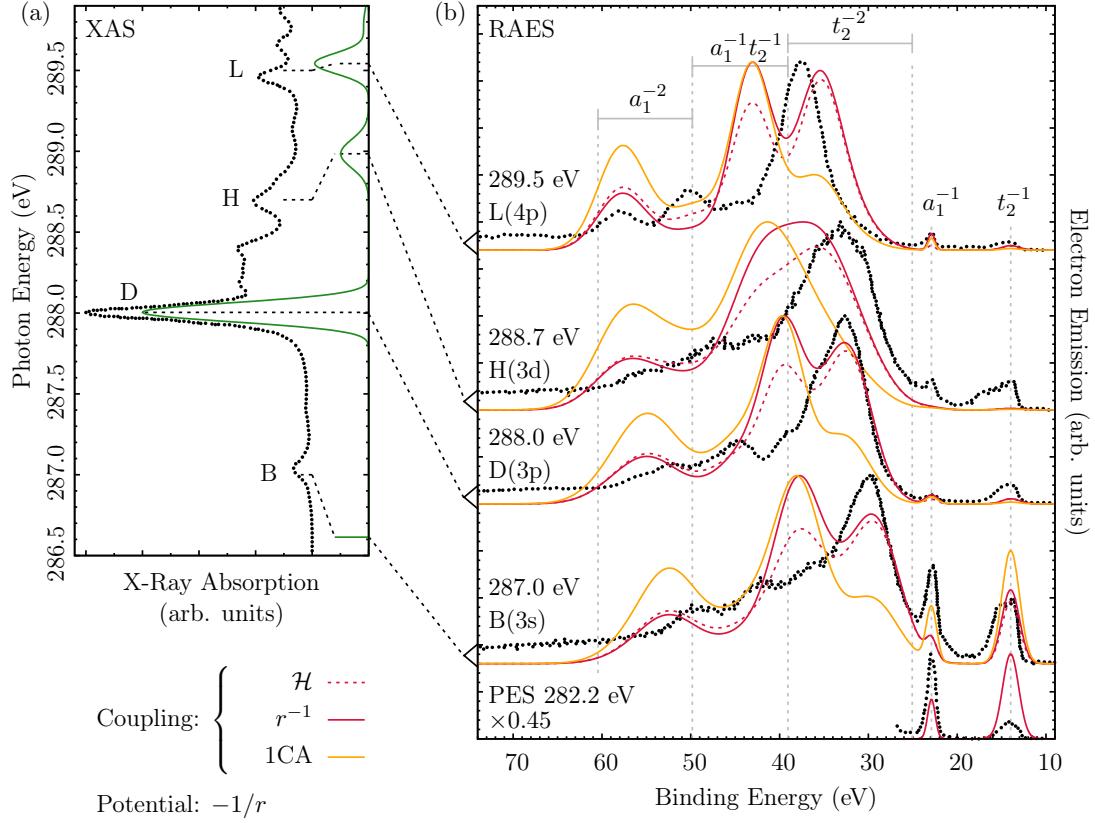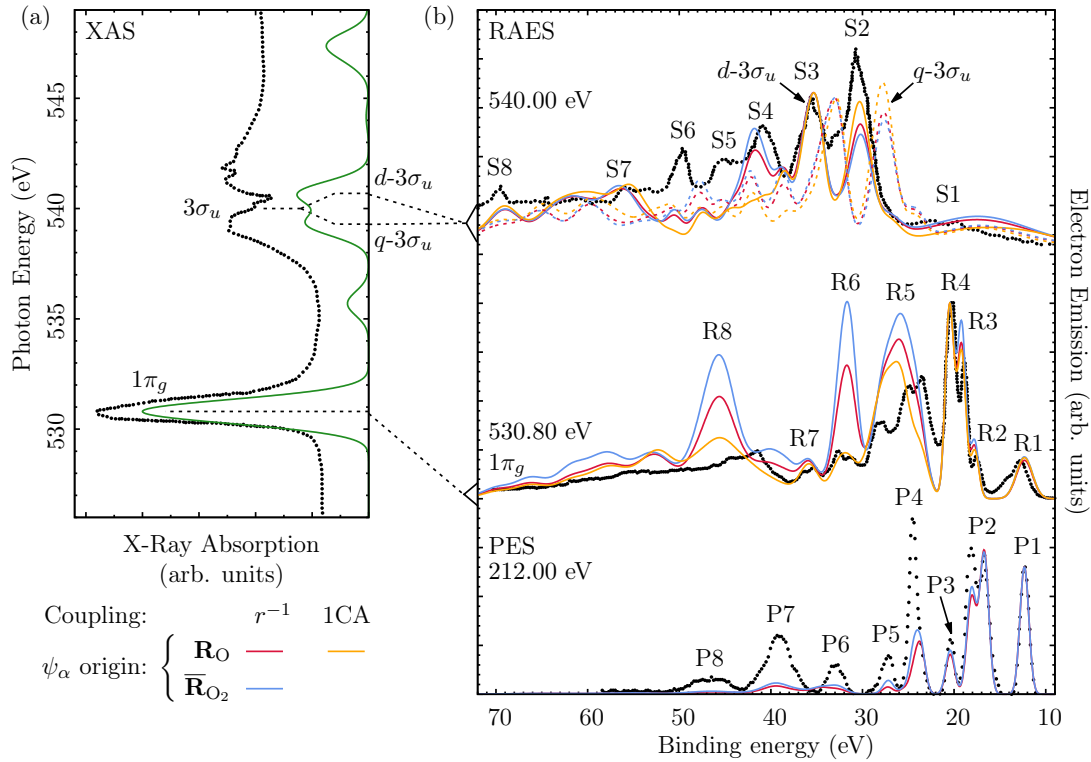
3

Figure S3. All experimental data (dotted) have been digitized from Kivimaeki et al.[2] (a) Calculated (green) and experimental XAS of methane at the carbon K-edge. The dipole-forbidden $3s(a_1)$ excitation is indicated by a single stick. The assignment of the experimental spectrum[5,6] is connected to the corresponding calculated core-excited states of CH_4. (b) For each resonance depicted in (a) the RAES calculated using continuum orbitals corresponding to the effective Coulomb potential $-1/r$ and the indicated couplings are shown together with the measured results. The $\mathcal{H}$, r^{-1}, and 1CA spectra for one resonance have been normalized with the same constant. The respective calculated carbon Rydberg contributions are given in paranthesis for each resonance. Further, spectral regions have been assigned to different valence hole states of CH_4^+ (gray). The experimental and theoretical valence PES obtained at a photon energy of 282.2 eV are shown as well. Shifts: see main text; broadenings: see Table S1.

In Figs. S2 and S3, the RAES and PES results obtained with continuum orbitals corresponding to the spherically averaged direct-exchange $V_f^{JX}(r)$ and effective Coulomb potential, $-1/r$, approaches, are depicted. For a better visual correspondence with Fig. 1 in the main text, which depicts data obtained with the spherically averaged direct potential $V_f^J(r)$, the same format has been chosen and the XAS are repeated as well. Note that in

4

comparison to the $V_f^{\mathrm{J}}(r)$ results in the main text, Fig. 1, the $V_f^{\mathrm{JX}}(r)$ RAES are slightly worse, leading to a more pronounced overestimation of the high binding energy tail (40-60 eV). The decay spectra obtained with the $-1/r$ potential, modelling the molecule as a point charge, however, deviate strongly from the $V_f^{\mathrm{J}}(r)$ and $V_f^{\mathrm{JX}}(r)$ ones. In particular the $a_1^{-1}t_2^{-1}$ region is strongly overestimated, leading to a shift of the main maximum towards the $a_1^{-1}t_2^{-1}$ part of the spectra. The 1CA enhances this characteristics even more.

B.   Oxygen O_2

Figure S4.   (a) Calculated (green) and experimental[7] (dotted) K-edge XAS of O_2. The theoretically obtained $1\pi_g$, q-$3\sigma_u$, and d-$3\sigma_u$ resonance positions are connected to the experimental excitation energies that have been used to obtain the respective RAES. In panel (b) the simulated PES and RAES are compared to the measurements by Caldwell et al.[8] Note that due to the low monochromater resolution present in the experiment[8], the whole exchange split $3\sigma_u$ double peak is excited by the incoming radiation at 540 eV. Hence, the theoretical RAES obtained for the q-$3\sigma_u$ (dashed) and d-$3\sigma_u$ (solid) resonances are depicted together with the experimental one. The theoretical results employ the $V_f^{\mathrm{J}}(r)$ potential centered at $\mathbf{R}_O$ or $\overline{\mathbf{R}}_{O_2}$, respectively. Further, the r^{-1} and 1CA couplings have been used. Shifts: see main text; broadenings: see Table S2.

5

To support the discussion in the main text, the theoretically obtained decay RAES for the $1\pi_g$, q-$3\sigma_u$, and d-$3\sigma_u$ resonances obtained with the r^{-1} an 1CA coupling are compared against the respective experimental measurements[8] in Fig. S4. The spectra have been calculated with the spherically averaged direct potential approach $V_f^J(r)$, as in the main text. Note that in particular the the $1\pi_g$ spectra are sensitive to the exclusion of the one-electron coupling terms within the approximate r^{-1} coupling approach, which leads to larger overestimations of the features R5, R6, and R8 than observed for $\mathcal{H}$ coupling (Fig. 2 of the main text). In addition, the r^{-1} $1\pi_g$ RAES show a stronger dependence on the continuum orbital origin, although the $\mathbf{R}_O$ spectra still seems to agree better with the experiment than the $\overline{\mathbf{R}}_{O_2}$ one.

6

II. BROADENING PARAMETERS

Note that unless stated otherwise, the broadening parameters compiled herein for the respective XAS, PES and RAES of the O_2, CH_4, NO_2 and $C_4H_4N_2$ molecules have been applied to to produce the spectra in all respective figures that are shown herein and in the main text.

A. Methane CH_4

The broadening parameters presented herein have been tuned such as to obtain the best representation of the respective experimental spectra that have been reported by Kivimäki et al. in Ref. 2. To construct the curve for the carbon K-edge XAS, the spectral regions corresponding to the D, H, and L features have been broadened with Gaussian profiles having respective full width at half maximums (FWHMs) parameters of 0.17 eV, 0.22 eV, and 0.21 eV. The PES, consisting of the t_2^{-1} and a_1^{-1} peaks have been obtained by broadening with a Gaussian FWHM of 1.75 eV and 1.15 eV, repsectively.

Table S1. Broadening parameters used for the CH_4 RAES corresponding to the indicated resonances. The respective binding energy intervals $\Delta\mathcal{E}_b$ and Gaussian FWHM parameters σ are given in eV.

B(3s)		D(3p)		H(3d)		L(4p)	
$\Delta\mathcal{E}_b$	σ	$\Delta\mathcal{E}_b$	σ	$\Delta\mathcal{E}_b$	σ	$\Delta\mathcal{E}_b$	σ
7.0-21.0	2.34	7.0-22.0	2.34	7.0-22.7	3.06	7.0-22.5	2.34
21.0-24.5	1.40	22.0-25.0	0.86	22.7-24.7	0.95	22.5-24.5	0.90
24.5-41.0	5.94	25.0-42.0	5.22	24.7-42.7	7.02	24.5-43.5	5.22
41.0-87.0	7.70	42.0-48.0	6.93	42.7-88.7	7.70	43.5-54.5	5.85
		48.0-88.0	7.70			54.5-89.5	6.17

7

B. Oxygen O_2

Table S2. Broadening parameters used for the O_2 XAS, PES, and RAES of the indicated resonances. The respective binding and excitation energy intervals $\Delta\mathcal{E}_b$, $\Delta\hbar\omega$, and Gaussian FWHM parameters σ are given in eV.

XAS		PES		$1\pi_g$ RAES		$3\sigma_u$ RAES	
$\Delta\hbar\omega$	σ	$\Delta\mathcal{E}_b$	σ	$\Delta\mathcal{E}_b$	σ	$\Delta\mathcal{E}_b$	σ
525-550	1.3	0.0-25.6	1.15	0.0-15.8	2.08	0.0-25.0	9.00
		25.6-29.6	1.25	15.8-21.8	1.05	25.0-33.0	2.60
		29.6-35.6	2.10	21.8-38.8	2.00	33.0-53.0	1.90
		35.6-42.6	2.85	38.8-75.0	3.50	53.0-75.0	3.50
		42.6-75.0	4.10				

C. Nitrogen dioxide NO_2

Table S3. Broadening parameters used for the NO_2 nitrogen K-edge XAS, PES, and RAES of the indicated resonances. The respective binding and excitation energy intervals $\Delta\mathcal{E}_b$, $\Delta\hbar\omega$ and Gaussian as well as Lorentzian FWHM parameters σ and γ are given in eV.

XAS		PES			$2b_1$ RAES at 402.86 eV		$2b_1$ RAES at 403.73 eV	
$\Delta\hbar\omega$	σ	$\Delta\mathcal{E}_b$	σ	γ	$\Delta\mathcal{E}_b$	σ	$\Delta\mathcal{E}_b$	σ
395.0-402.0	0.83	0.0-12.3	1.325		0.0-12.5	1.075	0.0-12.0	1.650
402.0-408.0	0.85	12.3-15.0	0.375		12.5-16.0	0.275	12.0-15.5	0.275
408.0-410.3	0.53	15.0-18.2	0.925		16.0-18.7	0.700	15.5-25.0	0.750
410.3-413.0	0.80	18.2-21.0	0.375		18.7-20.6	0.650		
413.0-425.0	5.00	21.0-21.5		0.10	20.6-25.0	0.750		
		21.5-24.0	0.375					

8

D. Pyrimidine $C_4H_4N_2$

Table S4. Broadening parameters used for the $C_4H_4N_2$ nitrogen K-edge XAS, PES, and RAES of the E6 resonance. The respective binding and excitation energy intervals $\Delta\mathcal{E}_b$, $\Delta\hbar\omega$, and Gaussian FWHM parameters σ are given in eV.

XAS		PES		E6 RAES	
$\Delta\hbar\omega$	σ	$\Delta\mathcal{E}_b$	σ	$\Delta\mathcal{E}_b$	σ
397.00-399.50	0.650	0.0-12.5	0.60	0.0-23.0	0.75
399.50-400.45	0.550	12.5-15.0	1.00	23.0-28.0	2.05
400.50-401.80	0.750	15.0-16.2	0.85	28.0-34.0	4.25
401.80-408.00	0.625	16.2-19.8	1.50	34.0-56.0	11.35
		19.8-22.5	0.95		
		22.5-28.0	1.70		
		28.0-56.0	3.10		

9

III. CARBON RYDBERG BASIS SET

This $(22s15p10d7f)/[7s5p3d2f]$ carbon Rydberg basis set has been used for the calculations regarding the CH_4 molecule, presented in the main text. It has been obtained in the following way: ANO-L exponents[9] have been supplemented by $(8s6p6d4f)$ Rydberg ones that have been generated according to the procedure in Ref. 10. The contraction coefficients have been obtained with the GENANO module[11] of OPENMOLCAS.[12] Therein the density matrices of the ground and 82 lowest core-excited states of triplet carbon, as well 229 valence-excited states of doublet C^+, have been evenly averaged. Further, the active spaces $RAS(6, 1, 1; 2, 3, 31)$ and $RAS(3, 1, 1; 1, 3, 31)$ have been employed for C and C^+, respectively.

```
C S
      50557.501    0.0000554   -0.0000141    0.0000027   -0.0000017    0.0000002   -0.0000040    0.0000011
      7524.7856    0.0004352   -0.0001105    0.0000215   -0.0000130    0.0000018   -0.0000303    0.0000082
      1694.3276    0.0023206   -0.0005900    0.0001155   -0.0000698    0.0000100   -0.0001694    0.0000478
      472.82279    0.0098932   -0.0025273    0.0004923   -0.0002964    0.0000421   -0.0006817    0.0001815
      151.71075    0.0353011   -0.0091501    0.0017944   -0.0010852    0.0001553   -0.0026706    0.0007638
      53.918746    0.1045054   -0.0281065    0.0054752   -0.0032833    0.0004662   -0.0073974    0.0019298
      20.659311    0.2422650   -0.0710452    0.0140257   -0.0084527    0.0012177   -0.0213846    0.0063148
      8.3839760    0.3848476   -0.1383681    0.0273606   -0.0162794    0.0023069   -0.0342747    0.0082613
      3.5770150    0.3062910   -0.1767318    0.0382435   -0.0242088    0.0035259   -0.0707672    0.0229626
      1.5471180    0.0661304   -0.0014742    0.0021911   -0.0029828    0.0001661    0.0188711   -0.0144040
      0.6130130    0.0024826    0.5412056   -0.1238081    0.0785679   -0.0109681    0.1228821   -0.0120022
      0.2460680    0.0031351    0.5449053   -0.2861114    0.2201439   -0.0364162    0.8980101   -0.3429385
      0.0990870   -0.0001376    0.0299654   -0.0953666   -0.0125505    0.0061750   -1.0530334    0.5598165
      0.0346800    0.0001895    0.0080153    0.6640376   -0.7107209    0.1879168   -1.8684776    0.4972325
      0.0112533   -0.0003146   -0.0112501    1.1734161   -1.7229839    0.4642457    8.1033402   -7.4432742
      0.0058584    0.0006563    0.0240021   -1.6328915    4.9423058   -2.6760962  -13.9083785   22.7282046
      0.0033460   -0.0010909   -0.0451430    2.0757306   -4.1095298    2.2678469   16.3796464  -34.0610756
      0.0020484    0.0014954    0.0678743   -2.3625403    4.4587858   -0.9719151  -19.8538822   31.9166589
      0.0013236   -0.0016393   -0.0756157    2.4793296   -5.3949310    2.6242232   21.7800560  -26.9204925
      0.0008931    0.0013110    0.0592119   -2.0103029    4.1518568   -1.9756217  -16.9049493   21.5236943
      0.0006243   -0.0006532   -0.0294083    0.9996186   -2.0494694    1.0046833    8.3077284  -10.5946867
      0.0004495    0.0001484    0.0069038   -0.2185765    0.4701302   -0.2377670   -1.8957386    2.4266113
C P
      83.333155    0.0016902   -0.0002597    0.0000917   -0.0005516    0.0000552
      19.557611    0.0130821   -0.0019827    0.0007045   -0.0041427    0.0002019
      6.0803650    0.0604217   -0.0091431    0.0032355   -0.0194424    0.0019347
      2.1793170    0.1908470   -0.0296103    0.0105390   -0.0627215    0.0019610
      0.8651500    0.3738639   -0.0640343    0.0223935   -0.1447959    0.0222276
      0.3619440    0.4121089   -0.0880526    0.0316131   -0.2029583   -0.0345343
      0.1547400    0.1542508   -0.0381202    0.0138100   -0.0273092    0.2203000
      0.0654290   -0.0025207    0.1908643   -0.0446433    1.3202008   -0.5961192
      0.0229000    0.0046373    0.6889854   -0.5616569   -0.4186885    0.5047919
      0.0099882   -0.0004755    0.4573422   -0.1469174   -2.0066859    2.2560562
      0.0056894    0.0000637   -0.3786981    1.3767454    2.6949480   -6.5298946
      0.0034757   -0.0037287    0.1431867   -0.2367263   -1.6198145    5.4086750
      0.0022421    0.0031604   -0.0853635    0.2101873    0.8394500   -1.2277959
      0.0010548   -0.0001188    0.0164980   -0.0413206   -0.2019057    0.5871641
      0.0005596    0.0000729   -0.0043503    0.0105962    0.0531507   -0.1386142
C D
      1.9000000    0.0009482   -0.0077763    0.0040482
      0.6650000    0.0050964   -0.0332340    0.0167271
      0.2327500    0.0151610   -0.1801961    0.1012733
      0.0814630    0.0806746   -0.6635421    0.3425014
      0.0274457    0.3997480   -0.4010929   -0.0644277
      0.0142044    0.4478216    0.7300550   -0.6082779
      0.0080766    0.2124006   -0.2118336   -0.1330624
      0.0049272   -0.0279700    0.3318272    0.8205665
      0.0021371   -0.0111903    0.0462477    0.4680205
      0.0010717   -0.0006853    0.0066452   -0.0424699
```

10

```
C F
      1.2500000    0.0005086   -0.0003031
      0.5000000    0.0016939    0.0058104
      0.2000000    0.0212941    0.0102196
      0.0790699    0.1328150    0.2156680
      0.0357629    0.4158943    0.1920921
      0.0184778    0.3477771    0.8923479
      0.0104930    0.2709021   -1.4985133
```

REFERENCES

[1] G. Grell, O. Kühn, and S. I. Bokarev, Phys. Rev. A **100**, 042512 (2019).

[2] A. Kivimäki, M. Neeb, B. Kempgens, H. M. Köppe, and A. M. Bradshaw, J. Phys. B At. Mol. Opt. Phys. **29**, 2701 (1996).

[3] G. Bieri and L. Åsbrink, J. Electron Spectrosc. Relat. Phenom. **20**, 149 (1979).

[4] T. Åberg, Phys. Rev. **156**, 35 (1967).

[5] K. Ueda, M. Okunishi, H. Chiba, Y. Shimizu, K. Ohmori, K. Sato, E. Shigemasa, and N. Kosugi, Chem. Phys. Let. **236**, 311 (1995).

[6] J. Schirmer, A. B. Trofimov, K. J. Randall, J. Feldhaus, A. M. Bradshaw, Y. Ma, C. T. Chen, and F. Sette, Phys. Rev. A **47**, 1136 (1993).

[7] Y. Ma, C. T. Chen, G. Meigs, K. Randall, and F. Sette, Phys. Rev. A **44**, 1848 (1991).

[8] C. D. Caldwell, S. J. Schaphorst, M. O. Krause, and J. Jiménez-Mier, J. Electron Spectrosc. Relat. Phenom. **67**, 243 (1994).

[9] P.-O. Widmark, P. Å. Malmqvist, and B. O. Roos, Theor. Chim. Acta **77**, 291 (1990).

[10] K. Kaufmann, W. Baumeister, and M. Jungen, J. Phys. B At. Mol. Opt. Phys. **22**, 2223 (1989).

[11] J. Almlöf and P. R. Taylor, J. Chem. Phys. **86**, 4070 (1987).

[12] I. Fernández Galván, M. Vacher, A. Alavi, C. Angeli, F. Aquilante, J. Autschbach, J. J. Bao, S. I. Bokarev, N. A. Bogdanov, R. K. Carlson, L. F. Chibotaru, J. Creutzberg, N. Dattani, M. G. Delcey, S. S. Dong, A. Dreuw, L. Freitag, L. M. Frutos, L. Gagliardi, F. Gendron, A. Giussani, L. González, G. Grell, M. Guo, C. E. Hoyer, M. Johansson, S. Keller, S. Knecht, G. Kovačević, E. Källman, G. Li Manni, M. Lundberg, Y. Ma, S. Mai, J. P. Malhado, P. Å. Malmqvist, P. Marquetand, S. A. Mewes, J. Norell, M. Olivucci, M. Oppel, Q. M. Phung, K. Pierloot, F. Plasser, M. Reiher, A. M. Sand, I. Schapiro, P. Sharma, C. J. Stein, L. K. Sørensen, D. G. Truhlar, M. Ugandi, L. Ungur, A. Valentini, S. Vancoillie, V. Veryazov, O. Weser, T. A. Wesołowski, P.-O. Widmark, S. Wouters,

11

182

A. Zech, J. P. Zobel, and R. Lindh, J. Chem. Theory Comput. **15**, 5925 (2019).

12

10 Publications not included in the thesis

J. Chem. Theory. Comput. 15, 5925, 2019

OpenMolcas: From Source Code to Insight

I. FDEZ. GALVÁN, M. VACHER, R. LINDH ET AL.

J. Chem. Theory Comput. 14, 5870, 2018

Tuned Range-separated Density Functional Theory and Dyson Orbital Formalism for Photoelectron Spectra

T. MÖHLE, O. S. BOKAREVA, **G. GRELL**, O. KÜHN, AND S. I. BOKAREV

Phys. Chem. Chem. Phys. 19, 14248, 2017

Light-induced relaxation dynamics of the ferricyanide ion revisited by ultrafast XUV photoelectron spectroscopy

N. ENGEL, S. I. BOKAREV, A. MOGUILEVSKI, A. A. RAHEEM, R. AL-OBAIDI, T. MÖHLE, **G. GRELL** ET AL.

Structural Dynamics 4, 044031, 2017

Ultrafast kinetics of linkage isomerism in $Na_2[Fe(CN)_5NO]$ aqueous solution revealed by time-resolved photoelectron spectroscopy

A. A. RAHEEM, M. WILKE, M. BORGWARDT, N. ENGEL, S. I. BOKAREV, **G. GRELL** ET AL.

Scientific Reports 6, 24659, 2016

Joint analysis of radiative and non-radiative electronic relaxation upon X-ray irradiation of transition metal aqueous solutions

R. GOLNAK, S. I. BOKAREV, R. SEIDEL, J. XIAO, **G. GRELL** ET AL.

J. Chem. Theory Comput. 11, 1700, 2015

Tuning range-separated density functional theory for photocatalytic water splitting systems

O. S. BOKAREVA, **G. GRELL**, S. I. BOKAREV AND O. KÜHN

J. Phys. Chem. Lett. 5, 1355, 2014

Electron- and energy-transfer processes in a photocatalytic system based on an Ir(III)-photosensitizer and an iron catalyst

A. NEUBAUER, **G. GRELL**, A. FRIEDRICH, S. I. BOKAREV, P. SCHWARZBACH ET AL.

Danksagungen